DOT/FAA/AR-09/4

Air Traffic Organization
NextGen & Operations Planning
Office of Aviation Research and
Technology Development
Washington, DC 20591

Effects of Disbonds, Lightning Strikes, and Low-Velocity Impact Damage on Adhesively Bonded Composite Joints

December 2009

Final Report

This document is available to the U.S. public through the National Technical Information Service (NTIS), Springfield, Virginia 22161.

U.S. Department of Transportation
Federal Aviation Administration

NOTICE

Technical Report Documentation Page

1. Report No.	2. Government Accession No.	3. Recipient's Catalog No.
DOT/FAA/AR-09/4		

4. Title and Subtitle	5. Report Date
EFFECTS OF DISBONDS, LIGHTNING STRIKES, AND LOW-VELOCITY IMPACT DAMAGE ON ADHESIVELY BONDED COMPOSITE JOINTS	December 2009
	6. Performing Organization Code
7. Author(s) John Tomblin, Waruna Seneviratne, and Govind Ramakrishna Pillai	8. Performing Organization Report No.
9. Performing Organization Name and Address Department of Aerospace Engineering Wichita State University Wichita, KS 67260-0093	10. Work Unit No. (TRAIS) 11. Contract or Grant No.
12. Sponsoring Agency Name and Address U.S. Department of Transportation Federal Aviation Administration Air Traffic Organization NextGen & Operations Planning Office of Research and Technology Development Washington, DC 20591	13. Type of Report and Period Covered Final Report 14. Sponsoring Agency Code ACE-110

15. Supplementary Notes

The Federal Aviation Administration Airport and Aircraft Safety R&D Division COTR was Curtis Davis.

16. Abstract

Development of advanced material and process technologies has significantly increased the use of adhesively bonded joints in aircraft structures due to the favorable characteristics of these joints compared with riveted, spot-welded, and mechanically fastened structures. Joints, doublers, sandwich constructions, and repair patches are some examples of bonded applications in aircraft primary structures. Applications on structures require rigorous characterization of the adhesive joints. Short- and long-term issues must be investigated so the certification of these joints can be instituted to ensure their structural integrity throughout the service life of the aircraft. For the damage tolerance design philosophy of adhesively bonded joints, it is vital for adhesive joints to demonstrate no-growth behavior with the presence of a discrete damage. There is also a need to demonstrate the ability of adhesive joints to contain larger amounts of damage or disbond that might be incurred during flight or production without catastrophic failure. Although the effects of defects on laminated composite and sandwich construction have been investigated in detail, limited studies have been conducted in the area of impact damage on bonded joints.

The purpose of this research was to investigate the static strength of adhesively bonded composite joints with the presence of large damage. The research addressed the concerns related to manufacturing and operational defects of bonded joints, i.e., different disbond geometries, lightning strike damages, fail-safe fastener installation, and low-velocity impact damages, and their impact on static strength. Specimens that were impacted with various impactor diameters and energy levels were subjected to shear and tensile loading using picture-frame shear and single-lap shear test configurations. The other defects were only addressed using picture-frame shear loading configuration.

Test data show that a rectangular defect that spreads completely across the joint overlap region results in approximately 20% reduction in shear strength. Rectangular defects repaired with fasteners completely restored the original strength of the bonded joint. In contrast to rectangular defects, the circular- and diamond-shaped defects and through holes that are continued within the elastic trough had minimal effect.

The results of picture frame tests with specimens impacted at the 270 in-lbf energy level show a 20% reduction in shear strength. Because all the single-lap specimens with and without impact damage failed in the adherend, the shear strength was the same, irrespective of impact energy or impactor diameter.

The results from this research will aid in increased use of adhesive joints in structures and help establish inspection and maintenance practices.

17. Key Words	18. Distribution Statement
Adhesive, Defects, Impact, Disbond, Debond	This document is available to the U.S. public through the National Technical Information Service (NTIS), Springfield, Virginia 22161.

19. Security Classif. (of this report)	20. Security Classif. (of this page)	21. No. of Pages	22. Price
Unclassified	Unclassified	146	

Form DOT F 1700.7 (8-72) Reproduction of completed page authorized

ACKNOWLEDGEMENTS

The authors would like to acknowledge the technical guidance and support of Mr. Curtis Davis, Dr. Larry Ilcewicz, and Mr. Peter Shyprykevich (retired) of the Federal Aviation Administration. The support of Mr. Shin-Liang Mah and the staff of the Structures Laboratory of the National Institute for Aviation Research was greatly appreciated during the tests and data analysis.

TABLE OF CONTENTS

APPENDICES

LIST OF FIGURES

LIST OF TABLES

LIST OF ACRONYMS

CFPW	Carbon fiber plain weave
CFPW-S	Carbon fiber plain weave
CFUT	Carbon fiber unidirectional tape
EOD	Effects of defects
EOI	Effects of impact
FGSW	F-glass satin weave
FH	Filled hole
J	Joules
LT1	Lightning strike Zone 1
LT2	Lightning strike Zone 2
LTI	Lightning Technologies, Inc.
NDI	Nondestructive inspections
OH	Open hole
PFS	Picture-frame shear
psi	Pounds per square inch
SLBJ	Shear-loaded bonded joint theory
SLS	Single-lap shear
TTU	Through-transmission ultrasonic

EXECUTIVE SUMMARY

The development of advanced material and process technologies has significantly increased the use of adhesively bonded joints in aircraft structures due to the favorable characteristics of these joints compared with riveted, spot-welded, and mechanically fastened structures. Joints, doublers, sandwich constructions, and repair patches are some examples of bonded applications in aircraft primary structures. Applications on structures require rigorous characterization of the adhesive joints. Short- and long-term issues must be investigated so the certification of these joints can be instituted to ensure the structural integrity of these joints throughout the service life of the aircraft. For the damage tolerance design philosophy of adhesively bonded joints, it is vital for adhesive joints to demonstrate no-growth behavior with the presence of a discrete damage. There is also a need to demonstrate the ability of adhesive joints to contain larger amounts of damage or disbond that might be incurred during flight or production without catastrophic failure. Although the effects of defects on laminated composite and sandwich constructions have been investigated in detail, limited studies have been conducted in the area of impact damage on bonded joints.

The purpose of this research was to investigate the static strength of adhesively bonded composite joints in the presence of large damage. The research addressed the concerns related to manufacturing and operational defects of bonded joints, i.e., different disbond geometries, lightning strike damages, fail-safe fastener installation, and low-velocity impact damages, and their impact on static strength. Specimens that were impacted using different impactor diameters and energy levels were subjected to shear and tensile loading using picture-frame shear and single-lap shear test configurations. Other defects were studied using only the picture-frame shear loading configuration. The results from this research will aid in increased use of adhesive joints in structures and help establish inspection and maintenance practices.

Test data show that a rectangular defect that spreads completely across the joint overlap region results in approximately 20% reduction in shear strength. Rectangular defects repaired with fasteners completely restored the original strength of the bonded joint. In contrast to rectangular defects, the circular- and diamond-shaped defects and through holes that are continued within the elastic trough had minimal effect.

The results of picture frame tests with specimens impacted at the 270 in-lbf energy level show a 20% reduction in shear strength. Because all the single-lap specimens with and without impact damage failed in the adherend, the shear strength was the same, irrespective of impact energy or impactor diameter.

1. INTRODUCTION.

The development of advanced material and process technologies has significantly increased the use of adhesively bonded joints in aircraft structures due to the favorable characteristics of these joints compared with riveted, spot-welded, and mechanically fastened structures. Joints, doublers, sandwich constructions, and repair patches are some of the examples of bonded applications in aircraft primary structures. Applications on structures require rigorous characterization of the adhesive joints. Short- and long-term issues must be investigated so the certification of these joints can be instituted to ensure their structural integrity throughout the service life of the aircraft. This approach can avoid a catastrophic failure of bonded structures, similar to Aloha Airline's Boeing 737 incident that led to the emphasis on damage tolerance investigation of mechanically fastened metallic structures. For damage-tolerant design philosophy of adhesively bonded joints, it is vital for adhesive joints to demonstrate no-growth behavior in the presence of discrete damage. There is also a need to demonstrate the ability of adhesive joints to contain larger amounts of damage or disbond that might be incurred during flight or production without failure. Successful demonstration of these characteristics will aid in the implementation of adhesive joints to other portions of aircraft structures, provide useful information to establish inspection and maintenance practices, and allow a comparison of analytical predictions of static strength and damage tolerance substantiation with experimental data.

The structural integrity of bonded joints can be weakened by the manufacturing defects and aging concerns of the adhesive, bondline, and adherend. During the manufacturing process, the adhesive properties can be affected by the process, contamination, and inaccurate cure temperature or pressure profile.

Bondline integrity can be affected by the imperfections and aging of the adherend surface, adhesive surface, and adhesive layer in composite joints. Additionally, in metal bonded joints, a poorly prepared oxide layer or the primer can contribute to adhesive joint failures. Poor surface preparation of composite surfaces is a major concern and one of the leading causes of joint failures. Insufficient consolidation pressure during the bonding process, mismatched adherend geometries, trapped air in the adhesive mixture, etc. can cause significantly large voids that will cause a stress concentration due to load redistribution. These also can cause porosity that will degrade the adhesive properties and entrap moisture and other fluids that come into contact with the bonded joint, thus contaminating the bondline. Changes in bondline thickness within the joint can also lead to unfavorable stress concentrations that can affect the integrity of joints. The loss of surface energy, possibly caused as a result of poor surface preparation or oxidation directly, in time, can affect the structural integrity of the joint as well. In addition, viscoelastic characteristics (creep and stress relaxation) of the adhesive joints under certain repeated loading conditions must be studied to prevent bonded structure failures. Furthermore, impact, overload, and exposure to excessive heat can result in large disbonds or weak areas of the adhesive joint that alter the load path.

Defects of composite adherend, such as delamination, under cured resin, resin contamination, and wrinkles or depressions during fabrication, have been studied extensively over the years. However, the effects on the integrity of the bondline of such defects need to be evaluated and addressed during certification and quality assurance. In addition, delamination of composite adherend, impact damages, exposure to heat and humidity, and overload can deteriorate the integrity of joints. Undesirable stress concentrations due to the presence of defects in the bondline or composite can cause failure of the adherend.

Although the effects of defects (EOD) on laminated composite and sandwich constructions have been investigated in detail, limited studies have been conducted in the area of impact damage on bonded joints. The goals of this research were to investigate the static strength of adhesively bonded composite joints with the presence of large damage and to assess the impact resistance of these joints. The research addressed the concerns related to manufacturing and operational defects and their impact on static strength. The effects of different disbond geometries, lightning strike damages, and fastener installation on the residual strength of the composite bonded joints were investigated using a picture-frame shear (PFS) test setup. In addition, the effects of low-velocity impact behavior on the residual strength of composite joints were investigated using PFS and single-lap shear (SLS) test configurations. Effects of impactor diameter and joint geometry, i.e., overlap length and bondline thickness, on the damage state and the residual strength of the joints also were investigated.

2. EXPERIMENTAL PROCEDURE.

To ensure the safety of adhesively bonded joints, it is vital for adhesive joints to demonstrate no-growth behavior with the presence of discrete damage. Defects can generally be categorized as either manufacturing defects or damages incurred during service. The experimental evaluation provided information to address the following:

- Acceptable defects—establish dimensions of manufacturing defects that are found during inspection, but do not degrade the ultimate load-carrying capability.

- Repairable defects—validate a repair technique for various structural configurations in various operating environments.

- Defects beyond repair—demonstrate the size limit of the selected repair for bonded composite and metallic structures.

The experimental data included in this report characterize the residual strength of specimens that have discrete damage configurations. Specimens with various types of defects were tested and compared with undamaged (baseline) specimens. EOD on composite-bonded joints were addressed mainly through static tests conducted on joints with disbonds, lightning strike damages, and low-velocity impact damages. These defect categories are common in adhesive joints in general aviation aircraft (figure 1) and threaten the structural integrity. The damage tolerance test matrix was divided into two sections: the EOD and the effects of low-velocity impact damages. A defects test matrix was developed to investigate the effects of manufacturing defects (such as disbonds) and operational defects (such as lightning strikes) on the residual strength of the adhesive joints. In addition, the failure mechanism (i.e., catastrophic failure or damage propagation before final failure) and the failure modes (i.e., adhesive, cohesive, or adherend) were also investigated. The damage growth or the onset of damage growth was delineated using full-field strain measurement techniques that capture the stress concentration and the out-of-plane deformation around the defects. Previous investigations demonstrated the sensitivity of these techniques to detect debonded areas as well as weakened sections.

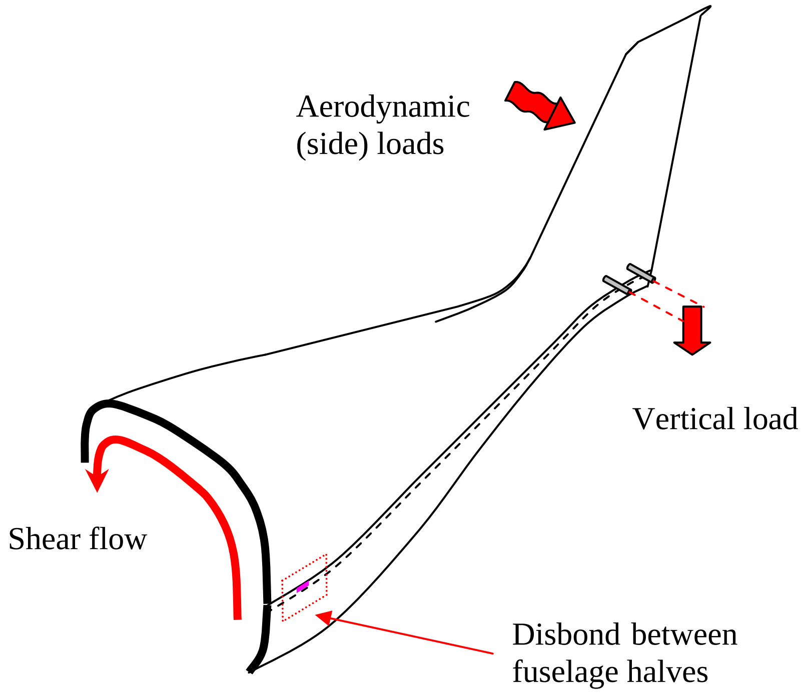

Figure 1. Typical General Aviation Fuselage Component Showing Disbond

The second segment of the damage tolerance investigation focused on investigating the effects of low-velocity impact damages on the residual strength of composite adhesive joints. This phase of the research also concentrated only on the static strength of joints. The results can also be used to refine analytical models that use progressive failure criteria and delamination or disbond growth techniques, such as virtual crack closure [1], or cohesive elements to predict the load-carrying capability of these joints with defects. These techniques are already built into finite element packages, such as ABAQUS, and can be used to investigate the progressive failure of both composite and adhesive.

2.1 THE EOD INVESTIGATION.

Large bonded regions in aircraft structures may contain disbonds due to insufficient adhesive application, poor processing, inclusions, or clamping forces. Such defects also can be a result of surface contamination or a propagation of smaller defects during cyclic loading. Inspecting these defects can be challenging; therefore, it is vital to investigate the load-carrying capabilities of adhesive joints that contain large defects. Effects of several different disbond geometries were investigated. Further, installation of fail-safe fasteners to repair such joints was also investigated. An interim step, the effect of fastener holes, was included for comparison purposes. During operation of the aircraft, adhesive joints are susceptible to lightning strikes that may endanger primary aircraft joints, such as the sections shown in figure 1. Therefore, EOD investigation was further expanded by including lightning strike damages. These composite-composite adhesive joints do not contain any lightning protection. Lightning strike zones are mainly classified according to the possibility of lightning attachment dwell time and current conduction (figure 2).

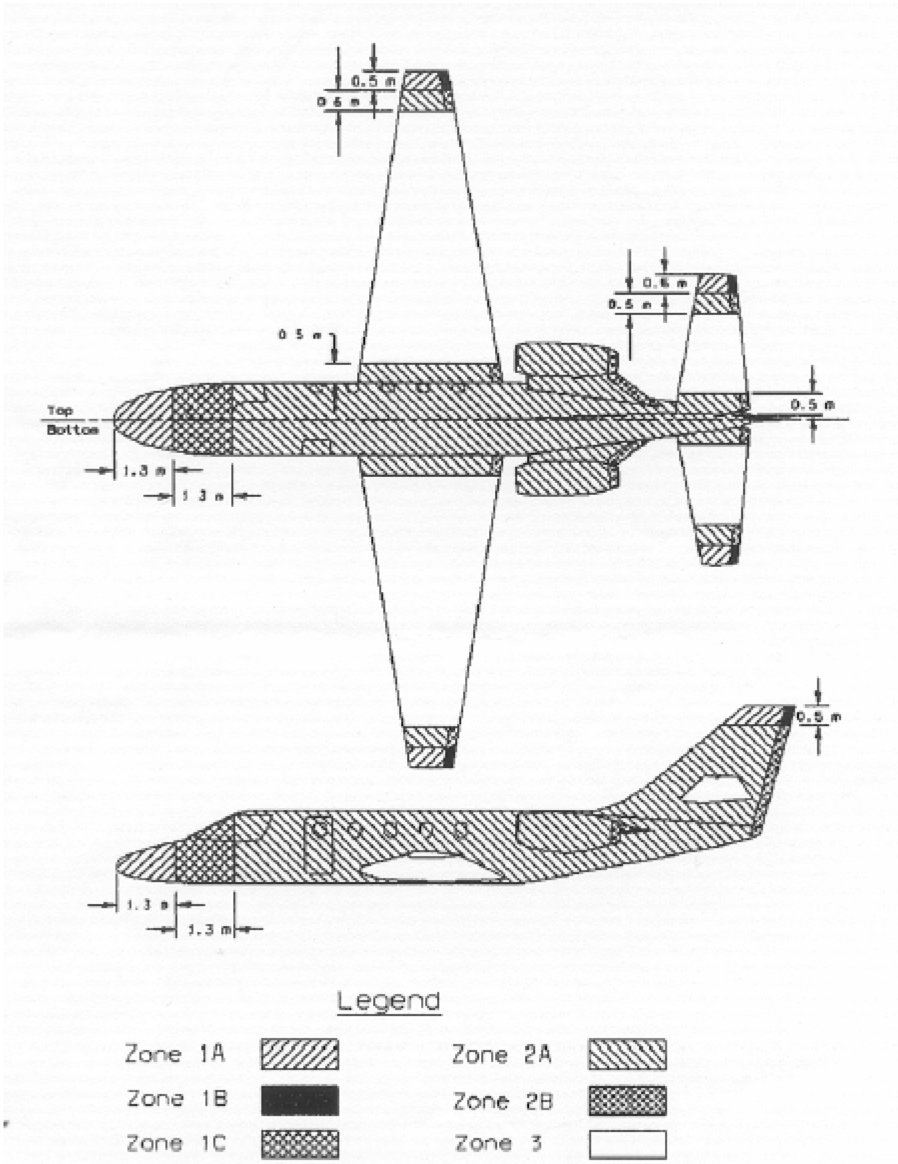

Zone 1—Initial attachment points of lightning flash and first return strokes.

Zone 2—Swept-stroke zone, or various surface locations to which lightning flashes attach and dwell. An aircraft in motion experiences more attachment points than the initial attachment point with a relatively stationary flash channel.

Zone 3—All areas not covered by Zones 1 and 2. Low possibility of any attachment, but may carry substantial amounts of current by conduction.

Figure 2. Lightning Strike Zone Details for Straight-Wing Business Jet [2]

To simulate a shear-loaded, bonded joint similar to the structure shown in figure 1, a PFS test specimen configuration was used for the EOD investigation. The overall specimen size was 17 by 17 inches, and the test section was approximately 11.6 by 11.6 inches (figure 3). Two composite panels were bonded and machined to form the single-lap joint, as shown in this figure. Mounting holes in the grip section and holes in the middle of the overlap section for open-hole (OH) and filled-hole (FH) specimens also were precision machined. The PFS test specimen was bolted rigidly to the test fixture on all four sides. Once bolted, the specimen was sandwiched between two steel picture frames that have pin joints at all four corners (figure 4). The test specimen is bolted to steel-edged plates to simulate fully clamped edge conditions at all four sides. A 70-in-lbf bolt torque is applied using a calibrated torque wrench to uniformly distribute the clamp-up force. These edge plates were connected using pins at the four corners. Two of the diagonally opposite corners of the fixture were connected to clevis attachments (pin joints), and a tensile load was applied. Four corner cutoffs were machined to prevent localized buckling or crippling of the test specimen in these areas.

Due to the rigidity of the picture-frame edges, this specimen produced a relatively uniform far-field shear deformation state, as shown in figure 5. However, due to minor misalignments, eccentricity of the test specimen and edge phenomenon can affect the uniformity of the state of pure shear [3].

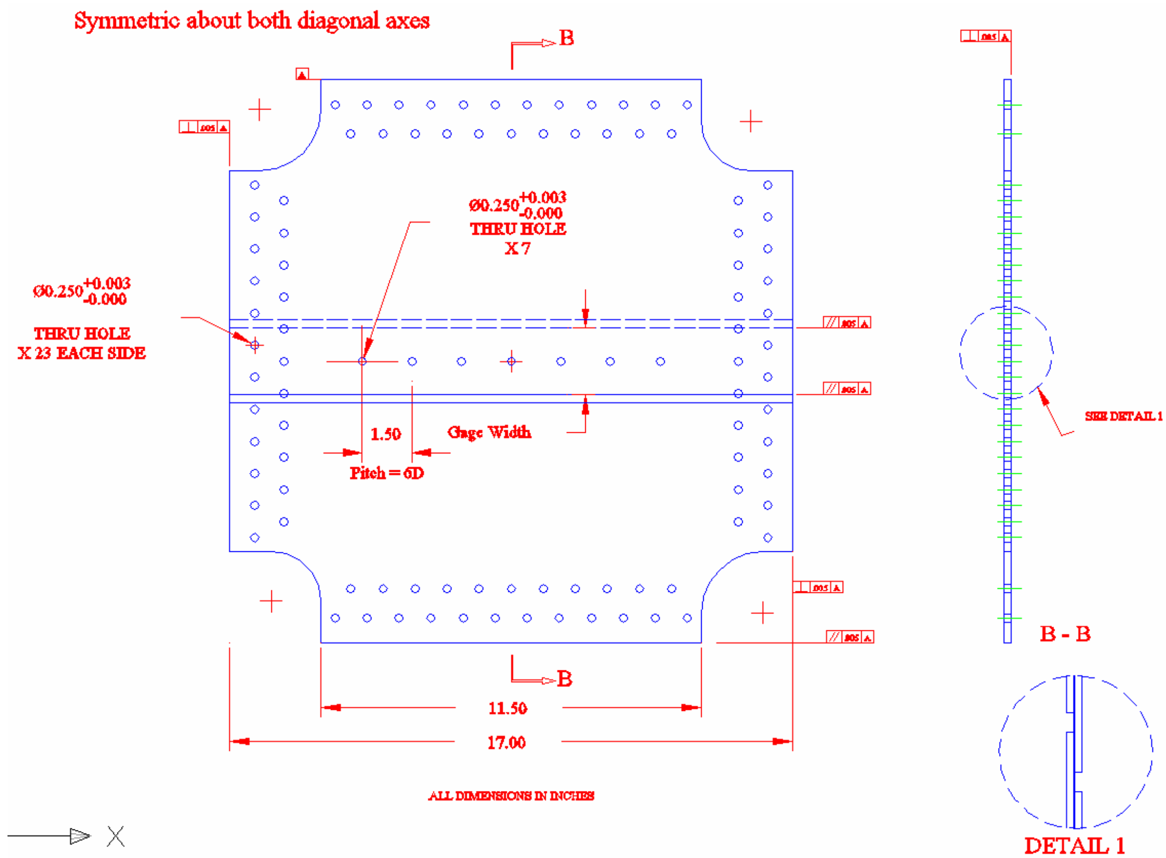

Figure 3. A PFS Test Specimen With a Single-Lap Joint

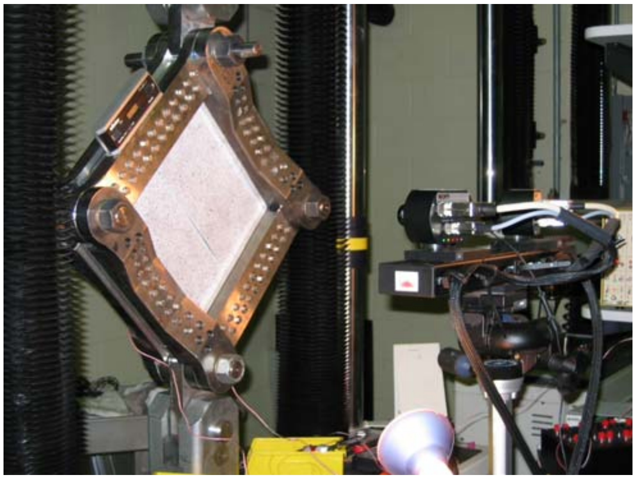

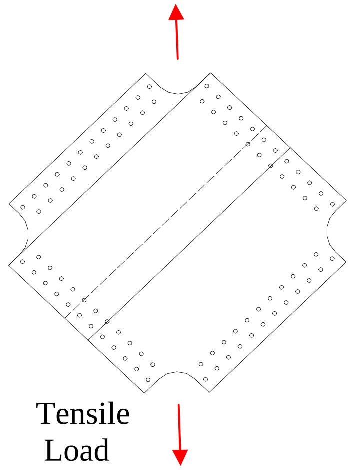

Figure 4. A PFS Test Setup

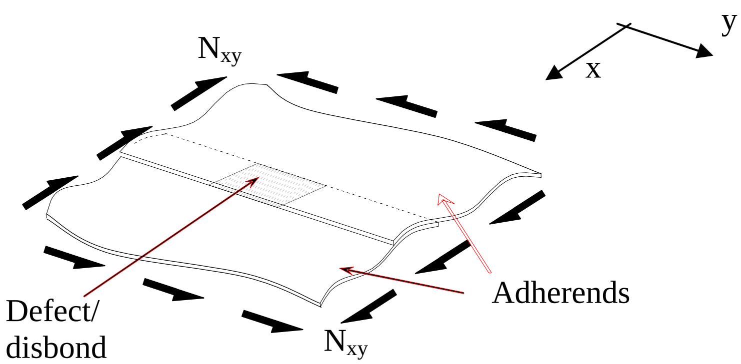

Figure 5. Shear-Loaded, Single-Lap Joint Section With Rectangular Disbond

A total of 38 specimens were prepared to investigate the effects of these disbond configurations. The resulting test matrix is summarized in table 1. Disbonds were fabricated by 0.0025-inch-thick polyester tape in the overlap region. Lightning strike specimens were impacted at Lightning Technologies, Inc. (LTI) laboratories. The nomenclature in appendix A is used for identification of different defect geometries shown in figure 6 with the following identification:

- Disbond: square (S), rectangular (R), circular (C), and diamond (D)
- Rectangular disbond: with bolt holes, with fail-safe fasteners (FH)
- Lightning strike: Zone 1 (LT1) and Zone 2 (LT2)

Table 1. Test Matrix for EOD Investigation

Defect Configuration	Disbond Geometry	Overlap (in.)	Number of Specimens
No Defect[1]	No Disbond	1.0	3
		1.5	3
		2.0	3
Disbond	Rectangular[2]	1.0	4
		2.0	4
	Square[3]	2.0	3
	Circle[4]	2.0	3
	Diamond[5]	2.0	3
Open Hole	Rectangular	2.0	3
Filled Hole[6]	Rectangular	2.0	3
Lightning Strike	Zone 1	2.0	3
	Zone 2	2.0	3

[1] Baseline test for comparison purposes and to determine effects of overlap
[2] Length is twice as much as overlap
[3] Length is the same as overlap
[4] Diameter is half the overlap length
[5] Major axis is half the overlap and aligned with the overlap direction
[6] NAS 6604 bolts

Several specimens with three different overlap lengths were tested to establish the baseline strength of the bonded joints with different overlap lengths. The FH specimen configuration simulated bolted repair or a fail-safe joint design. OH test specimens were included to investigate the possible effects due to the presence of a fastener hole (prior to installing fasteners) on the static strength of the joint.

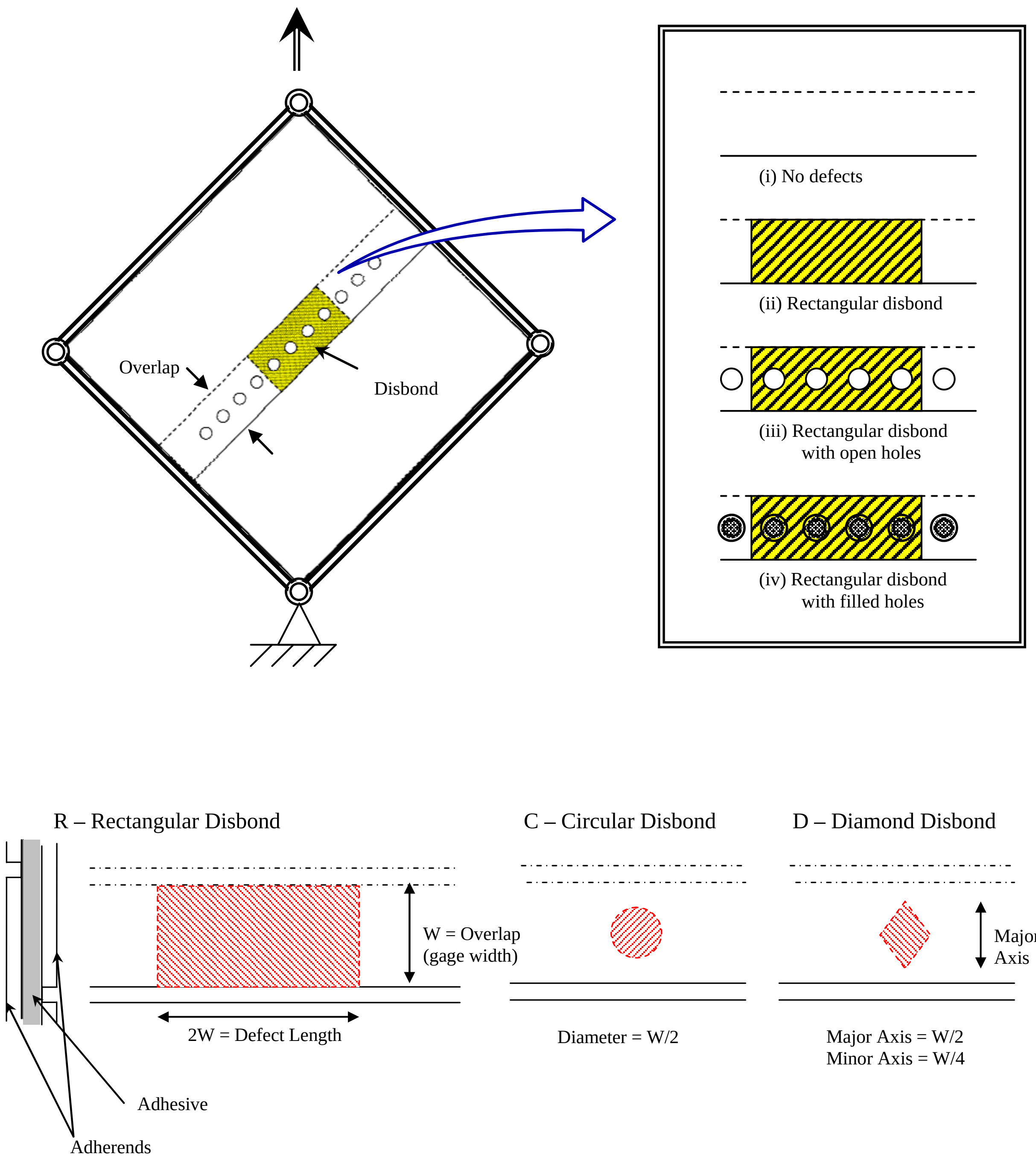

Figure 6. Defect Geometries for EOD Investigation

2.2 EFFECTS OF LOW-VELOCITY IMPACT INVESTIGATION.

This investigation was carried out in two phases: the first phase used PFS specimen configuration and the second phase used SLS configuration. Specimen geometry and test details are discussed separately in the following sections.

2.2.1 The PFS Test.

The same specimen geometry described in section 2.1 was used for the first phase of the effects of impact (EOI) investigation. Impact testing was conducted using a gravity-assisted drop tower with high-speed data acquisition and arrest mechanism to prevent rebound of the impactor. Test specimens are rigidly clamped using two picture frames and impacted with a targeted 270-in-lbf energy level (approximately 30.5 N-m). Several impactor diameters (0.25, 0.50, 0.75, 1.0, and 2.0 inches) were used to investigate the effects of impactor diameter on the damaged area and the indentation depth. Test specimens were impacted using support fixtures that have unsupported areas of 8 by 8 inches (long) and 4.5 by 4.5 inches (short) to investigate the effects of boundary conditions on the impact resistance and damage mechanism.

A total of 26 test specimens were tested (table 2). The test matrix was designed to evaluate the effects due to different impactor diameters for several different bondline thicknesses and overlap lengths using the PFS test setup, as described in section 2.1.

Table 2. Test Matrix for EOI Damages in Bonded Joints

Impactor Diameter (inches)	Bondline Thickness* (inches)	Overlap (inches)	Number of Specimens
0.25	T1	1.0	2
		2.0	3
0.50	T1	2.0	3
0.75	T1	2.0	3
1.00	T1	1.0	1
		1.5	3
		2.0	3
	T2	2.0	3
	T3	2.0	2
2.00	T2	2.0	3

*T1, T2, and T3 correspond to approximate bondline thicknesses of 0.007, 0.015, and 0.020 inch, respectively.

2.2.2 The SLS Test.

The second phase of the low-velocity impact investigation was carried out using the SLS specimen configuration that was loaded in tension. Composite laminates were bonded together to form a single-lap joint as opposed to machining two slots, similar to that used for PFS test specimens. The lap joint was considered the most suitable joint for this experimental study because of the ease of fabrication as well as the effectiveness to simulate an impact event occurring at joints in aircraft structures.

Currently, there are no standards that outline testing recommendation for bonded composite joints. However, using the ASTM standard guidelines, the test method for measuring the damage resistance of a fiber-reinforced polymer matrix composite to a drop-weight impact event (ASTM D 7136) is used with the necessary modification for the adhesive joint. Specimen geometry is selected to provide a 3- by 4-inch test section with a 3-inch overlap (figure 7). Brass spacers (0.007 inch thick) are used during the fabrication process of the test specimens to control bondline thickness. Once specimens are machined to the final dimensions, end tabs are secondarily bonded so the bonded plane is initially aligned with the loading direction.

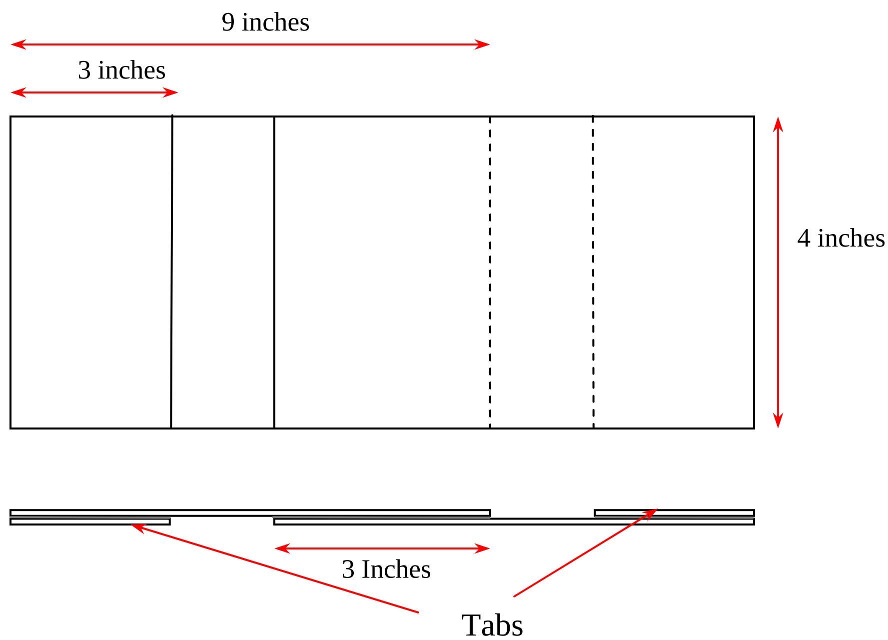

Figure 7. The SLS Test Specimen Geometry

Table 3 shows the test matrix for the second phase of the EOI investigation using the SLS test specimen configuration. Three impactor diameters (0.50, 0.75, and 1.00 inch) and three energy levels (88.5, 221.0, and 354.0 in-lbf) for three different material systems were studied.

Table 3. Test Matrix for Impact Tests

Material	Impactor Diameter (in.)	Impact Energy		Number of Specimens
		in-lbf	Joules	
NB321/7781 E-glass satin weave	0.50	88.5	10	2
		221.0	25	3
		354.0	40	3
	0.75	88.5	10	2
		221.0	25	3
		354.0	40	3
	1.00	88.5	10	2
		221.0	25	3
		354.0	40	3
	Unimpacted			2
T700G-12K/3900-2 Plain weave	0.50	88.5	10	2
		221.0	25	3
		354.0	40	3
	0.75	88.5	10	2
		221.0	25	3
		354.0	40	3
	1.00	88.5	10	2
		221.0	25	3
		354.0	40	3
	Unimpacted			2
T800S/3900-2B Unidirectional tape	0.50	88.5	10	2
		221.0	25	3
		354.0	40	3
	0.75	88.5	10	2
		221.0	25	3
		354.0	40	3
	1.00	88.5	10	2
		221.0	25	3
		354.0	40	3
	Unimpacted			2

2.3 MATERIALS.

This section describes the adhesive and composite material systems used for this research.

2.3.1 Adhesive.

All specimens used in this research were bonded using Hexel Corporation's EA9394 two-part paste adhesive system, which is commonly used in the aviation industry for a wide variety of applications. It can be cured at room temperature and possesses excellent strength at temperatures as high as 350°F (177°C). Furthermore, its thixotropic nature and excellent high-temperature compressive strength make it ideal for potting, filling, and liquid shim applications. Also, its long pot life and low toxicity make it a user-friendly adhesive for a research environment.

2.3.2 Adherends.

Test panels were fabricated using several different fiber-matrix systems and bonded with EA9394 paste adhesive. The material systems used in this research were abbreviated as follows:

- Newport NB321/7781 E-glass satin weave identified in this report for convenience as FGSW
- Toray T700S/#2510 carbon fabric plain weave identified in this report for convenience as CFPW-S
- Toray T700G-12K/3900-2 carbon fabric plain weave identified in this report for convenience as CFPW
- Toray T800S/3900-2B carbon unidirectional fiber tape identified in this report for convenience as CFUT

The first two material systems (250°F cure) are commonly used in general aviation, and the latter two (350°F cure) are primarily used in commercial aircraft applications. Quasi-isotropic lay-up sequences were used for all adherends.

PFS specimens in the EOD and EOI research were fabricated using CFPW-S. For EOD research, several PFS specimens were fabricated using FGSW for baseline comparison. SLS specimens in the second phase of the EOI investigation were fabricated using FGSW, CFPW, and CFUT material systems.

2.4 SPECIMEN FABRICATION.

Adherends for PFS test specimens were fabricated using CFPW-S and FGSW with an 8-ply quasi-isotropic lay-up sequence, $[-45/0/45/90]_s$. EA9394 two-part paste adhesive was used for bonding composite specimens. The composite panels were cured at 250°F, according to manufacture process documentation, and the bonded assembly was cured at 150°F for 60 minutes. Disbonds were simulated using 0.0025-inch-thick polyester tape. Adherends for SLS test specimens were fabricated using FGSW, CFPW, and CFUT with a quasi-isotropic lay-up sequence, $[0/45/90/-45]_s$. Composite laminates were fabricated using hand lay-up and a vacuum bag, and cured in an autoclave, according to the manufacturer-recommended cure cycle. The average panel thickness for PFS specimens were as follows: FGSW = 0.0892 in. and CFPW-S = 0.0693 in. The average panel thickness for SLS specimens were as follows: FGSW = 0.05238 in., CFUT = 0.05952 in., and CFPW = 0.0677 in.

Bondline thickness of the specimens was controlled by bonding brass shims with desired thickness to one of the adherends prior to application of the adhesive. These shims were placed away from the overlap region (test section) of the joint. PFS test panels were bonded using a bladder press, which was placed inside a large oven, and even pressure was applied to two steel surfaces that sandwich the bonded assembly. SLS specimens were bonded and held together by C-clamps and placed inside the oven for complete cure. The bonded assembly was cured for 1 hour at 150°F to achieve baseline properties.

2.5 EXPERIMENTAL PROCEDURE.

This section contains information regarding the experimental setup and equipment used for impacting, nondestructive inspections (NDI), residual indentation measurement, and residual strength testing.

2.5.1 Impact Tests.

PFS test specimens were impacted using a gravity-assisted drop tower (figure 8), while SLS specimens are impacted using an Instron Dynatup® 8250 drop-weight impact tester (figure 9). Impact force was measured using a piezoelectric load cell attached to the impact mass assembly. Both impactors were equipped with a pneumatic rebound catch mechanism that prevented secondary impacts on the test specimens and a photodetector or flag system that provided impact velocity information. Data acquisition software, which runs on a computer connected to each drop-weight impact tester, collected and reduced the impact test data. A sensor (flag), which was placed closer to the impact location, triggered the data acquisition system a few milliseconds prior to the impact event. This sensor and another flag placed a known distance adjacent to that were used for impact velocity calculation (velocity = distance/time).

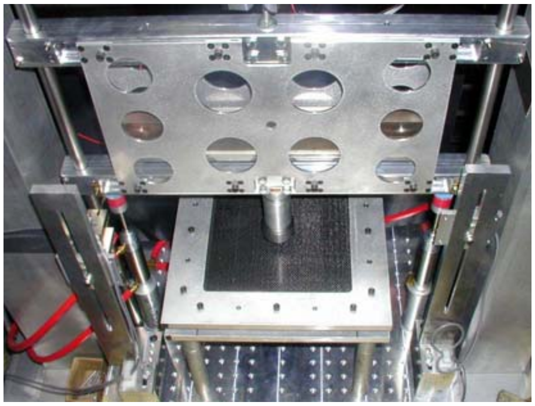

Figure 8. Gravity-Assisted Drop Tower and Support Fixture

Figure 9. Instron Dynatup Drop-Weight Tester

Prior to impact, specimens were placed in the support fixtures, as shown in figure 10, and held rigidly. These fixtures had dowel pins for aligning the specimens. Impactors used for the SLS specimens are shown in figure 11. SLS specimens were impacted with 0.50-, 0.75-, and 1.00-inch impactors, and PFS specimens were impacted with 0.25-, 0.50-, 0.75-, 1.00-, and 2.00-inch impactors. Several PFS specimens were impacted using a support fixture that had an 8 by 8-inch opening (unsupported region), and the remainder were impacted using a support fixture that had a 4.5- by 4.5-inch unsupported region. These two fixtures are referred to as large (L) and small (S) support fixtures throughout this report. All SLS specimens were impacted with a support fixture that had a 3-by 4-inch unsupported region.

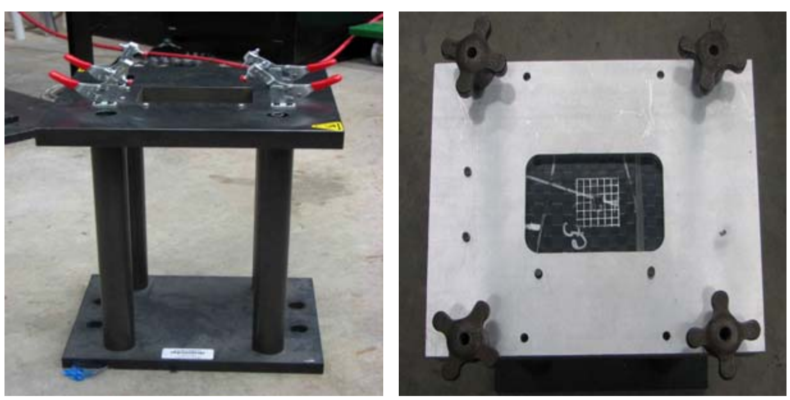

Figure 10. Support Fixture for SLS Impact Specimens

Figure 11. Impactors Used for SLS Specimens

The total impact event time duration for the specimens and energy levels used in this research was about 10 milliseconds or less. Therefore, using a triggering mechanism, a very high frequency was used to collect data during the impact event to minimize unnecessary data before and after the impact event. An Instron Dynatup 8250 drop tower was equipped with an Instron Dynatup Impulse® data acquisition system (figure 12).

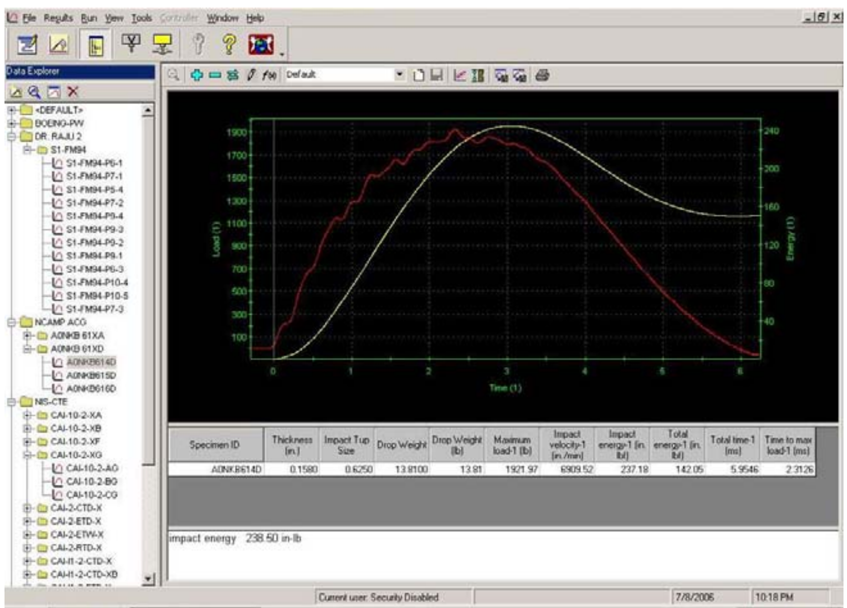

Figure 12. Dynatup Impulse Data Acquisition Software

2.5.2 Nondestructive Inspections.

The impacted specimens were subjected to through-transmission ultrasonic (TTU) NDI that generate C-scans to quantify the damaged planar areas using image-analysis software (figure 13). A TTU C-scan provided a projection of damage that was incurred on both adherends, the adhesive layer, and the adhesive/adherend interfaces. Therefore, care was exercised when interpreting the failure mechanism. Additional inspections, such as microscopy, x-ray, and thermal imaging, may be required to quantify the damage on adhesive, adherends, and interfaces.

For cases involving glass fiber composite, damage was clearly seen by the naked eye due to the translucent nature of these fibers. During this investigation, only TTU and visual inspections were conducted to determine the overall damage from impact. Initially, both 2.25- and 5-MHz transducers were used to scan the specimens to explore the sensitivity of the transducer frequency on the C-scan results.

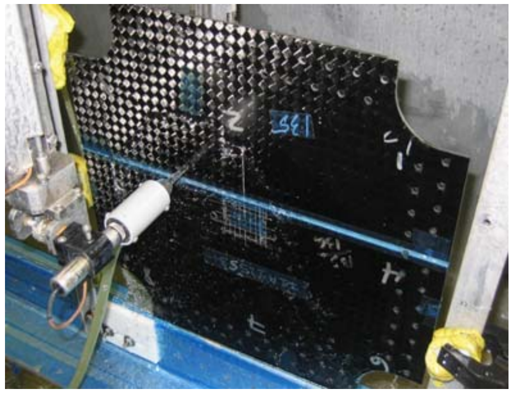

Figure 13. A TTU Scan of a PFS Test Specimen

2.5.3 Residual Indentation Measurement.

Once impacted, the residual indentations of these specimens were measured using a digital gage that was attached to a traverse (figure 14). With the center at the impact point, the postimpact surface contour was measured over an area of 1.5 by 1.5 inches. As shown in figure 15, the depth measurements relative to undamaged surface were measured and plotted, using the Golden Software Surfer® computer program, to visualize the surface indentation. The data, enhanced for easy visualization, is not shown to scale.

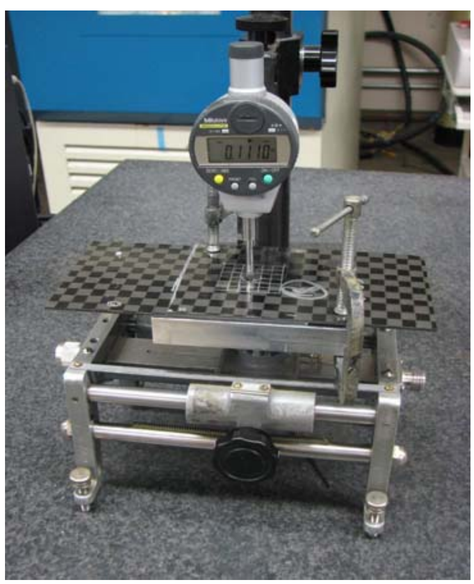

Figure 14. Setup for Residual Indentation Depth Measurement

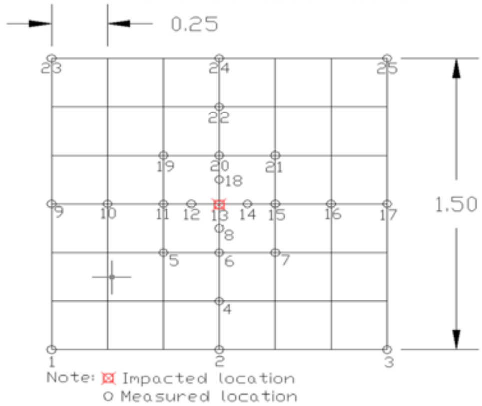

Figure 15. Depth Measurement Grid

2.5.4 Residual Strength Tests.

PFS and SLS residual strength tests were conducted using 110- and 55-kip MTS servo-hydraulic test frames, respectively. The picture-frame test fixture was mounted to clevis attachments of the test frame, as shown in figure 4. SLS specimens were mounted to the test frame using a hydraulic grip assembly, as shown in figure 16. The grip assembly was equipped with 4-inch-wide wedges and provided with a uniform pressure of 3000 pounds per square inch (psi). While gripping the specimens, the actuator was programmed in load-control mode to prevent unnecessary preloading due to grip pressure. Both PFS and SLS tests were conducted in displacement-control mode with a rate of 0.05 in/min, while acquiring data at a rate of 10 Hz.

Figure 16. The MTS Servo-Hydraulic Test Frame

For the PFS specimens, a linear variable differential transducer was mounted between clevis pins to measure the elongation of vertical or diagonal tension, Δ. Therefore, assuming the small-angle theory, the global shear strain was approximated using equation 1, where *w* is the length of the side of the test section (figure 17).

$$\gamma_{xy}^{G} = \frac{\pi}{2} - 2 \cdot ar\cos\left(\frac{1}{\sqrt{2}} + \frac{\Delta}{2 \cdot w}\right) \tag{1}$$

Subsequently, the resultant global stress and far-field stress was calculated using equations 2 and 3, respectively.

$$N_{xy}^{G} = \frac{P}{2 \cdot w}\left[\cos\left(\frac{\pi}{4} - \frac{\gamma_{xy}^{G}}{2}\right)\right]^{-1} \tag{2}$$

$$\tau_{xy}^{G} = \frac{N_{xy}^{G}}{t_{total}} \tag{3}$$

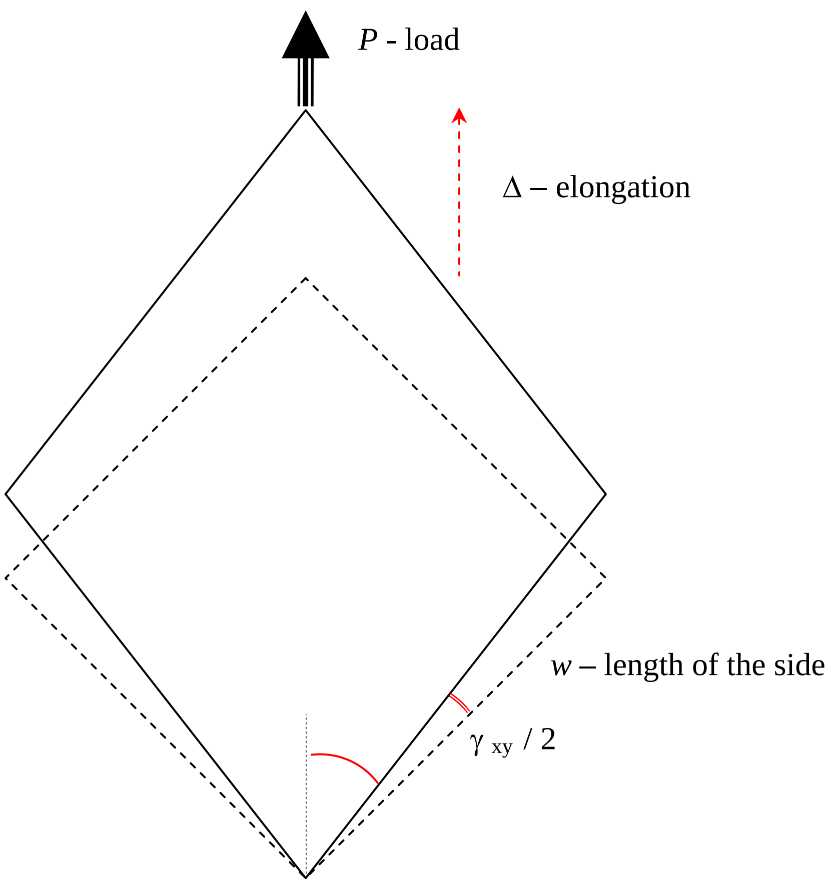

Figure 17. The PFS Data Reduction

Strain gage rosettes were mounted on the impacted PFS specimens, as shown in figure 18. For specimens with disbonds, an additional rosette was mounted at the center.

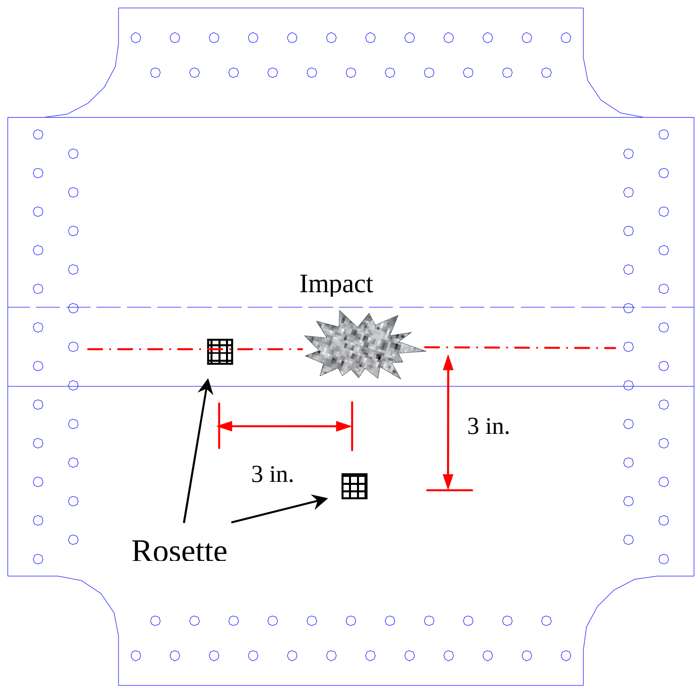

Figure 18. Strain Gage Installation for EOI Test Specimens

2.5.5 Full-Field, Three-Dimensional Displacement and In-Plain Strain Measurements.

The ARAMIS photogrammetry full-field strain measurement system was used to measure localized buckling in the region of disbonds and defects (see figue 19). ARAMIS [4] is a noncontact, optical, three-dimensional deformation-measuring system. It uses two high-definition cameras to track translation and rotation of the surface details (object characteristics) with subpixel accuracy. Surface details are obtained by applying a stochastic color pattern that follows surface displacement during loading. ARAMIS uses this pattern to recognize the surface structure and uses digitized images through both cameras for triangulation of surface details (micropattern) to determine precise location of each point. Therefore, this system has the capability of digitizing the precise shape (surface) of the structure during loading. The first set of coordinates for object characteristics are obtained in the undeformed stage. After load application, a new set of coordinates (digital images) are recorded. Then, ARAMIS compares the digital images and calculates the displacement and deformation of the object characteristics. ARAMIS is capable of three-dimensional deformation measurements under static and dynamic load to analyze deformations and the strain of real components. In addition, this system is able to eliminate the rigid body motion component from the displacement results. Therefore, it can be used for specimens that exhibit large displacements. Strain sensitivity of the system is approximately 100-200 microstrains, and the scan area can be as large as 47 by 47 inches.

Figure 19. Portable Version of ARAMIS Photogrammetry System [4]

Full-field displacement and strain data are then used to examine any propagation of the defects according to the procedure (NDI method) outlined in reference 5, which assesses the localized skin buckling (out-of-plane displacement) around the debonded or delaminated region. Once the rigid-body components are removed, this technique can be used to identify the defects in quasi-statically loaded joints as well as weakened sections and stress concentrations. A qualitative assessment of the size of damage can be conducted using the NDI method by comparing the images at different load levels or fatigue intervals. Once the data is analyzed, the size of the buckled region or the length across the damage, $\hat{S}+\Delta\hat{S}$ (figure 20), can be obtained from the graphical results. However, the NDI method will not be able to provide the size of the damaged region before applying the load ΔP ($\hat{S}$). If the damage growth, $\Delta\hat{S}$, for a small load step, ΔP, is negligible compared to the defect size, $\hat{S}$, then the size of the damage can be assessed as $\hat{S}$ at load P. For no-growth condition, $\Delta\hat{S}$ is zero, and the above statement still holds.

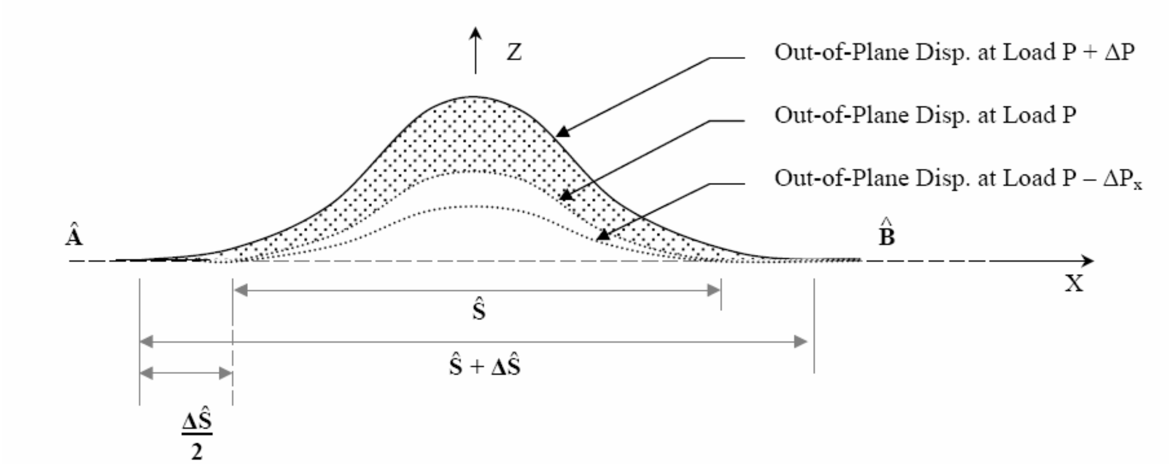

Figure 20. Damage Size Assessment at Load P Using NDI Method

3. RESULTS AND DISCUSSION.

3.1 EFFECTS OF DISBONDS AND LIGHTNING STRIKE DAMAGES.

The EOD test data for both CFPW-S and FGSW material systems are summarized in tables 4 and 5. (The numbering system used to identify the nomenclature for PFS specimens is located in appendix A.) Table 6 is a summary of the lightning strike damage specimens. Figure 21 shows the failure loads for specimens without disbonds that have overlap lengths of 1.0, 1.5, and 2.0 inches. The maximum load obtained for a 1.5-inch overlap is higher than a 2.0-inch overlap. Current data were not sufficient to confirm that this was a realistic phenomenon or due to test data scatter. Figure 22 shows the failure loads of EOD tests with a 2-inch overlap. The average maximum load of CFPW-S specimens for each defect type is shown in figure 23. Circular- and diamond-shaped defects indicate no effect on the load-carrying capability of the joint. This confirms that defects inside the elastic trough will not affect the static strength of the joint [6], as shown in figure 24. Due to test data scatter, some of the specimens with circular- and diamond-shaped defects indicate higher failure loads than those without disbonds.

Table 4. Summary of EOD Test Data for CFPW-S

Specimen	Bondline Thickness (in.)	Defect Type	Overlap (in.)	Max Load (lbf)	Stress Resultant, N_{xy} (lbf/in.)	Far-Field Stress, τ_{xy}^{G} (psi)
D1A11NN1	0.013	--	1.0	35621	2162	14772
D1A11NN2	0.016	--	1.0	36320	2209	16134
D1A11NN3	0.015	--	1.0	34722	2112	14901
D1A15NN1	0.018	--	1.5	39338	2388	16505
D1A15NN2	0.019	--	1.5	44604	2699	18624
D1A15NN3	0.021	--	1.5	46236	2794	19562
D1A12NN1	0.018	--	2.0	39131	2372	16508
D1A12NN2	0.013	--	2.0	39744	2413	17227
D1A12NN3	0.012	--	2.0	40550	2461	16612
D1A11DR1	0.011	1 x 2 R	1.0	27802	1694	11908
D1A11DR1(2)	(1)	1 x 2 R	1.0	28146	1720	11235
D1A11DR2	0.016	1 x 2 R	1.0	24536	1501	10429
D1A11DR3	0.018	1 x 2 R	1.0	24951	1520	10848
D1A12DR1	(1)	2 x 4 R	2.0	25027	1525	9483
D1A12DR(2)	0.019	2 x 4 R	2.0	21803	1334	9401
D1A12DR2	0.017	2 x 4 R	2.0	23116	1414	10012

Table 4. Summary of EOD Test Data for CFPW-S (Continued)

Specimen	Bondline Thickness (in.)	Defect Type	Overlap (in.)	Max Load (lbf)	Stress Resultant, N_{xy} (lbf/in.)	Far-Field Stress, τ_{xy}^G (psi)
D1A12DR3	0.016	2 x 4 R	2.0	24539	1499	10912
D1A12DS1	0.025	2 x 2 S	2.0	28960	1770	12914
D1A12DS2	0.017	2 x 2 S	2.0	28796	1763	13018
D1A12DS3	0.011	2 x 2 S	2.0	29067	1779	12823
D1A12DC1	0.018	Circle	2.0	39809	2429	17726
D1A12DC2	0.008	Circle	2.0	40981	2499	18030
D1A12DC3	0.011	Circle	2.0	38728	2362	16963
D1A12DD1	0.009	Diamond	2.0	44796	2730	19931
D1A12DD2	0.012	Diamond	2.0	38480	2351	17129
D1A12DD3	0.006	Diamond	2.0	43588	2651	19283
D1A12OR1	0.010	2 x 4 R (OH)	2.0	23827	1459	10746
D1A12OR2	0.015	2 x 4 R (OH)	2.0	25399	1554	11471
D1A12OR3	0.017	2 x 4 R (OH)	2.0	24033	1470	10739
D1A12FR1	0.011	2 x 4 R (FH)	2.0	40788	2484	18027
D1A12FR2	0.014	2 x 4 R (FH)	2.0	43708	2654	19265
D1A12FR3	0.013	2 x 4 R (FH)	2.0	43762	2662	19252

(1)lost data
(2)spare specimen

Table 5. Summary of EOD Test Data for FGSW

Specimen	Defect Type	Overlap (in.)	Max Load (lbf)	Stress Resultant, N_{xy} (lbf/in.)
D1C11NN1	--	1.0	38535	2341
D1C11NN2	--	1.0	34318	2092
D1C12NN2	--	2.0	36187	2199
D1C12NN3	--	2.0	40482	2464
D1C12DC1	Circle	2.0	40521	2463
D1C12DS2	2 x 2 S	2.0	30899	1883

Table 6. Summary of Lightning Strike Damage Test Data for CFPW-S

Specimen	Bondline Thickness (in.)	Defect Type	Overlap (in.)	Max Load (lbf)	Stress Resultant, N_{xy} (lbf/in.)	Far-Field Stress, τ_{xy}^{G} (psi)
D1A12GX1	0.014	Zone 1 [LTI]	2.0	32872	2010	14570
D1A12GX2	0.014		2.0	35215	2149	15824
D1A12GX3	0.013		2.0	33254	2029	14813
D1A12GX4	0.018	Zone 2 [LT2]	2.0	35954	2194	15912
D1A12GX5	0.012		2.0	37641	2296	16633
D1A12GX6	0.014		2.0	37670	2298	16806

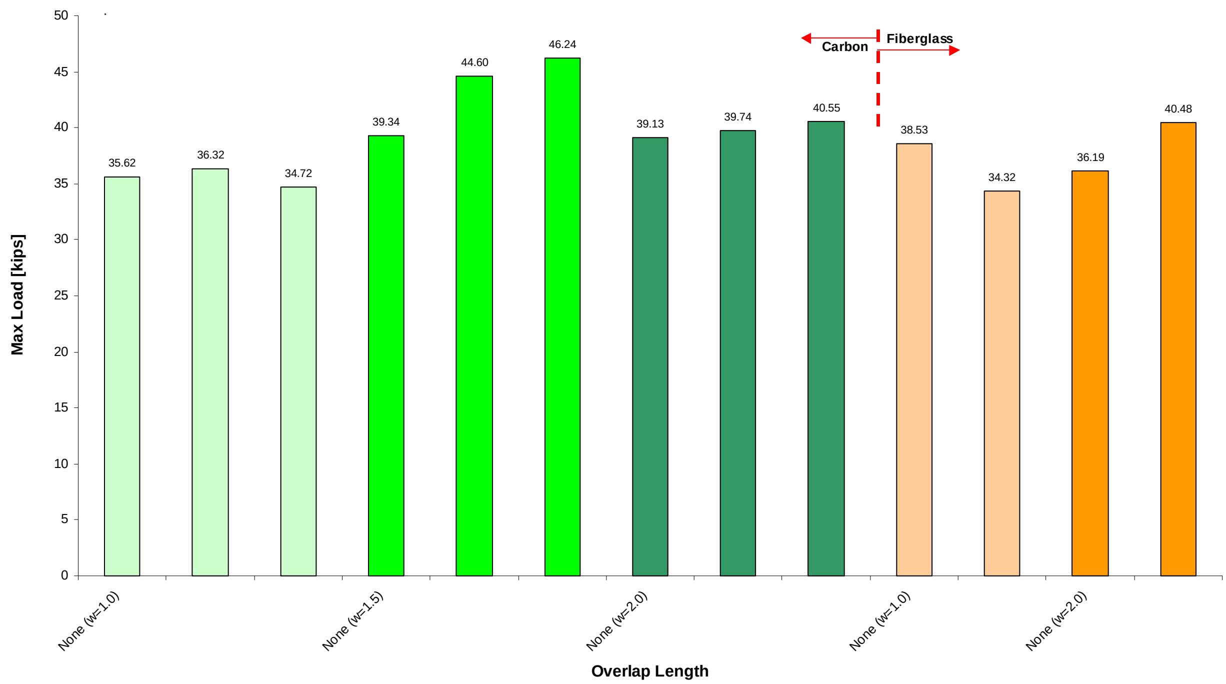

Figure 21. Effects of Overlap Length (No disbonds)

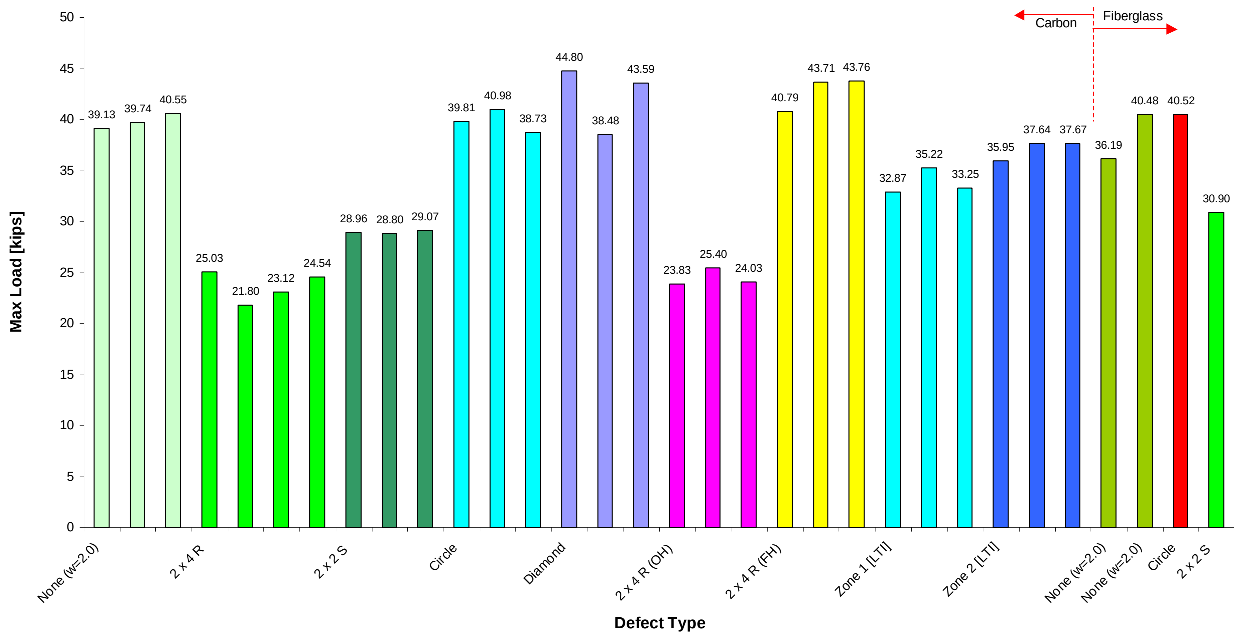

Figure 22. Comparison of EOD Test Results for 2.0-Inch Overlap

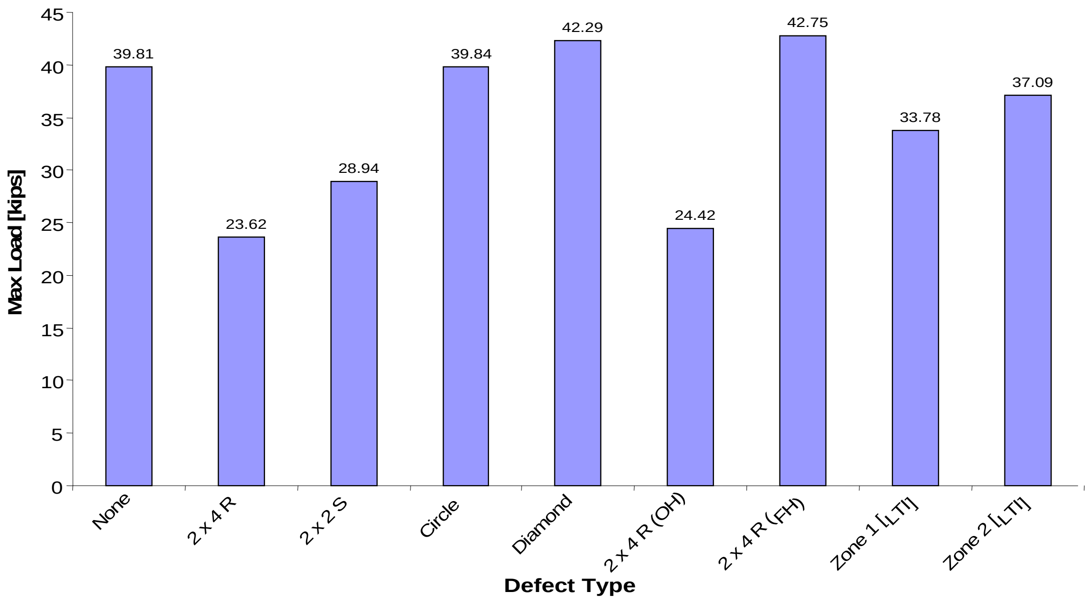

Figure 23. Average Failure Loads for CFPW EOD Specimens With 2-Inch Overlap

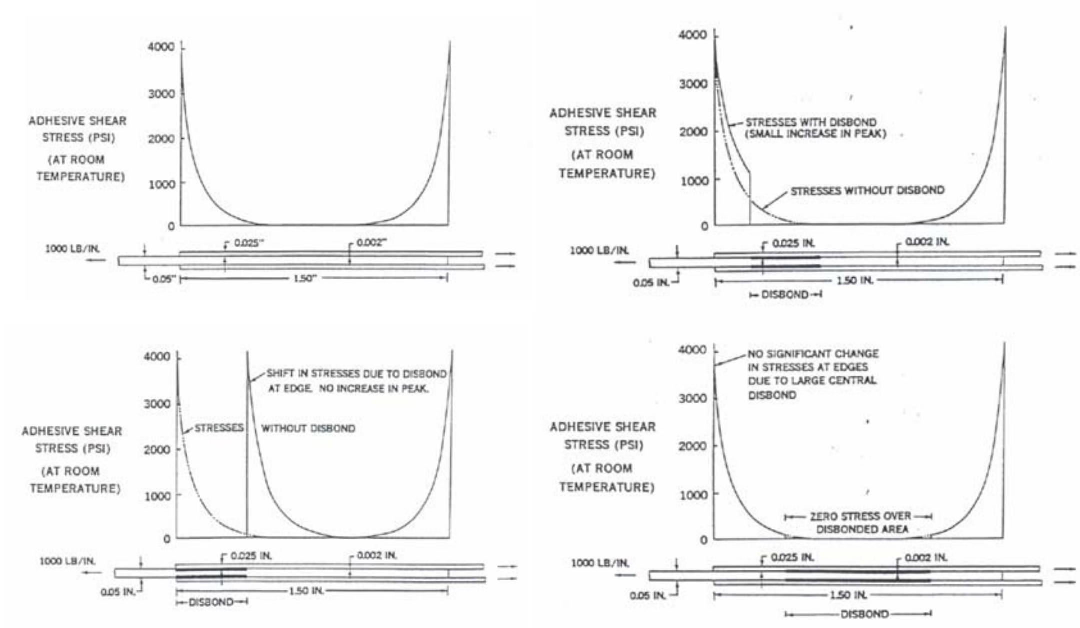

Figure 24. The EOD on the Stress Distribution of Bonded Joints [6]

For the specimens with 1- by 2-inch-rectangular disbonds (1-inch overlap), the reduction in static strength was approximately 26%. Specimens with 2- by 2-inch-square defects indicated a 27% reduction in static strength, and specimens with 2- by 4-inch-rectangular defects, prior to and after drilling fastener holes, indicated a 40% reduction in static strength. Since the maximum shear stresses of the joint occurred at the edges of the overlap, the defects closer to the edge of the overlap significantly affected the adhesive stress distribution and the elastic trough (figure 24). For specimens with square or rectangular disbonds that spread across the overlap, complete load redistribution occurred around the defect. In such cases, the undesirable stress concentrations of the joint adjacent to the four corners of the defects (figure 25) can cause premature failure or disbond and delamination initiation during cyclic loading.

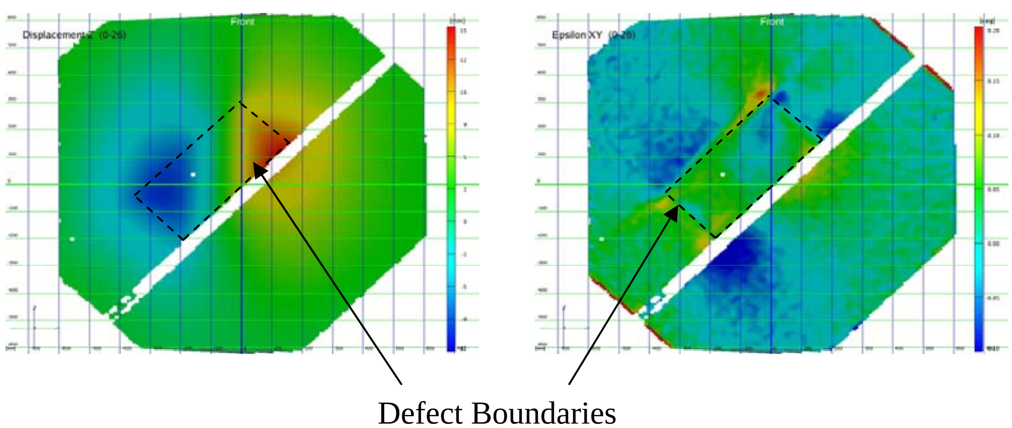

(a) Out-of-plane displacement (b) In-plane shear strain

Figure 25. Photogrammetry Data for Specimen With Rectangular Defect

Fastener installation (fail-safe or repair) completely restores the strength of the joints with 2- by 4-inch-rectangular defects. In addition to carrying the in-plane shear loads, fasteners are able to restrict the out-of-plane loading on the overlap region, especially around the defects, and increase the through-the-thickness strength of the bonded region. Also, the fasteners keep both adherend plates intact and significantly minimize peel stresses. For specimens without fasteners, the out-of-plane buckling caused a significant peel stress, and the failure mode was a direct result of the high peel stresses at the disbond corners, as shown in figure 26. Since the fastener holes were drilled within the elastic trough region of these specimens, they had no effect on the static strength of the joint.

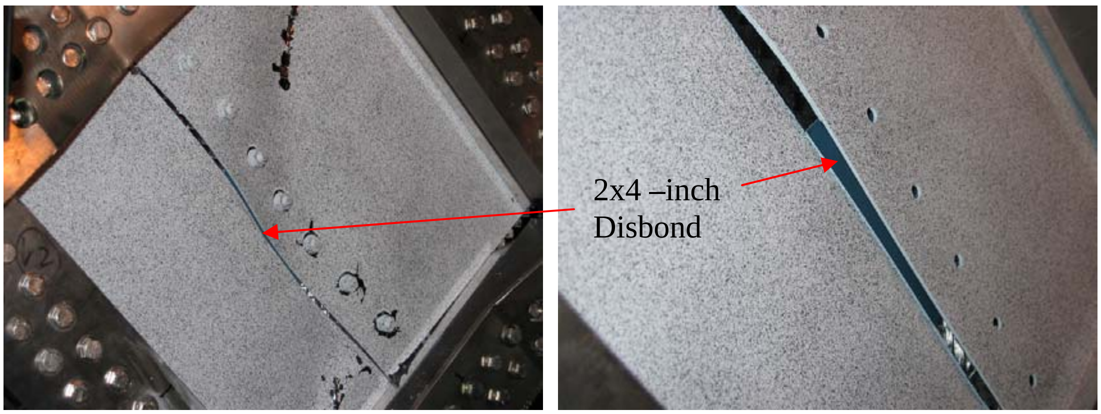

(a) FH (b) OH

Figure 26. Failure Modes of PFS Specimens With 2- by 4-Inch (Rectangular) Defects

Fiberglass specimens with circular disbonds also indicated no significant static strength loss, since the disbond was located within the elastic trough. However, similar to the carbon specimens, a 2- by 2-inch-square disbond caused about 19% reduction in static strength.

Lightning strike damages did not appear to have penetrated through the joint (or even through the first adherend). However, it caused significant local delamination around the impact location, which resulted in approximately 15% and 7% reduction in static strength for Zone 1 and Zone 2 energy impacts, respectively, mainly due to damage to the adherend.

The photogrammetry data indicated severe stress concentrations around the boundaries of rectangular defects and damage propagation prior to failure (appendix A), based on the NDI methodology outlined in reference 5. Failure modes of the specimens indicated delamination (adherend) failure due to significant out-of-plane buckling that caused secondary peel stresses adjacent to the disbond boundaries. Mode I fracture toughness obtained from double-cantilever beam tests indicated that the fracture toughness of EA9394 adhesive is 3.7 in-lbf/in^2 [7], which was about three times higher than the composite laminate. This caused the interlaminar (adherend) failure, rather than adhesion failure, of composite joints of all PFS specimens, see figure 26.

Shear-loaded bonded joint theory (SLBJ) [8], which was primarily developed and verified [9 and 10] for in-plane stresses, was used to approximate the maximum adhesive shear stress that occurs toward the free edge. These results shown in figure 27 are compared with the average shear stress (= load/area), assuming uniform shear stress distribution across the overlap region. This figure shows that the maximum stress at the free edge can be as much as five to seven times the average shear stress. For the specimens with defects, this difference is significantly higher than the specimens without defects. The SLBJ theory also was used to obtain the nominal adherend shear stress (table 7) and was compared with the far-field (global) stress, as shown in figure 28. This figure indicates that both SLBJ and global stresses are comparable.

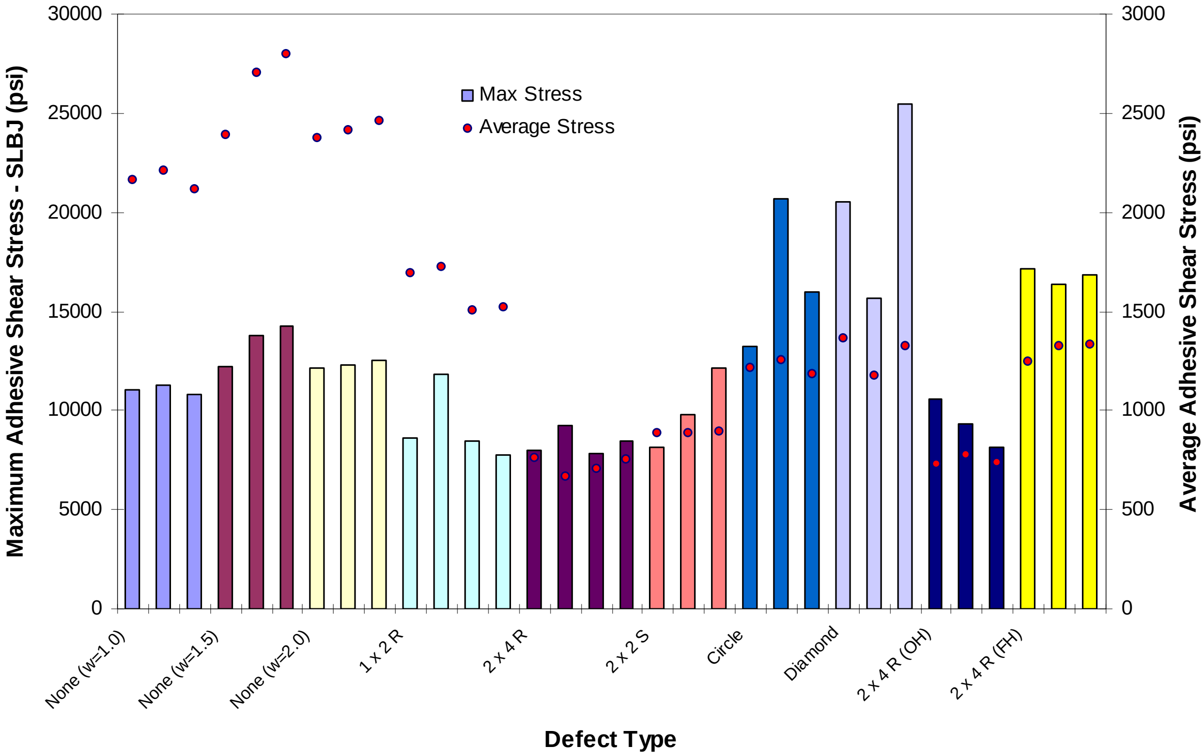

Figure 27. Comparison of Maximum SLBJ and Average Shear Stress, τ_{xz}, at Failure

Table 7. The SLBJ Theory Approximations for CFPW-S

Defect Type	SLBJ Shear Stress (psi)		Average Adhesive Shear Stress, $\tau_{xz}^{a}{}_{-avg}$ (psi)
	Adherend - τ_{xy}^{o}	Adhesive - τ_{xz}^{a}	
None (w = 1.0)	14698	11042	2162
	15015	11280	2209
	14360	10788	2112
None (w = 1.5)	16236	12197	2388
	18349	13785	2699
	18993	14269	2794
None (w = 2.0)	16124	12114	2372
	16406	12325	2413
	16728	12567	2461
1 x 2 R	11514	8650	1694
	11637	11846	1720
	10180	8486	1501
	10332	7762	1520
2 x 4 R	10307	7995	763
	9012	9225	667
	9557	7818	707
	10130	8482	750
2 x 2 S	11962	8158	885
	11912	9802	881
	12019	12111	889
Circle	16413	13260	1215
	16886	20660	1250
	15963	15961	1181
Diamond	18449	20513	1365
	15888	15696	1176
	17910	25453	1325
2 x 4 R (OH)	9858	10582	729
	10500	9310	777
	9931	8179	735
2 x 4 R (FH)	16783	17181	1242
	17932	16397	1327
	17988	16809	1331

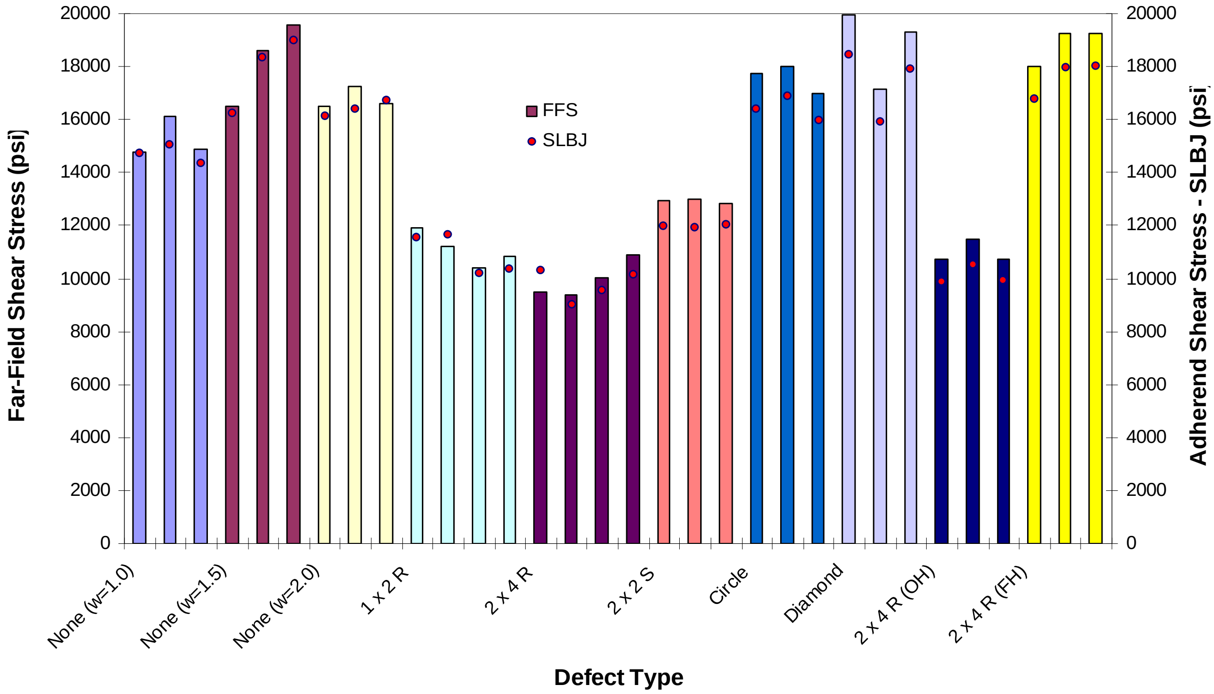

Figure 28. Comparison of Far-Field Shear Stress and SLBJ Adherend Shear Stress at Failure

3.2 THE EOI DAMAGES.

In this section, the results for the effects of low-velocity impact damages are presented for both PFS and SLS test specimens.

3.2.1 The PFS Test Results.

Tables 8 and 9 summarize the impact test results and residual strength test data for PFS specimens, respectively. Nomenclature for the specimens in these tables is located in appendix A. Failure loads for these specimens are also shown in figure 29. For the 2-inch overlap length and an energy level (270 in-lbf) impact, the residual strength is reduced by 20% for a 0.25-inch-diameter impactor and by 9% for the other diameter impactors (see figures 29 and 30). This is significantly less than the reductions observed on honeycomb composite structures [11] that were caused by the increased damage size as the impactor diameter was increased. However, the honeycomb panels were tested in compression, not in shear. The loading mode is a significant factor here. Moreover, the support fixture during the impact tests had a significant effect on the force and displacement history and the damage area. Specimens that were clamped using a large support fixture absorb energy through large displacements and exhibited smaller-sized damage compared to specimens that were clamped using a small support fixture.

Table 8. Summary of Impact Test Results for CFPW-S

Specimen	Bondline Thickness* (in.)	Overlap (in.)	Impactor Diameter (in.)	Energy Level (in-lbf)	Damage Area (in^2)	Residual Indentation (in.)
D1A12NN1	0.007	2.0	N/A	N/A	N/A	N/A
D1A12NN2	0.015	2.0	N/A	N/A	N/A	N/A
D1A12NN3	0.020	2.0	N/A	N/A	N/A	N/A
I1A124S1	0.007	2.0	0.25	261	6.595	0.032
I1A124S2	0.015	2.0	0.25	273	6.848	0.081
I1A124S3	0.020	2.0	0.25	267	7.530	0.096
I1A125S1	0.007	2.0	0.50	269	6.427	0.014
I1A125L2	0.015	2.0	0.50	273	3.152	†
I1A125S3	0.020	2.0	0.50	272	5.725	0.013
I1A127L1	0.007	2.0	0.75	281	5.403	†
I1A127S2	0.015	2.0	0.75	262	6.819	0.013
I1A127S3	0.020	2.0	0.75	275	6.778	0.015
I1A111L1	0.007	1.0	1.00	260	6.218	†
I1A114S2	0.015	1.0	0.25	273	2.752	0.022
I1A114S3	0.020	1.0	0.25	270	3.552	0.042
I1A151L1	0.007	1.5	1.00	260	4.754	†
I1A151S2	0.015	1.5	1.00	293	5.710	0.011
I1A151S3	0.020	1.5	1.00	266	6.694	0.010
I1A121L1	0.007	2.0	1.00	243	5.298	†
I1A121S2	0.015	2.0	1.00	279	5.971	0.009
I1A121S3	0.020	2.0	1.00	270	6.861	0.004
I1A221L1	0.007	2.0	1.00	254	5.072	†
I1A221S2	0.015	2.0	1.00	249	5.314	0.010
I1A221S3	0.020	2.0	1.00	271	7.314	0.007
I1A321L1	0.007	2.0	1.00	279	3.926	†
I1A321S2	0.015	2.0	1.00	254	6.773	0.003
I1A122L1	0.007	2.0	2.00	262	3.270	†
I1A122S2	0.015	2.0	2.00	301	7.194	0.006
I1A122X3	0.020	2.0	2.00	268	7.530	0.011

*As determined by spacers (shims)
†Lost data

Table 9. Summary of EOI Test Data for CFPW-S

Specimen	Bondline Thickness* (in.)	Overlap (in.)	Impactor Diameter (in.)	Energy Level (in-lbf)	Max Load (lbf)	Stress Resultant, N_{xy} (lbf/in.)	Far-Field Stress, τ_{xy}^G (psi)
D1A12NN1	0.007	2.0	---	N/A	39131	2372	16508
D1A12NN2	0.015	2.0	---	N/A	39745	2413	17227
D1A12NN3	0.020	2.0	---	N/A	40550	2461	16612
I1A124S1	0.007	2.0	0.25	261	33116	2025	14991
I1A124S2	0.015	2.0	0.25	273	30331	1853	13550
I1A124S3	0.020	2.0	0.25	267	31644	1934	14404
I1A125S1	0.007	2.0	0.50	269	36120	2204	16385
I1A125L2	0.015	2.0	0.50	273	35816	2186	16123
I1A125S3	0.020	2.0	0.50	272	36391	2226	16429
I1A127L1	0.007	2.0	0.75	281	37502	2288	16964
I1A127S2	0.015	2.0	0.75	262	32945	2015	14482
I1A127S3	0.020	2.0	0.75	275	35884	2190	15885
I1A111L1	0.007	1.0	1.00	260	23190	1415	10341
I1A114S2	0.015	1.0	0.25	273	14078	1109	8103
I1A114S3	0.020	1.0	0.25	270	15902	1115	8314
I1A151L1	0.007	1.5	1.00	260	29136	1783	13039
I1A151S2	0.015	1.5	1.00	293	31610	1933	14490
I1A151S3	0.020	1.5	1.00	266	24041	1471	11098
I1A121L1	0.007	2.0	1.00	243	33451	2045	14828
I1A121S2	0.015	2.0	1.00	279	34272	2094	15331
I1A121S3	0.020	2.0	1.00	270	33235	2030	15052
I1A221L1	0.007	2.0	1.00	254	38480	2347	17497
I1A221S2	0.015	2.0	1.00	249	33879	2070	15267
I1A221S3	0.020	2.0	1.00	271	--	--	--
I1A321L1	0.007	2.0	1.00	279	36777	2245	16840
I1A321S2	0.015	2.0	1.00	254	37141	2270	17019
I1A122L1	0.007	2.0	2.00	262	37327	2279	16904
I1A122S2	0.015	2.0	2.00	301	35213	2152	16094
I1A122X3	0.020	2.0	2.00	268	35874	2188	16273

*As determined by spacers (shims)

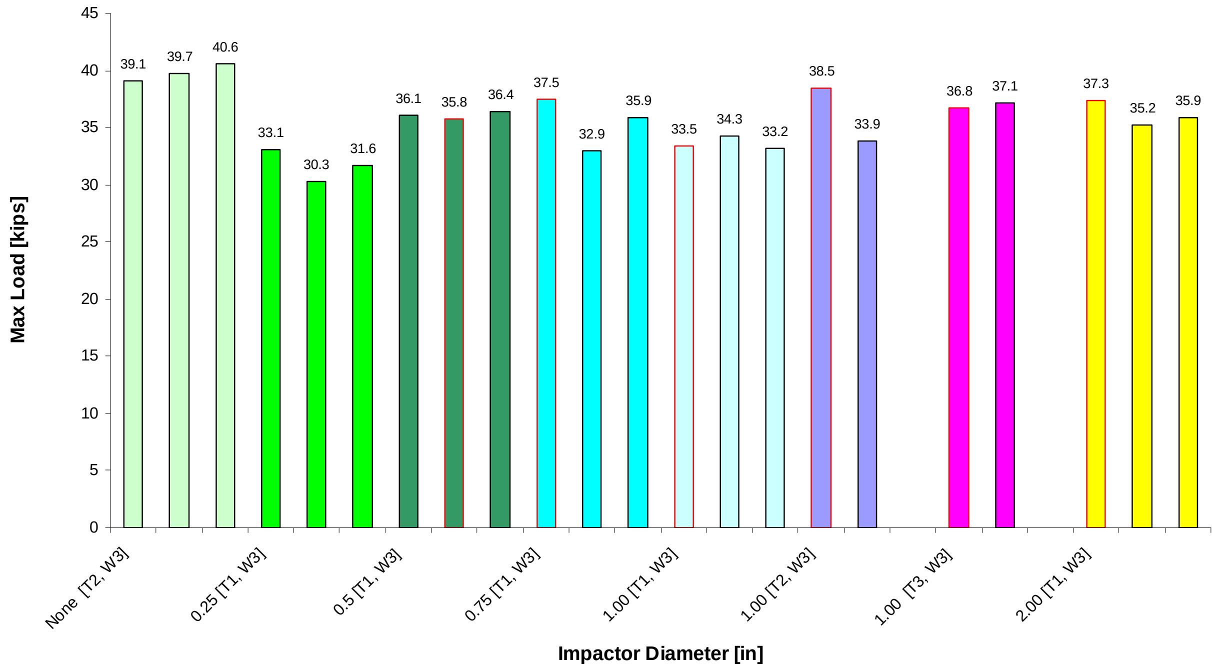

Figure 29. Summary of Failure Load for EOI Specimens With 2-Inch Overlap

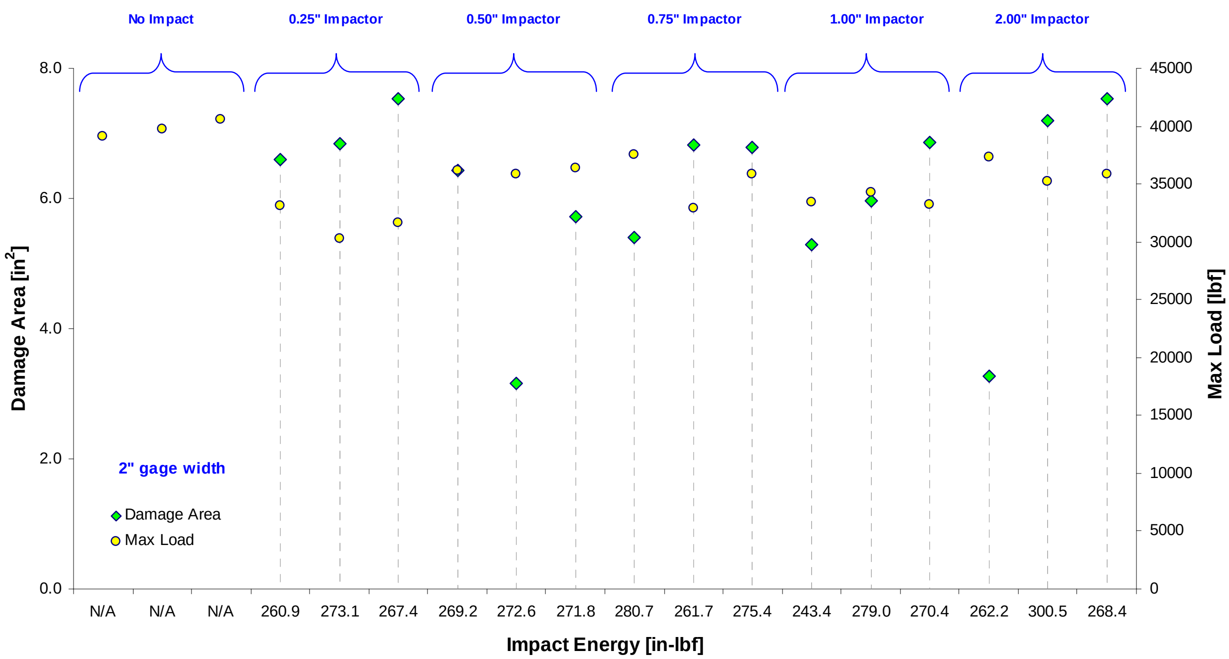

Figure 30. Effects of Impactor Diameter With 2-Inch Overlap

Except for the 0.25-inch impactor, PFS specimens with a 2-inch overlap indicated approximately 9% residual strength reduction due to impact damages (figure 31). Postimpact TTU C-scans of PFS specimens were made to evaluate the extent of damage. A typical result with explanations is shown in figure 32. The 0.25-inch impactor penetrated through most of the joint and caused extensive localized ply failure on the opposite side (figure 33). See appendix A for a complete description of figure 33. As the impactor diameter increased, the residual indention reduced, resulting in barely visible impact damages on the side of the impact for 1- and 2-inch impactors. However, the back side localized fiber failure was evident for all cases, and the overall damage areas seem to be the same for a given energy level and support fixture (figures 30 and 33). During impact, the free edge on the impact side undergoes compression, while the free edge on the opposite side undergoes tension in the Mode I (opening mode through-the-thickness) loading direction. For a short overlap length, the impact damage spreads across the overlap region and through a large area of the bonded region. For a given impactor diameter, an increase in overlap length minimizes the free-edge peel (tensile) stresses and reduces the damage propagation along this edge under high Mode I (peel) loading (figure 34). Also, the damage area toward the free edge, under compression, forms a bell-shaped curve, especially for large support fixtures, indicating that the free-edge stresses are reduced away from the impact location as the overlap length increases. A similar shape is observed for damage incurred by smaller impactors for the energy level investigated. As shown in figure 34, the support fixture greatly influences impact damage shape and size. The small fixture increases the overall system stiffness and restricts large deflections. Thus, the energy is dissipated through severely fractured adhesive layers and adherends.

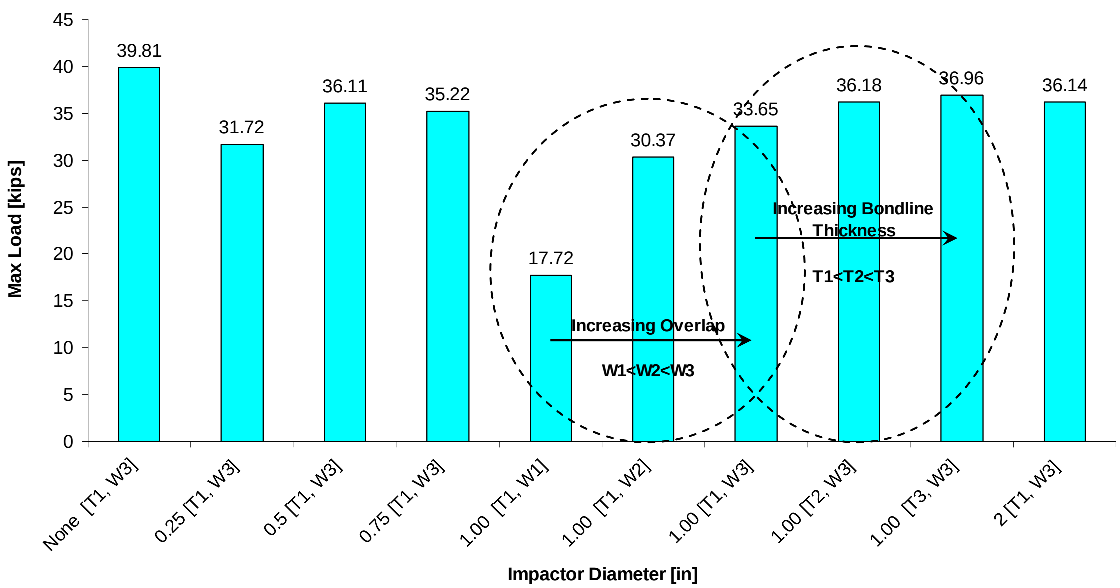

Figure 31. Failure Loads of Impacted Specimens

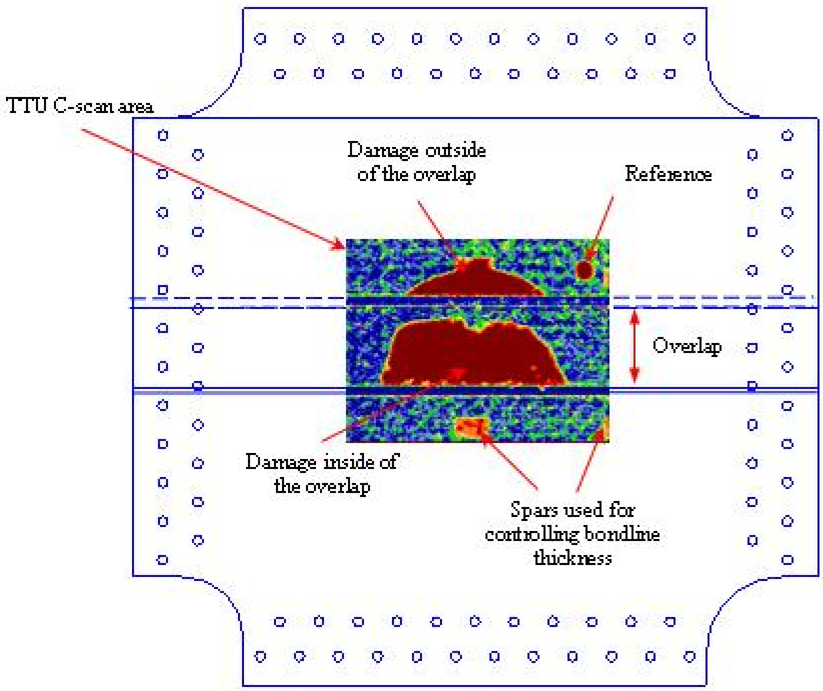

Figure 32. Postimpact TTU C-Scan of PFS Specimen

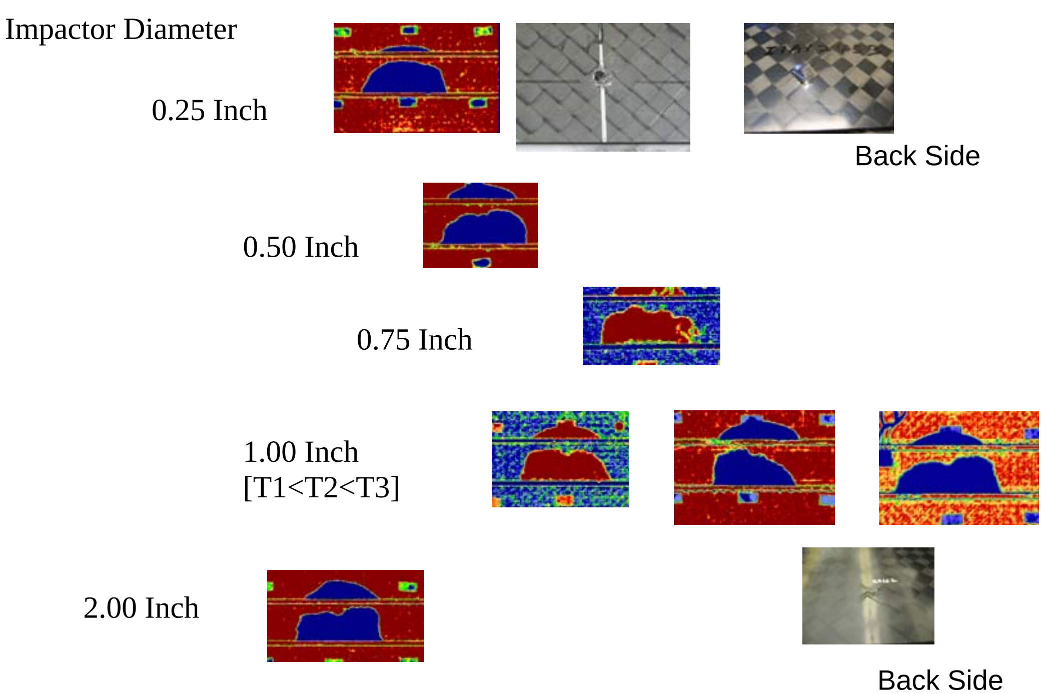

Figure 33. Effects of Impactor Diameter on Damage Size

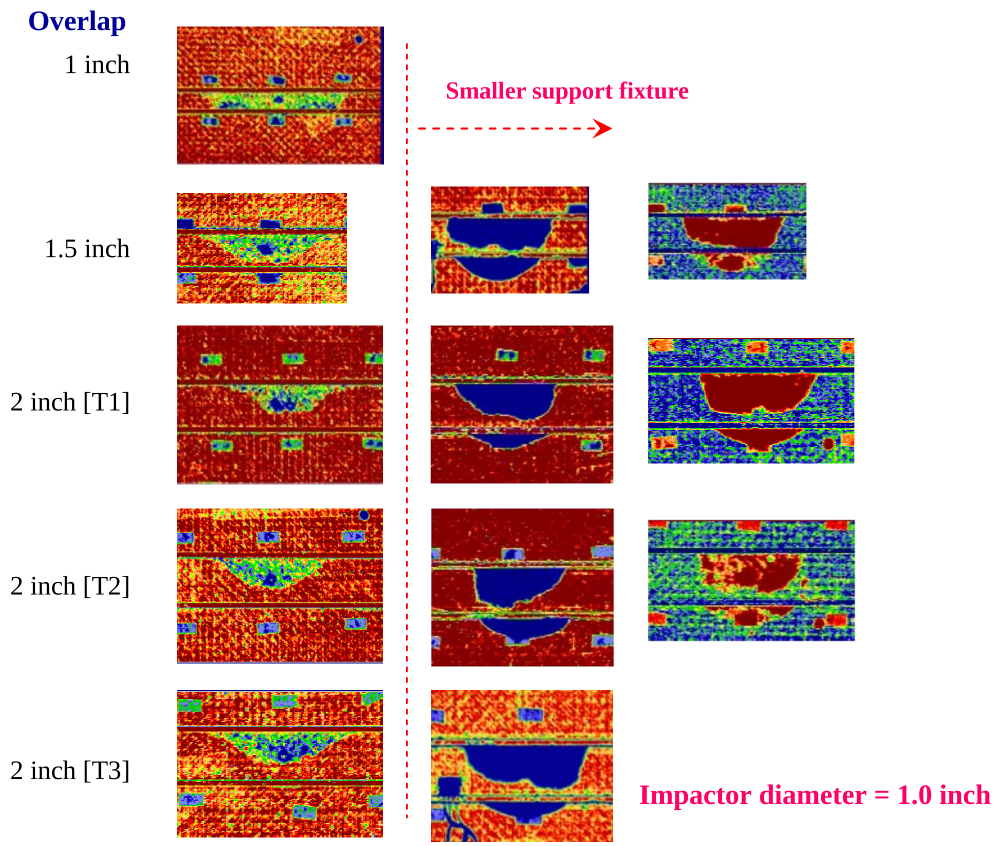

Figure 34. Effects of Overlap Length on Damage State

Contrary to the static strength decrease observed in previous studies [9 and 12] for thicker bondlines, the effects of bondline thickness on impacted specimens indicate an increase in residual strength as the bondline thickness increased. This may have been caused by the increased energy-absorbing capability of thicker bondlines due to the dampening effects of the viscoelastic adhesive layer. This agrees with the findings of Zelalem, et al. [13] and reveals the importance of accounting for the viscoelastic characteristics of adhesives for design and analysis of joints.

3.2.2 The SLS Test Results.

The effects of low-velocity impacts on SLS specimens with different impact energy levels and with different impactor diameters are discussed in this section. All test specimens were clamped to the test fixture, as shown in figure 10, with a 3- by 5-inch unsupported section. Impact force and displacement history were recorded to characterize the impact resistance of these specimens.

Figures 35 through 43 show the typical force displacement, impact force history, and energy history plots for SLS specimens impacted with energy of 354 in-lbf (40 joules (J)), using impactors having diameters of 0.5, 0.75, and 1.0 inch, respectively. Similar plots for cases using energy impacts of 221 in-lbf (25 J) and 88.5 in-lbf (10 J) are included in appendix B. Impact force and displacement history for each material changed significantly, except for the 354 in-lbf/in. in which the force history for all three material systems for a given energy level was insensitive to the impactor diameters. For 354 in-lbf/in. energy impacts, larger impactors produced higher impact forces, especially for carbon fiber-reinforced composites. However, the impact durations for these cases were shorter than for lower-energy impacts.

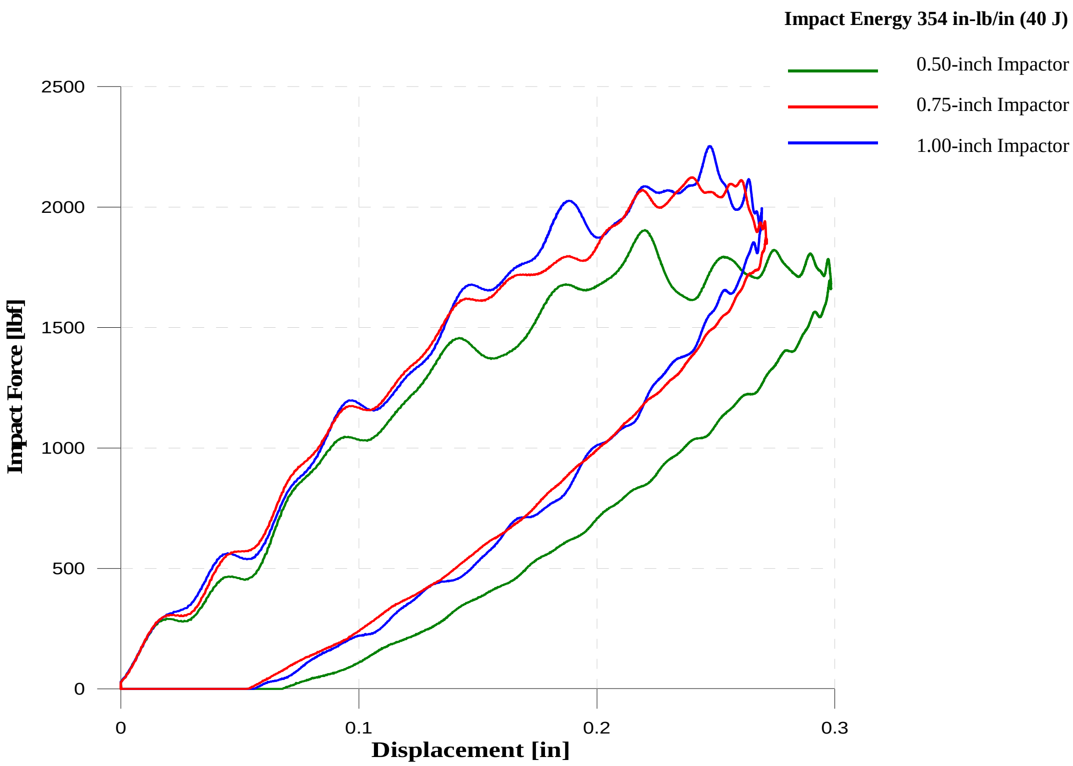

Figure 35. Typical Force-Displacement Curves for FGSW SLS Specimens

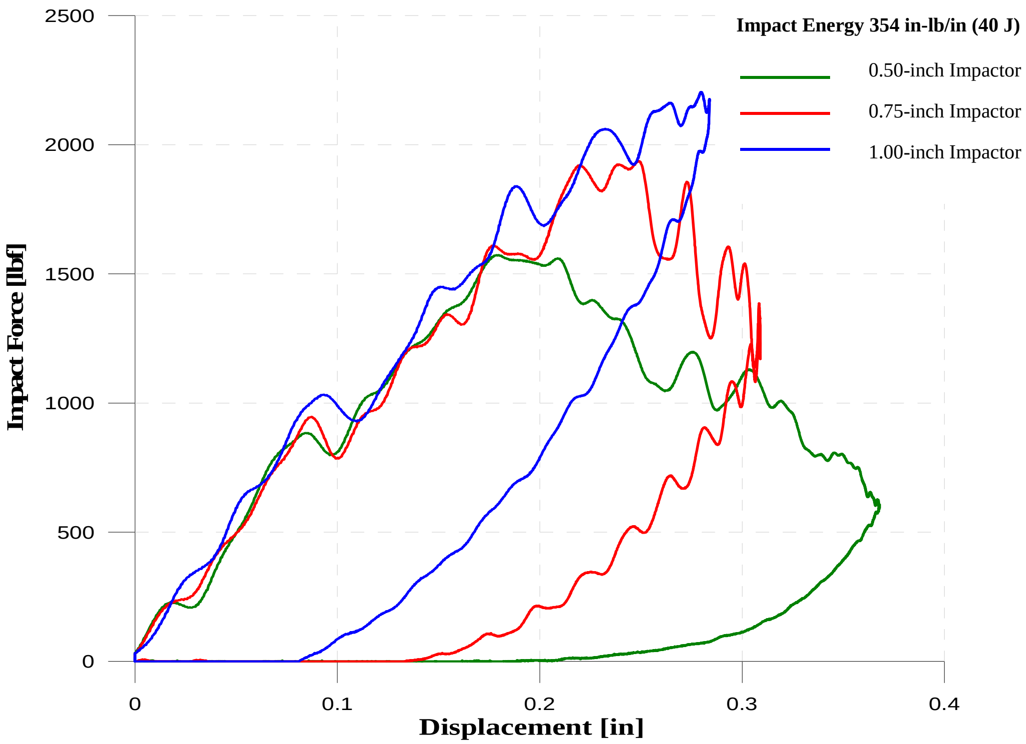

Figure 36. Typical Force-Displacement Curves for CFPW SLS Specimens

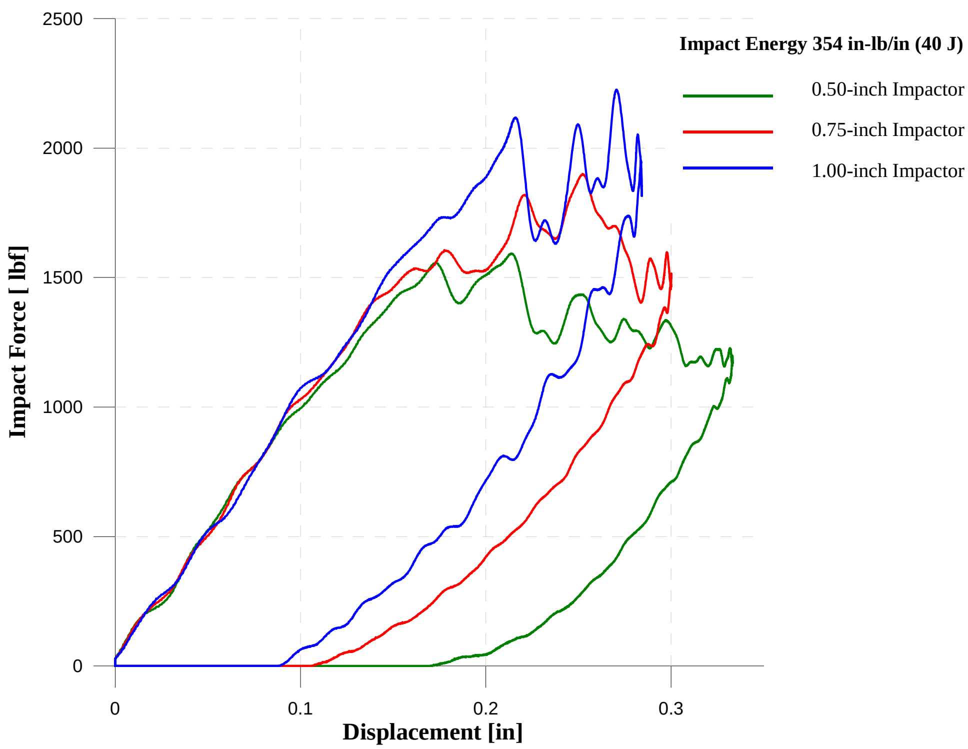

Figure 37. Typical Force-Displacement Curves for CFUT SLS Specimens

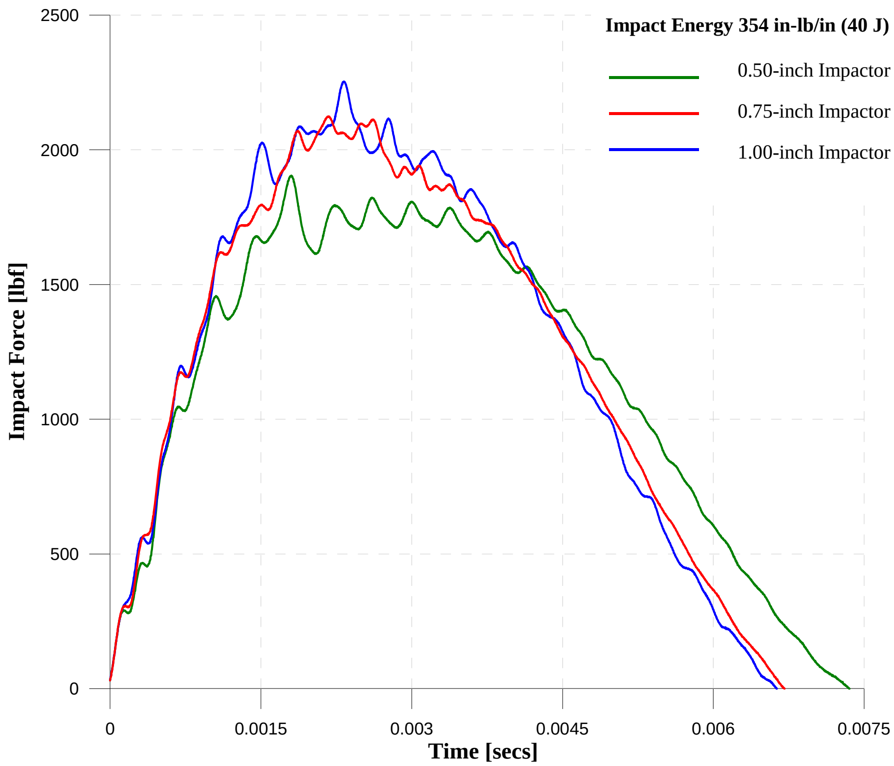

Figure 38. Typical Impact Force-Time Curves for FGSW SLS Specimens

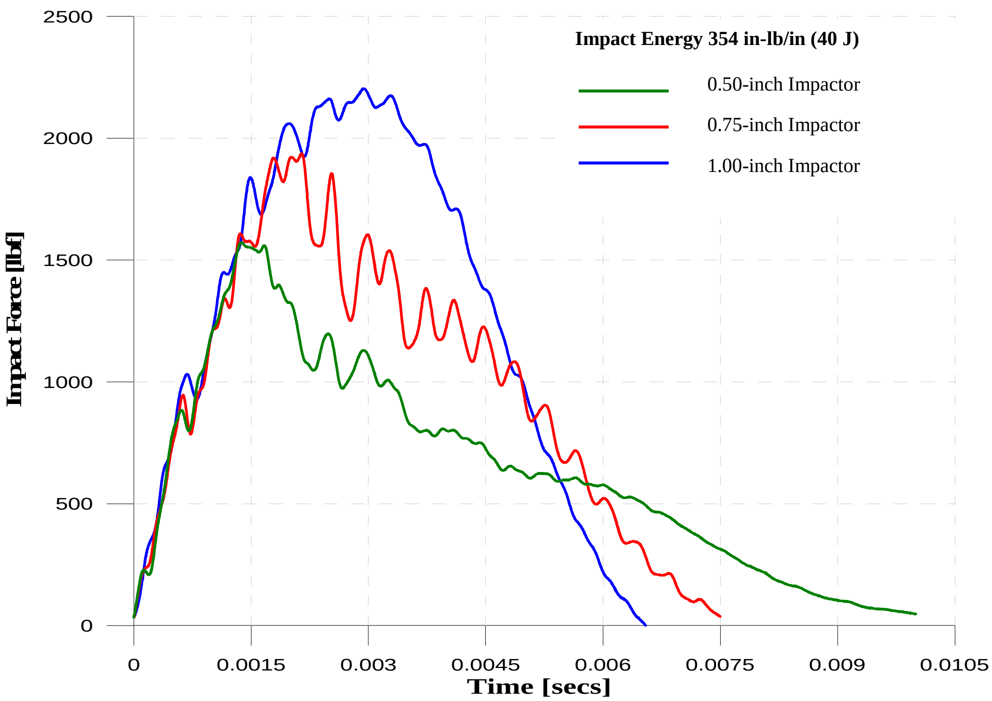

Figure 39. Typical Impact Force-Time Curves for CFPW SLS Specimens

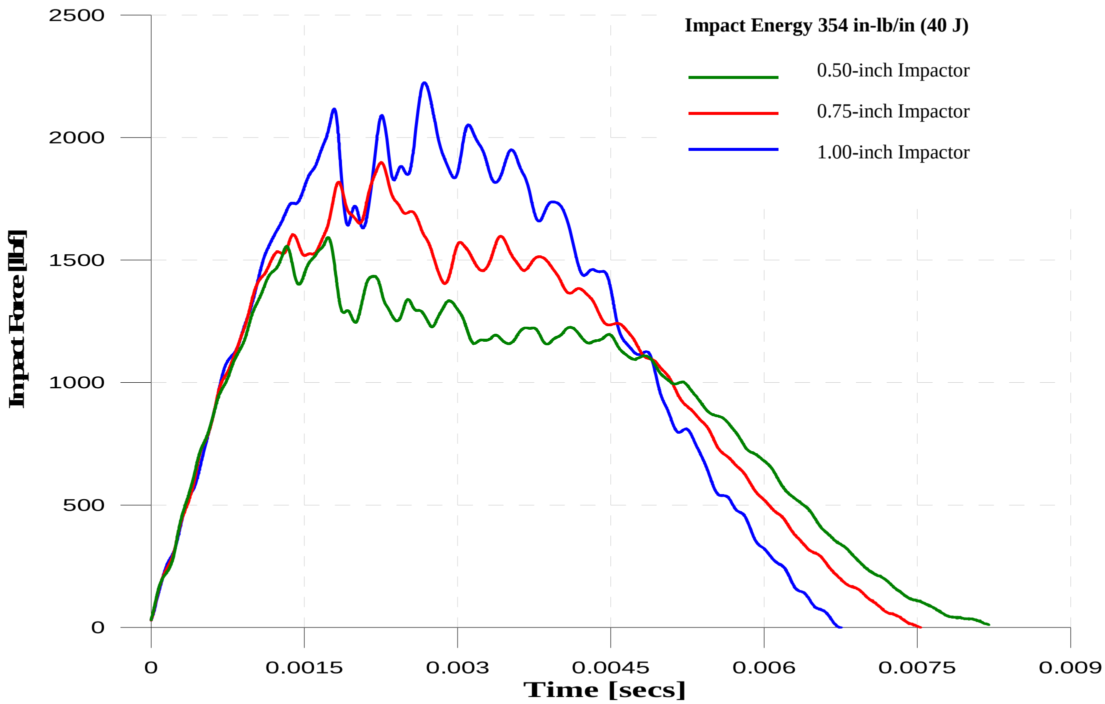

Figure 40. Typical Impact Force-Time Curves for CFUT SLS Specimens

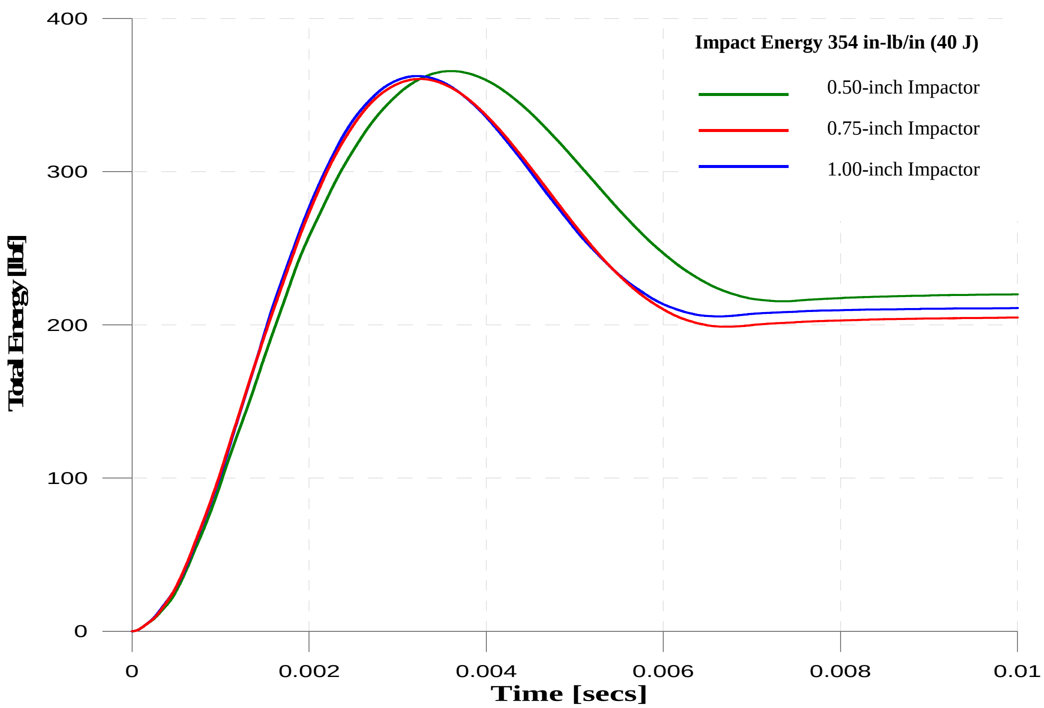

Figure 41. Typical Total Energy-Time Curves for FGSW SLS Specimens

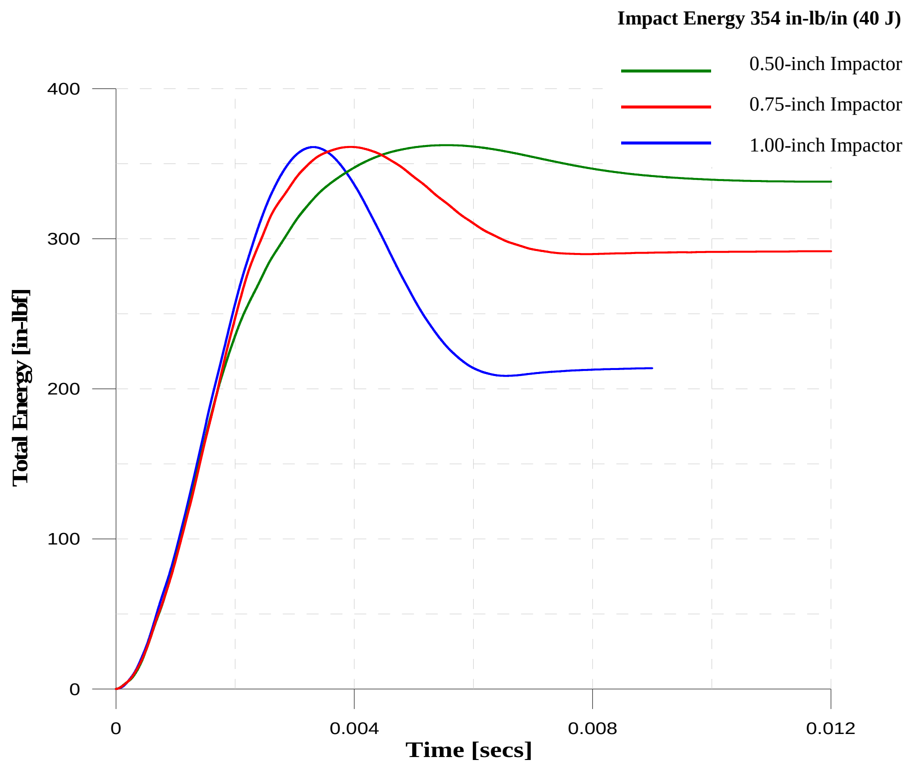

Figure 42. Typical Total Energy-Time Curves for CFPW SLS Specimens

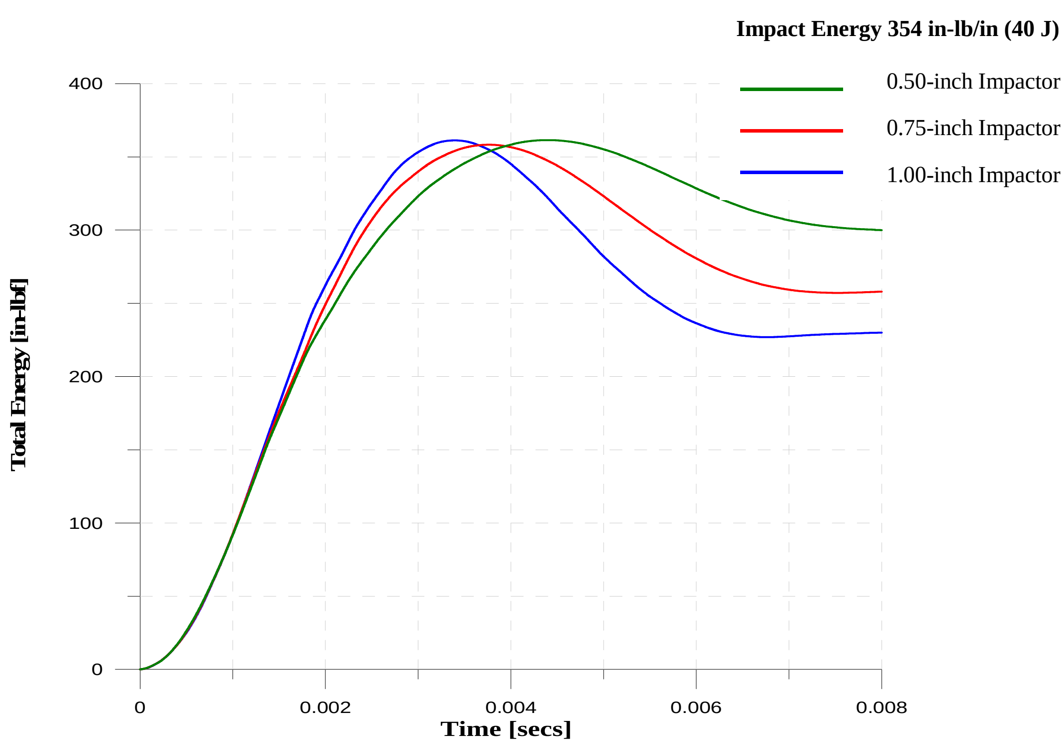

Figure 43. Typical Total Energy-Time Curves for CFUT SLS Specimens

The area under the loading portion of the force-displacement plot is the energy used to indent the joint, while the area under the unloading portion is the energy recovered during unloading. These energy values for laminated composites can be approximated using the contact force and indentation [14]. An impactor with a smaller diameter induces more damage in the form of matrix cracking and fiber breakage that leads to penetration. Therefore, for the cases of higher-impact energy levels on CFPW-S and CFUT, the difference between loading and unloading curves for the 0.5-inch-diameter impactor is pronounced, and the consequences are prominent in the energy histories. Figure 44 shows that the impact force and displacement histories of FGSW are significantly affected by the impact energy level more than the impactor diameter. Impactors with larger diameters induce more impact (contact) force and consequently lead to larger internal damages.

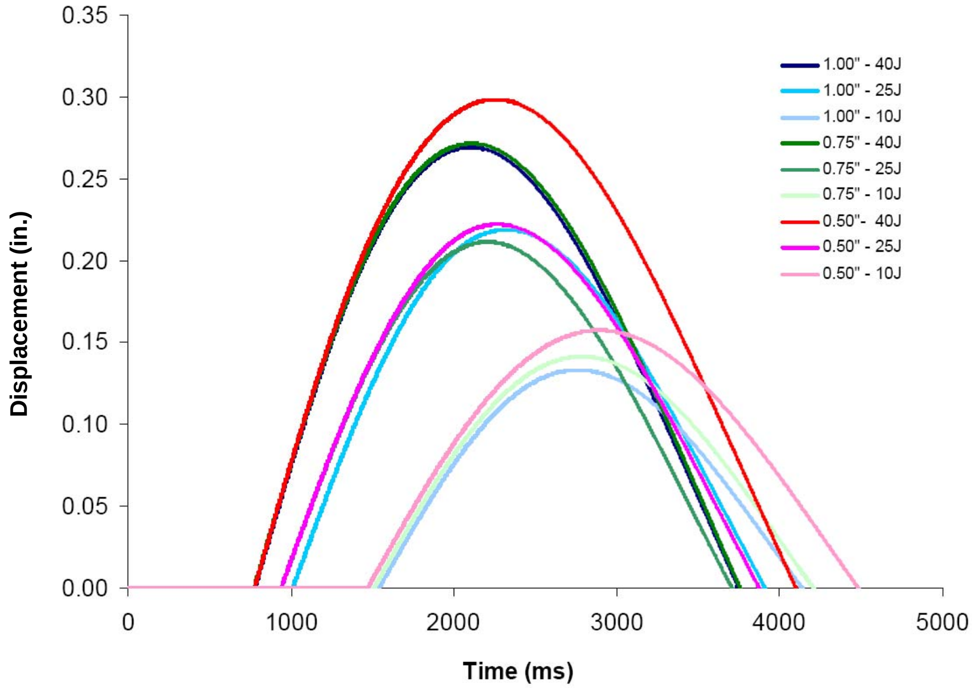

(a) Displacement vs time

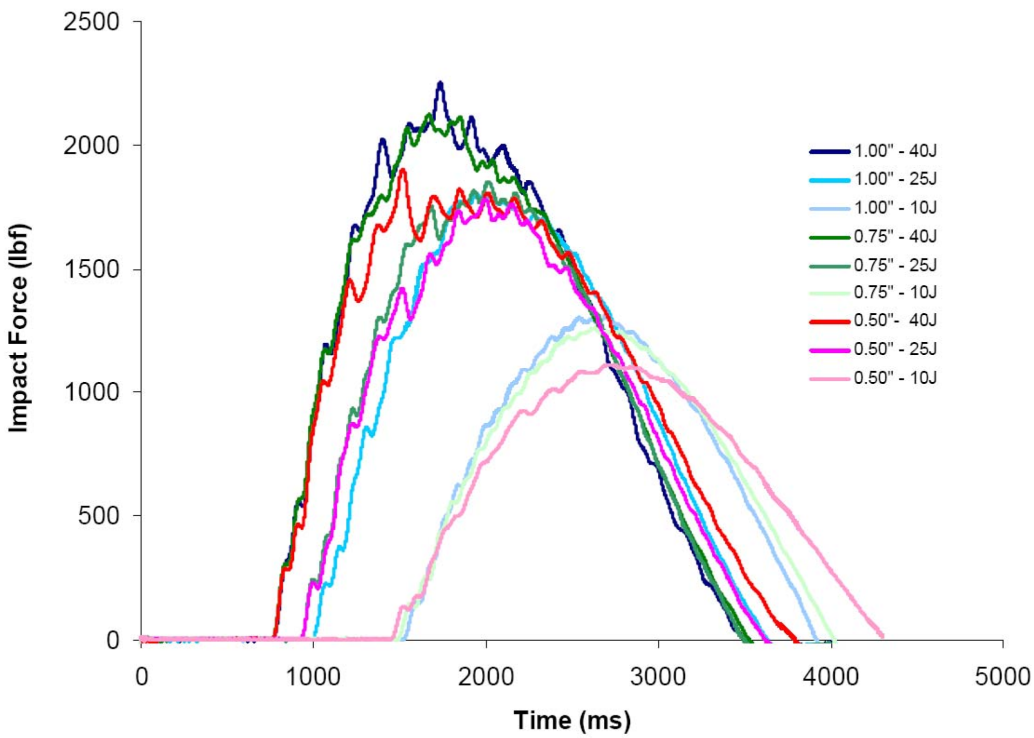

(b) Impact force vs time

Figure 44. Comparison vs Time for (a) Displacement and (b) Impact Force for FGSW Specimens

3.2.2.1 Nondestructive Inspection Results.

Figures 45 through 53 show the damage induced on the impact side (left) and back sides (right) of FGSW, CFPW, and CFUT SLS specimens for impact energy of 354 in-lbf (40 J) using impactors with diameters of 0.5, 0.75, and 1.0 inch, respectively. Due to the translucent nature of glass fibers, the damage on FGSW specimens can be seen with the naked eye.

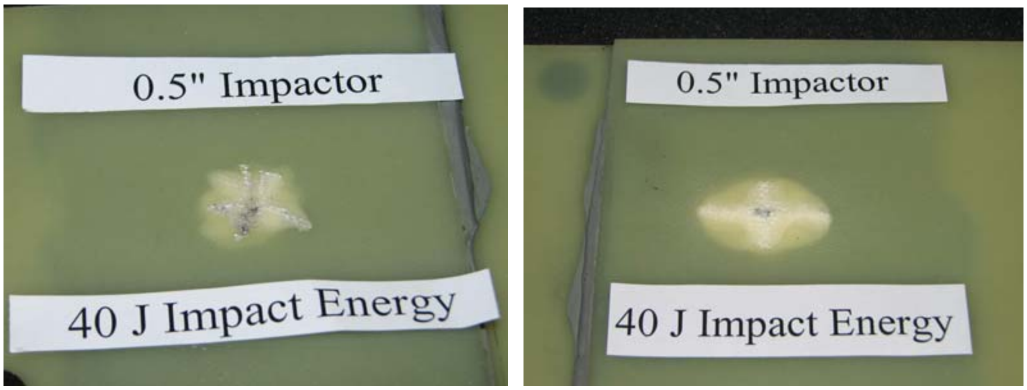

Figure 45. Impact Damage Induced on FGSW With 0.5-Inch Impactor

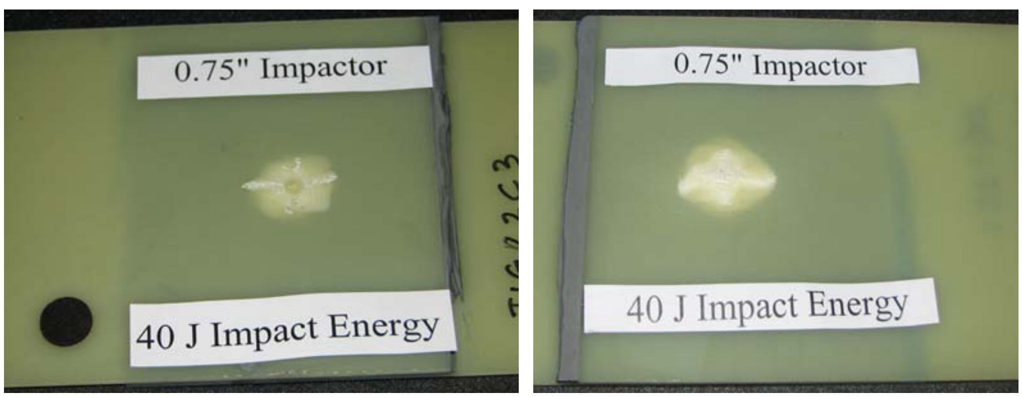

Figure 46. Impact Damage Induced on FGSW With 0.75-Inch Impactor

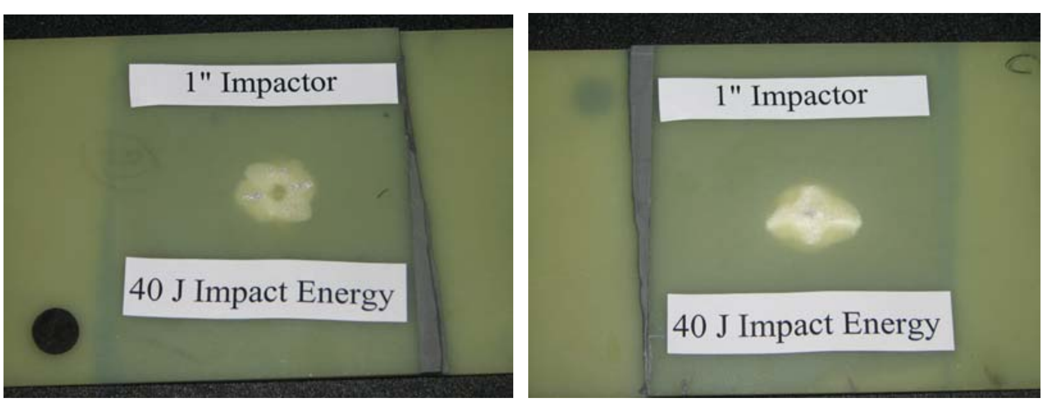

Figure 47. Impact Damage Induced on FGSW With 1.00-Inch Impactor

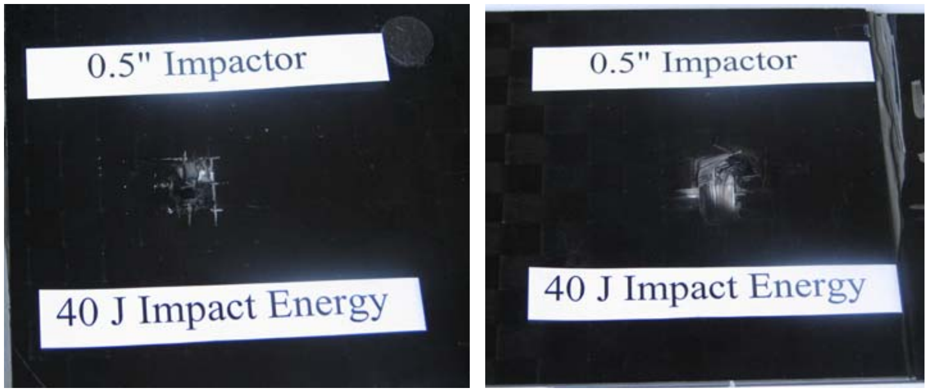

Figure 48. Impact Damage Induced on CFPW With 0.5-Inch Impactor

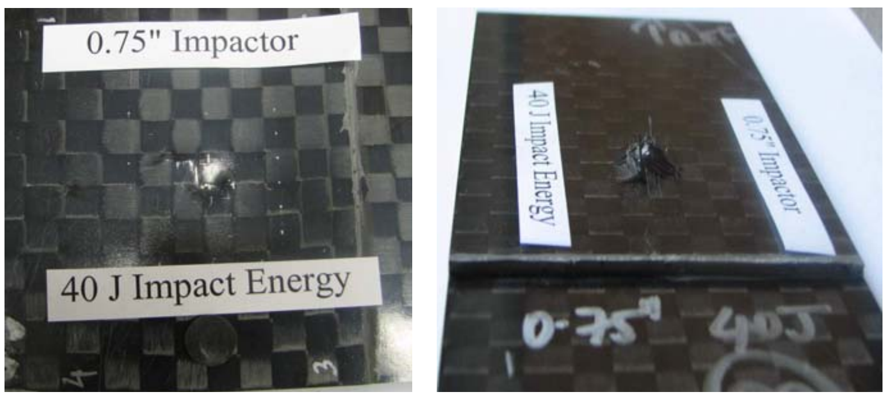

Figure 49. Impact Damage Induced on CFPW With 0.75-Inch Impactor

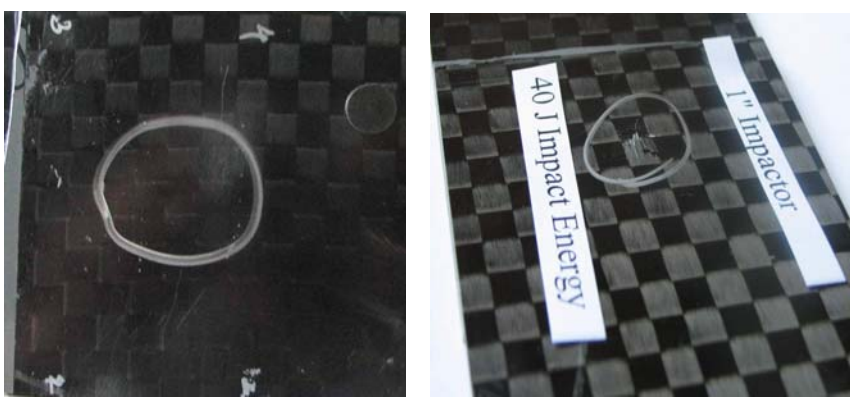

Figure 50. Impact Damage Induced on CFPW With 1.00-Inch Impactor

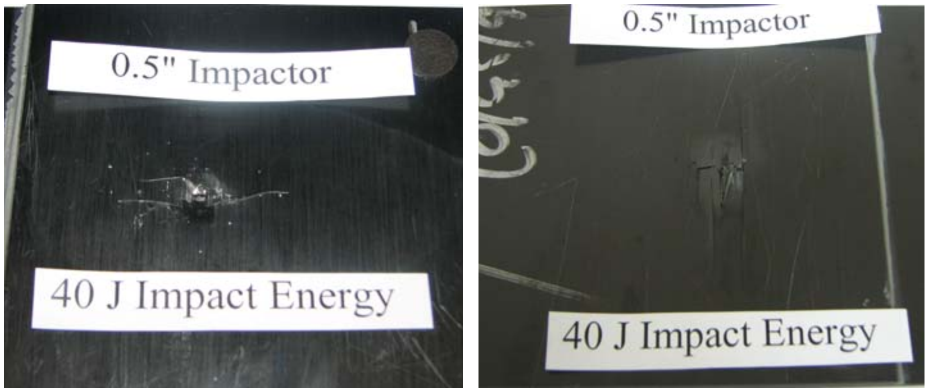

Figure 51. Impact Damage Induced on CFUT With 0.5-Inch Impactor

Figure 52. Impact Damage Induced on CFUT With 0.75-Inch Impactor

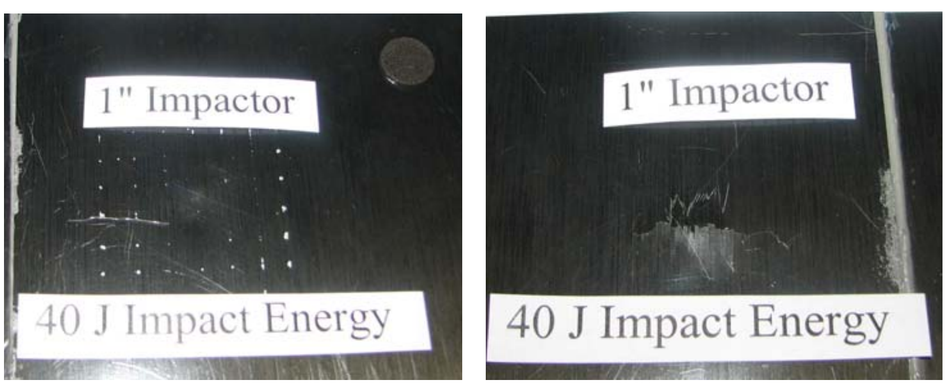

Figure 53. Impact Damage Induced on CFUT With 1.00-Inch Impactor

Figures 54 through 56 show the TTU C-scan images of the damage induced on woven FGSW, CFPW, and CFUT specimens for impact energy of 354 in-lbf (40 J) using impactors with diameters of 0.5, 0.75, and 1.0 inch, respectively. These image areas represent the projected damage that consists of delamination, matrix cracking, and fiber breakage on several layers of composite adherend, as well as damages within the bondline and the interface. The difference in response behavior FGSW (fiberglass) and carbon CFPW laminates is striking. The FGSW seems to be unaffected by impactor diameter.

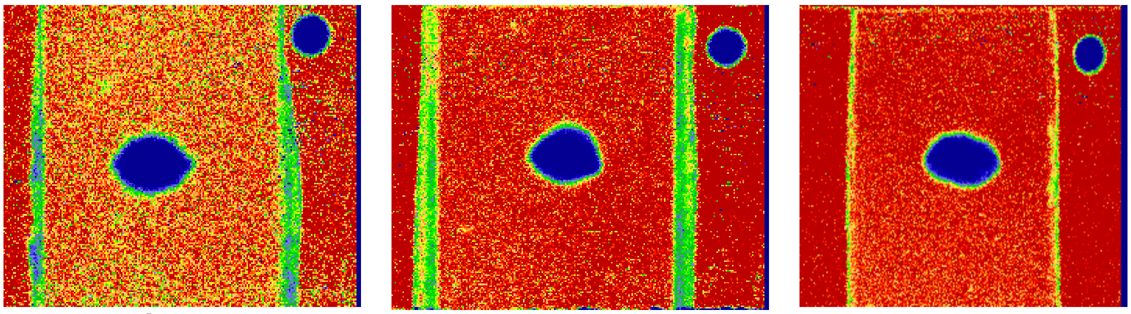

1-Inch Impactor　　0.75-Inch Impactor　　0.5-Inch Impactor

Figure 54. Ultrasonic C-Scan of FGSW (354 in-lbf)

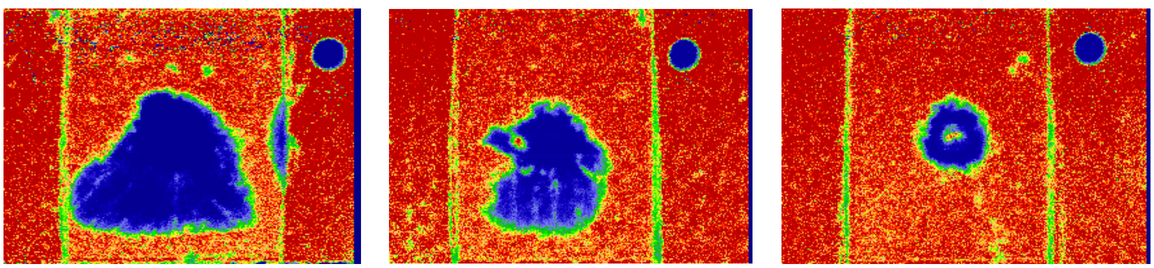

1-Inch Impactor　　0.75-Inch Impactor　　0.5-Inch Impactor

Figure 55. Ultrasonic C-Scan of CFPW (354 in-lbf)

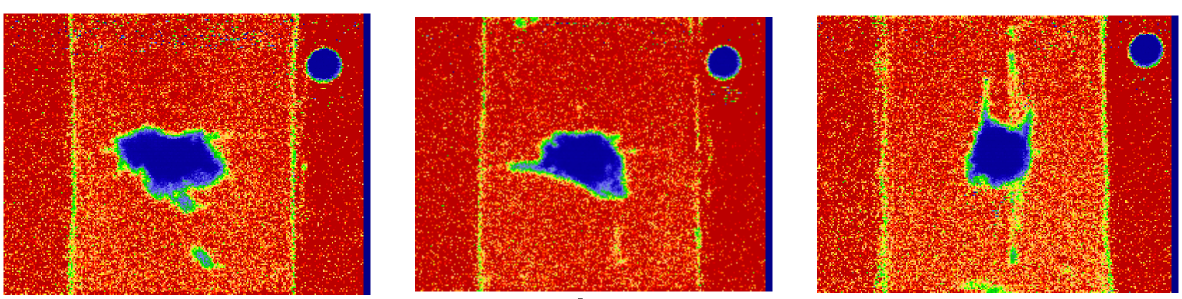

1-Inch Impactor　　0.75-Inch Impactor　　0.5-Inch Impactor

Figure 56. Ultrasonic C-Scan of CFUT (354 in-lbf)

Figures 57 through 59 show the relationship between damage area and impact energy. Impact damage in laminated composites takes place as a result of matrix cracking, delamination, and fiber breakage. Highly localized compressive force at the impact location caused both matrix cracks and fiber breakage, which subsequently resulted in delamination and penetration, respectively. Initially, the matrix cracks were induced on the first layer, because of the highly localized stresses. Further progression of the damage occurs from the upper to bottom layers. This progression follows a pattern, which is called the pine tree pattern. Furthermore, the high tensile stress on the bottom plies, due to bending, caused fiber breakage.

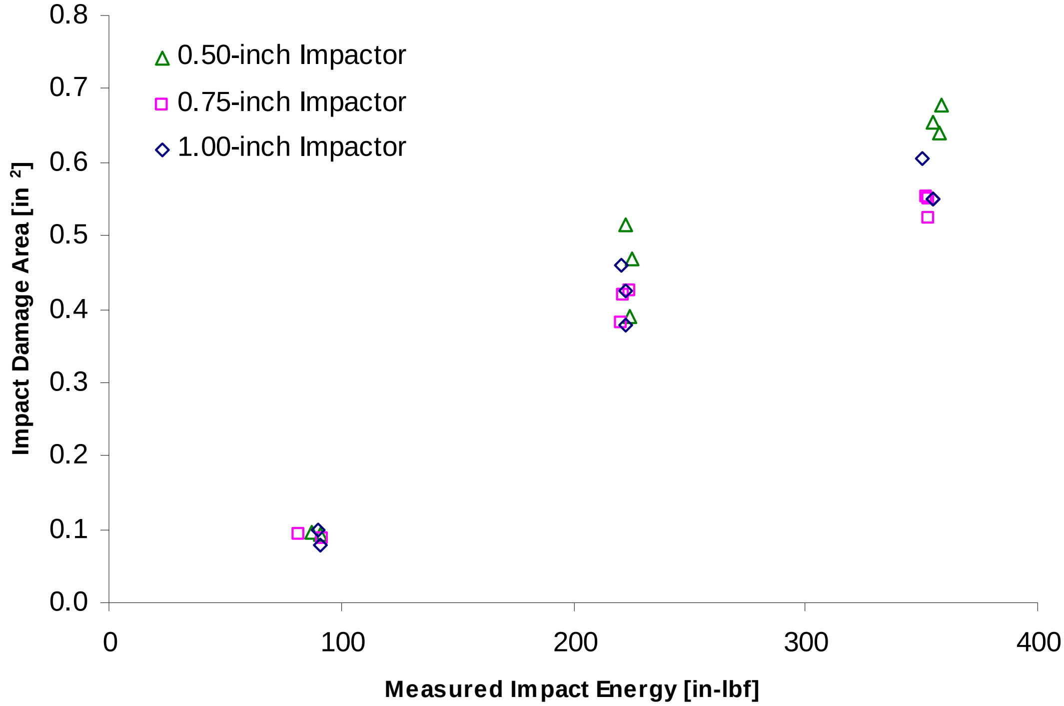

Figure 57. Damage Area and Energy Level for FGSW

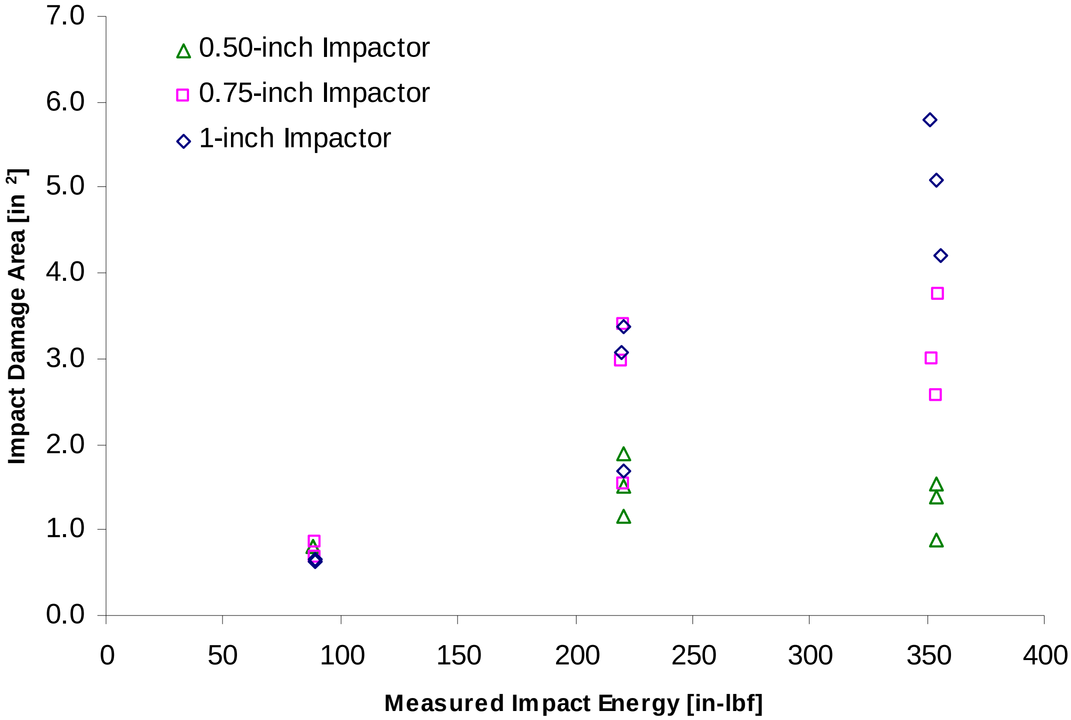

Figure 58. Damage Area and Energy Level for CFPW

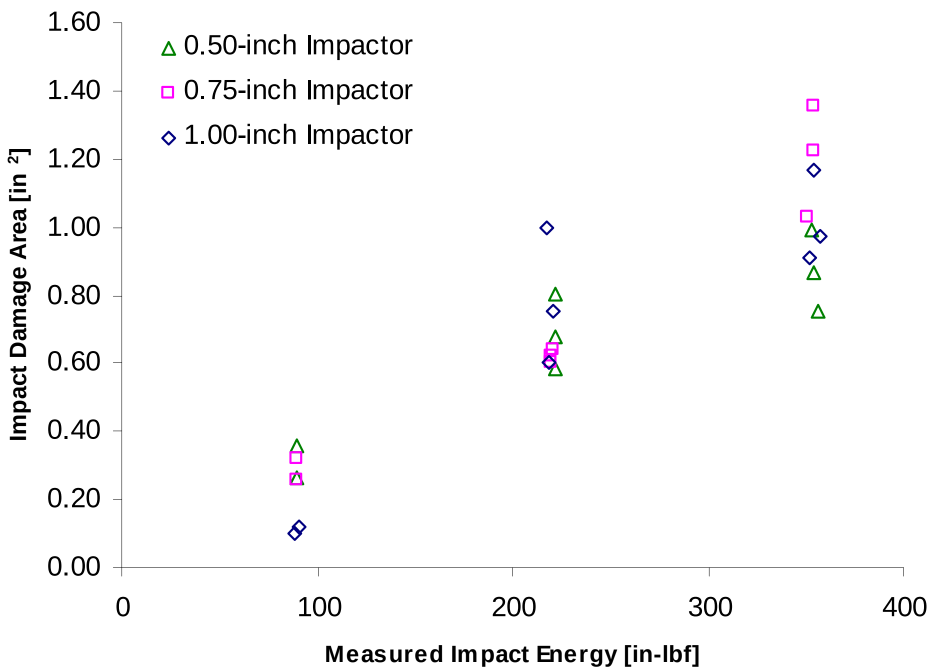

Figure 59. Damage Area and Energy Level for CFUT

For FGSW, the damage area was independent of the impactor diameter, especially at smaller energy levels, and was proportional to the energy level. Impact damage results obtained for CFPW and CFUT (same matrix) indicated that the fiber form significantly influenced the damage area and failure mode. A larger damage area was observed in carbon fiber adherends compared to glass fiber adherends. For carbon plain weave adherends, the damage area increased and reached a maximum, and then decreased with an increase in energy level, resulting in penetration. The CFUT specimen absorbed the impact energy in the form of matrix cracks and fiber breakage, and indicated significantly larger matrix cracks that extended beyond the circular damage area shown in TTU C-scans.

Figures 60 through 62 show (not to scale) the residual indentation induced on the test specimens on woven glass/epoxy, carbon plain weave, and carbon unitape test specimens at 40 J impact energy induced by impactors with diameters of 0.5, 0.75, and 1.0 inch, respectively. Measured residual indentation values are tabulated in appendix B.

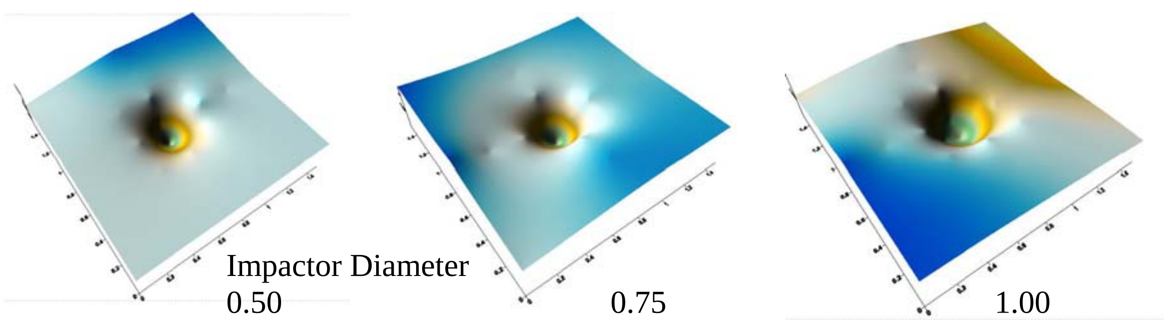

Figure 60. Residual Indentation for FGSW (354 in-lbf)

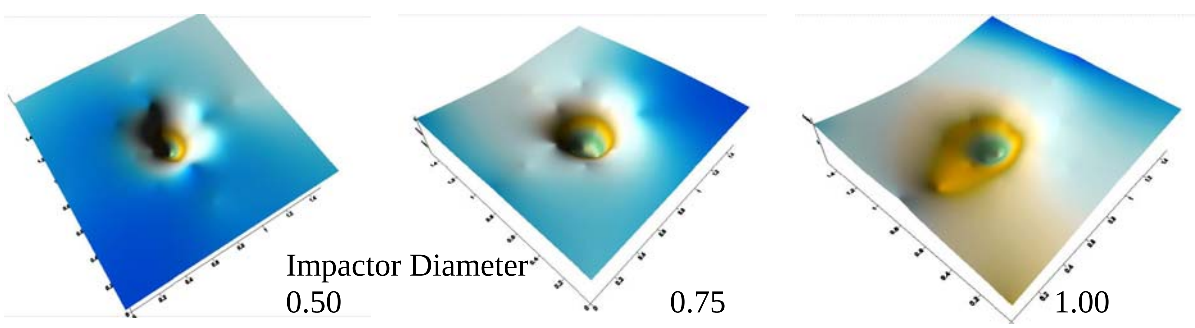

Figure 61. Residual Indentation for CFPW (354 in-lbf)

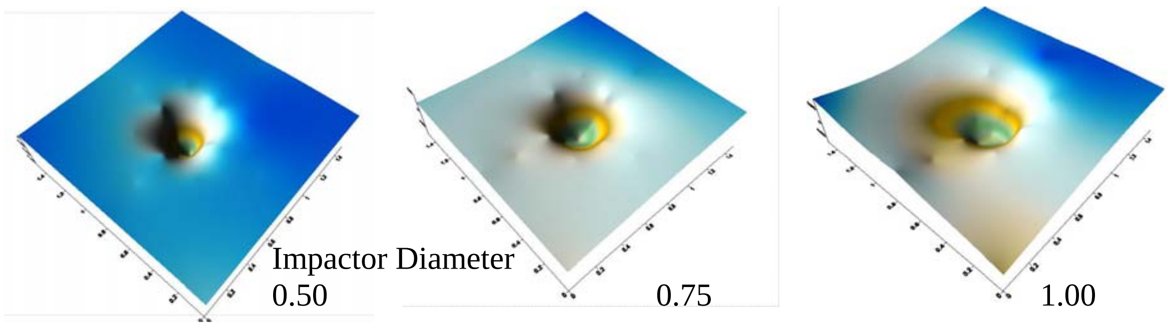

Figure 62. Residual Indentation for CFUT (354 in-lbf)

3.2.2.2 Residual Strength Tests.

Figures 63 through 65 show typical failure modes observed for FGSW, CFPW, and CFUT SLS specimens. The primary failure mode for all residual strength tests on lap joints was adherend failure (mostly first ply).

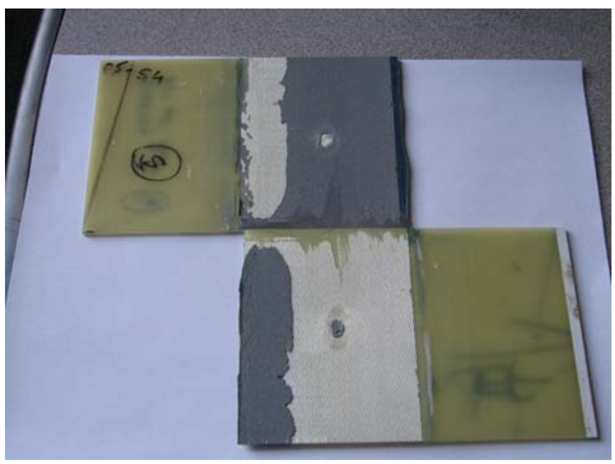

Figure 63. Typical Failure Mode Observed for FGSW SLS Specimens

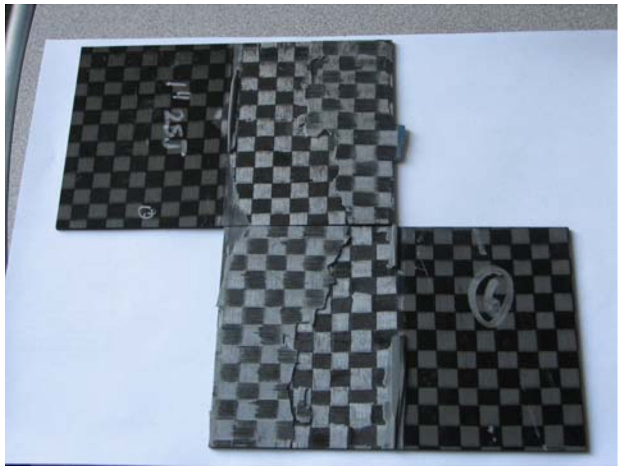

Figure 64. Typical Failure Mode Observed for CFPW SLS Specimens

Figure 65. Typical Failure Mode Observed for CFUT SLS Specimens

Tables 10 through 12 provide a summary of the impact test results and the residual strength results. These data are also shown in figures 66 through 74. The maximum impact force, maximum residual indentation, and impact area increased as the energy level increased. Because the failure was in the adherends, residual strength does not show any significant differences due to impact damages at all three energy levels. Detailed test results for SLS experiments are included in appendix B.

Table 10. Residual Strength Test Results for FGSW SLS Specimens

Specimen Name	Overlap (in.)	Width (in.)	Impactor Diameter (in.)	Impact Energy (in-lbf)	Maximum Load (lb)	Shear Strength (ksi)	Failure Mode
RSWI-G1*	3.0	4.0	N/A	N/A	8,419	0.702	Adherend failure
RSWI-G2*	3.0	4.0	N/A	N/A	9,014	0.751	Adherend failure
I1G31C1	3.0	4.0	1.00	354.0	9,784	0.815	Adherend failure
I1G21C2	3.0	4.0	1.00	354.0	10,578	0.881	Adherend failure
I1G31B1	3.0	4.0	1.00	221.0	9,418	0.785	Adherend failure
I1G31B3	3.0	4.0	1.00	221.0	9,806	0.817	Adherend failure
I1G61A1	3.0	4.0	1.00	88.5	9,144	0.762	Adherend failure
I1G61A2	3.0	4.0	1.00	88.5	9,725	0.810	Adherend failure
I1G22C1	3.0	4.0	0.75	354.0	11,091	0.924	Adherend failure
I1G22C3	3.0	4.0	0.75	354.0	10,370	0.864	Adherend failure
I1G32B1	3.0	4.0	0.75	221.0	10,047	0.837	Adherend failure
I1G42B3	3.0	4.0	0.75	221.0	10,739	0.895	Adherend failure
I1G42A1	3.0	4.0	0.75	88.5	10,883	0.907	Adherend failure
I1G42A2	3.0	4.0	0.75	88.5	10,170	0.847	Adherend failure
I1G53C2	3.0	4.0	0.50	354.0	9,972	0.831	Adherend failure
I1G83C3	3.0	4.0	0.50	354.0	9,372	0.781	Adherend failure
I1G53B1	3.0	4.0	0.50	221.0	10,161	0.847	Adherend failure
I1G53B4	3.0	4.0	0.50	221.0	10,474	0.873	Adherend failure
I1G73A2	3.0	4.0	0.50	88.5	6,425	0.535	Adherend failure
I1G73A3	3.0	4.0	0.50	88.5	10,037	0.836	Adherend failure

* RSWI-G1 and RSWI-G2 were not impacted.

Table 11. Residual Strength Test Results for CFPW SLS Specimens

Specimen Name	Overlap (in.)	Width (in.)	Impactor Diameter (in.)	Impact Energy (in-lbf)	Maximum Load (lb)	Shear Strength (ksi)	Failure Mode
RSWI-P1 *	3.0	4.0	N/A	N/A	9,751	0.813	Adherend failure
RSWI-P2 *	3.0	4.0	N/A	N/A	10,257	0.855	Adherend failure
I1P41C1	3.0	4.0	1.00	354.0	10,251	0.854	Adherend failure
I1P91C2	3.0	4.0	1.00	354.0	9,970	0.831	Adherend failure
I1P61B1	3.0	4.0	1.00	221.0	9,143	0.762	Adherend failure
I1P61B3	3.0	4.0	1.00	221.0	9,331	0.778	Adherend failure
I1P41A1	3.0	4.0	1.00	88.5	10,270	0.856	Adherend failure
I1P81A2	3.0	4.0	1.00	88.5	10,126	0.844	Adherend failure
I1P52C1	3.0	4.0	0.75	354.0	10,593	0.883	Adherend failure
I1P52C3	3.0	4.0	0.75	354.0	10,028	0.836	Adherend failure
I1P52B2	3.0	4.0	0.75	221.0	10,062	0.838	Adherend failure
I1P52B3	3.0	4.0	0.75	221.0	10,261	0.855	Adherend failure
I1P92A1	3.0	4.0	0.75	88.5	11,093	0.924	Adherend failure
I1P92A2	3.0	4.0	0.75	88.5	10,398	0.866	Adherend failure
I1P43C1	3.0	4.0	0.50	354.0	10,798	0.900	Adherend failure
I1P43C2	3.0	4.0	0.50	354.0	11,002	0.917	Adherend failure
I1P23B1	3.0	4.0	0.50	221.0	10,078	0.840	Adherend failure
I1P23B2	3.0	4.0	0.50	221.0	10,234	0.853	Adherend failure
I1P23A1	3.0	4.0	0.50	88.5	9,914	0.826	Adherend failure
I1P23A2	3.0	4.0	0.50	88.5	10,432	0.869	Adherend failure

* RSWI-P1 and RSWI-P2 were not impacted.

Table 12. Residual Strength Test Results for CFUT SLS Specimens

Specimen Name	Overlap (in.)	Width (in.)	Impactor Diameter (in.)	Impact Energy (in-lbf)	Maximum Load (lb)	Shear Strength (ksi)	Failure Mode
RSWI-U1 *	3.0	4.0	N/A	N/A	12,332	1.028	Adherend failure
RSWI-U2 *	3.0	4.0	N/A	N/A	12,323	1.027	Adherend failure
I1U31C1	3.0	4.0	1.00	354.0	12,200	1.017	Adherend failure
I1U51C4	3.0	4.0	1.00	354.0	11,305	0.942	Adherend failure
I1U21B1	3.0	4.0	1.00	221.0	10,808	0.901	Adherend failure
I1U21B2	3.0	4.0	1.00	221.0	11,797	0.983	Adherend failure
I1U61A1	3.0	4.0	1.00	88.5	12,413	1.034	Adherend failure
I1U21A2	3.0	4.0	1.00	88.5	11,902	0.992	Adherend failure
I1U72C1	3.0	4.0	0.75	354.0	11,553	0.963	Adherend failure
I1U42C3	3.0	4.0	0.75	354.0	11,381	0.948	Adherend failure
I1U12B2	3.0	4.0	0.75	221.0	10,650	0.887	Adherend failure
I1U12B3	3.0	4.0	0.75	221.0	11,423	0.952	Adherend failure
I1U12A1	3.0	4.0	0.75	88.5	12,098	1.008	Adherend failure
I1U52A2	3.0	4.0	0.75	88.5	10,239	0.853	Adherend failure
I1U53C1	3.0	4.0	0.50	354.0	11,745	0.979	Adherend failure
I1U73C2	3.0	4.0	0.50	354.0	10,199	0.850	Adherend failure
I1U43B1	3.0	4.0	0.50	221.0	10,993	0.916	Adherend failure
I1U33B3	3.0	4.0	0.50	221.0	11,364	0.947	Adherend failure
I1U63A1	3.0	4.0	0.50	88.5	11,781	0.982	Adherend failure
I1U63A2	3.0	4.0	0.50	88.5	12,185	1.015	Adherend failure

* RSWI-U1 and RSWI-U2 were not impacted.

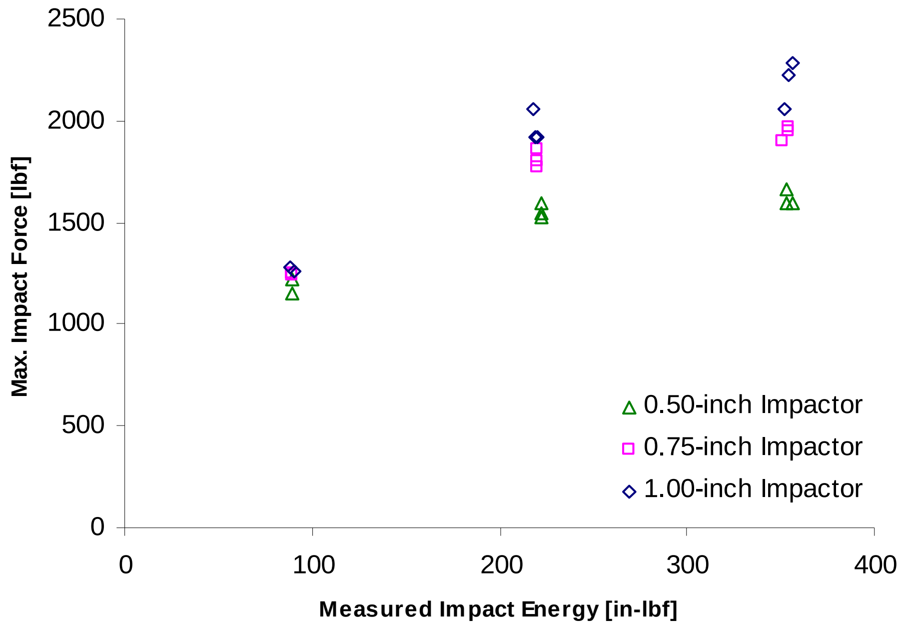

Figure 66. Maximum Impact Force for CFUT

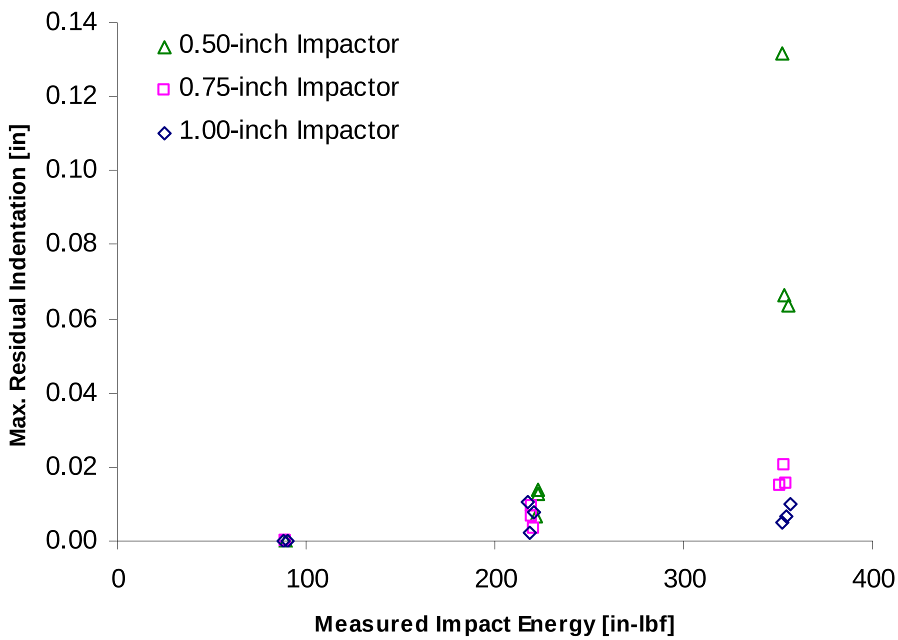

Figure 67. Maximum Residual Indentation for CFUT

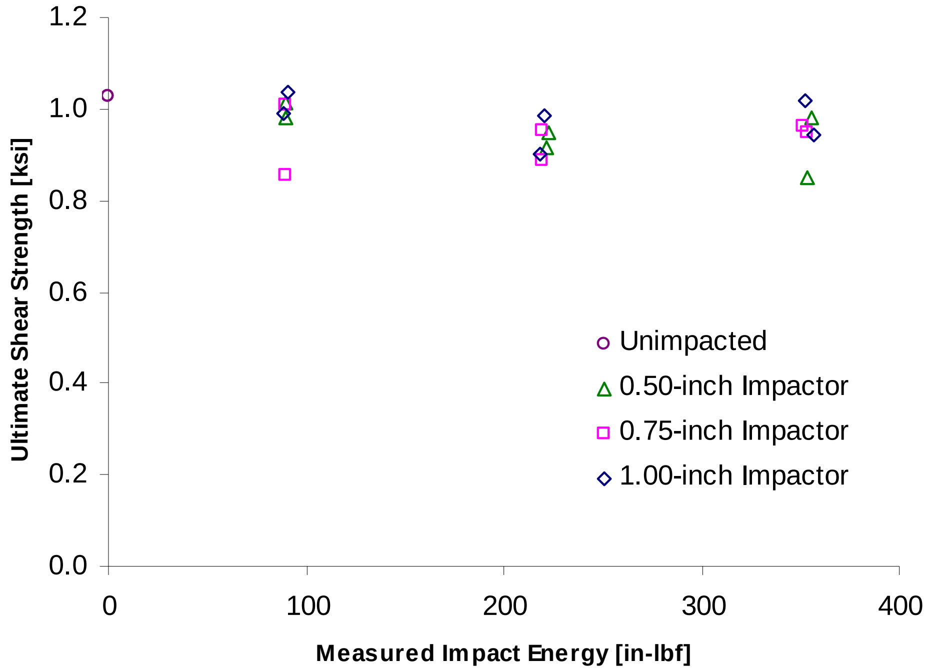

Figure 68. Ultimate Shear Strength for CFUT

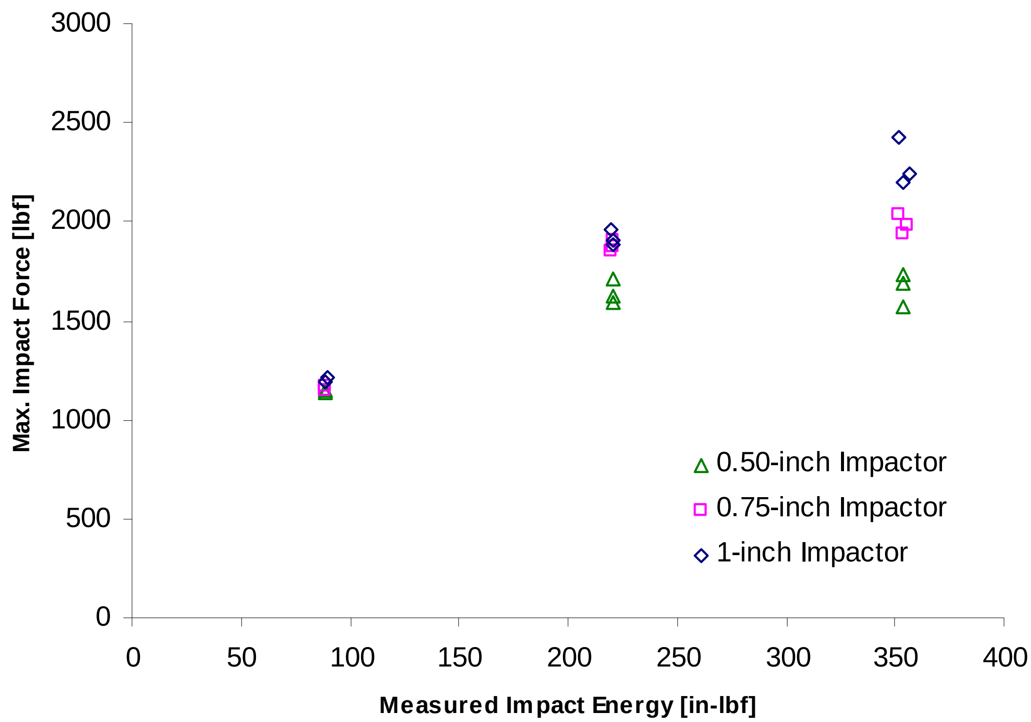

Figure 69. Maximum Impact Force for CFPW

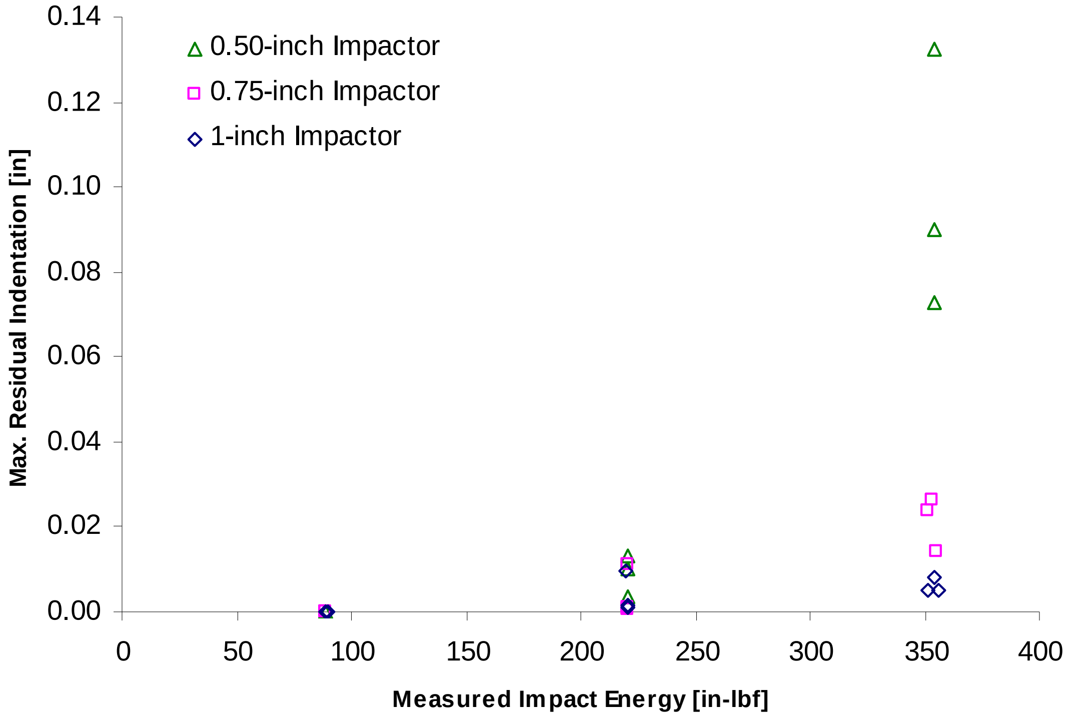

Figure 70. Maximum Residual Indentation for CFPW

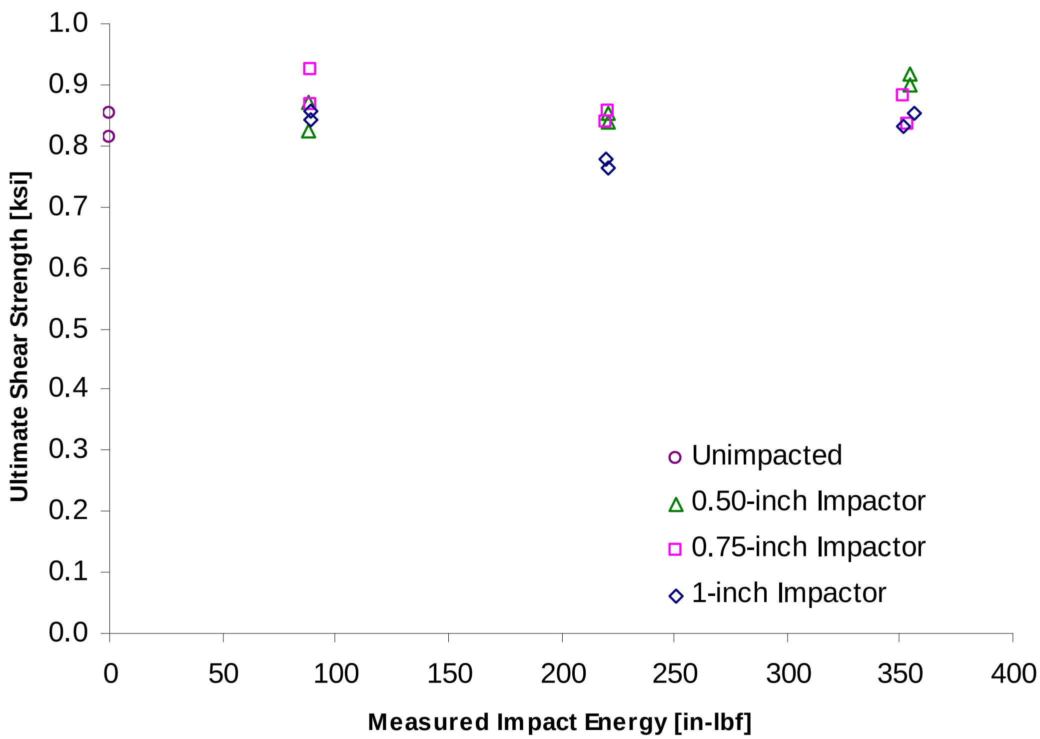

Figure 71. Residual Shear Strength for CFPW

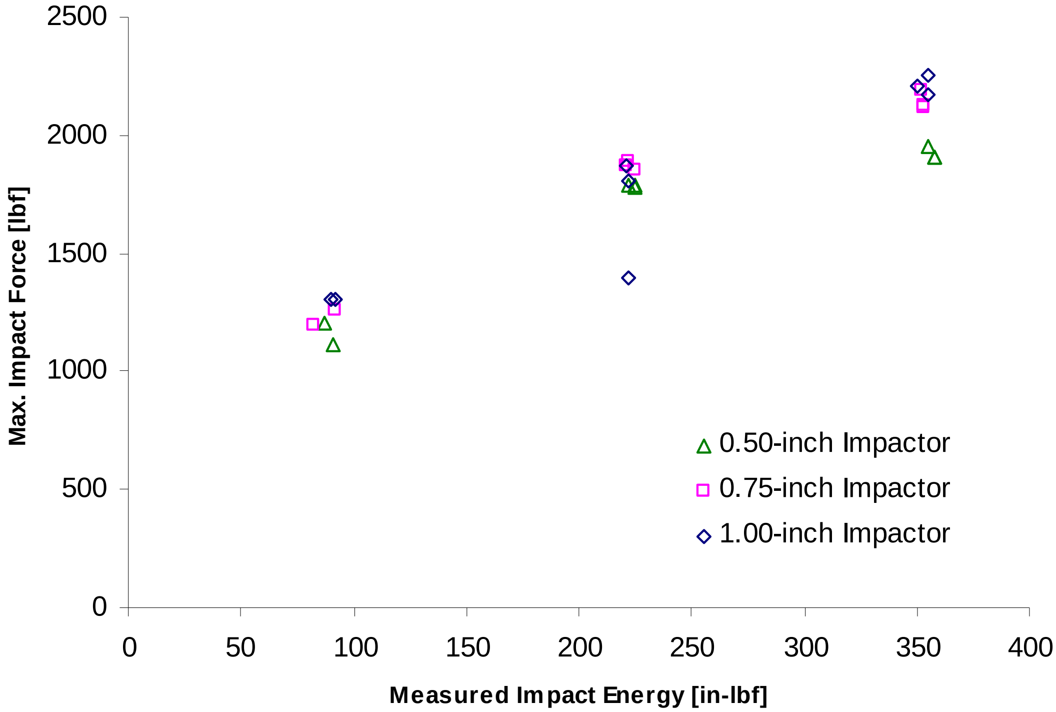

Figure 72. Maximum Impact Force for FGSW

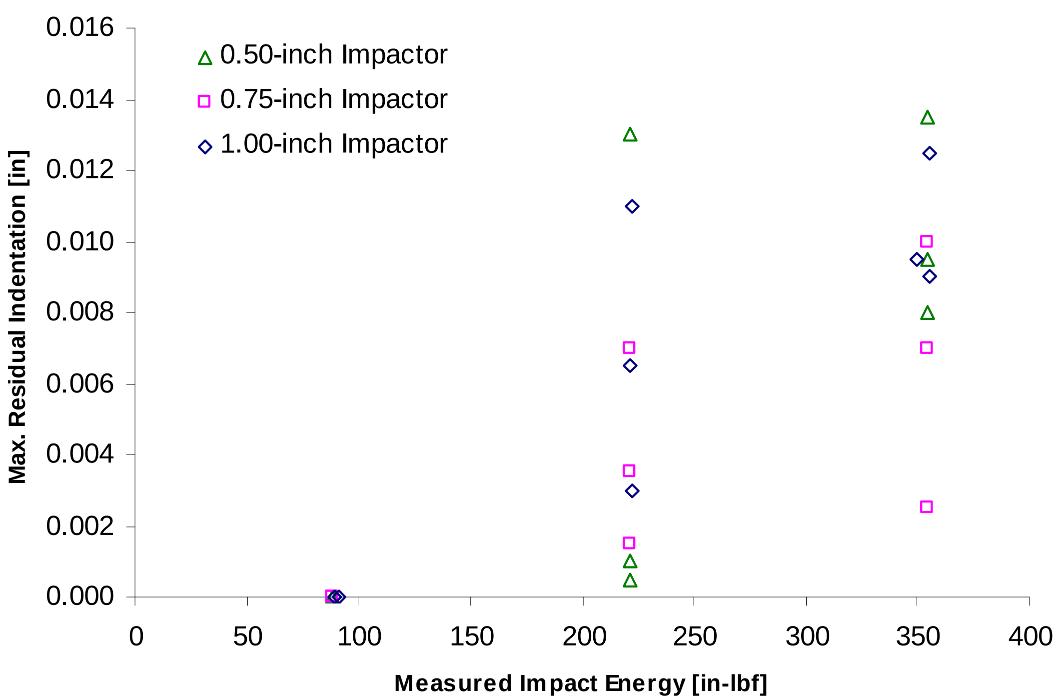

Figure 73. Maximum Residual Indentation for FGSW

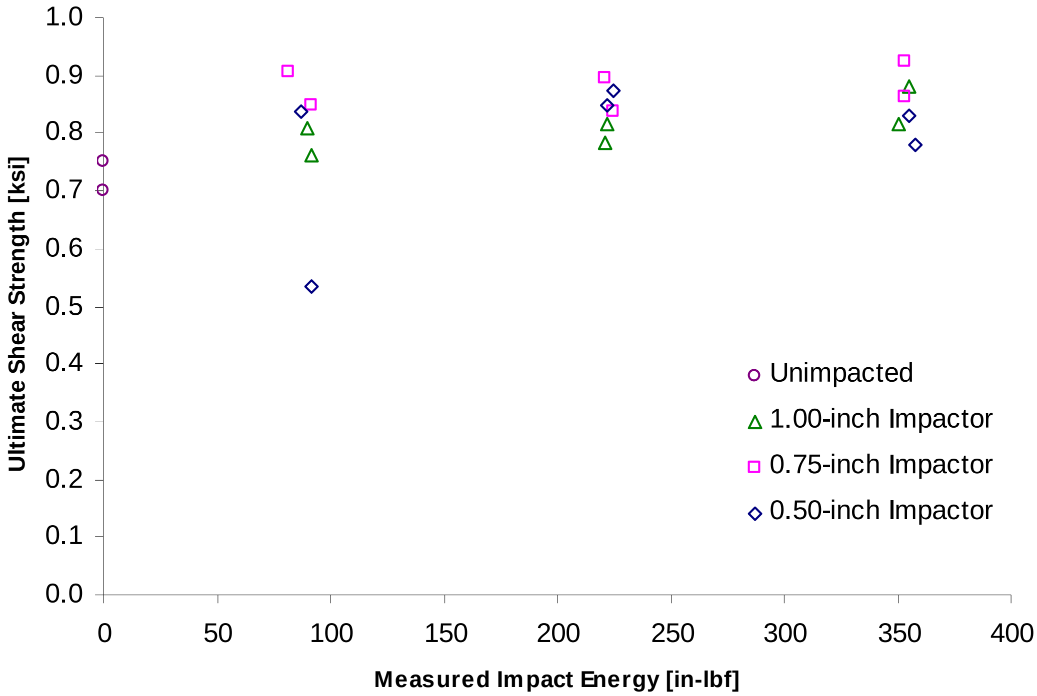

Figure 74. Residual Strength for FGSW

3.2.3 Photomicrography of Impacted Specimens.

Regardless of the material system, impact damage shown in the TTU C-scan is a generalized planar picture of the extent of damage and does not provide any particulars on what type of damage was sustained through-the-thickness of the adhesive joint. To obtain a clearer picture of the details of the damage, sections were cut and photomicrographs were taken. These show that the damage was a combination of adherend failure, adhesive fracture, and adhesive (adhesive/adherend interface debond) failure. Adherend damages included delamination, longitudinal and transverse (through-the-thickness) cracks, and fiber breakage. Primary damage in the adhesive layer were cracks through-the-thickness at an angle from the midsurface due to transverse shear, as shown in figure 75. There were also adhesive/adherend interfacial failures due to interlaminar shear stresses, as shown in figure 76. Figure 76 also shows several transverse matrix cracks due to in-plane compression stresses (above the adhesive layer) and tension stresses (below the adhesive layer) caused by bending. Adhesive/adherend interfacial damage mostly emanated at the end of transverse cracks through the adhesive layer possibly due to high peel stresses at the interface. Nevertheless, the majority of the damage was in the adherends. For the 0.5-inch impactor, tensile fracture or fiber breaks on the bottom side (opposite to impacted side) was significantly higher than the 1-inch impactor. The bottom-most plies of the bottom adherend had severe tensile cracks and fiber breakage as a result of in-plane normal stress (due to bending moment) exceeding the tensile strength of individual plies. Because lateral (90°) tensile strength of unidirectional tape was significantly lower than in the longitudinal direction, CFUT specimen had high-density transverse cracks. Due to comparatively high bending stiffness of both CFUT and CFPW material systems and the brittleness of their matrix materials, impact damages were highly scattered and chaotic. In contrast, impact damages in FGSW primarily resulted in small matrix cracks that formed circular-shaped damage regardless of the energy level and impactor diameter.

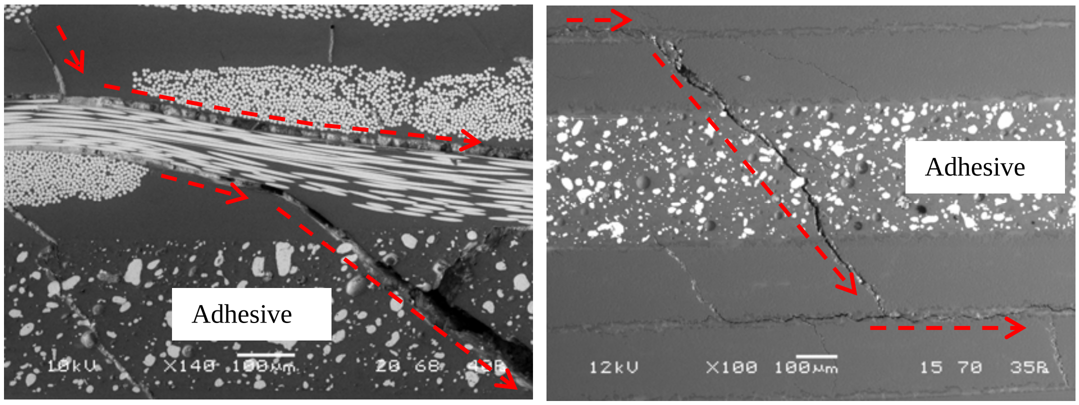

(a) Fabric adherend, CFPW (b) Unidirectional tape adherend, CFUT

Figure 75. Transverse Crack Propagation

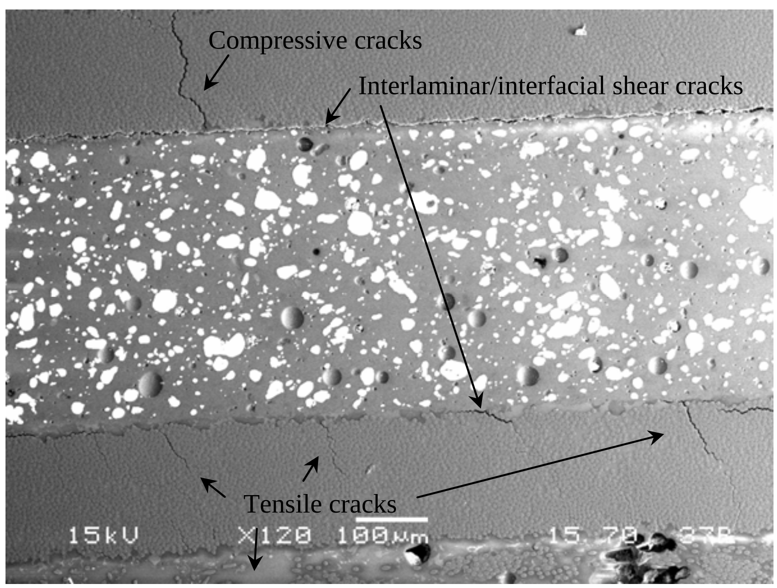

Figure 76. Fracture Due to Bending

During the impact event, matrix cracks and fiber breakage resulted in a complex damage pattern that was difficult to predict, especially for the impacts that did not result in complete penetration. There was a significant compressive stress due to contact stress and the resulting bending moment at the impact location, which resulted in a fracture along the fiber directions of the adherend layers. This was evident by the cross-shaped (bright white) marking on the contact face of the specimen where the top-most fibers are in 0°/90° orientation (figure 77). The stiffness mismatch in fiber matrix might be the reason that the cracks formed along the fiber directions during deflection. For unidirectional composite, the damage took an oblong or peanut shape with the major axis oriented in the fiber direction [14]. Since FGSW adherend lay-up is quasi-isotropic, i.e., $[0°/45°/90°/-45°]_s$, these cross-shaped damage zones, possibly concentrated in a 45° radial spacing along fiber directions at each layer through-the-thickness and smaller cracks in between, result in an observed circular damage shape in the FGSW specimens. In addition to cracks, localized contact stress results in fiber breaks and transverse cracks on the first few plies that result in cracks through-the-thickness of these plies. At these crack tips, where they meet the lower ply, high peel stress was created at the ply interface that resulted in interfacial cracks or delamination. Because of the matrix cracks along the fiber directions, the delamination propagated along the fiber directions of adjacent plies. Because the adjacent fabric plies in the case of FGSW are oriented 45° apart, the delamination may have spread in a circular pattern, as shown in figure 77, i.e., matrix cracks in adjacent layers coalesce within the small layer of matrix material between plies. Additional microscopic analysis may be required to verify this conjecture.

The conical or pine tree-shaped damage can be attributed to fiber breakage and delamination or debonding caused by transverse and interlaminar shear forces, as shown in figure 78. Transverse cracks, due to transverse shear, tend to be at an angle with respect to midsurface. When these transverse cracks met the bottom ply that had a different fiber orientation, they tended to propagate along the fibers, i.e., in-plane rotation of crack propagation direction to align with fiber direction, until bending of fibers caused a tensile failure or fiber break. Fracture due to fiber break continued though the matrix material of the next ply until arrested and realigned by fibers running perpendicular to the fracture orientation. For the cases of fabric materials, this phenomenon can occur within a layer, as shown in figure 75(a). As shown in this figure, the transverse crack continues on the bottom side of the fiber, although the crack path is offset along the fiber direction. For CFUT, there was a considerable amount of transverse cracks due to its low transverse tensile strength. Thus, these cracks passed through layers without difficulty. Consequently, the damage was contained within a small area, except for the outermost layer that resulted in long longitudinal cracks. However, for CFPW, interlaced or woven fiber architecture functioned as a crack arrest mechanism within the layer and resulted in large interlaminar fractures. Thus, the CFPW damage area was considerably larger compared to CFUT. FGSW that had a ductile matrix system and flexible fibers compared to the CFPW system resulted in smaller damages that were contained within the impact area by larger residual deformation and a high concentration of small cracks within the pine tree-shaped impact damage zone.

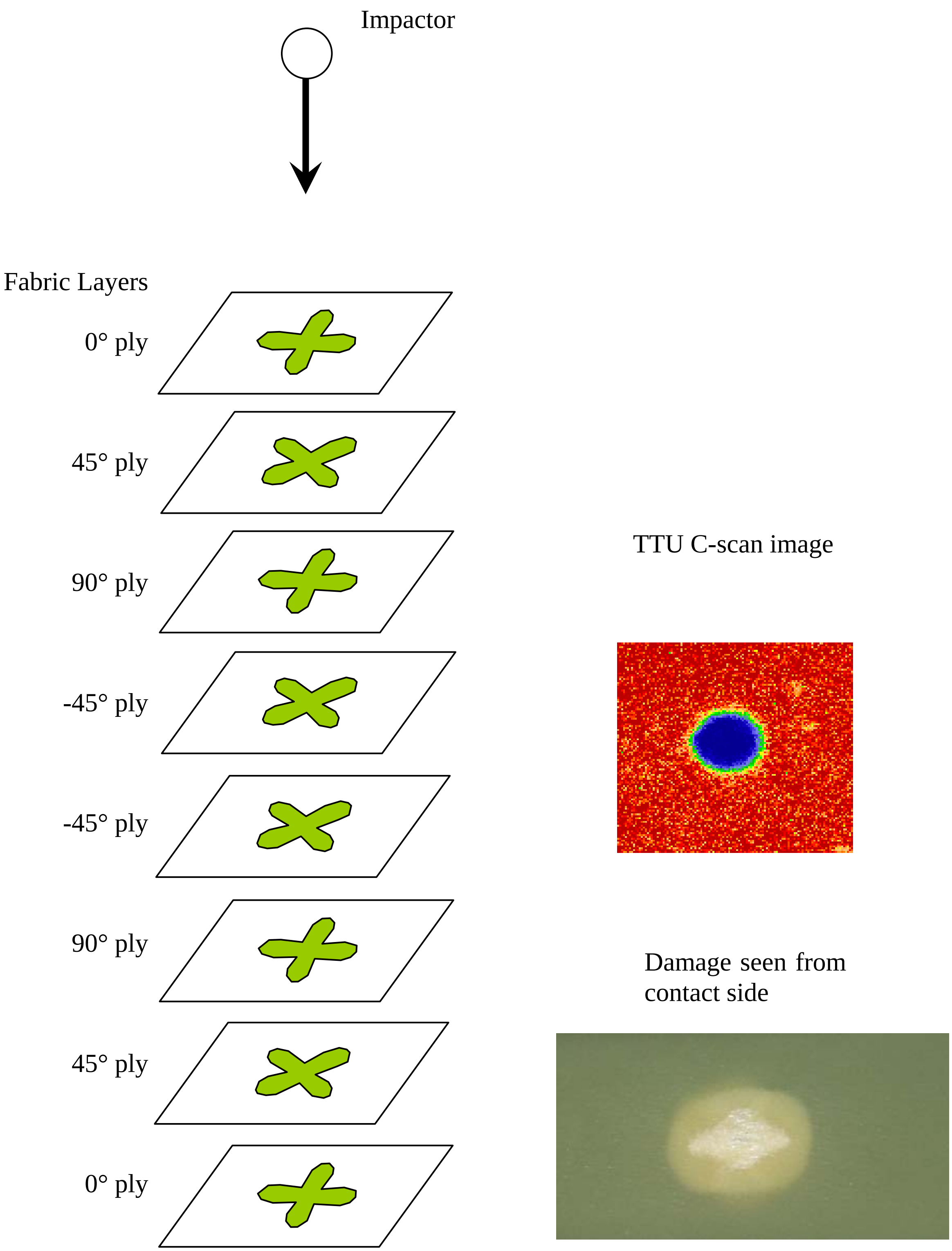

Figure 77. Orientation of Matrix Crack Concentrations of Glass Fabric Layers (Top Adherend) Due to Impact

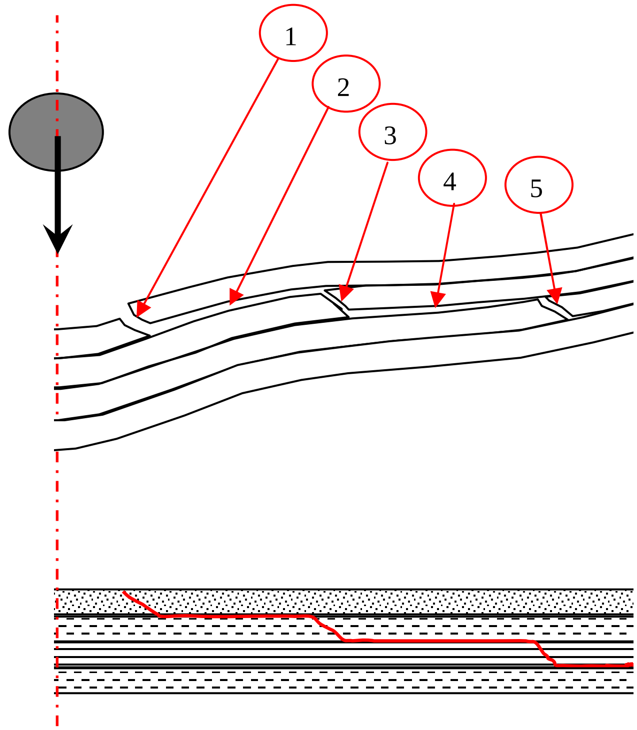

1. Transverse crack (0° ply)
2. Delamination
3. Transverse crack (±45° ply)
4. Delamiantion
5. Fiber break (0° ply)

Figure 78. Fracture Propagation on First Few Layers of Adherend Due to Impact

Figures 79 though 90 show photomicrographs of the impacted SLS specimens with different impactors for several different energy levels. These figures show visual damage on the impacted and opposite sides of the specimen (top), TTU C-scan image of the damage area (center), and photomicrographs of the specimen (bottom). These specimens are dissected along the impact point to investigate through-the-thickness damage. The cutting planes were chosen so that one of the two specimen surfaces represents the centerline of the impact, while the other surface is one blade thickness (0.08 inch) away. Photomicrographic image that matches the centerline is labeled as C, while the surface that is offset due to blade thickness is labeled as B. Since overall damage distribution is conical, offset (B) images show less damage than centerline (C) images.

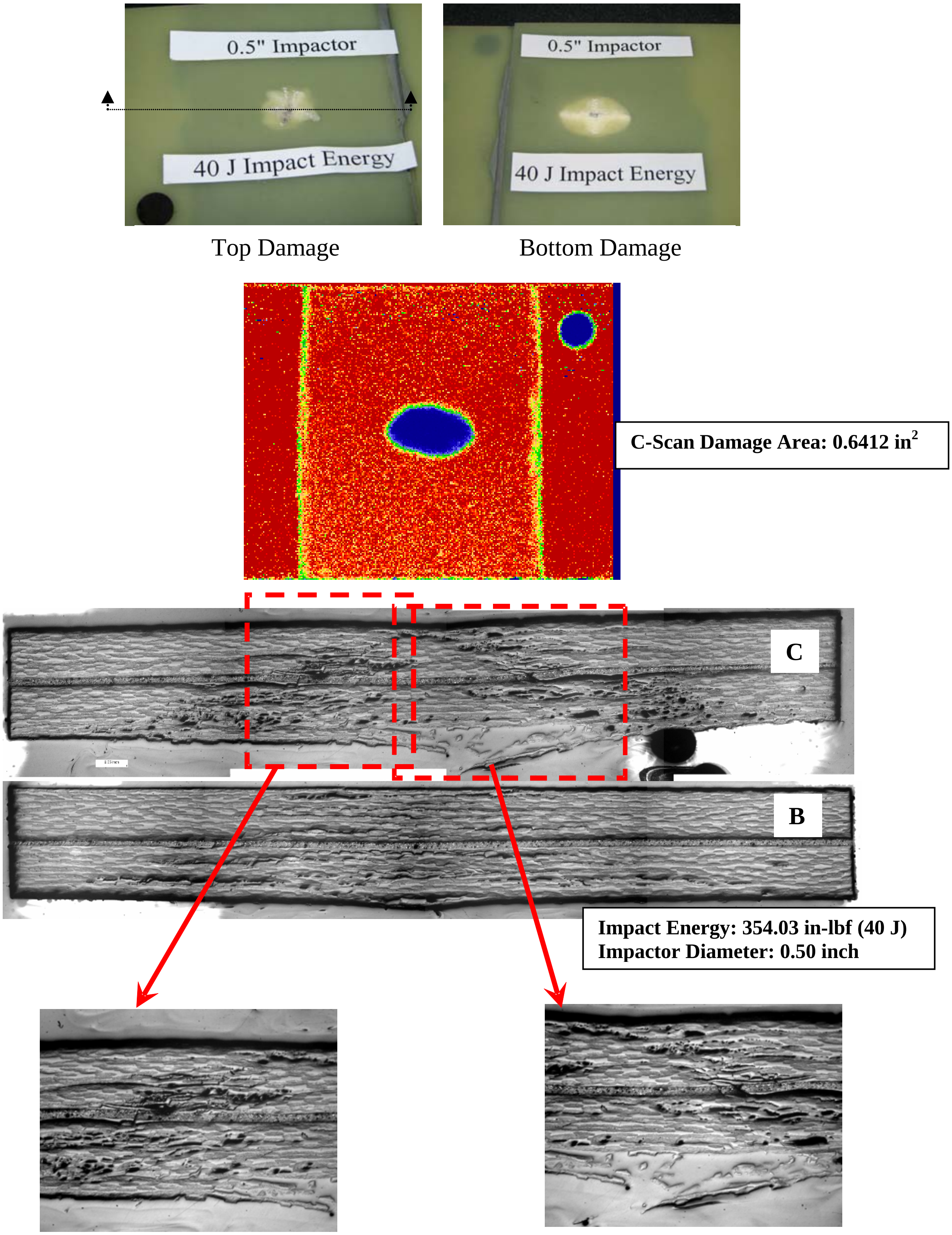

Figure 79. Photomicrograph of FGSW—I1G83C3: 0.50-Inch Impactor and 354.03 in-lbf

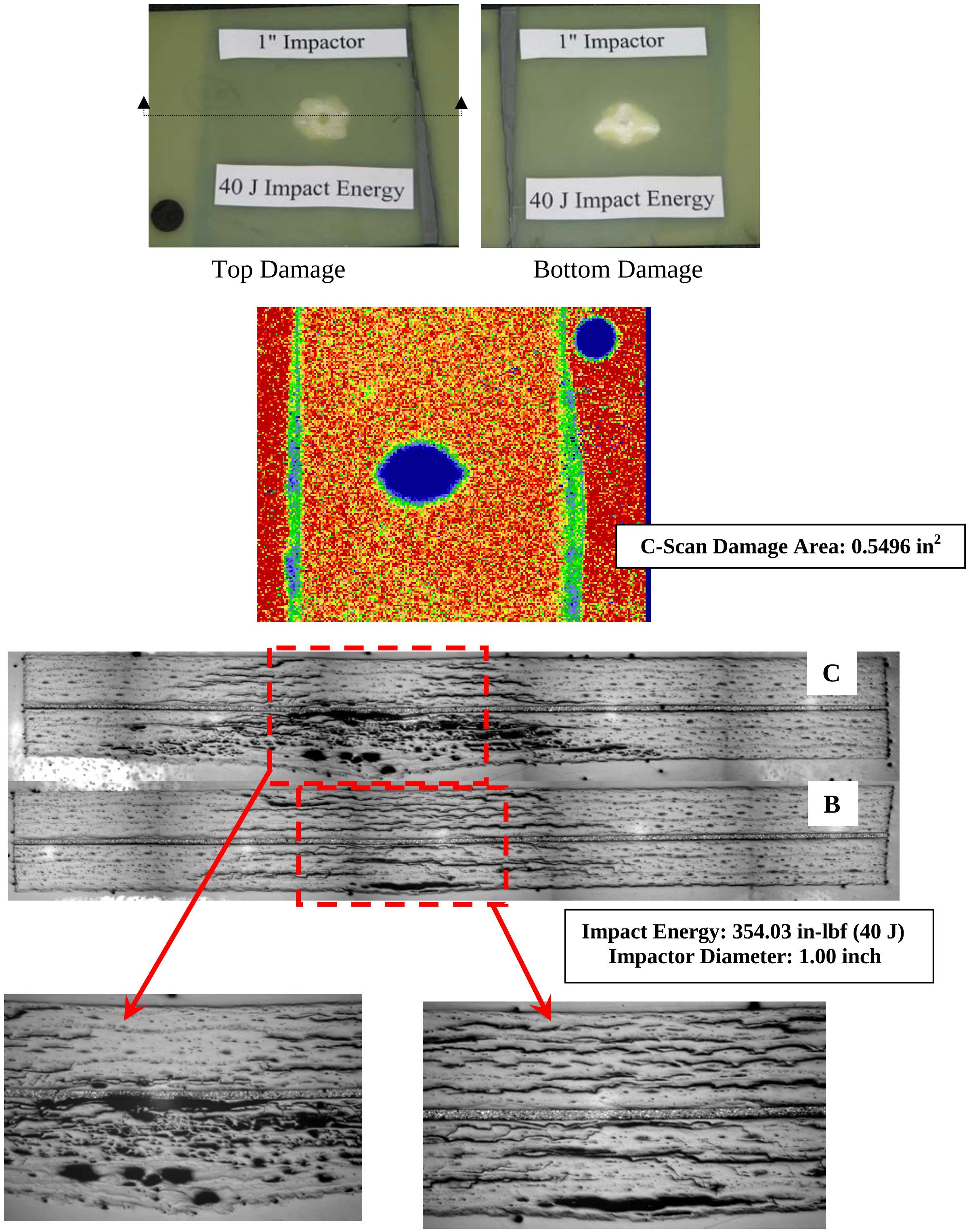

Figure 80. Photomicrograph of FGSW—I1G61C3: 1.00-Inch Impactor and 354.03 in-lbf

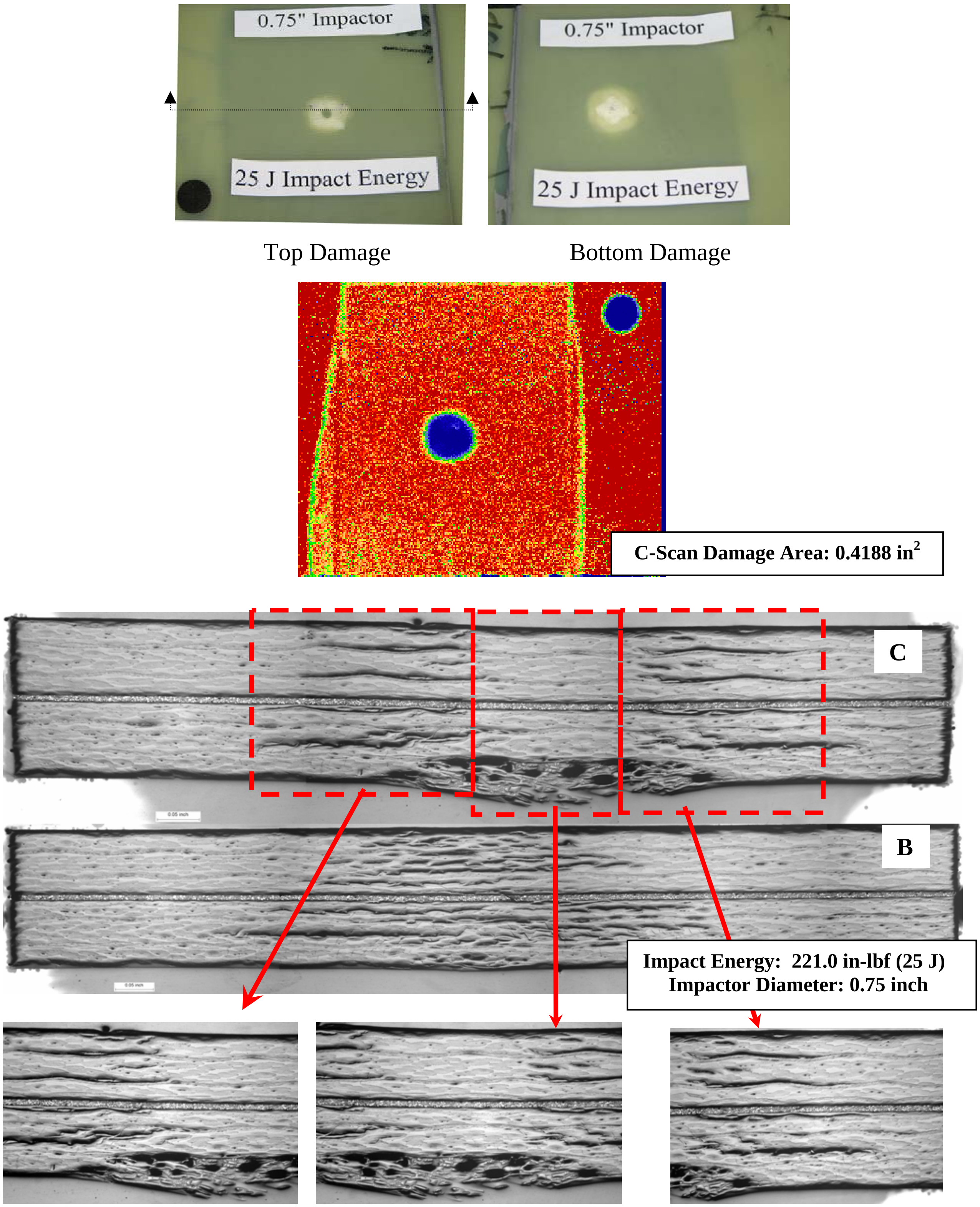

Figure 81. Photomicrograph of FGSW—I1G42B2: 0.75-Inch Impactor and 221.0 in-lbf

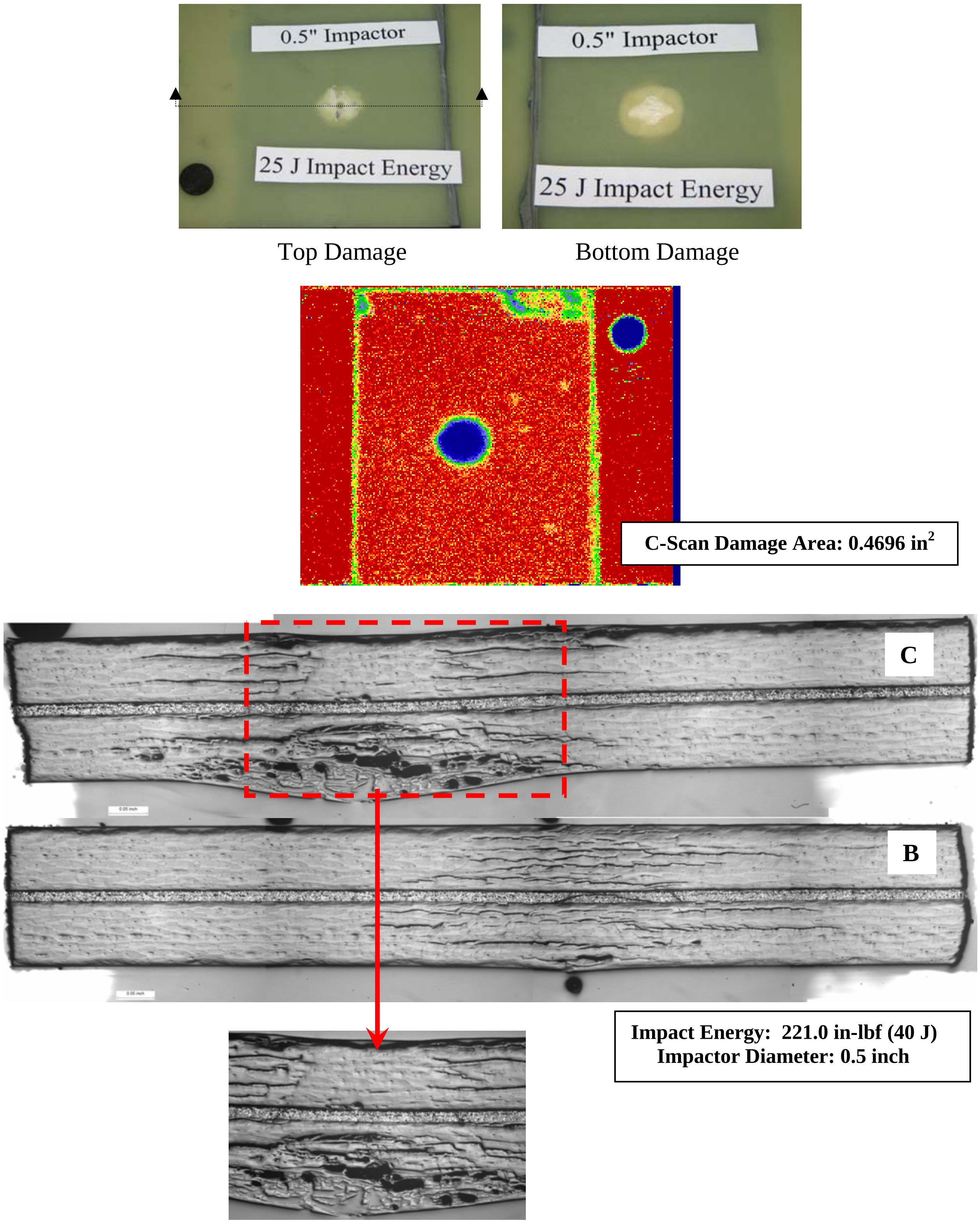

Figure 82. Photomicrograph of FGSW—I1G73B5: 0.5-Inch Impactor and 221.0 in-lbf

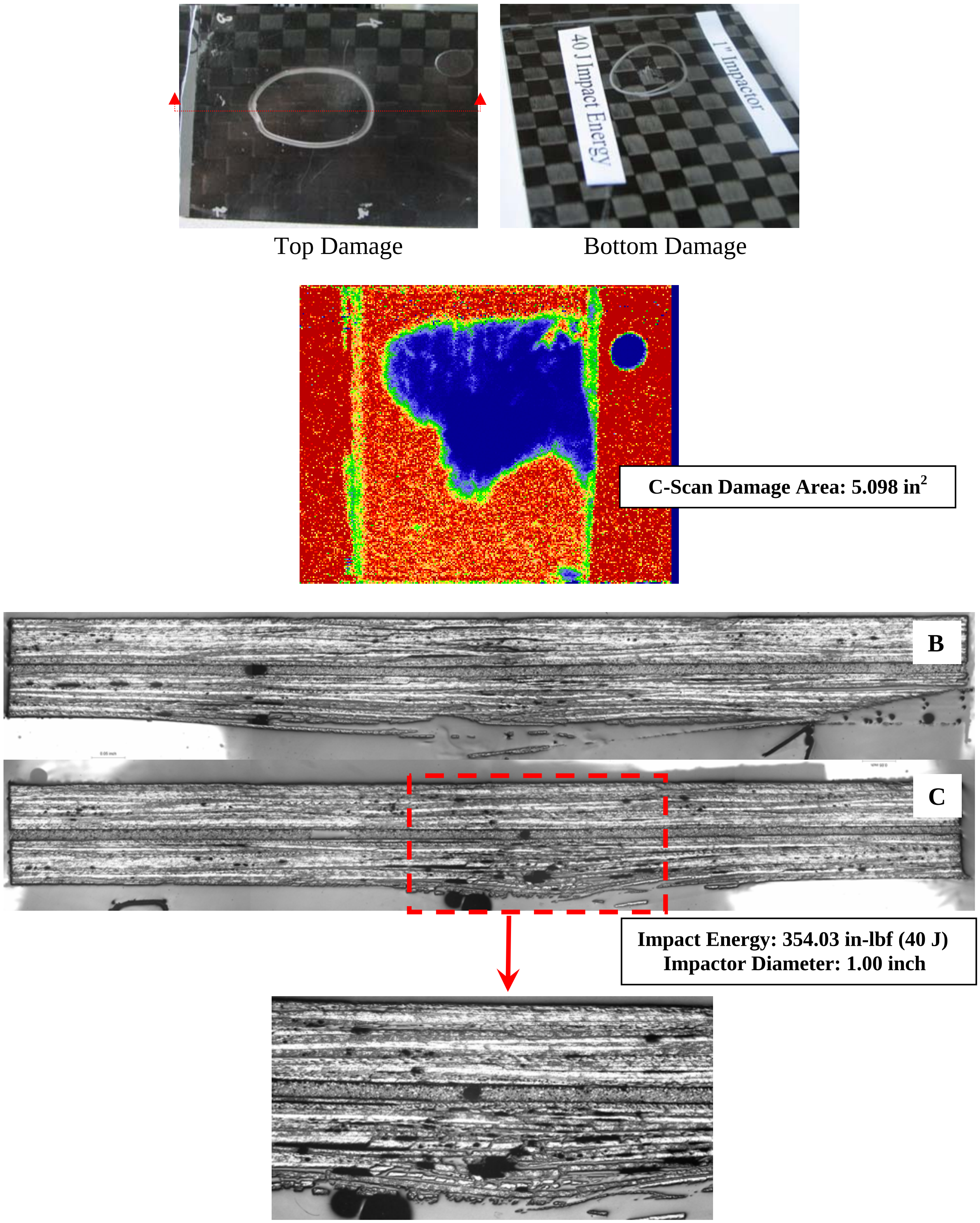

Figure 83. Photomicrograph of CFRP—I1P11C3: 1-Inch Impactor and 354.03 in-lbf

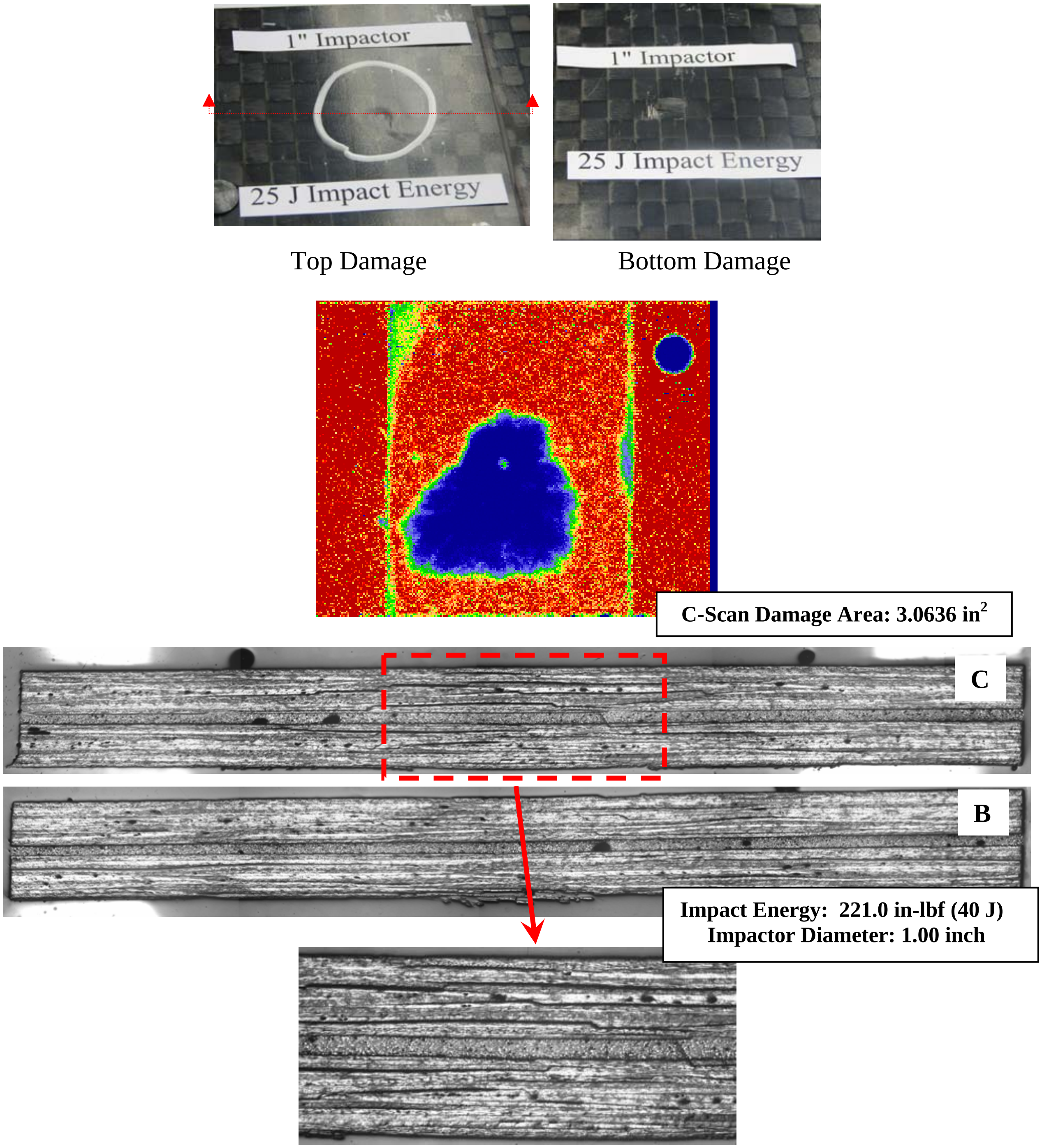

Figure 84. Photomicrograph of CFRP—I1P61B2: 1-Inch Impactor and 221.0 in-lbf

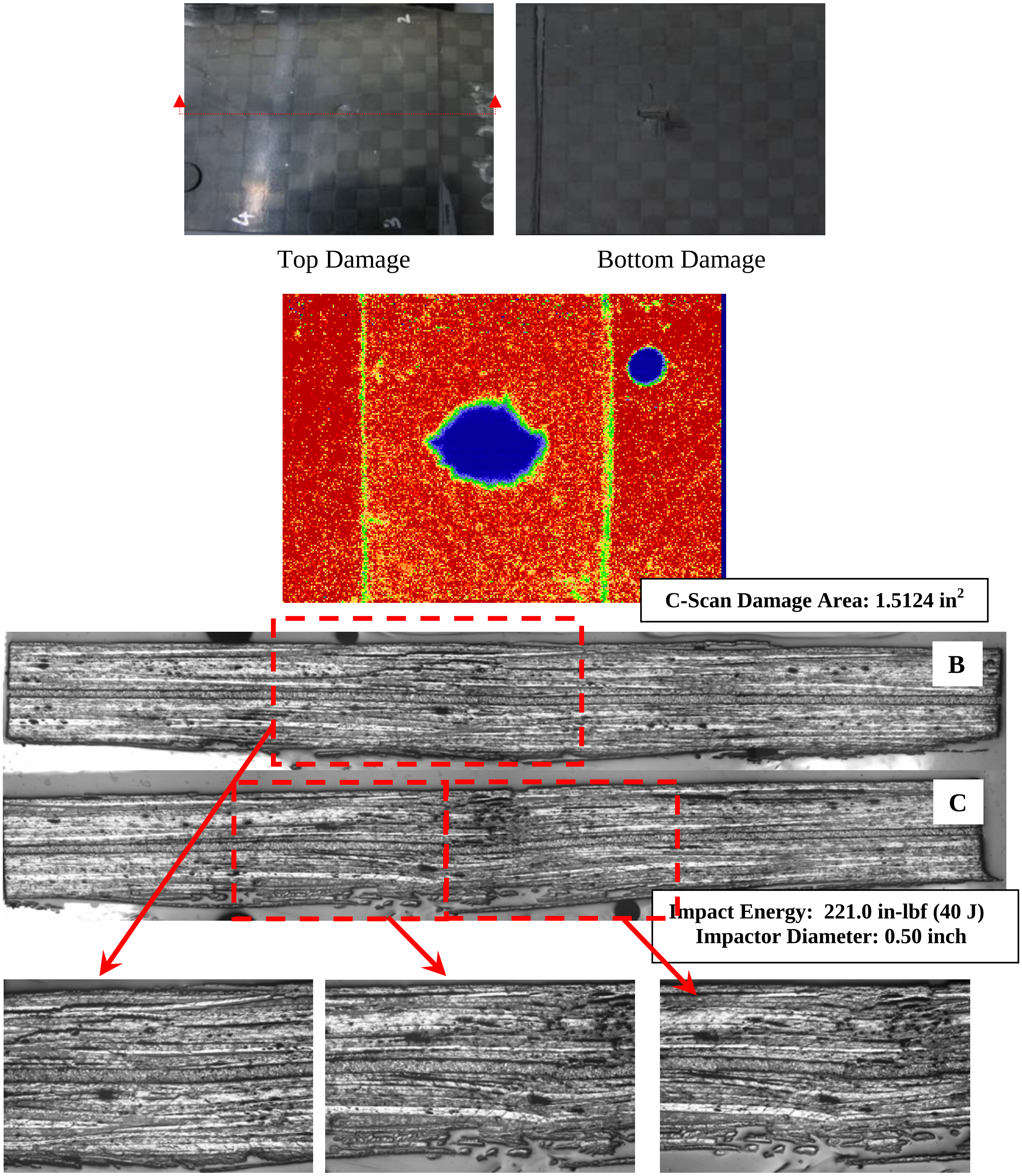

Figure 85. Photomicrograph of CFRP—I1P43B4: 0.5-Inch Impactor and 221.0 in-lbf

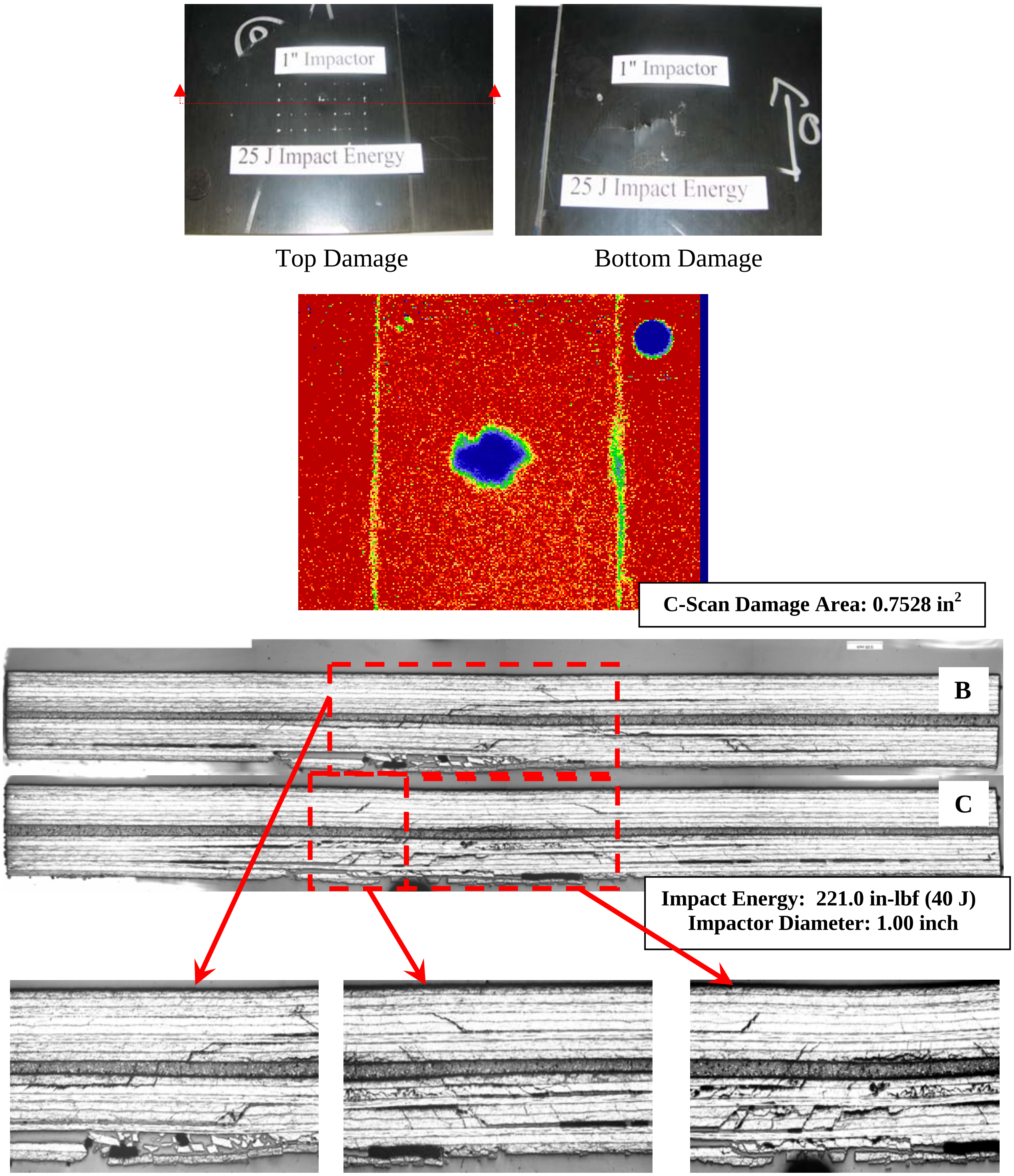

Figure 86. Photomicrograph of CFUT—I1U21B3: 1-Inch Impactor and 221.0 in-lbf

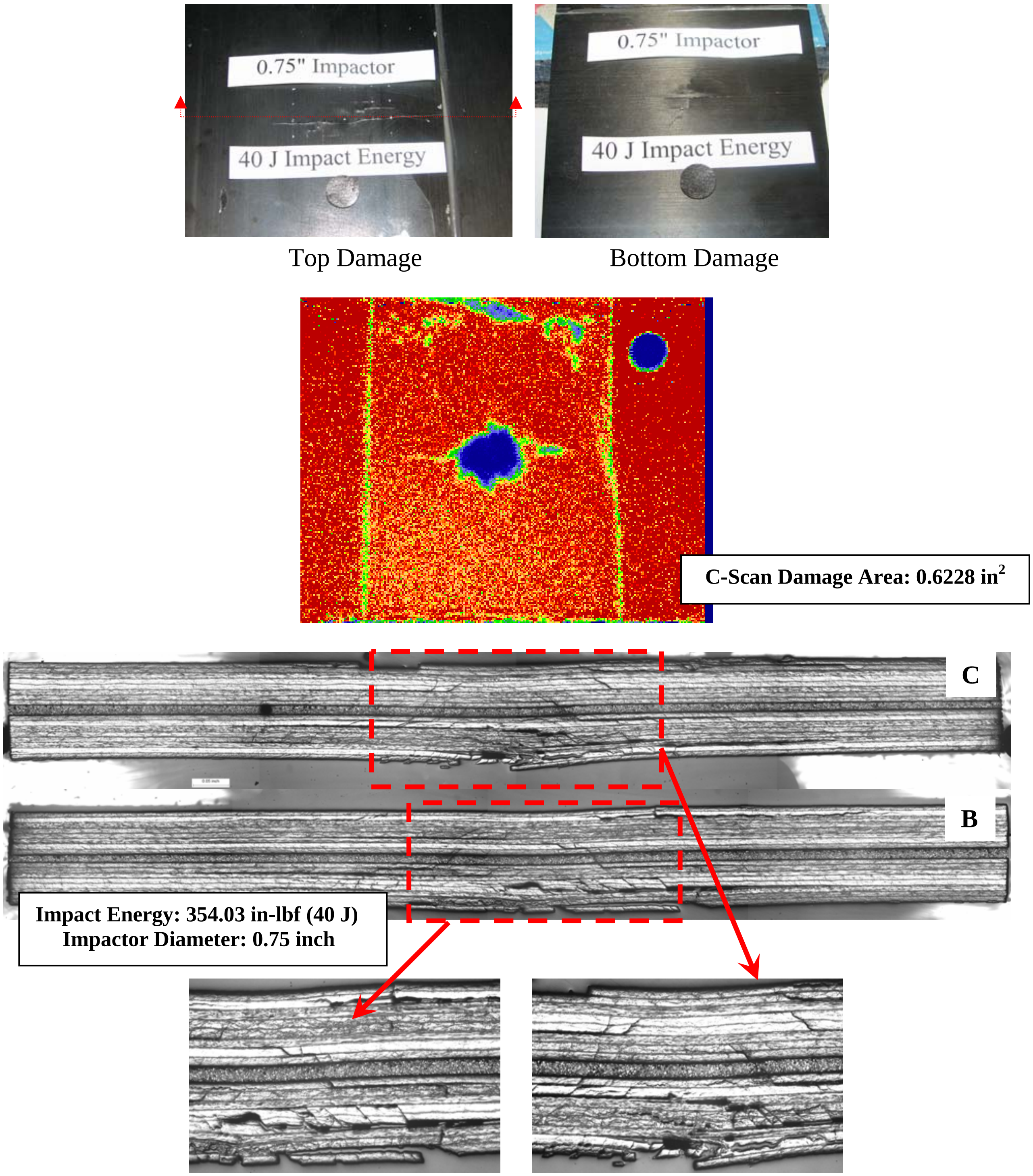

Figure 87. Photomicrograph of CFUT—I1U12B1: 0.75-Inch Impactor and 354.03 in-lbf

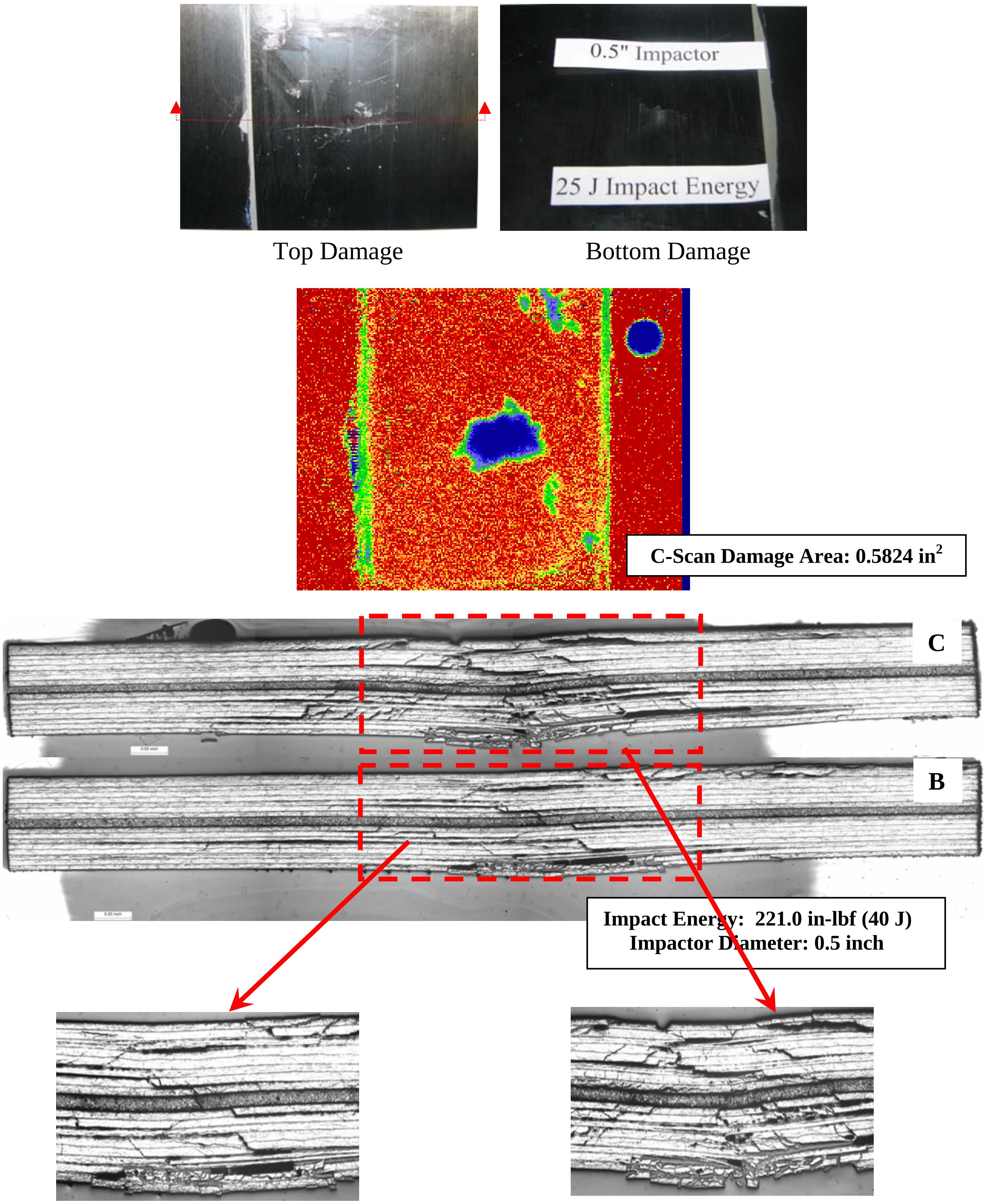

Figure 88. Photomicrograph of CFUT—I1U73B2: 0.5-Inch Impactor and 221.0 in-lbf

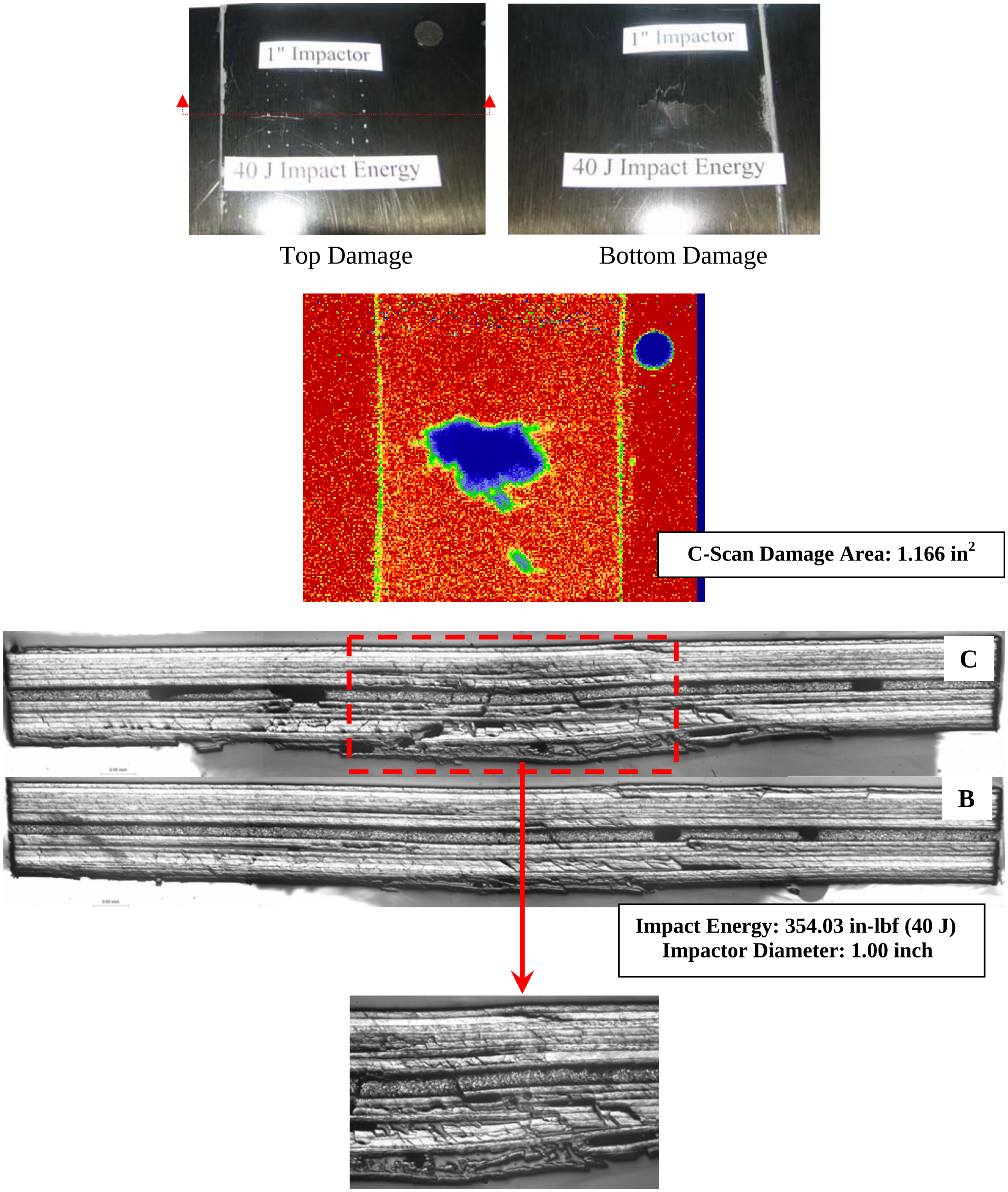

Figure 89. Photomicrograph of CFUT—I1U31C2: 1-Inch Impactor and 354.03 in-lbf

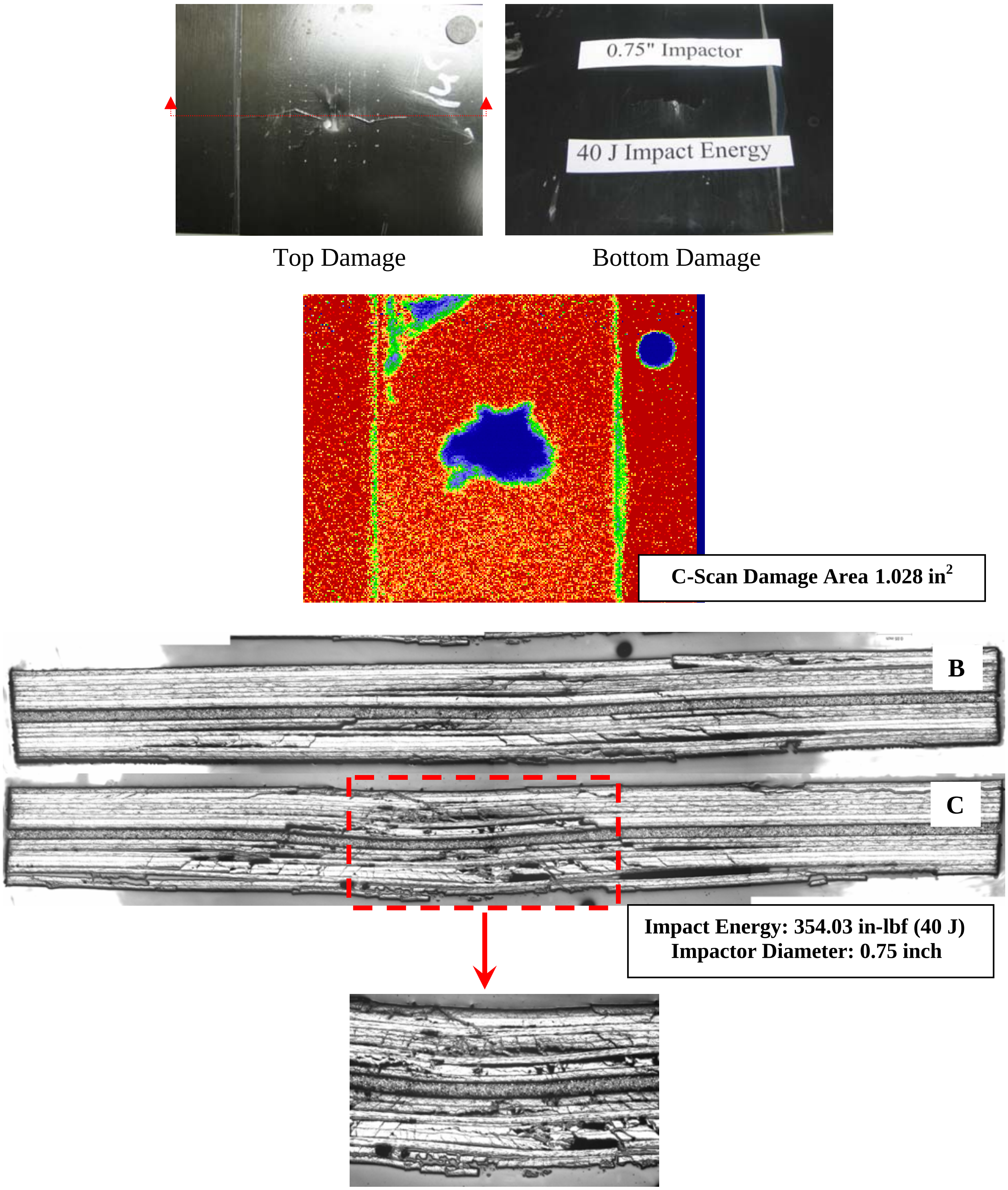

Figure 90. Photomicrograph of CFUT—I1U42C2: 0.75-Inch Impactor and 354.03 in-lbf

The delaminations along 0° and 90° layers on the impacted side of the FGSW specimens are clearly shown in figures 81 and 82 (C images) and the small cracks are clearly seen on the surface offset by the blade thickness (B images). Pine tree-shaped damage zone is clearly visible in FGSW specimens. Thus, photomicrographs reconfirm the circular damage shape observed with TTU C-scan and visual inspections. Damage to the adhesive layer or to the interface is limited to several transverse shear cracks.

Figures 83 through 85 show large interlaminar delaminations in CFPW specimens. These figures also showed that, for these specimens, the tensile fiber failure is limited to the bottom-most plies compared to specimens from the other two material systems. The damage area shown on the C-scan images is primarily due to large delaminations shown in the photomicrographs. Figures 86 through 90 show a substantial amount of transverse matrix cracks and relatively short delaminations in CFUT specimen that are concentrated within the pine tree-shaped damage zone. These fracture areas are projected in TTU C-scan images, including some of the longitudinal cracks in the outer-most ply that propagate out of the primary damage zone. There is a considerable amount of fractures across the adhesive layer that emanates from the transverse matrix crack of adjacent 0° plies. In addition, some compressive and tensile cracks propagated to cause multiple adhesive/adherend failures (interfacial failures).

4. CONCLUSIONS.

The effects of defects on adhesive joints were evaluated using picture-frame test specimens under shear loading. The resulting test data show that a rectangular defect that spreads completely across the joint overlap region results in a 27% reduction in shear strength for carbon epoxy fabric and a corresponding 19% reduction for glass epoxy fabric. Full-field displacement and strain information obtained using photogrammetry indicated damage progression prior to failure. Nevertheless, these specimens failed in the adherend rather than by adhesive or cohesive failure mode. The stress concentrations observed around square and rectangular disbonds resulted in matrix cracks that lead to delamination of the composite adherend. In contrast to rectangular defects, the circular- and diamond-shaped defects and through holes that are contained within the elastic trough had minimal or no effect, as these defects did not grow and thus remain in the elastic trough. Rectangular defects repaired with fail-safe fasteners completely restored the original strength of the bonded joint. The fasteners increased through-the-thickness strength and prevented large deformations (buckling) that occur without fasteners. Furthermore, fasteners change the strain distribution and minimize peel stresses. Lightning strike damages caused substantial adherend delaminations with small or no damage to the adhesive layer or to the adherend that is away from the strike. The reduction in shear strengths due to the lightning strike was approximately 15% and 17% for Zone 1 and Zone 2 energy levels, respectively.

The effects of impacts on adhesive joints were evaluated using picture-frame and single-lap test shear specimens. For the picture-frame specimens, at the 270 in-lbf energy level, the damage area was the same, irrespective of impactor diameter, which ranged between 0.25 and 2 inches. This was in contrast with observations of composite sandwich structures where there was a strong correlation between damage and impactor diameter that was a result of a weak bond between the facesheet and honeycomb. However, the smaller diameter impactors caused severe localized permanent damage in the impacted adherend that resulted in a 20% reduction in shear strength for 2-inch overlap specimens compared to no-defect specimens. This again was a smaller reduction in strength than the composite honeycomb specimens. However, the composite honeycomb panels were tested in compression and not shear. For the larger diameter impactors and the same 2-inch overlap, the reduction in strength was 9%. For the 1-inch overlap, the reduction in strength was much greater, 60%. Thus, an increase in overlap decreases the damage area as a percentage of the overall bond area and increases the load-carrying capability of the adhesive joint. For the picture-frame shear specimens, the load-carrying capability increases for thicker bondlines. The additional adhesive volume increases the energy-absorbing characteristics and may result in fewer microcracks within the bondline, although this is conjecture as these microcracks were undetectable by C-scan. Investigation of viscoelastic characteristics of composites may be needed to fully understand this phenomenon.

Single-lap shear specimens were made from three materials, carbon/epoxy fabric, tape, and glass/epoxy fabric. These were tested at various impact energy levels and different impactor diameters. For glass/epoxy, the damage area was independent of the impactor diameter, especially at smaller energy levels, and was proportional to the energy level. Impact damage results obtained from the tape and fabric carbon/epoxy laminates that had identical matrices show that the prepreg form significantly influenced the damage area and the failure mode. A larger damage area was observed in carbon fiber adherends compared to glass fiber adherends. Also, at higher energy-levels, these joints indicated an increase in damage area for larger impactor diameters. For carbon fabric adherends, the damage area increased, reached a maximum, and then decreased with increase in energy level until penetration. For larger energy levels, the back-side fiber break was notably increased for smaller impactor diameters, possibly due to the reduction in contact area that resulted in larger indentation or penetration. Carbon tape adherend specimens absorb impact energy by matrix cracking and fiber breakage, and show significantly larger matrix cracks that extend beyond the circular damage area identified by through-transmission ultrasound C-scans. The maximum impact force, maximum residual indentation, and impact area increased as the energy level increased. However, because all the single-lap specimens with and without impact damage failed in the adherend, the shear strength was the same, irrespective of impact energy or impactor diameter. Thus, the test results did not evaluate the effect of impact damage. The impact damages in this investigation were contained mostly within the elastic trough and away from the side edges. Therefore, a further study is recommended varying the impact location along the overlap direction and across the width to investigate the effects of such impact scenarios, which will result in large load redistribution and stress concentration. The results of these particular tests show that the critical area of the adhesive joint is the adherend, if the adhesive joint is properly designed and fabricated with proper processing.

5. REFERENCES.

1. Krueger, R., “Virtual Crack Closure Technique: History, Approach, and Applications,” *Applied Mechanics Reviews*, Vol. 57, No. 2, March 2004, pp. 109-143.

2. SAE, “Aircraft Lightning Zoning,” Aerospace Recommended Practice–5414, 1999, pp. 24-25.

3. Hyer, M.W., “A Comparison Between Experiments and Theory for a Borsic-Aluminum Picture-Frame Shear Test,” Interim Report, NASA-CR-148931, NASA Langley Research Center, Hampton, Virginia, 1976.

4. ARAMIS, v. 5.3.0 User Manual, GOM mbH.

5. Tomblin, J.S., Seneviratne, W.P., and Borgman, M.D., “Electronic Speckle Pattern Interferometry for Investigating Defect Propagation of Honeycomb Sandwich Specimens,” *34th International SAMPE Technical Conference*, November 2002.

6. Hart-Smith, L.J., “Effects of Flaws and Porosity on Strength of Adhesive-Bonded Joints,” *29th Annual SAMPE Symposium and Technical Conference*, Reno, Nevada, April 3-5, 1984.

7. Seneviratne, W., Tomblin, J., and Gunawardana, S., “Experimental Fracture Mechanics for Adhesive Joint Design,” *International Conference on Computational & Experimental Engineering and Sciences*, Miami, Florida, January 2007.

8. Kim, H. and Lee, J., “Box Beam Lap Shear Torsion Testing for Evaluating Structural Performance of Adhesive Bonded Joints,” *Joining and Repair of Composites Structures*, ASTM STP 1455, K.T. Kedward and H. Kim, eds., ASTM International, W. Conshohocken, Pennsylvania, 2004, pp. 22-41.

9. Tomblin, J.S., Seneviratne, W.P., Kim, H., and Lee, J., “Box Beam Lap Shear Torsion Testing for Evaluating Structural Performance of Adhesive Bonded Joints,” *Joining and Repair of Composites Structures*, ASTM STP 1455, K.T. Kedward and H. Kim, eds., ASTM International, W. Conshohocken, Pennsylvania, 2004, pp. 42-54.

10. Tomblin, J.S., Seneviratne, W.P., Kim, H., and Lee, J., “Characterization of In-Plane, Shear-Loaded Adhesive Lap Joints: Experiments and Analysis,” FAA report DOT/FAA/AR-03/21, May 2003.

11. Tomblin, J.S., Raju, K.S., Liew, J., and Smith, B.L., “Impact Damage Characterization and Damage Tolerance of Composite Sandwich Airframe Structures,” FAA report DOT/FAA/AR-00/44, January 2001.

12. Tomblin, J., Hater, P., Seneviratne, W., and Yang, C., “Characterization of Bondline Thickness Effects in Adhesive Joints,” *Journal of Composites Technology and Research*, Vol. 24, No. 2, April 2002, pp. 332-344.

13. Zelalem, A. and Eyassu, W., “Bond Thickness Effects on Impact Response and Damage of Adhesively-Bonded graphite/Epoxy Composites,” *Journal of Adhesion Science and Technology*, Vol. 21, No. 1, 2007, pp. 21-34.

14. Abrate S., *Impact on Composite Structures*, Cambridge University Press, United Kingdom, 1998.

APPENDIX A—THROUGH-TRANSMISSION ULTRASOUND C-SCANS AND ARAMIS PHOTOGRAMMETRY DATA FOR PICTURE-FRAME SHEAR TEST SPECIMENS

This section contains the through-transmission ultrasound (TTU) C-scan data for impacted picture-frame shear (PFS) test specimens. Figure A-1 shows the numbering system used to identify the PFS test specimens.

Sub-Task	Adhesive	Adherend	Bondline Thickness	Overlap	Special 1	Special 2	Specimen #
D Disbond	**1** EA 9394	**A** CFPW-S	**1** 0.007	**1** 1.00"	**N** No Disbond	**N** No Disbond	**1** Specimen 1
I Impact		**C** FGSW	**2** 0.010	**5** 1.50"	**D** Disbond	**R** Rectangular	**2** Specimen 2
			3 0.015	**2** 2.00"	**O** Open Hole	**S** Square	**3** Specimen 3
					F Filled Hole	**C** Circle	
						D Diamond	
					4 0.25" Impactor	**L** Large Support	
					5 0.50" Impactor	**S** Small Support	
					7 0.75" Impactor		
					1 1.00" Impactor		
					2 2.00" Impactor		
					3 3.00" Impactor		
					G Lightning Strike	**X** Not Applicable	

D Disbond
I Impact
G Lightning Strike

General (Adhesive through Overlap) | **General** (Specimen #)

Figure A-1. Nomenclature for PFS Test Specimens

Figure A-2 explains the extra details found in the TTU C-scan results. The damage area outside of the overlap region is disregarded for damage area calculations.

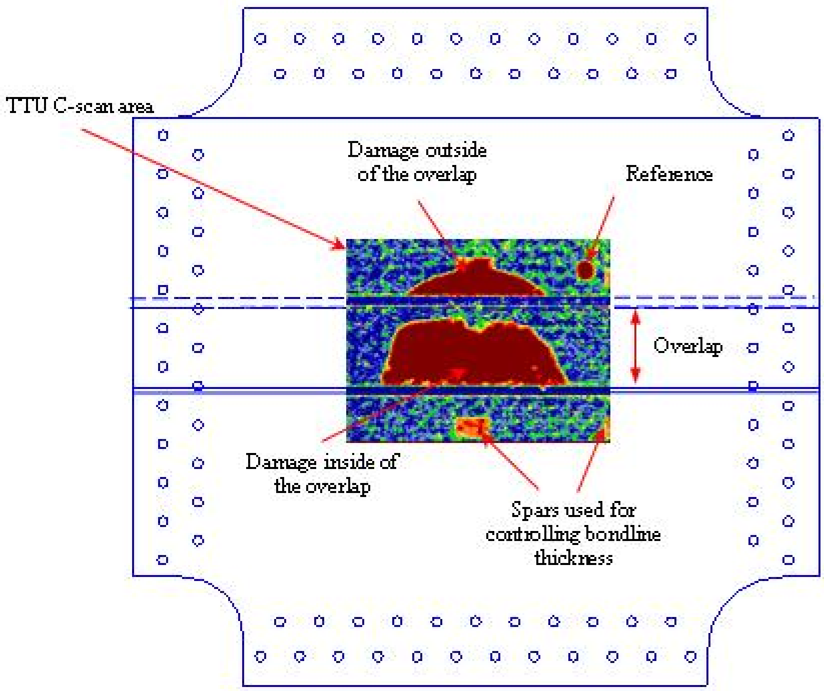

Figure A-2. Postimpact TTU C-Scan of PFS Specimen

A-1. DAMAGE AREAS FOR DIFFERENT SPECIMENS OF CFPW-S.

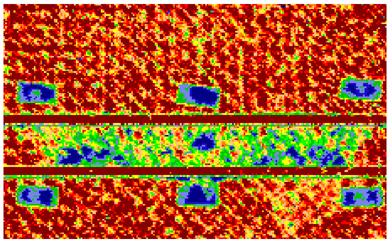
I1A111L1

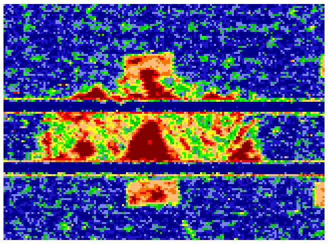
I1A114S2

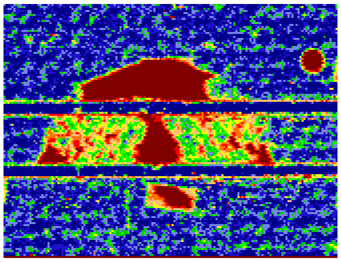
I1A114S3

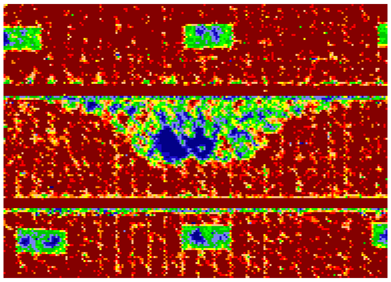
I1A121L1

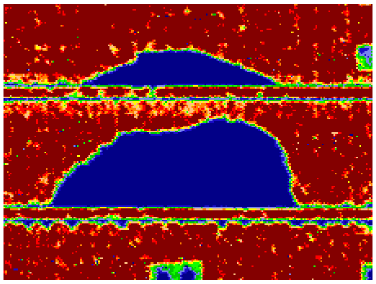
I1A121S2

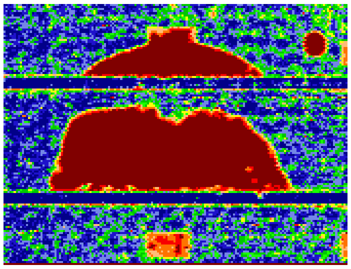
I1A121S3

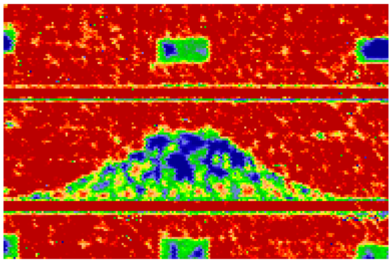
I1A122L1

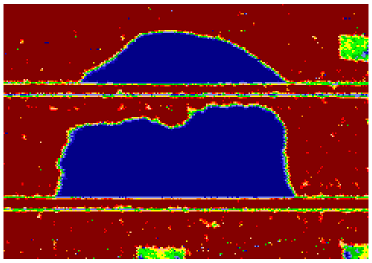
I1A122S2

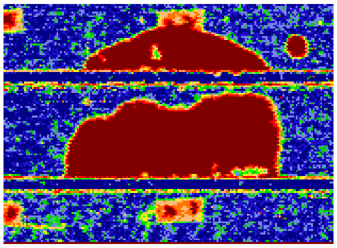
I1A122S3

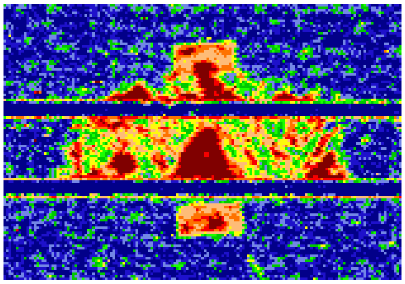
I1A114S2

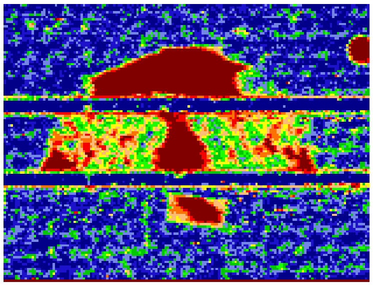
I1A114S3

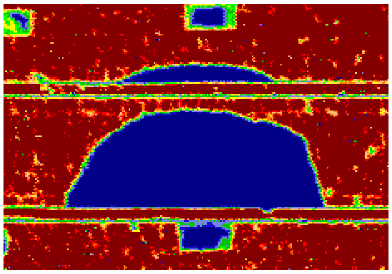
I1A124S1

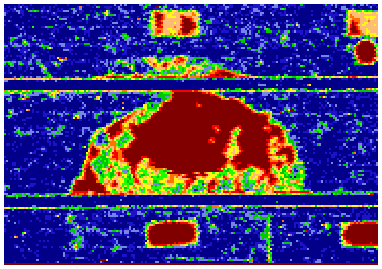
I1A124S2

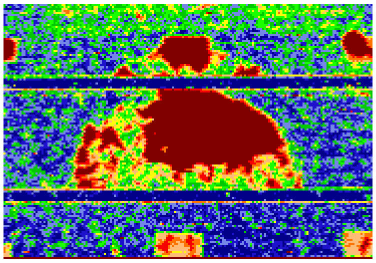
I1A124S3

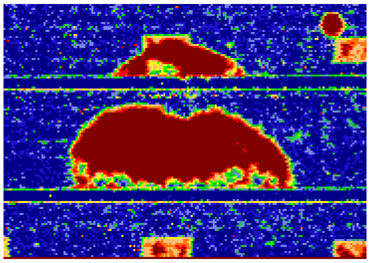
I1A125S1

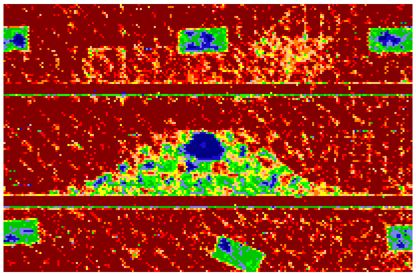
I1A125L2

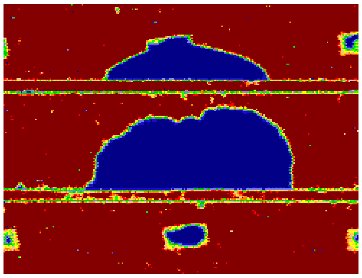
I1A125S3

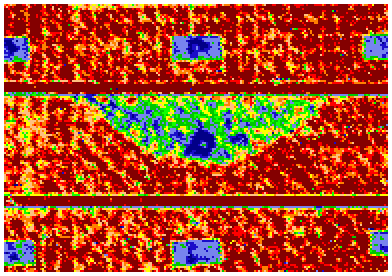
I1A221L1

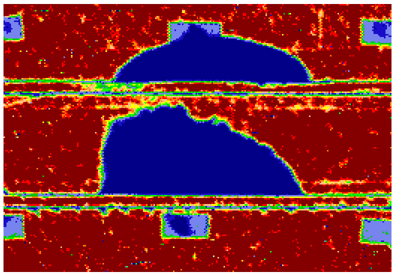
I1A221S2

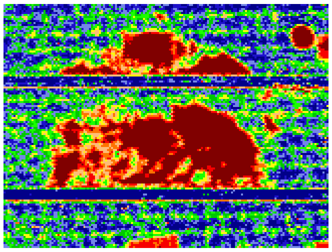
I1A221S3

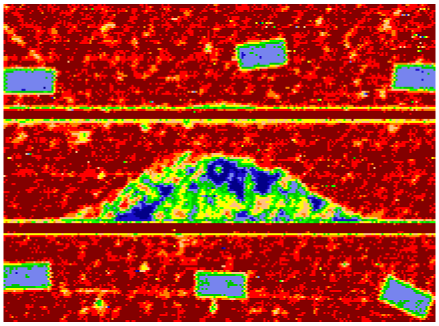
I1A321L1

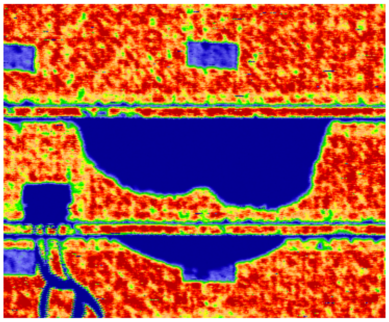
I1A321S2

A.2 DAMAGE AREAS FOR DIFFERENT SPECIMENS OF FGSW.

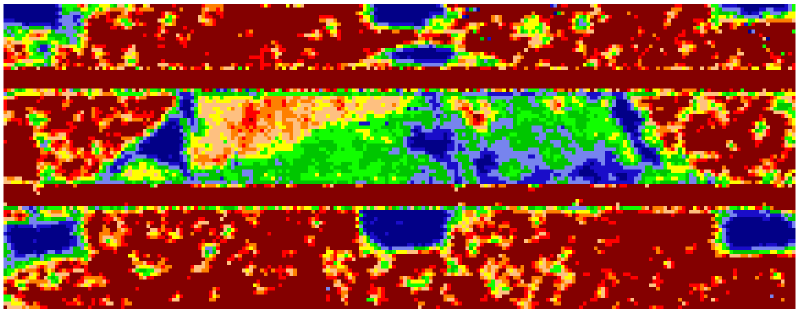

DIC11NL3

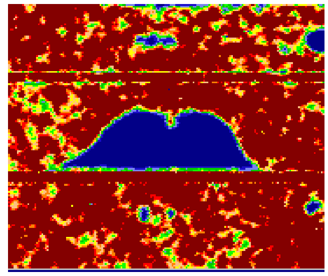

D1C12NN1

<u>A.3 CFPW-S ARAMIS PHOTOGRAMMETRY RESULTS</u>.

<u>A.3.1 PHOTOGRAMMETRY RESULTS FOR DIFFERENT SPECIMENS</u>.

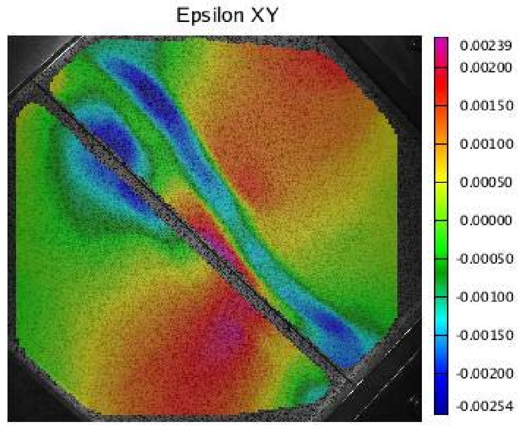

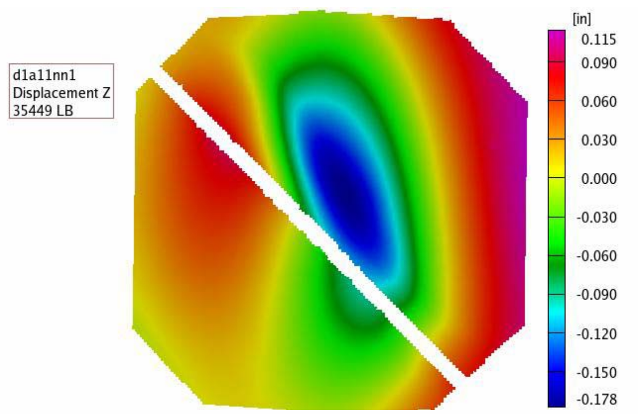

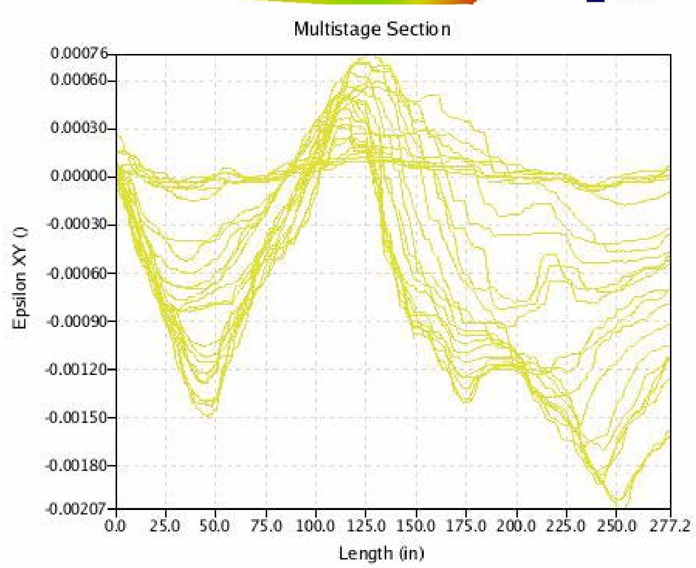

D1A11NN1

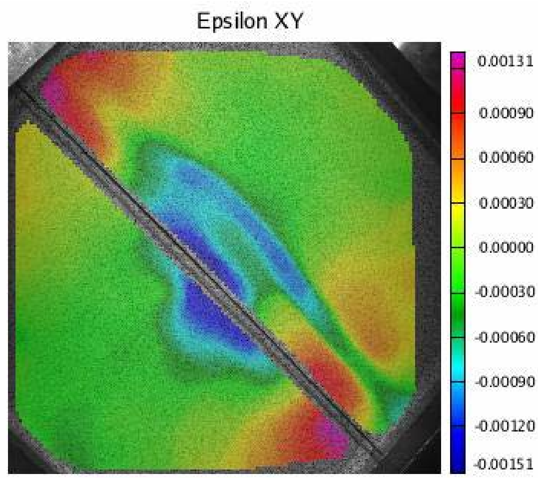
Epsilon XY
0.00131
0.00090
0.00060
0.00030
0.00000
-0.00030
-0.00060
-0.00090
-0.00120
-0.00151

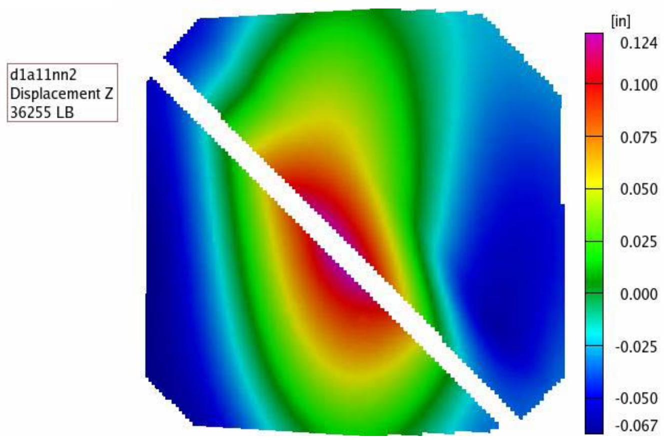
d1a11nn2
Displacement Z
36255 LB
[in]
0.124
0.100
0.075
0.050
0.025
0.000
-0.025
-0.050
-0.067

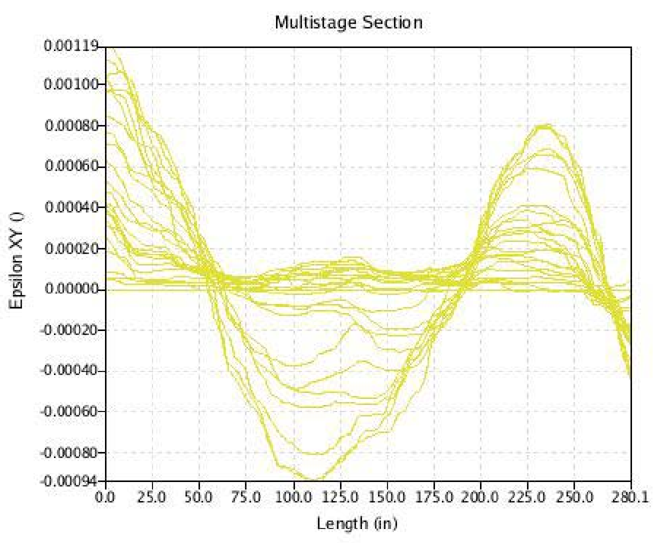
Multistage Section
0.00119
0.00100
0.00080
0.00060
0.00040
0.00020
0.00000
-0.00020
-0.00040
-0.00060
-0.00080
-0.00094
Epsilon XY ()
0.0
25.0
50.0
75.0
100.0
125.0
150.0
175.0
200.0
225.0
250.0
280.1
Length (in)

D1A11NN2

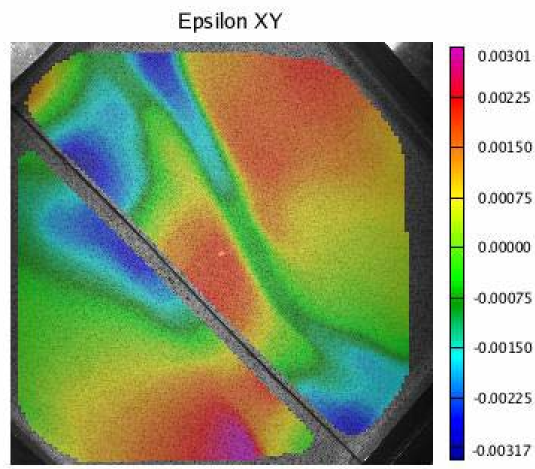
Epsilon XY
0.00301
0.00225
0.00150
0.00075
0.00000
-0.00075
-0.00150
-0.00225
-0.00317

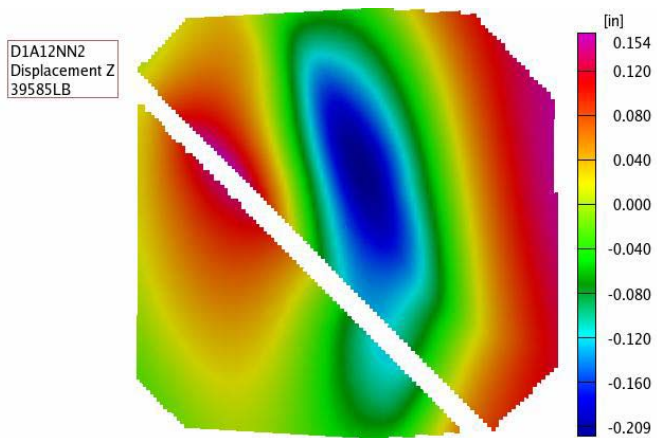
D1A12NN2
Displacement Z
39585LB
[in]
0.154
0.120
0.080
0.040
0.000
-0.040
-0.080
-0.120
-0.160
-0.209

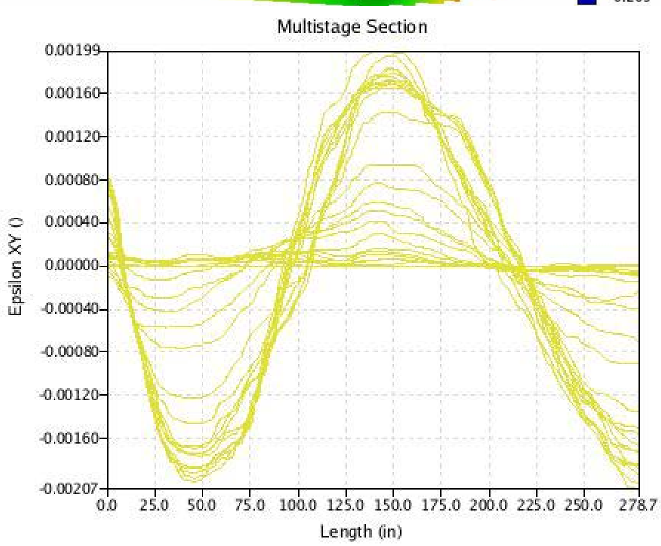
Multistage Section
0.00199
0.00160
0.00120
0.00080
0.00040
0.00000
-0.00040
-0.00080
-0.00120
-0.00160
-0.00207
Epsilon XY ()
0.0
25.0
50.0
75.0
100.0
125.0
150.0
175.0
200.0
225.0
250.0
278.7
Length (in)

D1A12NN2

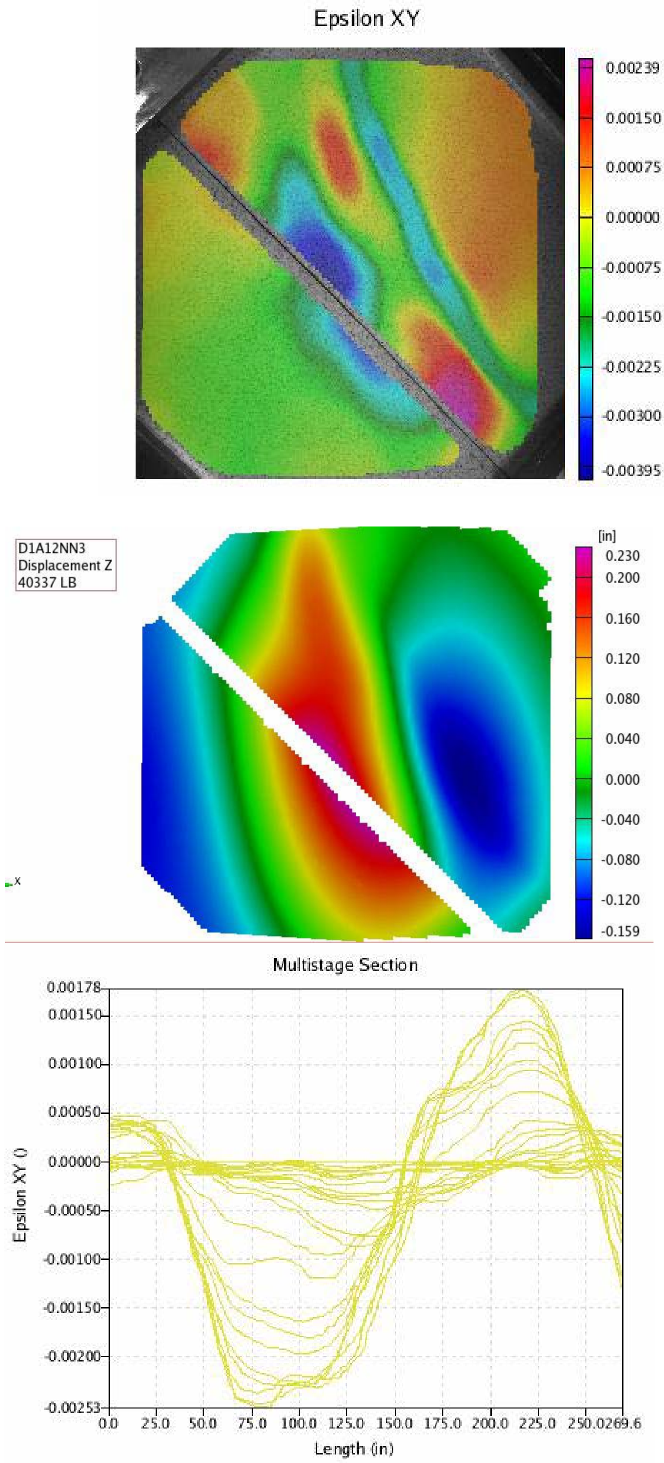
Epsilon XY
0.00239
0.00150
0.00075
0.00000
-0.00075
-0.00150
-0.00225
-0.00300
-0.00395
D1A12NN3
Displacement Z
40337 LB
[in]
0.230
0.200
0.160
0.120
0.080
0.040
0.000
-0.040
-0.080
-0.120
-0.159
Multistage Section
Epsilon XY ()
0.00178
0.00150
0.00100
0.00050
0.00000
-0.00050
-0.00100
-0.00150
-0.00200
-0.00253
0.0
25.0
50.0
75.0
100.0
125.0
150.0
175.0
200.0
225.0
250.0
269.6
Length (in)

D1A12NN3

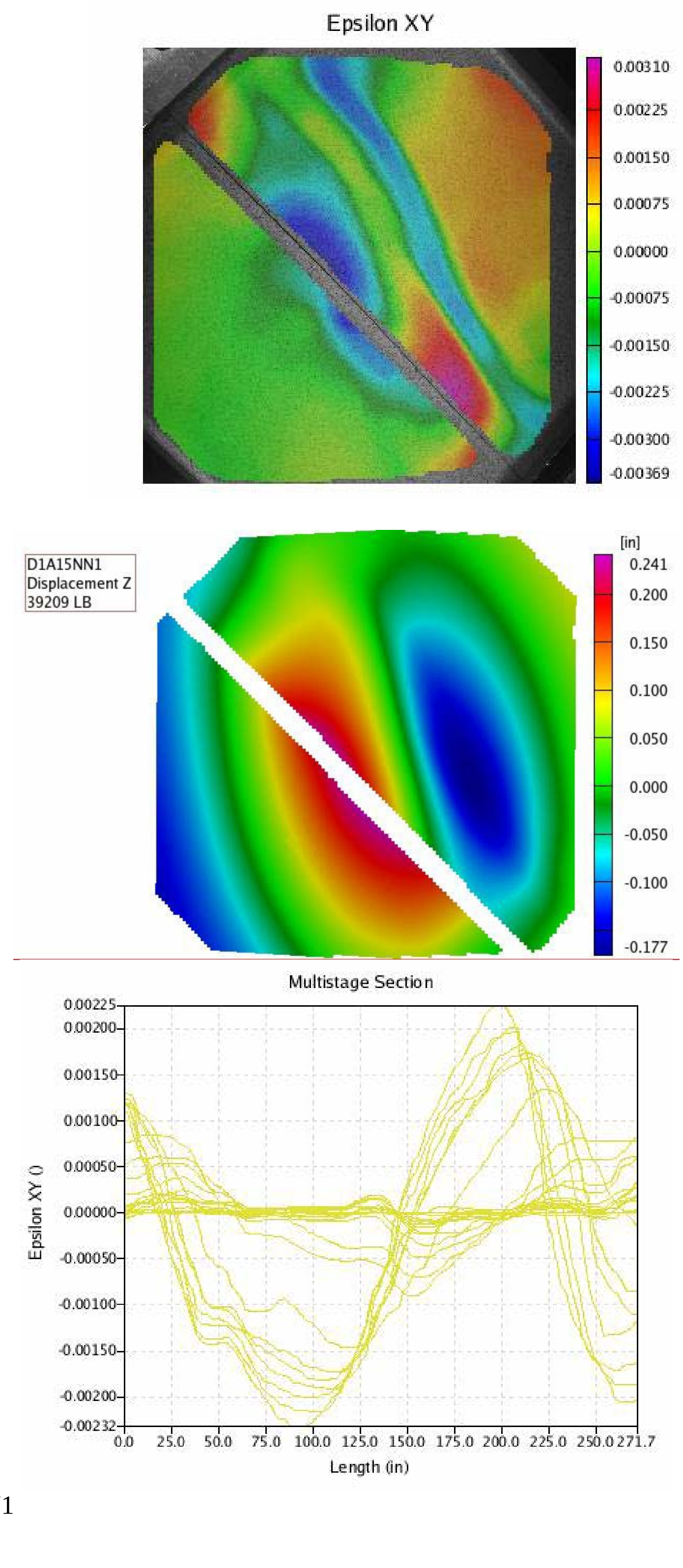
Epsilon XY
0.00310
0.00225
0.00150
0.00075
0.00000
-0.00075
-0.00150
-0.00225
-0.00300
-0.00369
D1A15NN1
Displacement Z
39209 LB
[in]
0.241
0.200
0.150
0.100
0.050
0.000
-0.050
-0.100
-0.177
Multistage Section
Epsilon XY ()
0.00225
0.00200
0.00150
0.00100
0.00050
0.00000
-0.00050
-0.00100
-0.00150
-0.00200
-0.00232
0.0 25.0 50.0 75.0 100.0 125.0 150.0 175.0 200.0 225.0 250.0 271.7
Length (in)

D1A15NN1

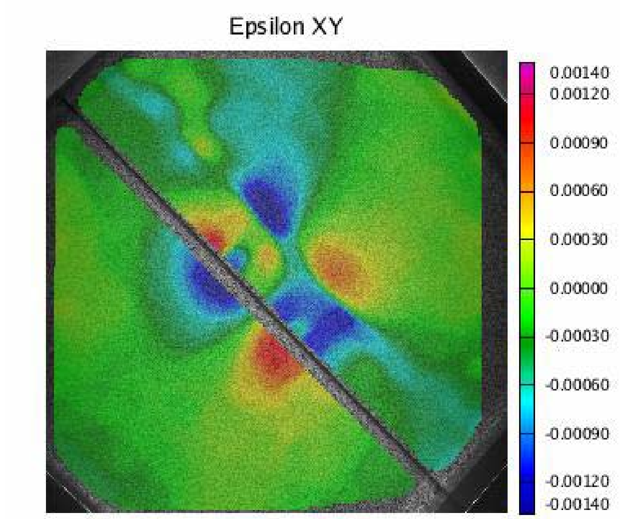
Epsilon XY
0.00140
0.00120
0.00090
0.00060
0.00030
0.00000
-0.00030
-0.00060
-0.00090
-0.00120
-0.00140

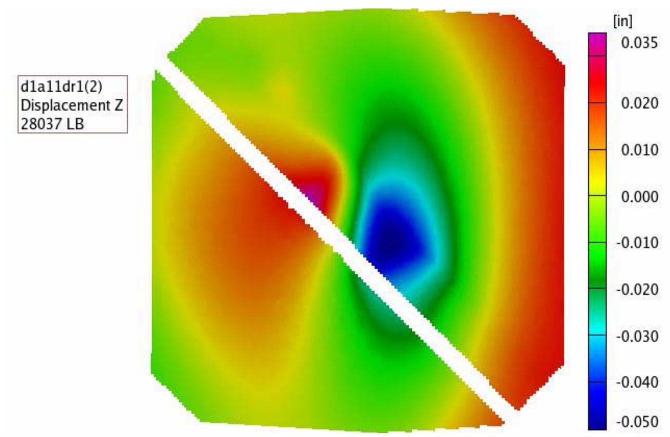
d1a11dr1(2)
Displacement Z
28037 LB
[in]
0.035
0.020
0.010
0.000
-0.010
-0.020
-0.030
-0.040
-0.050

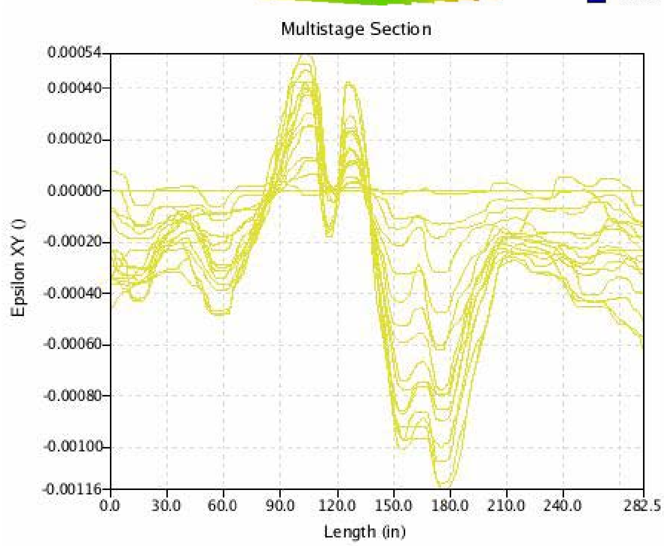
Multistage Section
Epsilon XY ()
0.00054
0.00040
0.00020
0.00000
-0.00020
-0.00040
-0.00060
-0.00080
-0.00100
-0.00116
0.0
30.0
60.0
90.0
120.0
150.0
180.0
210.0
240.0
282.5
Length (in)

D1A11DR1(2)

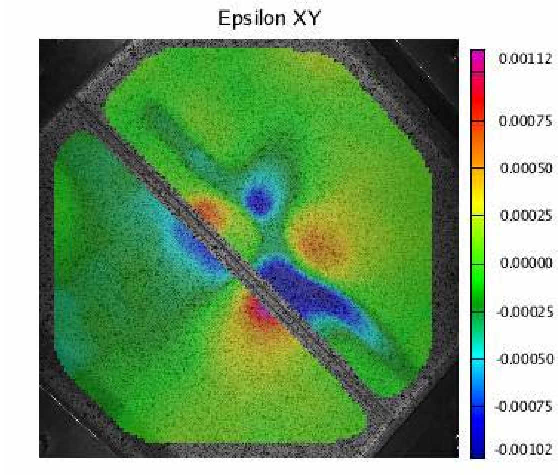
Epsilon XY
0.00112
0.00075
0.00050
0.00025
0.00000
-0.00025
-0.00050
-0.00075
-0.00102

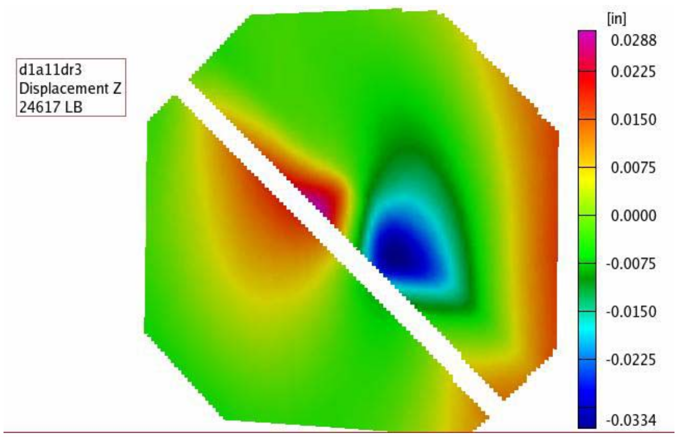
d1a11dr3
Displacement Z
24617 LB
[in]
0.0288
0.0225
0.0150
0.0075
0.0000
-0.0075
-0.0150
-0.0225
-0.0334

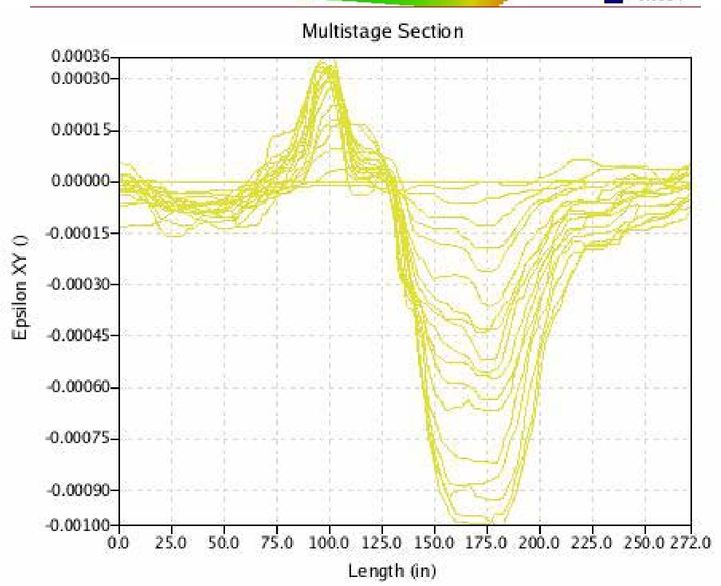
Multistage Section
Epsilon XY ()
Length (in)
0.00036
0.00030
0.00015
0.00000
-0.00015
-0.00030
-0.00045
-0.00060
-0.00075
-0.00090
-0.00100
0.0
25.0
50.0
75.0
100.0
125.0
150.0
175.0
200.0
225.0
250.0
272.0

D1A11DR13

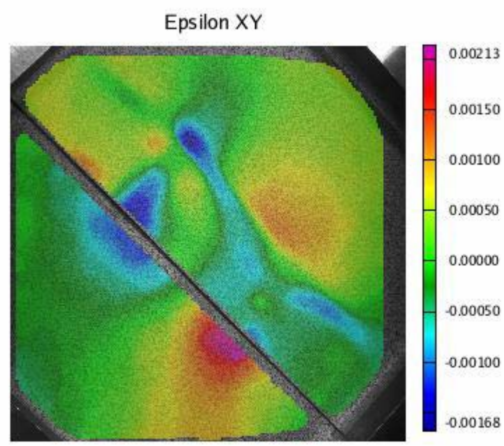
Epsilon XY
0.00213
0.00150
0.00100
0.00050
0.00000
-0.00050
-0.00100
-0.00168

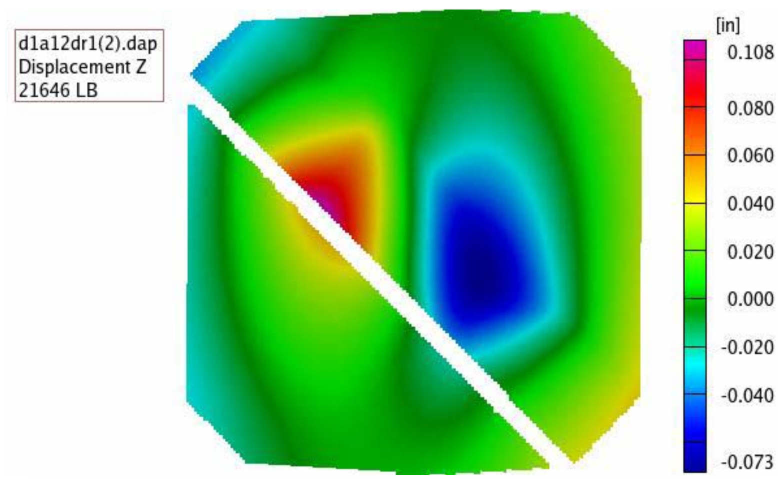
d1a12dr1(2).dap
Displacement Z
21646 LB
[in]
0.108
0.080
0.060
0.040
0.020
0.000
-0.020
-0.040
-0.073

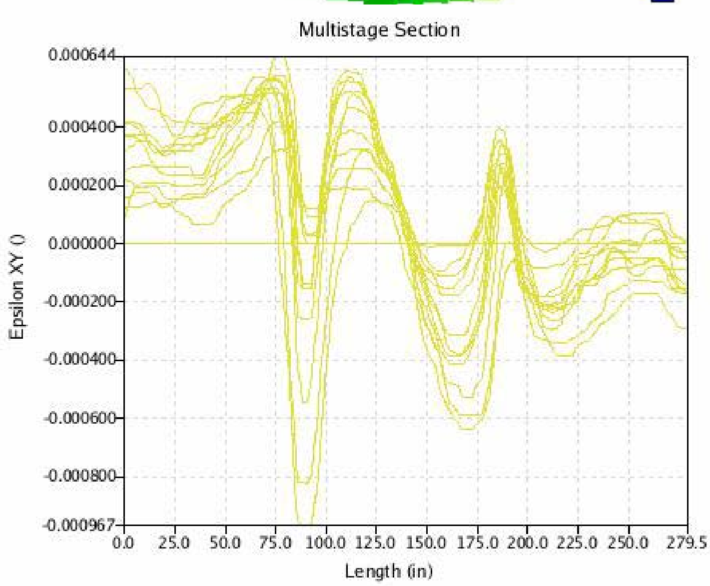
Multistage Section
0.000644
0.000400
0.000200
0.000000
-0.000200
-0.000400
-0.000600
-0.000800
-0.000967
Epsilon XY ()
0.0
25.0
50.0
75.0
100.0
125.0
150.0
175.0
200.0
225.0
250.0
279.5
Length (in)

D1A12DR1(2)

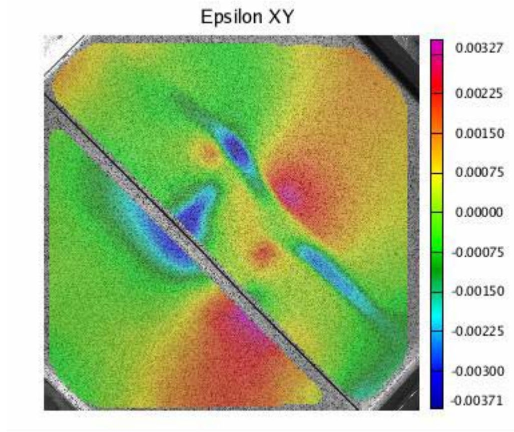
Epsilon XY
0.00327
0.00225
0.00150
0.00075
0.00000
-0.00075
-0.00150
-0.00225
-0.00300
-0.00371

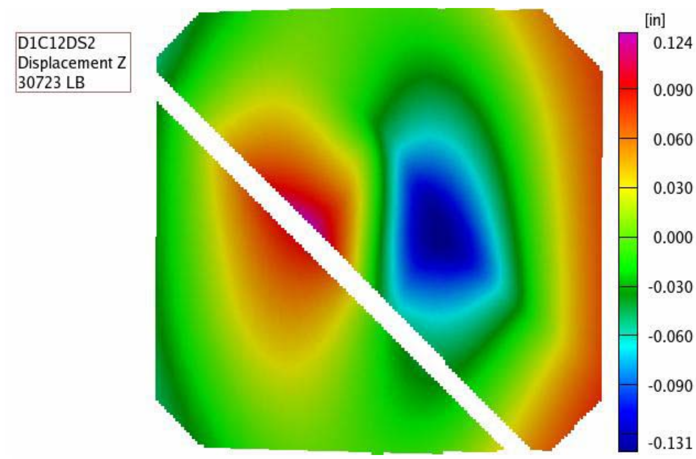
D1C12DS2
Displacement Z
30723 LB
[in]
0.124
0.090
0.060
0.030
0.000
-0.030
-0.060
-0.090
-0.131

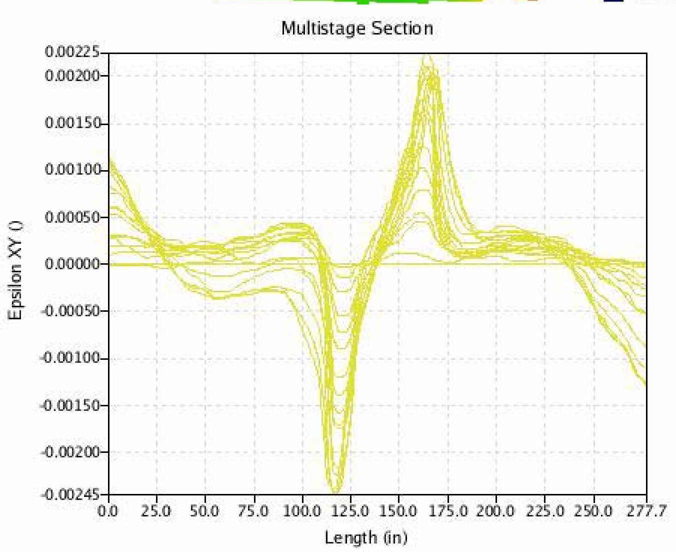
Multistage Section
0.00225
0.00200
0.00150
0.00100
0.00050
0.00000
-0.00050
-0.00100
-0.00150
-0.00200
-0.00245
Epsilon XY ()
0.0
25.0
50.0
75.0
100.0
125.0
150.0
175.0
200.0
225.0
250.0
277.7
Length (in)

D1C12DS2

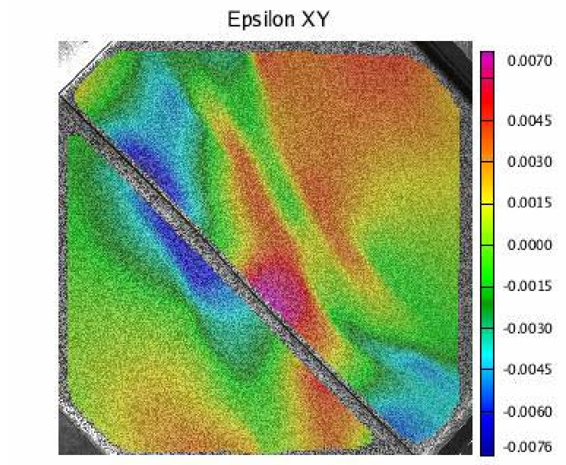
Epsilon XY
0.0070
0.0045
0.0030
0.0015
0.0000
-0.0015
-0.0030
-0.0045
-0.0060
-0.0076

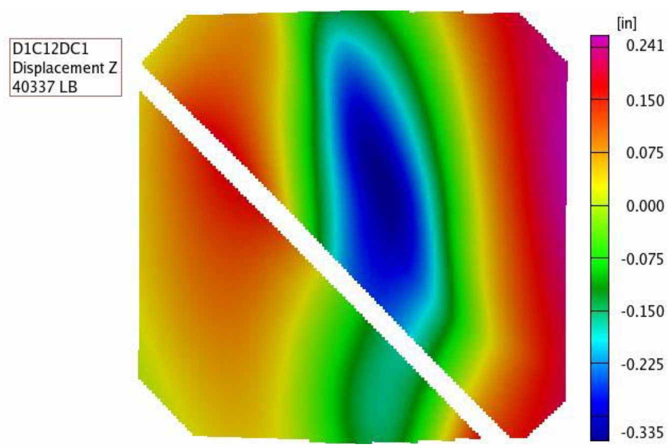
D1C12DC1
Displacement Z
40337 LB
[in]
0.241
0.150
0.075
0.000
-0.075
-0.150
-0.225
-0.335

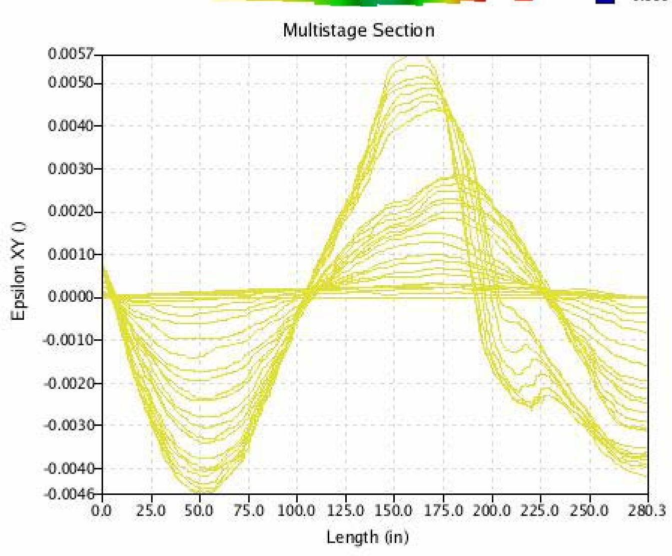
Multistage Section
Epsilon XY ()
0.0057
0.0050
0.0040
0.0030
0.0020
0.0010
0.0000
-0.0010
-0.0020
-0.0030
-0.0040
-0.0046
0.0
25.0
50.0
75.0
100.0
125.0
150.0
175.0
200.0
225.0
250.0
280.3
Length (in)

D1C12DC1

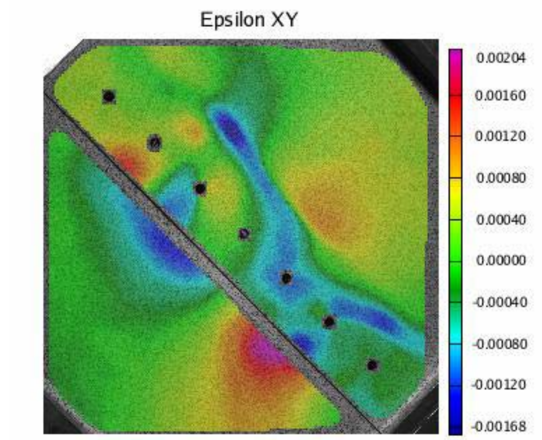
Epsilon XY
0.00204
0.00160
0.00120
0.00080
0.00040
0.00000
-0.00040
-0.00080
-0.00120
-0.00168

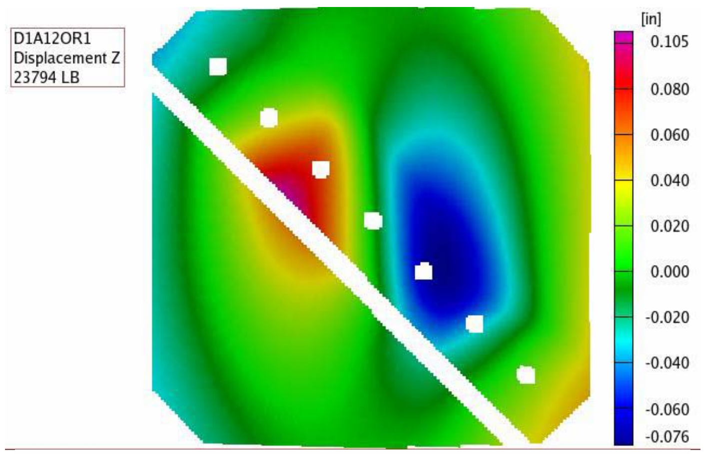
D1A12OR1
Displacement Z
23794 LB
[in]
0.105
0.080
0.060
0.040
0.020
0.000
-0.020
-0.040
-0.060
-0.076

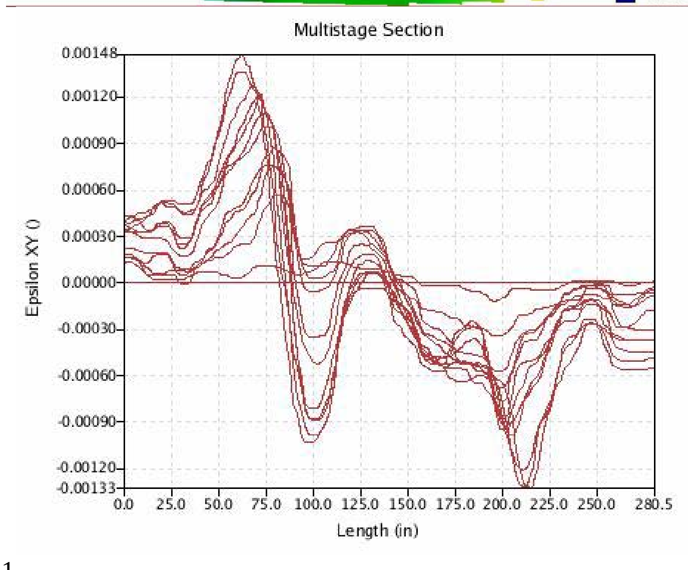
Multistage Section
0.00148
0.00120
0.00090
0.00060
0.00030
0.00000
-0.00030
-0.00060
-0.00090
-0.00120
-0.00133
Epsilon XY ()
0.0
25.0
50.0
75.0
100.0
125.0
150.0
175.0
200.0
225.0
250.0
280.5
Length (in)

D1A12OR1

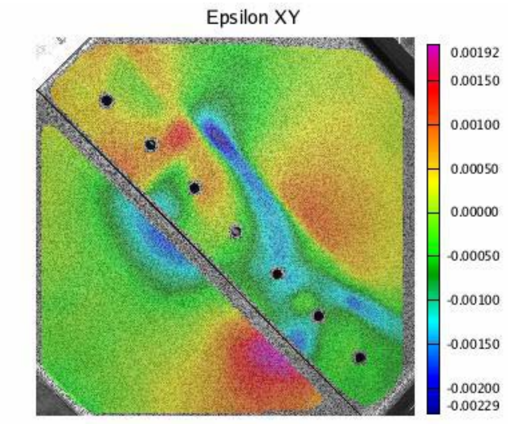
Epsilon XY
0.00192
0.00150
0.00100
0.00050
0.00000
-0.00050
-0.00100
-0.00150
-0.00200
-0.00229

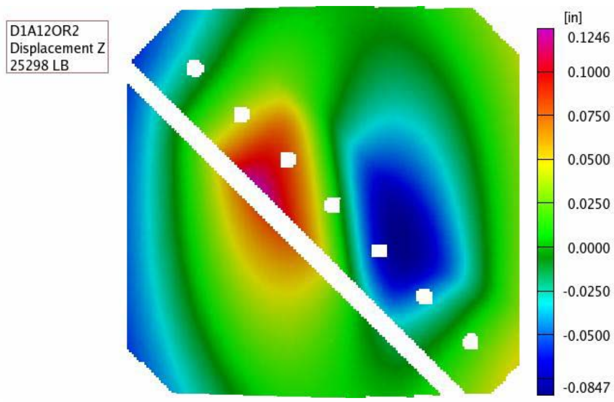
D1A12OR2
Displacement Z
25298 LB
[in]
0.1246
0.1000
0.0750
0.0500
0.0250
0.0000
-0.0250
-0.0500
-0.0847

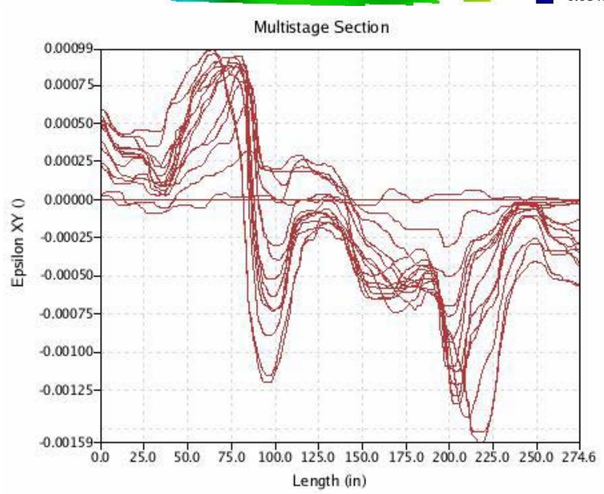
Multistage Section
Epsilon XY ()
0.00099
0.00075
0.00050
0.00025
0.00000
-0.00025
-0.00050
-0.00075
-0.00100
-0.00125
-0.00159
0.0
25.0
50.0
75.0
100.0
125.0
150.0
175.0
200.0
225.0
250.0
274.6
Length (in)

D1A12OR2

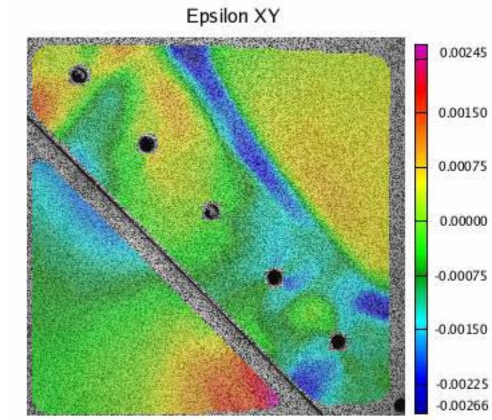
Epsilon XY
0.00245
0.00150
0.00075
0.00000
-0.00075
-0.00150
-0.00225
-0.00266

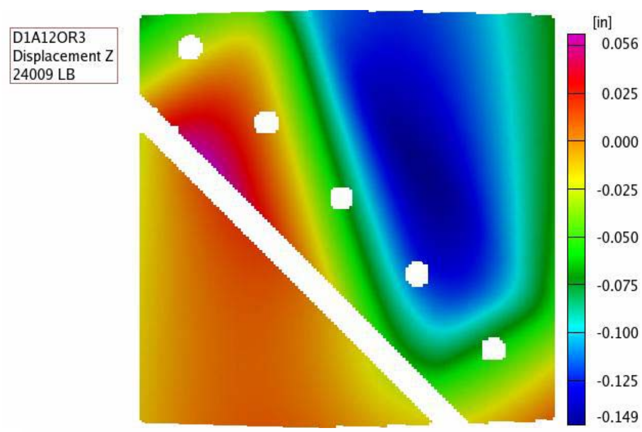
D1A12OR3
Displacement Z
24009 LB
[in]
0.056
0.025
0.000
-0.025
-0.050
-0.075
-0.100
-0.125
-0.149

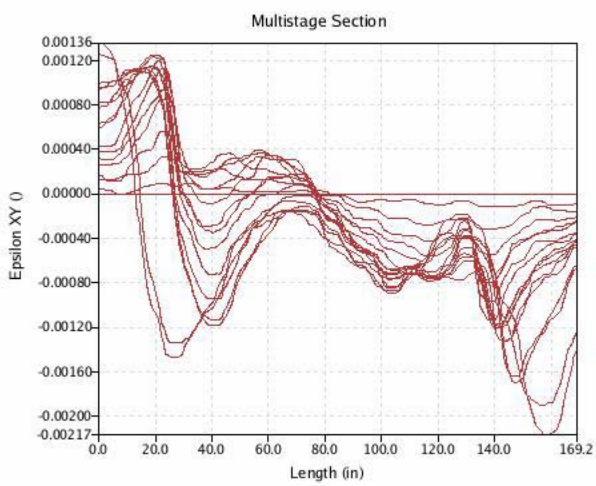
Multistage Section
Epsilon XY ()
Length (in)
0.00136
0.00120
0.00080
0.00040
0.00000
-0.00040
-0.00080
-0.00120
-0.00160
-0.00200
-0.00217
0.0
20.0
40.0
60.0
80.0
100.0
120.0
140.0
169.2

D1A12OR3

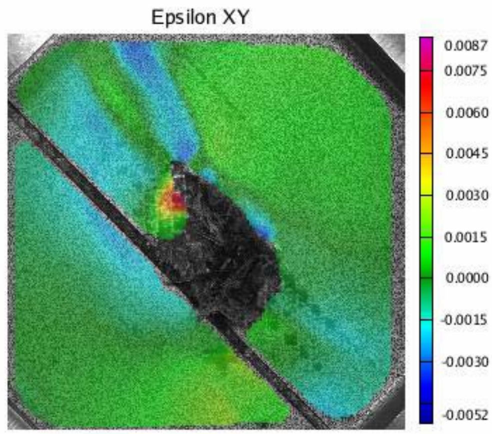
Epsilon XY
0.0087
0.0075
0.0060
0.0045
0.0030
0.0015
0.0000
-0.0015
-0.0030
-0.0052

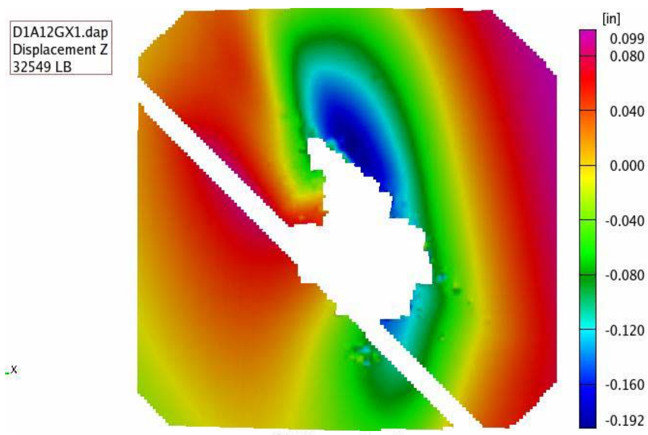
D1A12GX1.dap
Displacement Z
32549 LB
[in]
0.099
0.080
0.040
0.000
-0.040
-0.080
-0.120
-0.160
-0.192

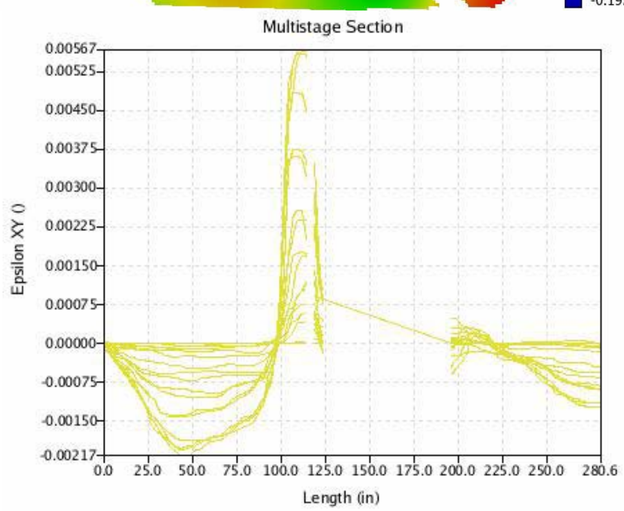
Multistage Section
Epsilon XY ()
Length (in)
0.00567
0.00525
0.00450
0.00375
0.00300
0.00225
0.00150
0.00075
0.00000
-0.00075
-0.00150
-0.00217
0.0
25.0
50.0
75.0
100.0
125.0
150.0
175.0
200.0
225.0
250.0
280.6

D1A12GX1

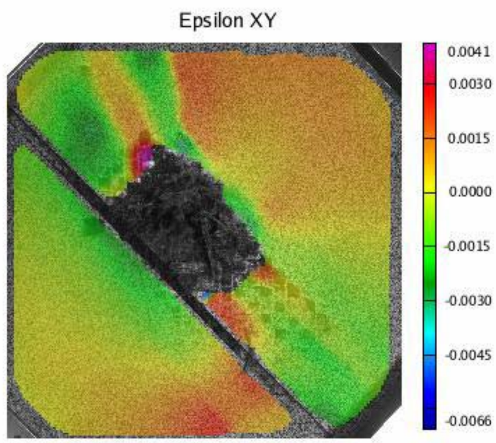
Epsilon XY
0.0041
0.0030
0.0015
0.0000
-0.0015
-0.0030
-0.0045
-0.0066

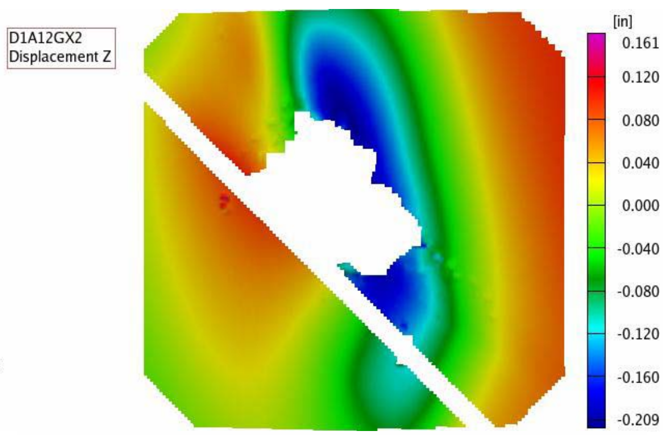
D1A12GX2
Displacement Z
[in]
0.161
0.120
0.080
0.040
0.000
-0.040
-0.080
-0.120
-0.160
-0.209

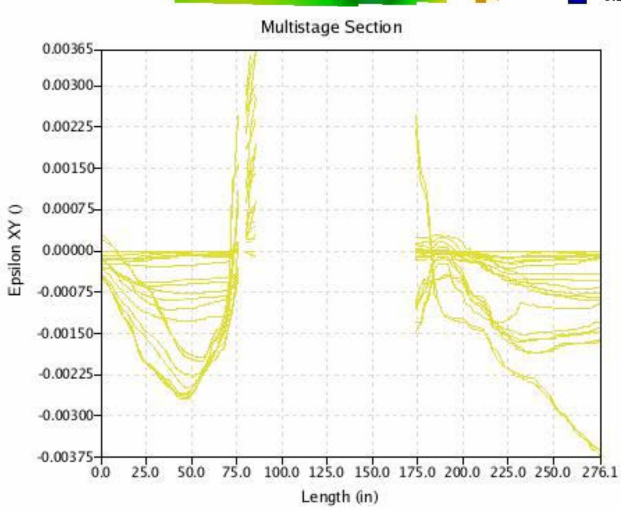
Multistage Section
Epsilon XY ()
0.00365
0.00300
0.00225
0.00150
0.00075
0.00000
-0.00075
-0.00150
-0.00225
-0.00300
-0.00375
0.0
25.0
50.0
75.0
100.0
125.0
150.0
175.0
200.0
225.0
250.0
276.1
Length (in)

D1A12GX2

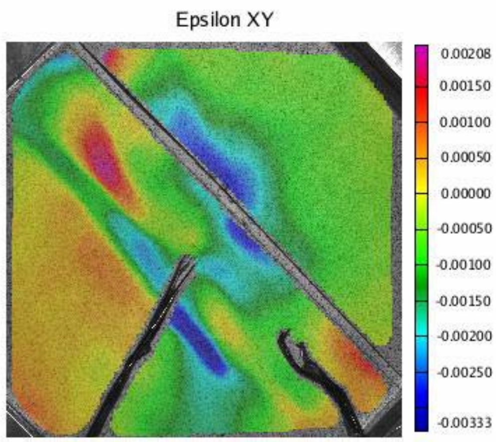
Epsilon XY
0.00208
0.00150
0.00100
0.00050
0.00000
-0.00050
-0.00100
-0.00150
-0.00200
-0.00250
-0.00333

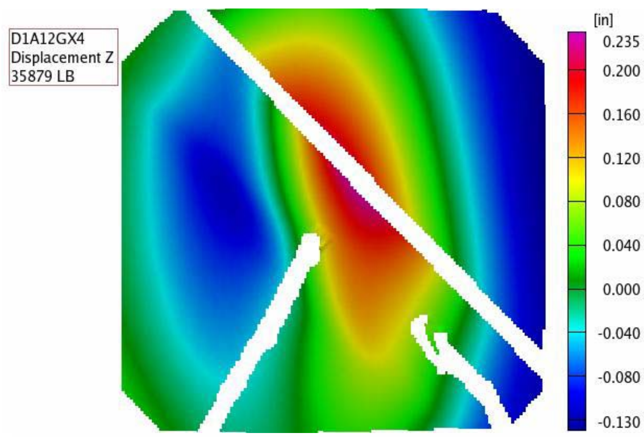
D1A12GX4
Displacement Z
35879 LB
[in]
0.235
0.200
0.160
0.120
0.080
0.040
0.000
-0.040
-0.080
-0.130

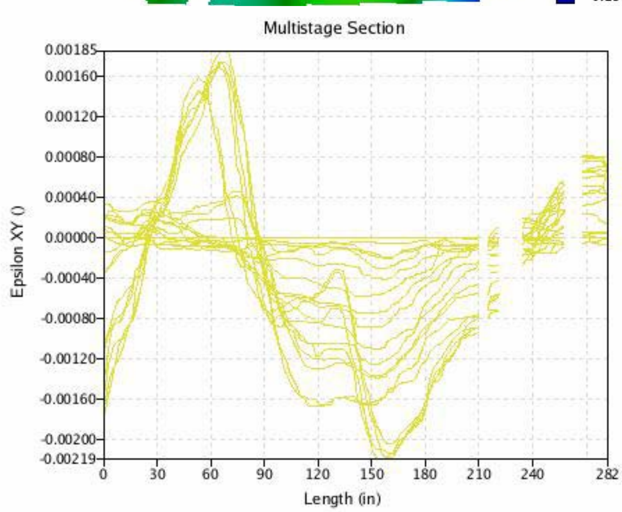
Multistage Section
Epsilon XY ()
Length (in)
0.00185
0.00160
0.00120
0.00080
0.00040
0.00000
-0.00040
-0.00080
-0.00120
-0.00160
-0.00200
-0.00219
0
30
60
90
120
150
180
210
240
282

D1A12GX4

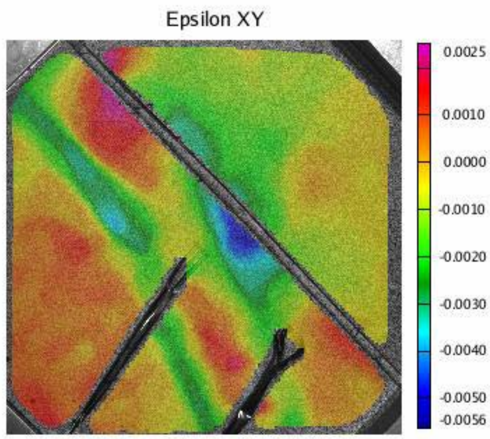
Epsilon XY
0.0025
0.0010
0.0000
-0.0010
-0.0020
-0.0030
-0.0040
-0.0050
-0.0056

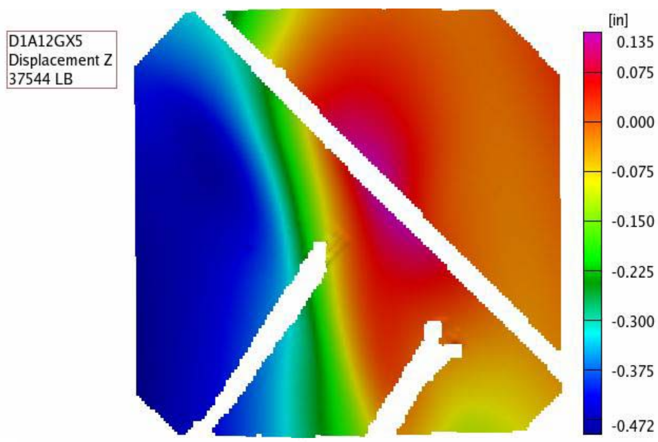
D1A12GX5
Displacement Z
37544 LB
[in]
0.135
0.075
0.000
-0.075
-0.150
-0.225
-0.300
-0.375
-0.472

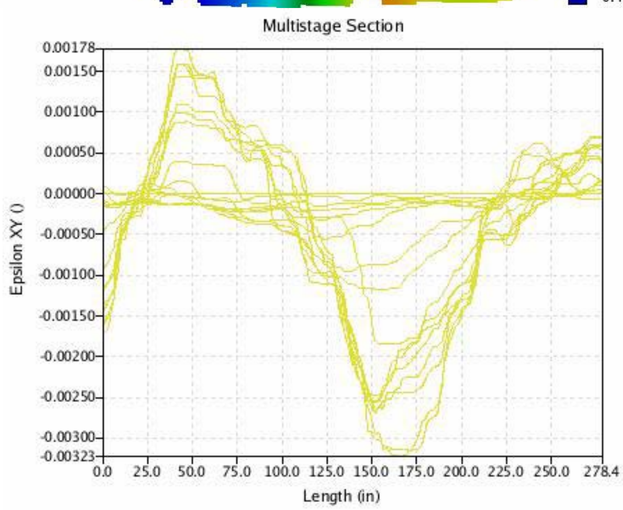
Multistage Section
Epsilon XY ()
0.00178
0.00150
0.00100
0.00050
0.00000
-0.00050
-0.00100
-0.00150
-0.00200
-0.00250
-0.00300
-0.00323
0.0
25.0
50.0
75.0
100.0
125.0
150.0
175.0
200.0
225.0
250.0
278.4
Length (in)

D1A12GX5

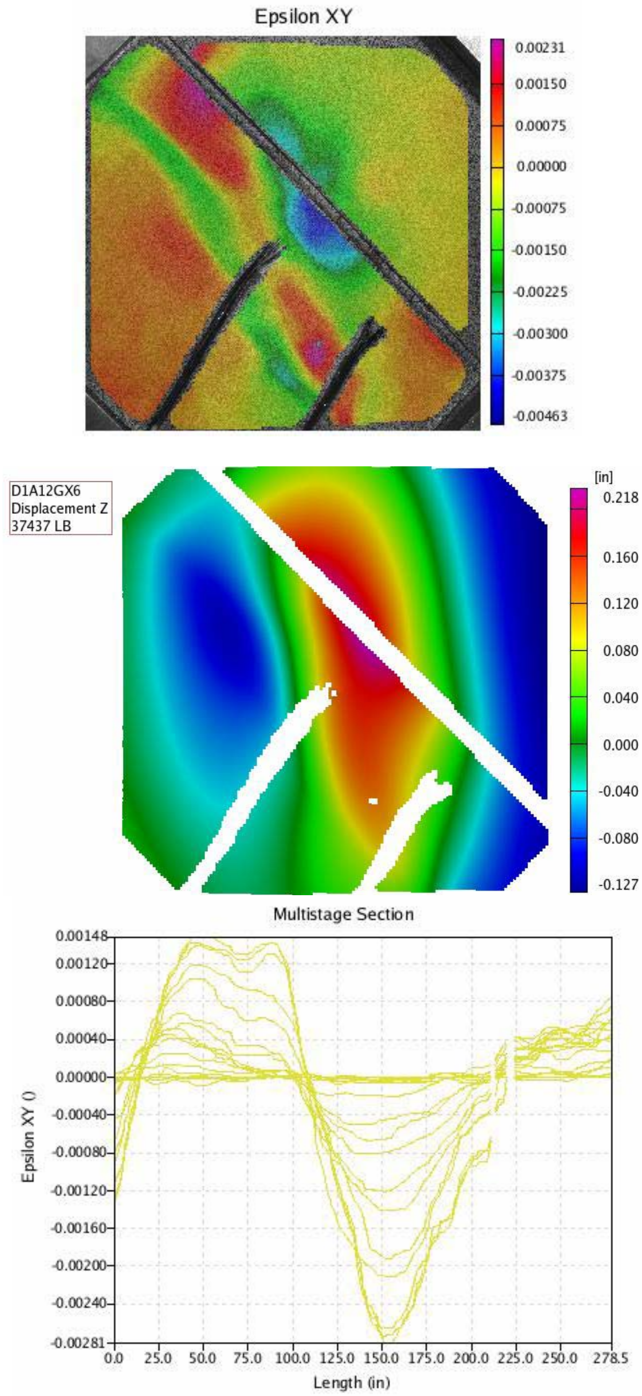
Epsilon XY
0.00231
0.00150
0.00075
0.00000
-0.00075
-0.00150
-0.00225
-0.00300
-0.00375
-0.00463
D1A12GX6
Displacement Z
37437 LB
[in]
0.218
0.160
0.120
0.080
0.040
0.000
-0.040
-0.080
-0.127
Multistage Section
0.00148
0.00120
0.00080
0.00040
0.00000
-0.00040
-0.00080
-0.00120
-0.00160
-0.00200
-0.00240
-0.00281
Epsilon XY ()
0.0 25.0 50.0 75.0 100.0 125.0 150.0 175.0 200.0 225.0 250.0 278.5
Length (in)

D1A12GX6

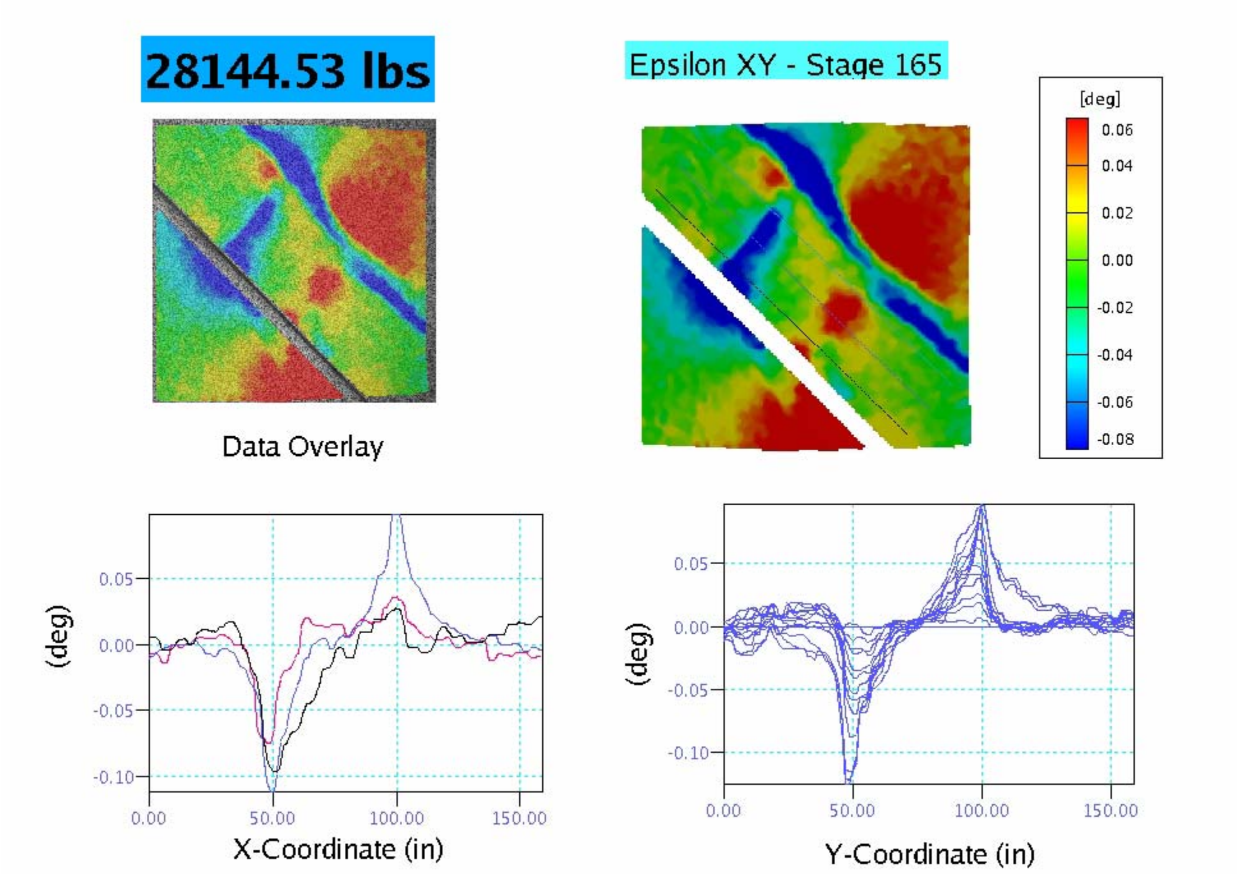
28144.53 lbs
Data Overlay
Epsilon XY - Stage 165
[deg]
0.06
0.04
0.02
0.00
-0.02
-0.04
-0.06
-0.08
(deg)
0.05
0.00
-0.05
-0.10
0.00
50.00
100.00
150.00
X-Coordinate (in)
Y-Coordinate (in)

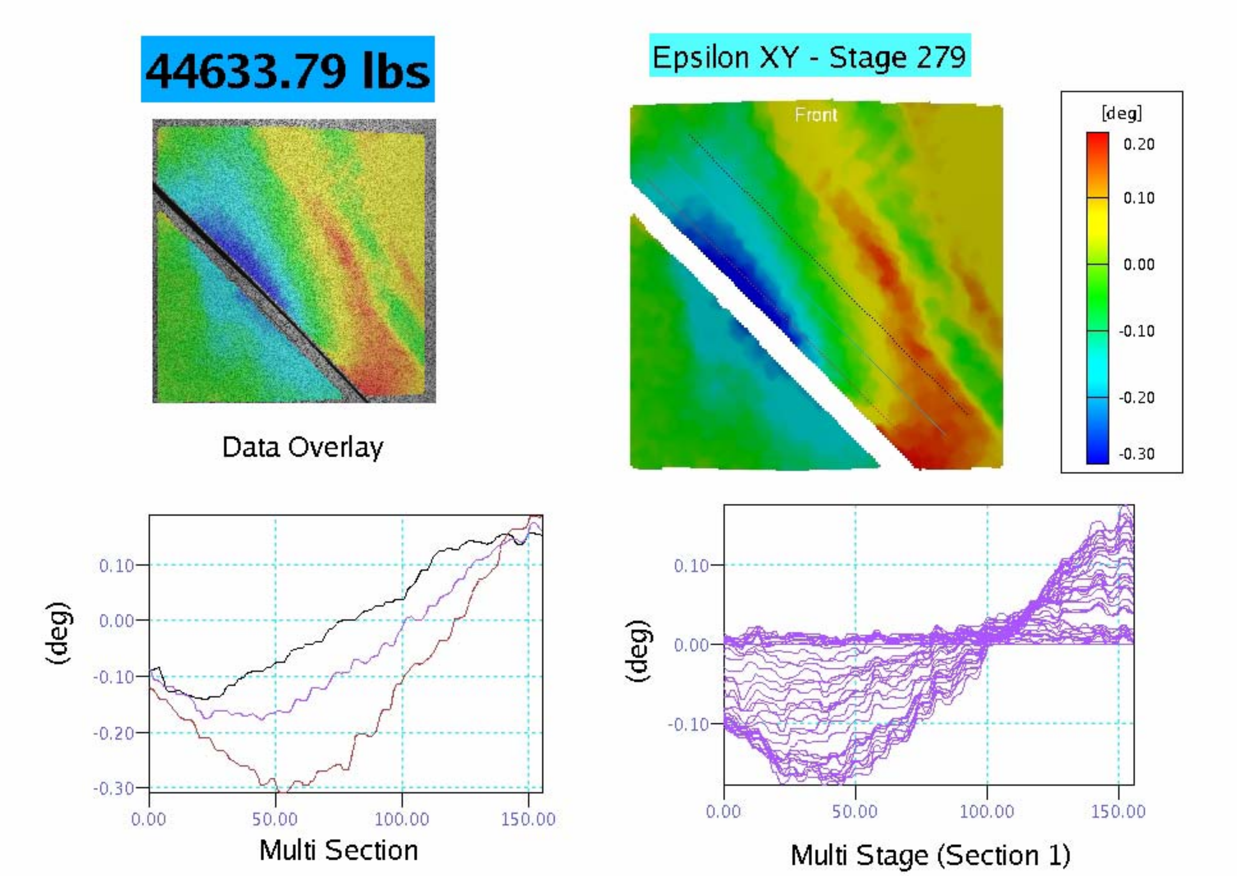
44633.79 lbs
Data Overlay
Epsilon XY - Stage 279
Front
[deg]
0.20
0.10
0.00
-0.10
-0.20
-0.30
(deg)
0.10
0.00
-0.10
-0.20
-0.30
0.00
50.00
100.00
150.00
Multi Section
(deg)
0.10
0.00
-0.10
0.00
50.00
100.00
150.00
Multi Stage (Section 1)

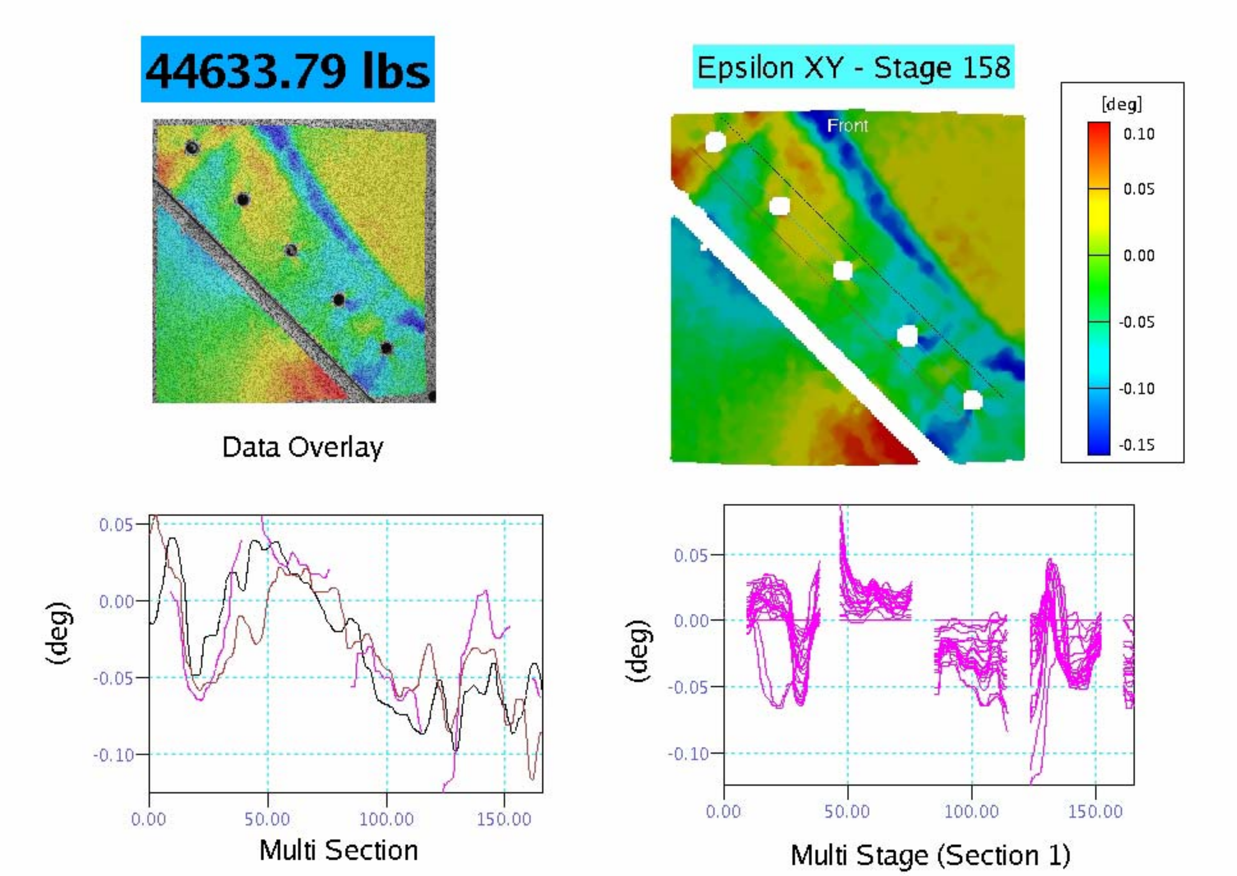
44633.79 lbs
Data Overlay
Epsilon XY - Stage 158
Front
[deg]
0.10
0.05
0.00
-0.05
-0.10
-0.15
0.05
0.00
-0.05
-0.10
(deg)
0.00
50.00
100.00
150.00
Multi Section
0.05
0.00
-0.05
-0.10
(deg)
0.00
50.00
100.00
150.00
Multi Stage (Section 1)

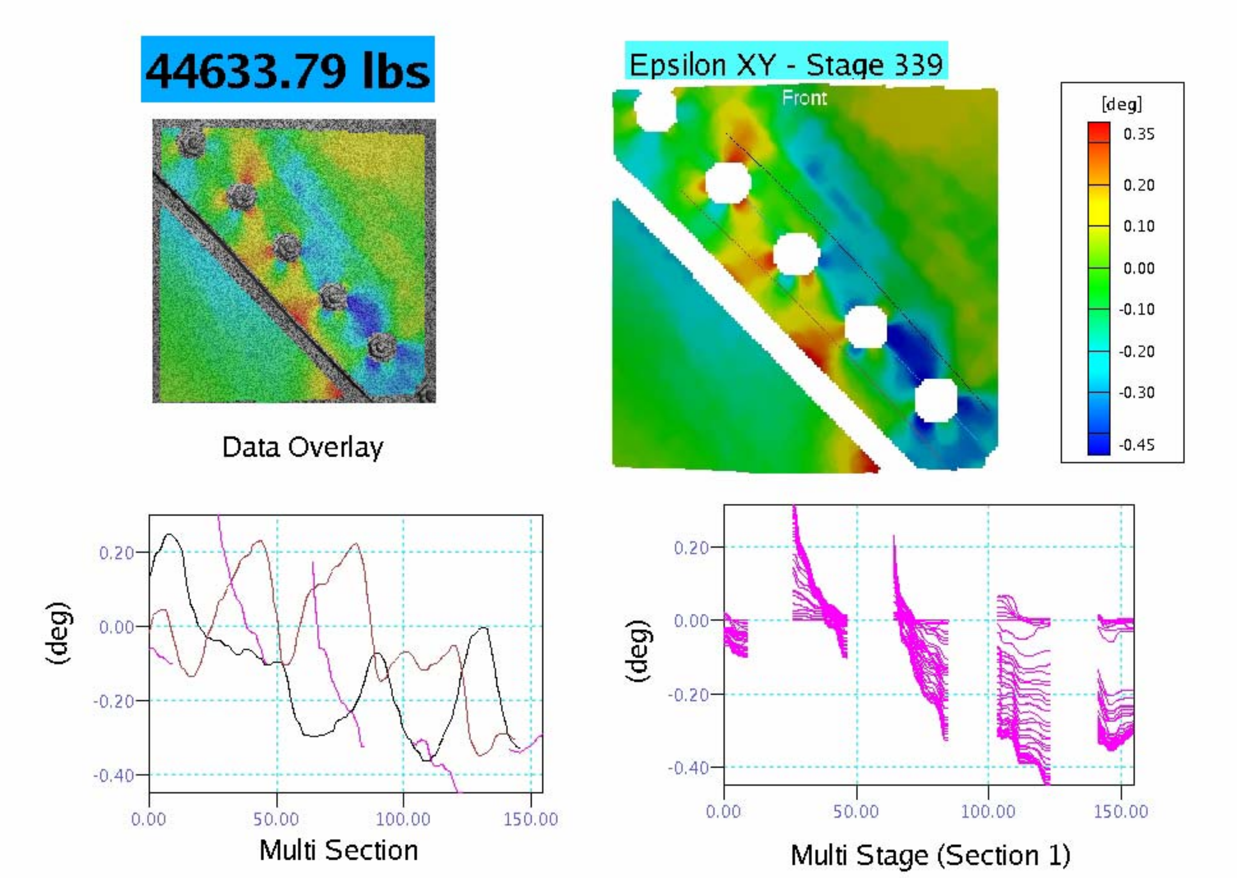

44633.79 lbs
Data Overlay
Epsilon XY - Stage 339
Front
[deg]
0.35
0.20
0.10
0.00
-0.10
-0.20
-0.30
-0.45
(deg)
0.20
0.00
-0.20
-0.40
0.00
50.00
100.00
150.00
Multi Section
Multi Stage (Section 1)

A.3.2 PHOTOGRAMMETRY RESULTS FOR EFFECTS OF IMPACT INVESTIGATION.

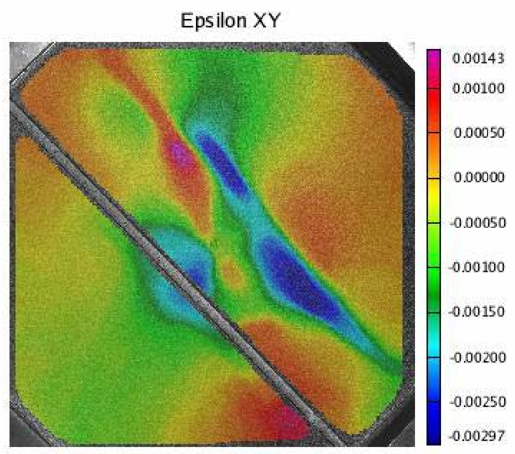

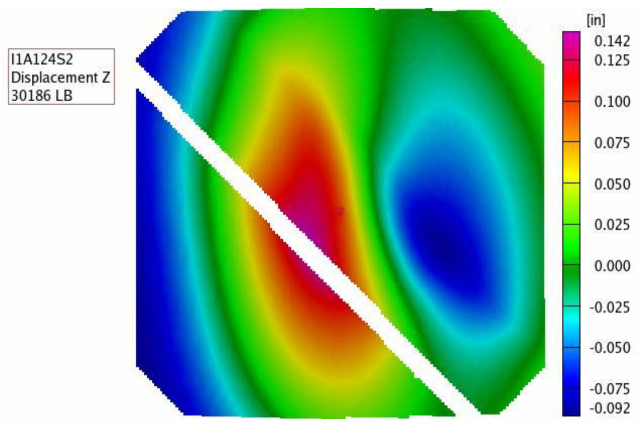

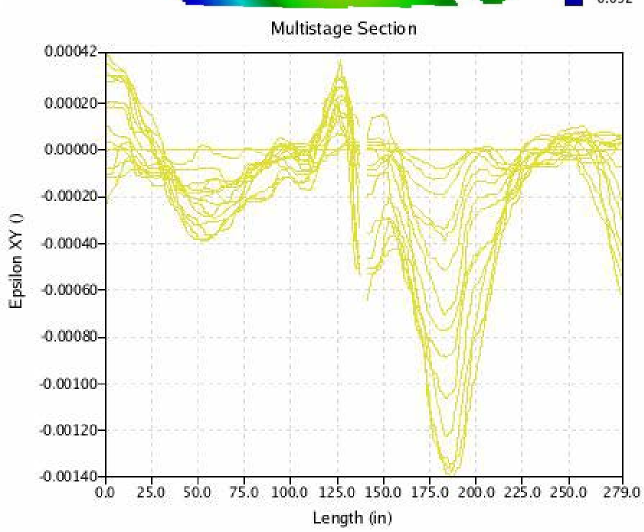

I1A124S2

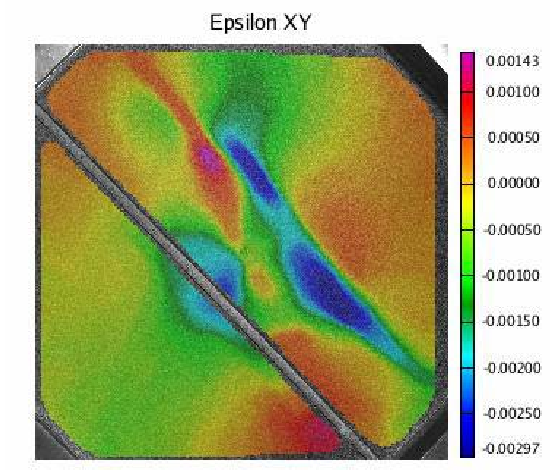
Epsilon XY
0.00143
0.00100
0.00050
0.00000
-0.00050
-0.00100
-0.00150
-0.00200
-0.00250
-0.00297

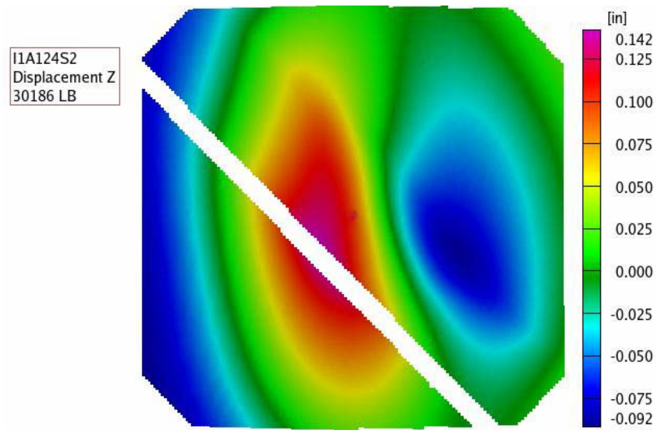
I1A124S2
Displacement Z
30186 LB
[in]
0.142
0.125
0.100
0.075
0.050
0.025
0.000
-0.025
-0.050
-0.075
-0.092

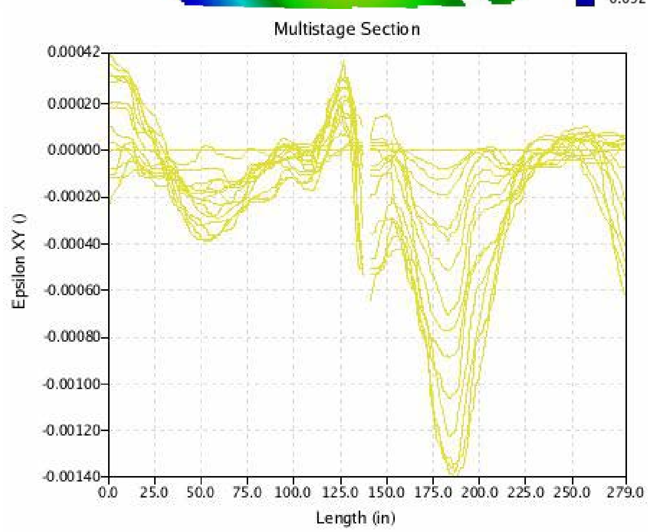
Multistage Section
Epsilon XY ()
0.00042
0.00020
0.00000
-0.00020
-0.00040
-0.00060
-0.00080
-0.00100
-0.00120
-0.00140
0.0
25.0
50.0
75.0
100.0
125.0
150.0
175.0
200.0
225.0
250.0
279.0
Length (in)

I1A124S3

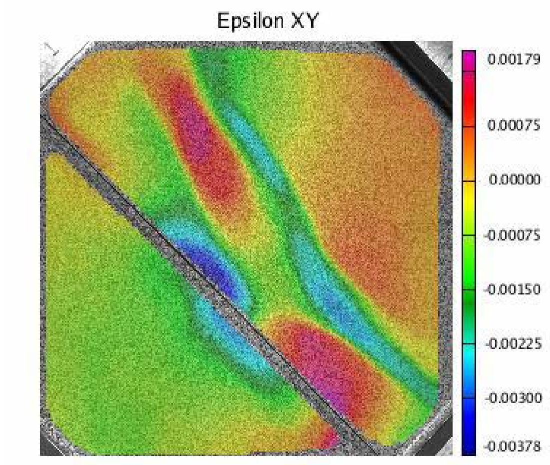
Epsilon XY
0.00179
0.00075
0.00000
-0.00075
-0.00150
-0.00225
-0.00300
-0.00378

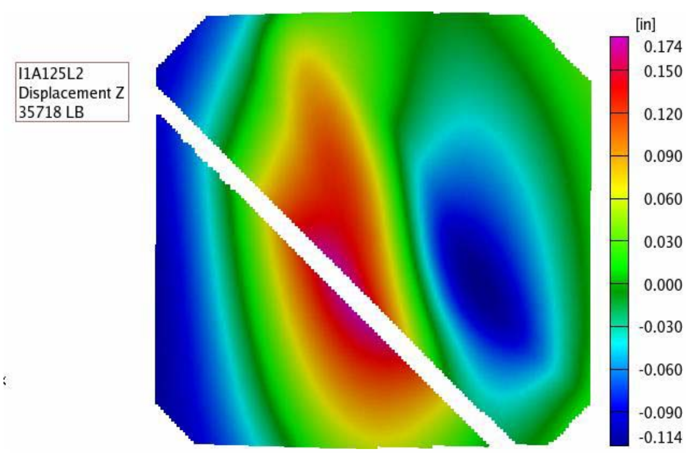
I1A125L2
Displacement Z
35718 LB
[in]
0.174
0.150
0.120
0.090
0.060
0.030
0.000
-0.030
-0.060
-0.090
-0.114

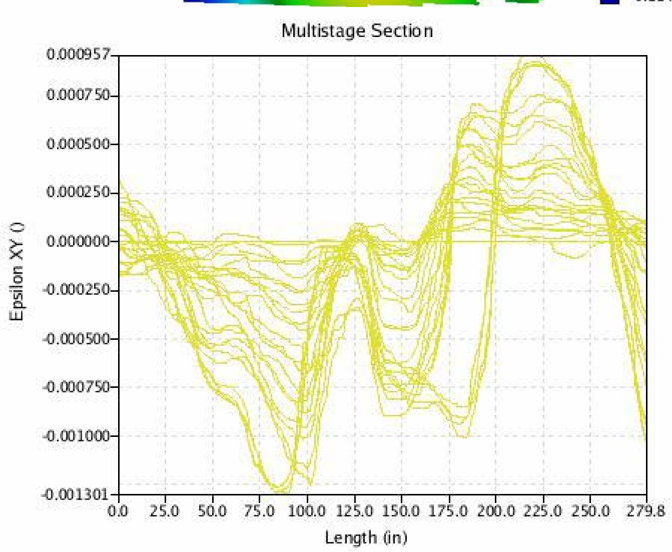
Multistage Section
Epsilon XY ()
Length (in)
0.000957
0.000750
0.000500
0.000250
0.000000
-0.000250
-0.000500
-0.000750
-0.001000
-0.001301
0.0
25.0
50.0
75.0
100.0
125.0
150.0
175.0
200.0
225.0
250.0
279.8

I1A125L2

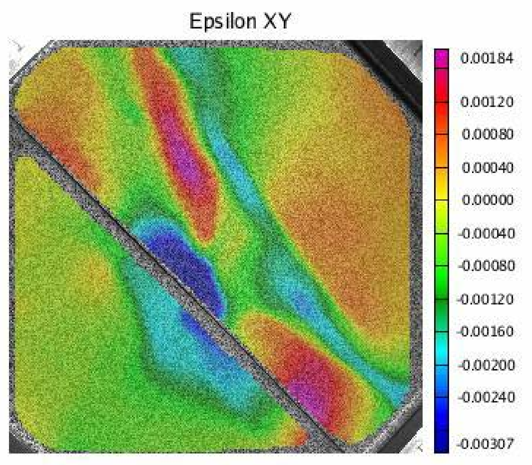
Epsilon XY
0.00184
0.00120
0.00080
0.00040
0.00000
-0.00040
-0.00080
-0.00120
-0.00160
-0.00200
-0.00240
-0.00307

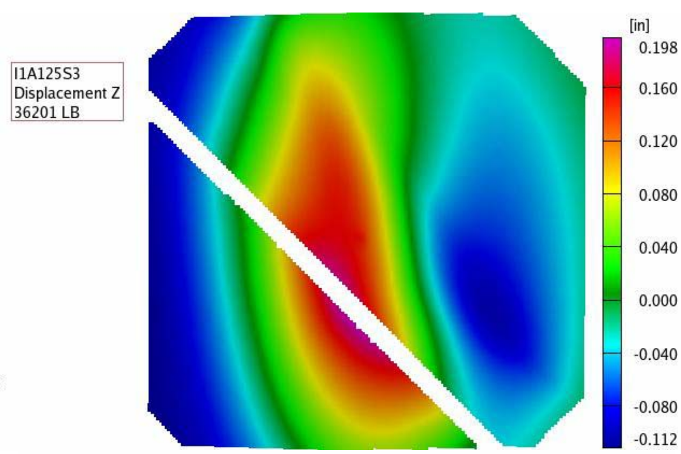
I1A125S3
Displacement Z
36201 LB
[in]
0.198
0.160
0.120
0.080
0.040
0.000
-0.040
-0.080
-0.112

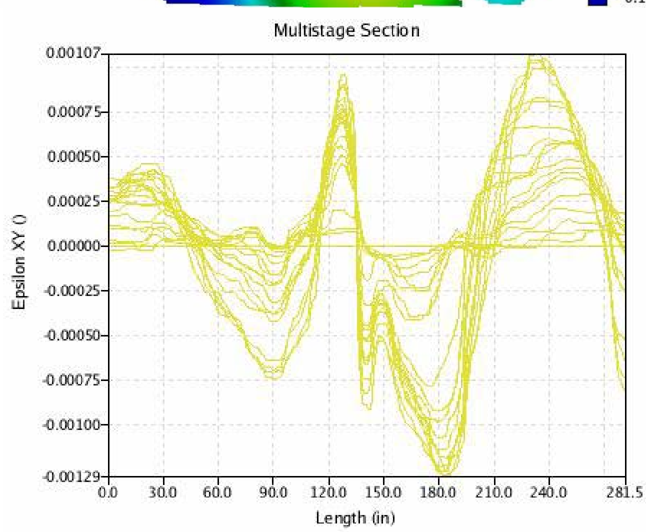
Multistage Section
Epsilon XY ()
0.00107
0.00075
0.00050
0.00025
0.00000
-0.00025
-0.00050
-0.00075
-0.00100
-0.00129
0.0
30.0
60.0
90.0
120.0
150.0
180.0
210.0
240.0
281.5
Length (in)

I1A125S3

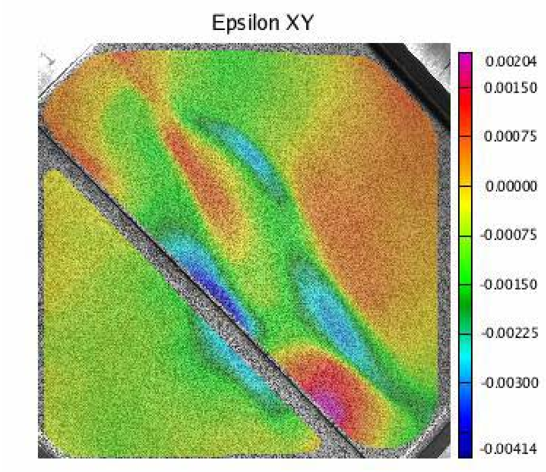
Epsilon XY
0.00204
0.00150
0.00075
0.00000
-0.00075
-0.00150
-0.00225
-0.00300
-0.00414

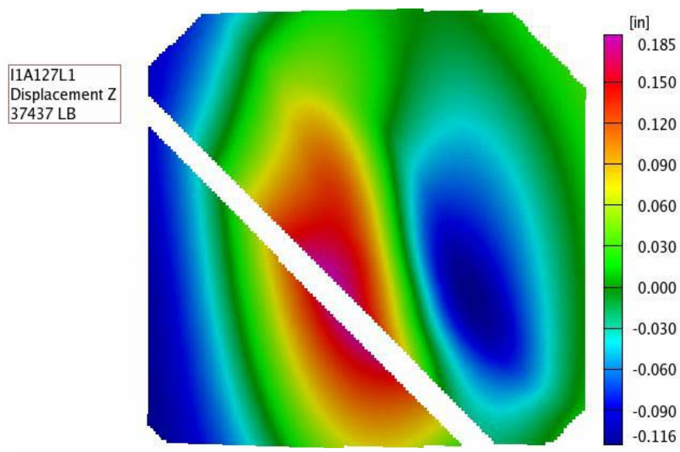
I1A127L1
Displacement Z
37437 LB
[in]
0.185
0.150
0.120
0.090
0.060
0.030
0.000
-0.030
-0.060
-0.090
-0.116

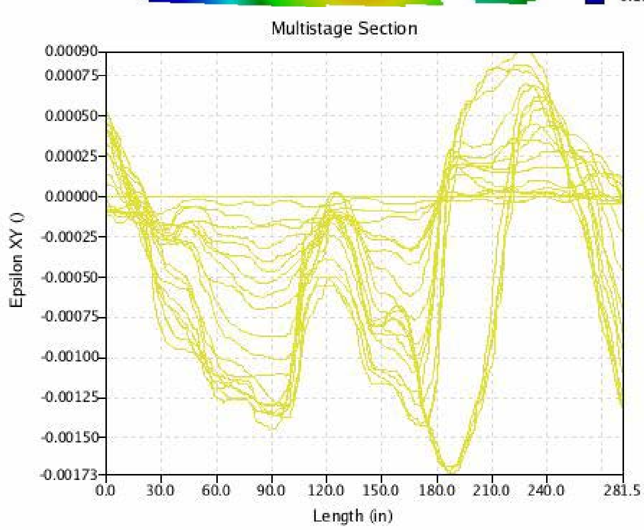
Multistage Section
Epsilon XY ()
Length (in)
0.00090
0.00075
0.00050
0.00025
0.00000
-0.00025
-0.00050
-0.00075
-0.00100
-0.00125
-0.00150
-0.00173
0.0
30.0
60.0
90.0
120.0
150.0
180.0
210.0
240.0
281.5

I1A127L1

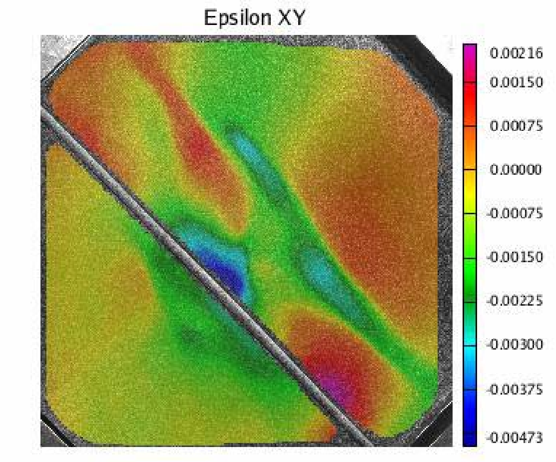
Epsilon XY
0.00216
0.00150
0.00075
0.00000
-0.00075
-0.00150
-0.00225
-0.00300
-0.00375
-0.00473

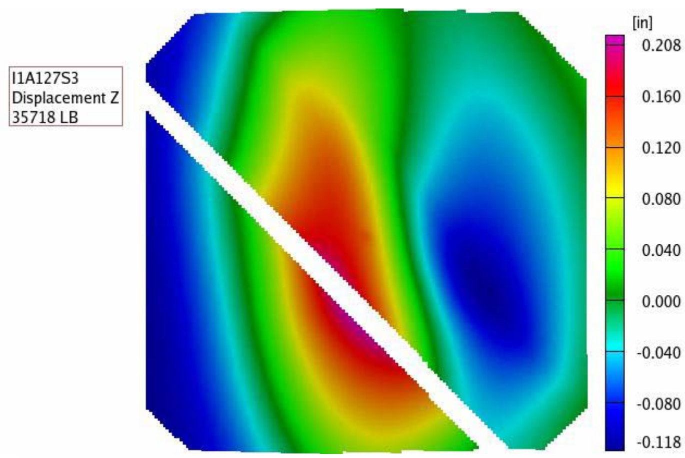
I1A127S3
Displacement Z
35718 LB
[in]
0.208
0.160
0.120
0.080
0.040
0.000
-0.040
-0.080
-0.118

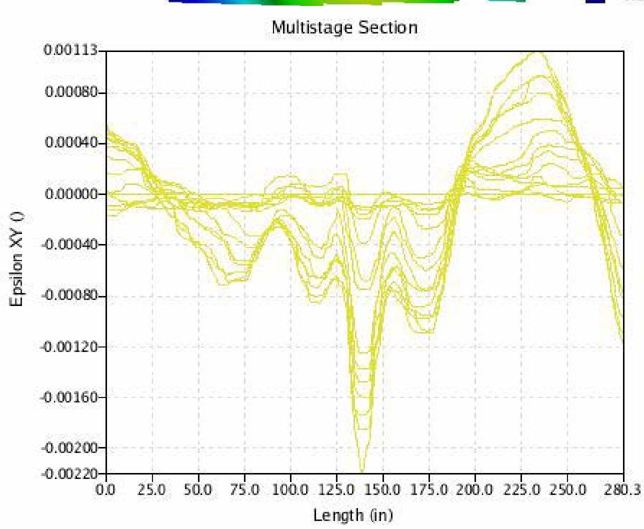
Multistage Section
Epsilon XY ()
Length (in)
0.00113
0.00080
0.00040
0.00000
-0.00040
-0.00080
-0.00120
-0.00160
-0.00200
-0.00220
0.0
25.0
50.0
75.0
100.0
125.0
150.0
175.0
200.0
225.0
250.0
280.3

I1A127S3

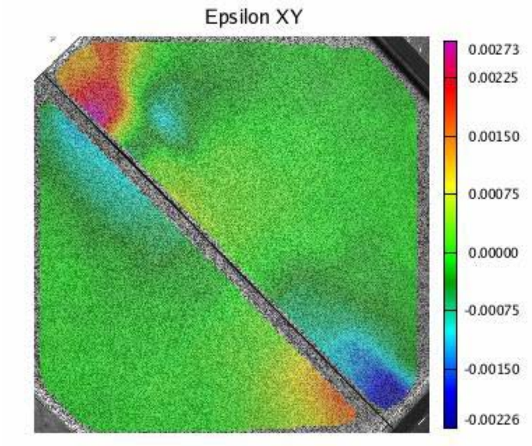
Epsilon XY
0.00273
0.00225
0.00150
0.00075
0.00000
-0.00075
-0.00150
-0.00226

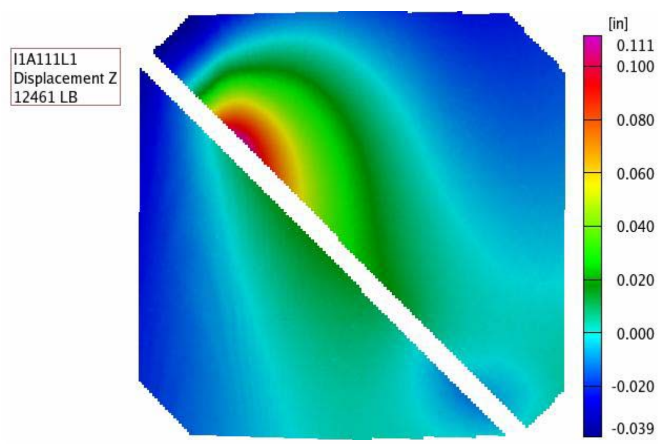
I1A111L1
Displacement Z
12461 LB
[in]
0.111
0.100
0.080
0.060
0.040
0.020
0.000
-0.020
-0.039

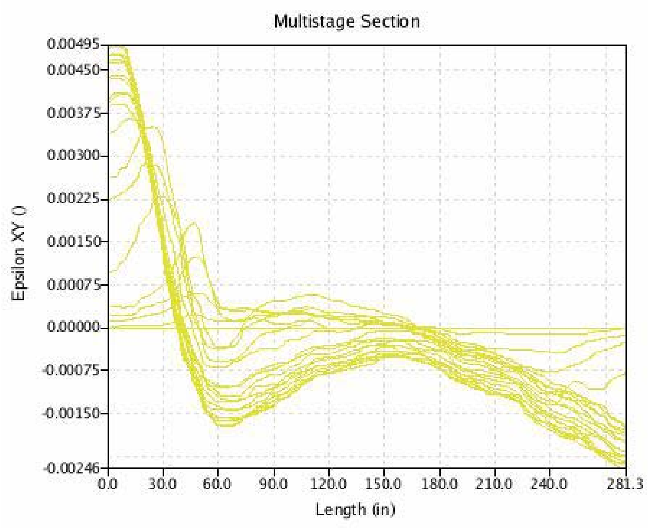
Multistage Section
Epsilon XY ()
0.00495
0.00450
0.00375
0.00300
0.00225
0.00150
0.00075
0.00000
-0.00075
-0.00150
-0.00246
0.0
30.0
60.0
90.0
120.0
150.0
180.0
210.0
240.0
281.3
Length (in)

I1A111L1

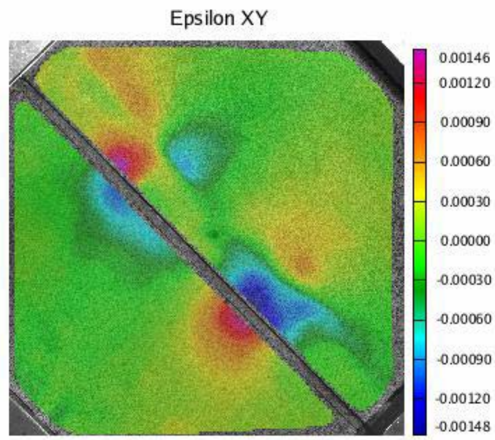
Epsilon XY
0.00146
0.00120
0.00090
0.00060
0.00030
0.00000
-0.00030
-0.00060
-0.00090
-0.00120
-0.00148

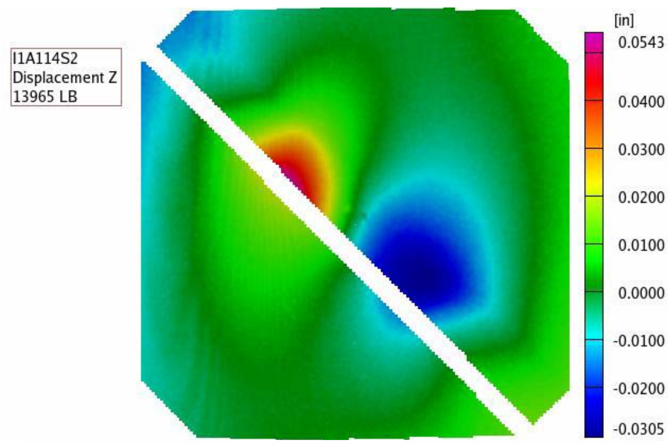
I1A114S2
Displacement Z
13965 LB
[in]
0.0543
0.0400
0.0300
0.0200
0.0100
0.0000
-0.0100
-0.0200
-0.0305

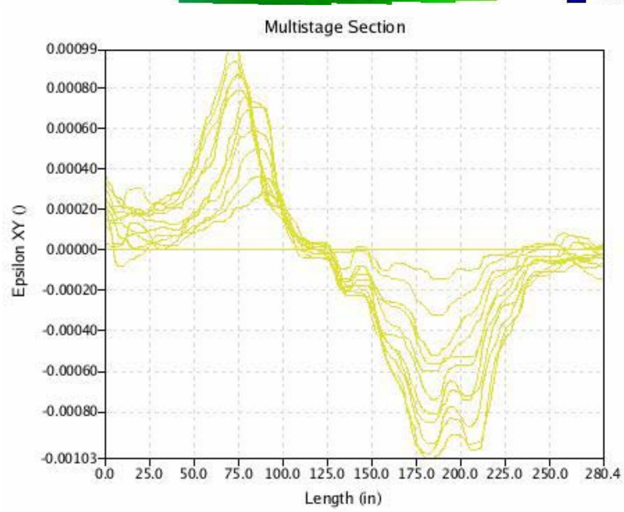
Multistage Section
Epsilon XY ()
Length (in)
0.00099
0.00080
0.00060
0.00040
0.00020
0.00000
-0.00020
-0.00040
-0.00060
-0.00080
-0.00103
0.0
25.0
50.0
75.0
100.0
125.0
150.0
175.0
200.0
225.0
250.0
280.4

I1A114S2

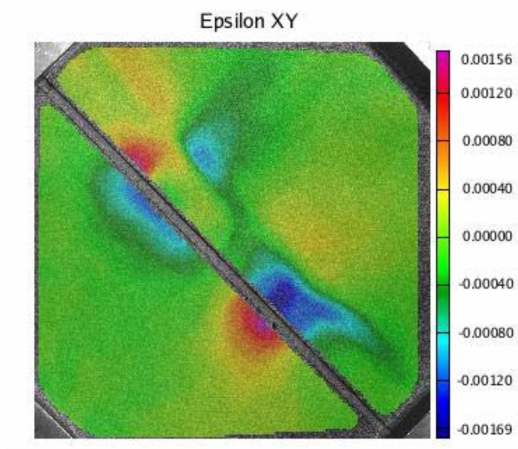
Epsilon XY
0.00156
0.00120
0.00080
0.00040
0.00000
-0.00040
-0.00080
-0.00120
-0.00169

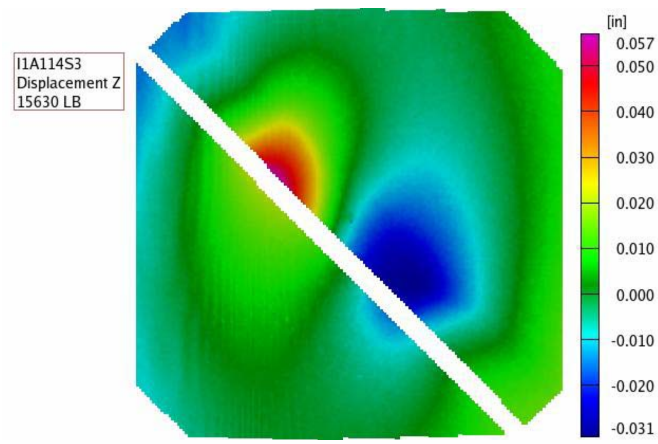
I1A114S3
Displacement Z
15630 LB
[in]
0.057
0.050
0.040
0.030
0.020
0.010
0.000
-0.010
-0.020
-0.031

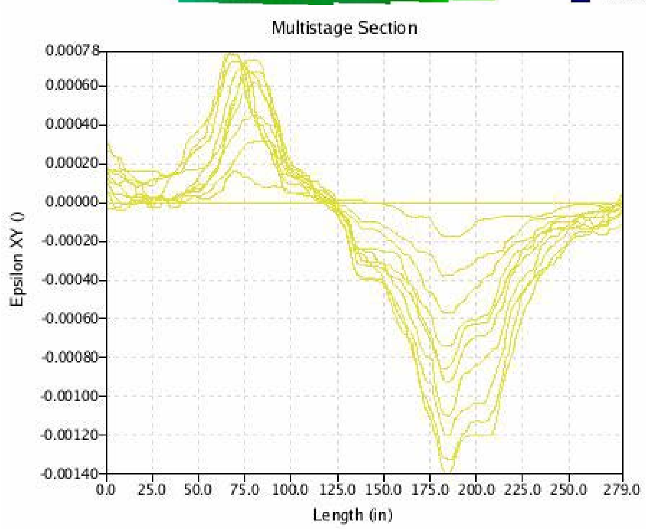
Multistage Section
Epsilon XY ()
Length (in)
0.00078
0.00060
0.00040
0.00020
0.00000
-0.00020
-0.00040
-0.00060
-0.00080
-0.00100
-0.00120
-0.00140
0.0
25.0
50.0
75.0
100.0
125.0
150.0
175.0
200.0
225.0
250.0
279.0

I1A114S3

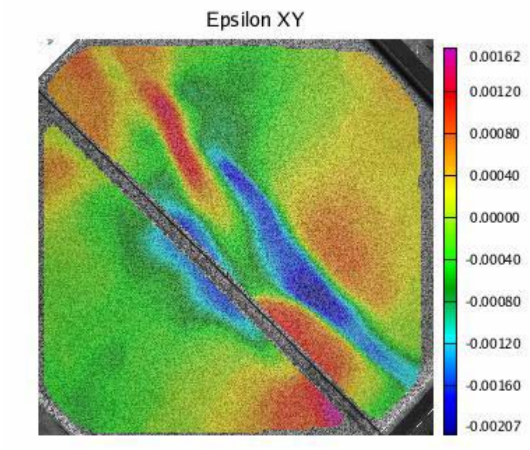
Epsilon XY
0.00162
0.00120
0.00080
0.00040
0.00000
-0.00040
-0.00080
-0.00120
-0.00160
-0.00207

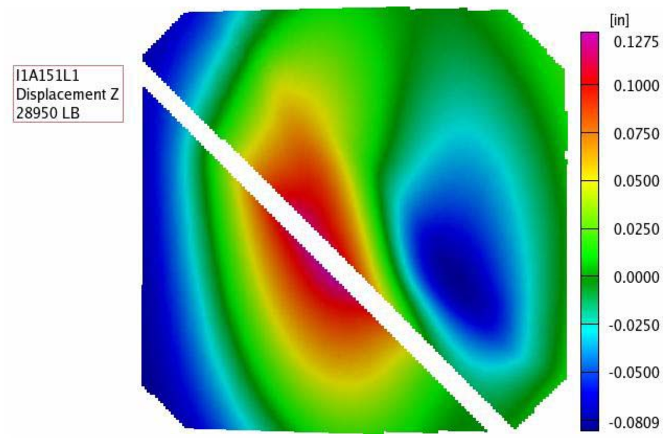
I1A151L1
Displacement Z
28950 LB
[in]
0.1275
0.1000
0.0750
0.0500
0.0250
0.0000
-0.0250
-0.0500
-0.0809

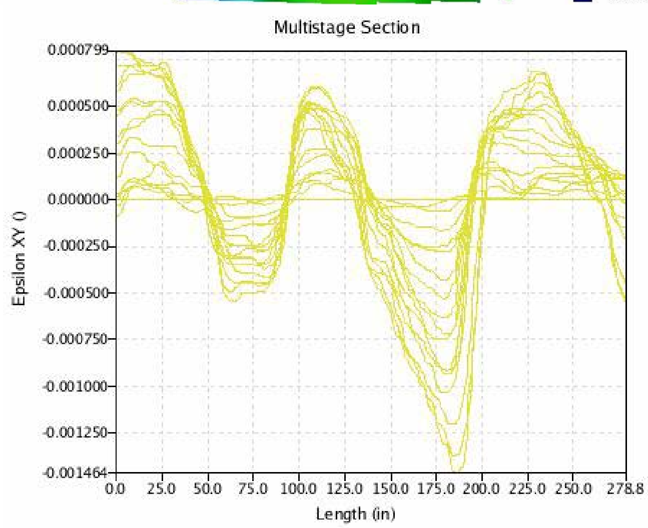
Multistage Section
0.000799
0.000500
0.000250
0.000000
-0.000250
-0.000500
-0.000750
-0.001000
-0.001250
-0.001464
Epsilon XY ()
0.0 25.0 50.0 75.0 100.0 125.0 150.0 175.0 200.0 225.0 250.0 278.8
Length (in)

I1A151L1

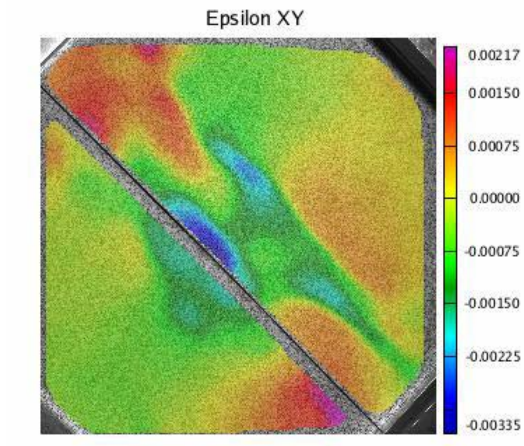
Epsilon XY
0.00217
0.00150
0.00075
0.00000
-0.00075
-0.00150
-0.00225
-0.00335

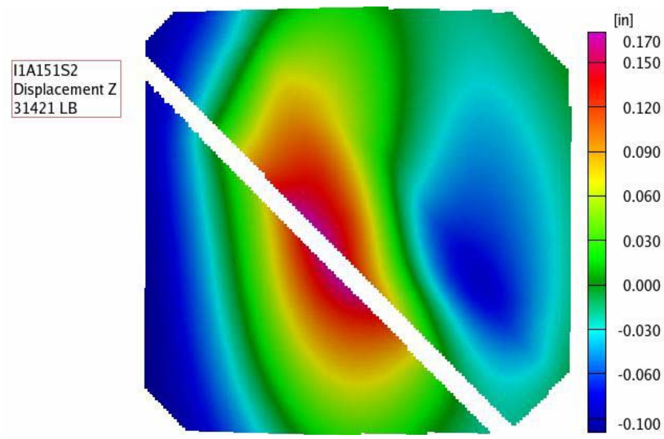
I1A151S2
Displacement Z
31421 LB
[in]
0.170
0.150
0.120
0.090
0.060
0.030
0.000
-0.030
-0.060
-0.100

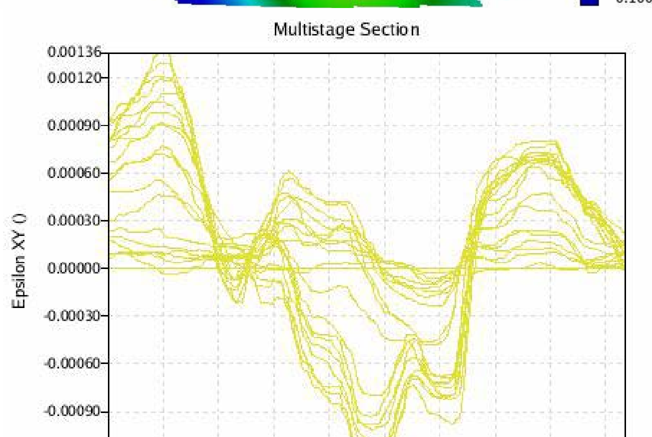
Multistage Section
0.00136
0.00120
0.00090
0.00060
0.00030
0.00000
-0.00030
-0.00060
-0.00090
-0.00130
Epsilon XY ()
0.0
30.0
60.0
90.0
120.0
150.0
180.0
210.0
240.0
280.7
Length (in)

I1A151S2

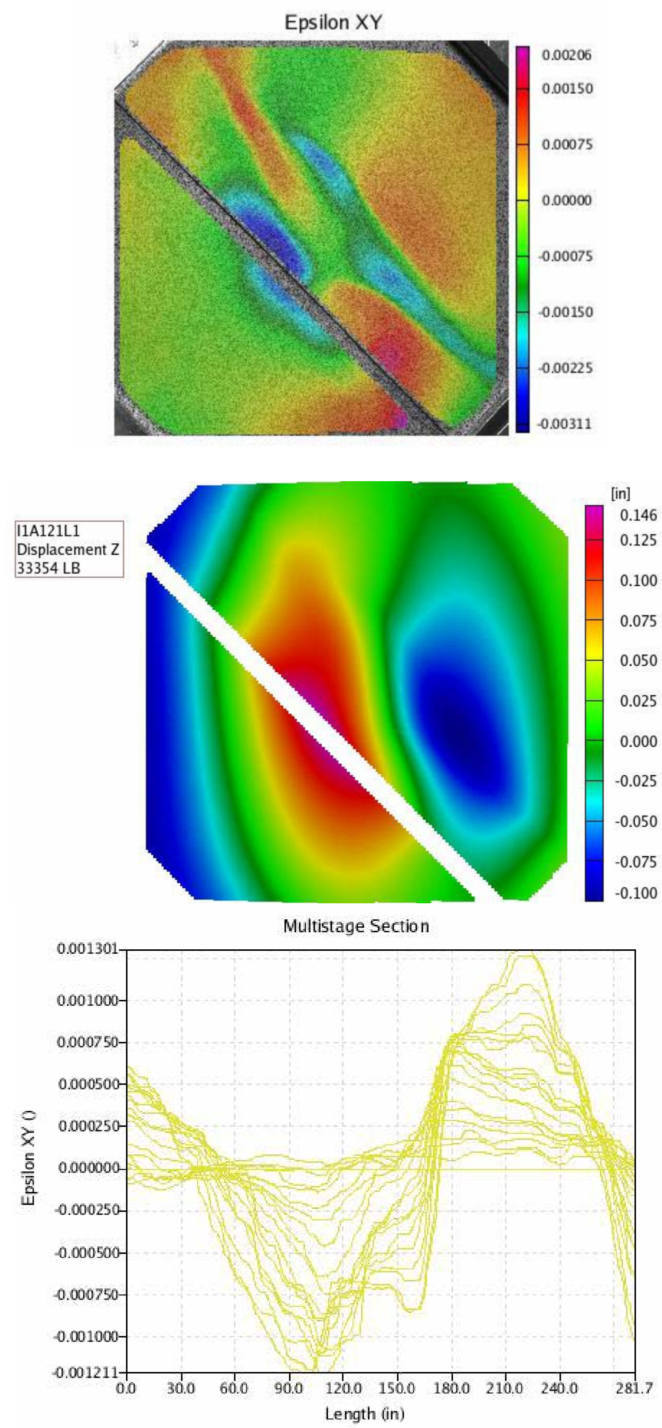
Epsilon XY
0.00206
0.00150
0.00075
0.00000
-0.00075
-0.00150
-0.00225
-0.00311
I1A121L1
Displacement Z
33354 LB
[in]
0.146
0.125
0.100
0.075
0.050
0.025
0.000
-0.025
-0.050
-0.075
-0.100
Multistage Section
0.001301
0.001000
0.000750
0.000500
0.000250
0.000000
-0.000250
-0.000500
-0.000750
-0.001000
-0.001211
Epsilon XY ()
0.0
30.0
60.0
90.0
120.0
150.0
180.0
210.0
240.0
281.7
Length (in)

I1A121L1

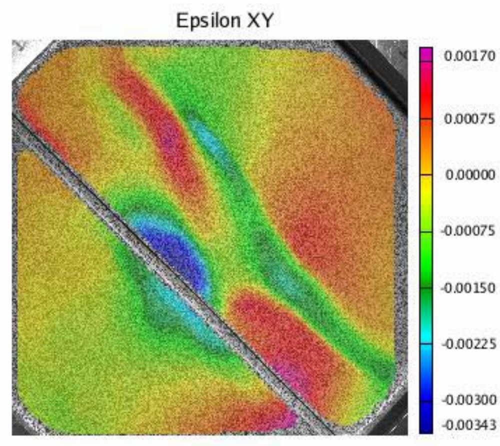
Epsilon XY
0.00170
0.00075
0.00000
-0.00075
-0.00150
-0.00225
-0.00300
-0.00343

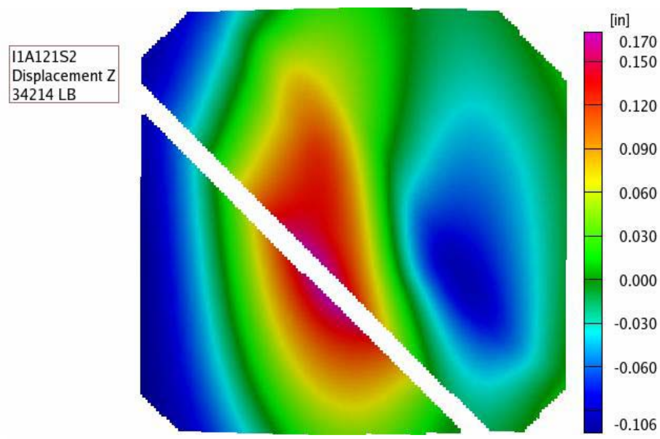
I1A121S2
Displacement Z
34214 LB
[in]
0.170
0.150
0.120
0.090
0.060
0.030
0.000
-0.030
-0.060
-0.106

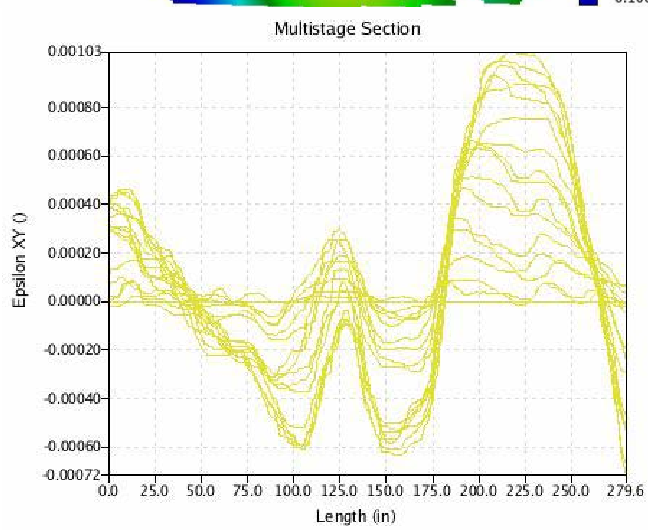
Multistage Section
Epsilon XY ()
0.00103
0.00080
0.00060
0.00040
0.00020
0.00000
-0.00020
-0.00040
-0.00060
-0.00072
0.0
25.0
50.0
75.0
100.0
125.0
150.0
175.0
200.0
225.0
250.0
279.6
Length (in)

I1A121S2

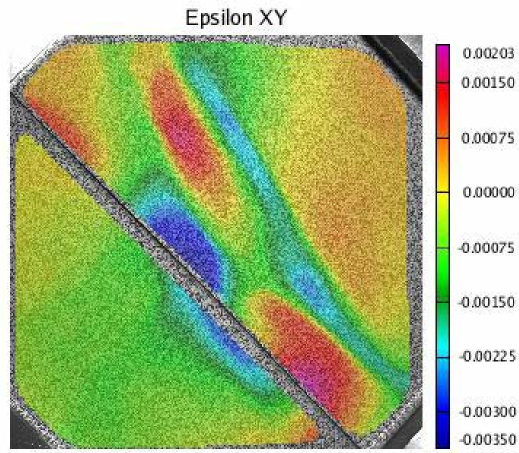

Epsilon XY
0.00203
0.00150
0.00075
0.00000
-0.00075
-0.00150
-0.00225
-0.00300
-0.00350

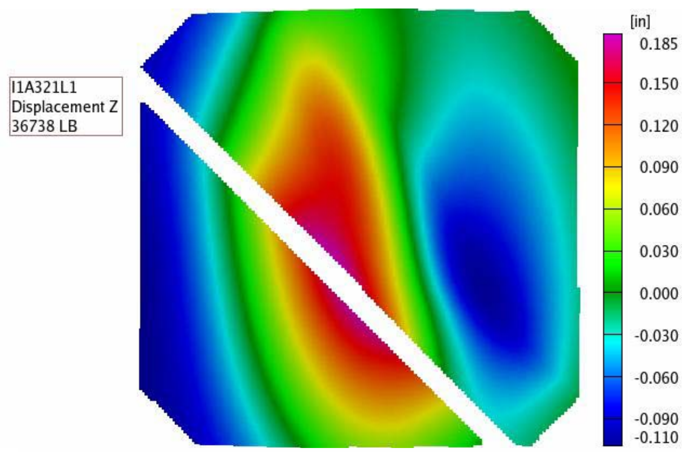

I1A321L1
Displacement Z
36738 LB
[in]
0.185
0.150
0.120
0.090
0.060
0.030
0.000
-0.030
-0.060
-0.090
-0.110

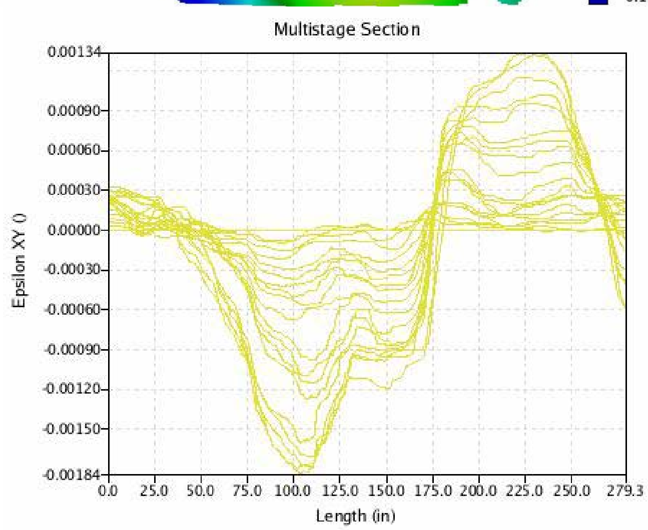

Multistage Section
Epsilon XY ()
0.00134
0.00090
0.00060
0.00030
0.00000
-0.00030
-0.00060
-0.00090
-0.00120
-0.00150
-0.00184
0.0 25.0 50.0 75.0 100.0 125.0 150.0 175.0 200.0 225.0 250.0 279.3
Length (in)

I1A321L1

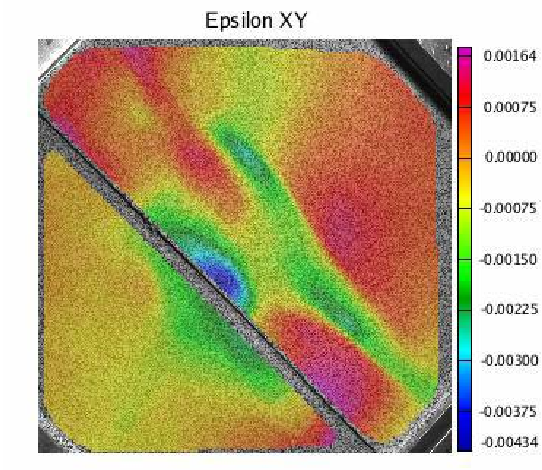
Epsilon XY
0.00164
0.00075
0.00000
-0.00075
-0.00150
-0.00225
-0.00300
-0.00375
-0.00434

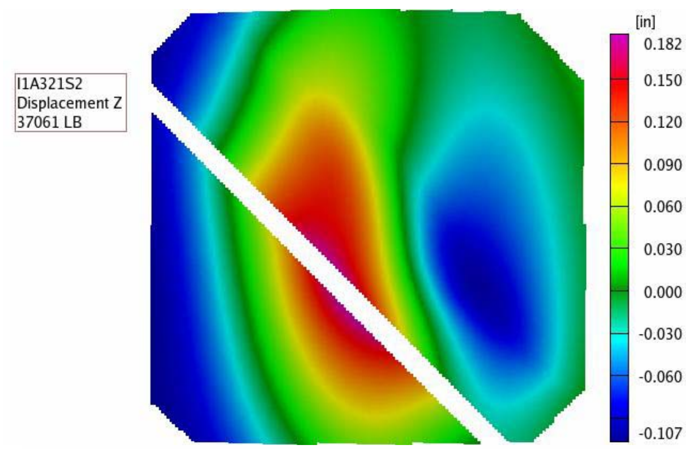
I1A321S2
Displacement Z
37061 LB
[in]
0.182
0.150
0.120
0.090
0.060
0.030
0.000
-0.030
-0.060
-0.107

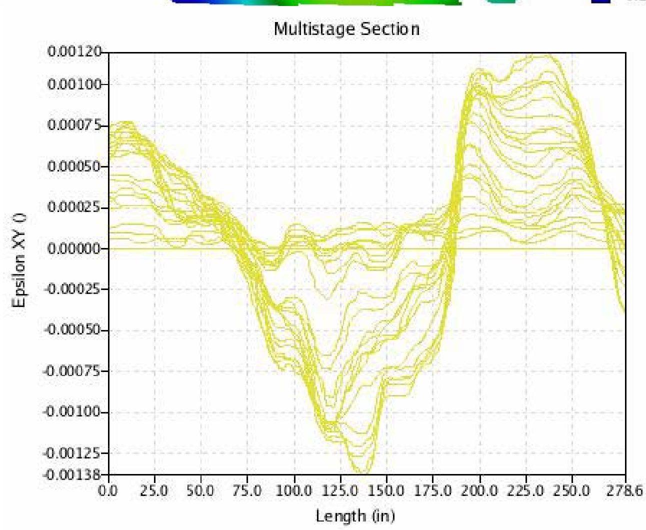
Multistage Section
Epsilon XY ()
0.00120
0.00100
0.00075
0.00050
0.00025
0.00000
-0.00025
-0.00050
-0.00075
-0.00100
-0.00125
-0.00138
0.0
25.0
50.0
75.0
100.0
125.0
150.0
175.0
200.0
225.0
250.0
278.6
Length (in)

I1A321S2

APPENDIX B—SINGLE-LAP SHEAR IMPACT TEST RESULTS

This section contains the impact test data, damage area, and residual indentation data for single-lap shear (SLS) test specimens. Figure B-1 shows the numbering system used to identify the SLS test specimens.

Task	Adhesive	Adherend	Panel Number	Impactor	Energy Level	Specimen #
I -Impact	1 -EA9394	G -FGSW	#	1 -1.00"	A - 88.5 in-lbf (10 J)	#
		P -CFPW		2 -0.75"	B - 221 in-lbf (25 J)	
		U -CFUT		3 -0.50"	B - 354 in-lbf (40 J)	

Figure B-1. Numbering System for SLS Specimens

Tables B-1 to B-3 contain all test results for F-glass satin weave (FGSW), carbon fiber plain weave (CFPW), and carbon fiber unidirectional tape (CFUT) specimens, respectively. Figures B-2 to B-4 show typical force-displacement plots for impact energy of 221 in-lbf (25 J) for FGSW, CFPW, and CFUT specimens, respectively. Figures B-5 to B-7 show typical force-displacement plots for impact energy of 88.5 in-lbf (10 J) for FGSW, CFPW, and CFUT specimens, respectively. Figures B-8 to B-10 show typical force-time plots for impact energy of 221 in-lbf (25 J) for FGSW, CFPW, and CFUT specimens, respectively. Figures B-11 to B-13 show typical force-time plots for impact energy of 88.5 in-lbf (10 J) for FGSW, CFPW, and CFUT specimens, respectively. Figures B-14 through B-16 show typical energy-time plots for impact energy of 221 in-lbf (25 J) for FGSW, CFPW, and CFUT specimens, respectively. Figures B-17 through B-19 show typical energy-time plots for impact energy of 85 in-lbf (10 J) for FGSW, CFPW, and CPUT specimens, respectively.

Table B-1. Impact Test Results for FGSW

Specimen	Bondline Thickness (in.)	Impactor Diameter (in.)	Target Impact Energy (in-lbf)	Measured Impact Energy (in-lbf)	Target Impact Velocity (ft/sec)	Measured Impact Velocity (ft/sec)	Maximum Force (lbf)	Total Energy (in-lbf)	Damage Area (in^2)	Max Surface Indentation (in.)
RSWI-G1*	0.1890	N/A	N/A	N/A	N/A	N/A	N/A	N/A	N/A	N/A
RSWI-G2*	0.1890	N/A	N/A	N/A	N/A	N/A	N/A	N/A	N/A	N/A
I1G31C1	0.1890	1.00	354.0	350.1	11.715	11.647	2207	194.7	0.606	0.010
I1G21C2	0.1900	1.00	354.0	355.1	11.623	11.637	2173	196.9	0.550	0.013
I1G61C3	0.1875	1.00	354.0	354.9	11.623	11.634	2253	199.2	0.550	0.009
I1G31B1	0.1890	1.00	221.0	221.0	9.184	9.180	1867	104.5	0.458	0.007
I1G71B2	0.1900	1.00	221.0	222.2	9.184	9.205	1400	134.6	0.426	0.011
I1G31B3	0.1890	1.00	221.0	222.2	9.184	9.205	1803	110.8	0.378	0.003
I1G61A1	0.1875	1.00	88.5	91.5	5.812	5.907	1308	31.3	0.078	
I1G61A2	0.1875	1.00	88.5	89.7	5.812	5.850	1302	30.3	0.098	
I1G22C1	0.1900	0.75	354.0	353.0	11.690	11.670	2125	192.6	0.522	0.010
I1G62C2	0.1875	0.75	354.0	352.5	11.690	11.661	2189	193.9	0.553	0.003
I1G22C3	0.1900	0.75	354.0	352.8	11.690	11.666	2118	195.5	0.550	0.007
I1G32B1	0.1890	0.75	221.0	224.7	9.237	9.310	1853	105.6	0.424	0.004
I1G42B2	0.1885	0.75	221.0	221.7	9.237	9.247	1888	93.2	0.419	0.002
I1G42B3	0.1885	0.75	221.0	221.1	9.237	9.236	1872	92.8	0.382	0.007
I1G42A1	0.1885	0.75	88.5	82.1	5.845	5.627	1191	26.6	0.092	
I1G42A2	0.1885	0.75	88.5	91.6	5.845	5.945	1261	27.6	0.087	
I1G53C2	0.1933	0.50	354.0	355.4	11.715	11.735	1951	249.3	0.654	0.008
I1G83C3	0.1900	0.50	354.0	357.8	11.715	11.783	1905	209.3	0.641	0.014
I1G53C4	0.1933	0.50	354.0	358.2	11.724	11.790	1904	217.8	0.677	0.010
I1G53B1	0.1933	0.50	221.0	222.2	9.257	9.278	1789	107.8	0.516	0.001
I1G53B4	0.1933	0.50	221.0	225.0	9.263	9.343	1783	107.8	0.470	0.013
I1G73B5	0.1900	0.50	221.0	224.5	9.263	9.334	1787	110.4	0.388	0.001
I1G73A2	0.1900	0.50	88.5	91.3	5.862	5.953	1115	27.8	0.092	
I1G73A3	0.1900	0.50	88.5	87.4	5.862	5.825	1202	26.8	0.095	

*Unimpacted baseline specimens

Table B-2. Impact Test Results for CFPW Test Specimens

Specimen	Bondline Thickness (in.)	Impactor Diameter (in.)	Target Impact Energy (in-lbf)	Measured Impact Energy (in-lbf)	Target Impact Velocity (ft/sec)	Measured Impact Velocity (ft/sec)	Maximum Force (lbf)	Total Energy (in-lbf)	Damage Area (in^2)	Max Surface Indentation (in.)
RSWI-P1 *	0.1505	N/A	N/A	N/A	N/A	N/A	N/A	N/A	N/A	N/A
RSWI-P2 *	0.1505	N/A	N/A	N/A	N/A	N/A	N/A	N/A	N/A	N/A
I1P41C1	0.1505	1.00	354.0	356.3	11.615	11.648	2244	217.1	4.213	0.005
I1P91C2	0.1423	1.00	354.0	351.6	11.623	11.579	2423	183.2	5.782	0.005
I1P11C3	0.1422	1.00	354.0	353.8	11.623	11.617	2204	203.2	5.098	0.008
I1P61B1	0.1467	1.00	221.0	220.5	9.184	9.169	1886	113.0	1.685	0.002
I1P61B2	0.1467	1.00	221.0	220.3	9.184	9.165	1911	105.6	3.378	0.001
I1P61B3	0.1467	1.00	221.0	219.9	9.184	9.157	1962	106.5	3.064	0.010
I1P41A1	0.1505	1.00	88.5	89.4	5.812	5.840	1208	42.4	0.645	
I1P81A2	0.1477	1.00	88.5	88.8	5.812	5.821	1190	40.4	0.640	
I1P52C1	0.1482	0.75	354.0	351.8	11.694	11.654	2036	262.1	3.002	0.024
I1P62C2	0.1467	0.75	354.0	355.3	11.694	11.713	1987	253.7	3.742	0.014
I1P52C3	0.1482	0.75	354.0	353.7	11.694	11.686	1937	284.9	2.562	0.027
I1P92B1	0.1423	0.75	221.0	220.7	9.240	9.231	1877	109.0	3.409	0.001
I1P52B2	0.1483	0.75	221.0	220.2	9.240	9.220	1850	107.1	2.980	0.011
I1P52B3	0.1483	0.75	221.0	220.4	9.240	9.225	1902	107.8	1.526	0.001
I1P92A1	0.1423	0.75	88.5	88.9	5.847	5.858	1165	38.5	0.670	
I1P92A2	0.1423	0.75	88.5	88.9	5.847	5.859	1149	39.9	0.864	
I1P43C1	0.1505	0.50	354.0	354.0	11.724	11.720	1689	317.1	1.377	0.073
I1P43C2	0.1505	0.50	354.0	353.8	11.715	11.709	1573	333.6	0.889	0.090
I1P83C3	0.1477	0.50	354.0	354.6	11.724	11.731	1728	350.8	1.545	0.133
I1P23B1	0.1495	0.50	221.0	220.6	9.263	9.251	1710	146.3	1.888	0.010
I1P23B2	0.1495	0.50	221.0	220.3	9.263	9.246	1628	143.0	1.512	0.013
I1P43B4	0.1464	0.50	221.0	224.5	9.257	9.327	1597	128.2	1.160	0.004
I1P23A1	0.1500	0.50	88.5	89.4	5.862	5.889	1145	38.7	0.798	
I1P23A2	0.1422	0.50	88.5	88.8	5.862	5.871	1139	37.8	0.808	

*Unimpacted baseline specimens

Table B-3. Impact Test Results for CFUT Test Specimens

Specimen	Bondline Thickness (in.)	Impactor Diameter (in.)	Target Impact Energy (in-lbf)	Measured Impact Energy (in-lbf)	Target Impact Velocity (ft/sec)	Measured Impact Velocity (ft/sec)	Maximum Force (lbf)	Total Energy (in-lbf)	Damage Area (in^2)	Max Surface Indentation (in.)
RSWI-U1 *	0.1310	N/A	N/A	N/A	N/A	N/A	N/A	N/A	N/A	N/A
RSWI-U2 *	0.1310	N/A	N/A	N/A	N/A	N/A	N/A	N/A	N/A	N/A
I1U31C1	0.1310	1.00	354.0	352.2	11.623	11.589	2053	220.9	0.907	0.005
I1U31C2	0.1310	1.00	354.0	353.9	11.623	11.618	2225	221.4	1.166	0.007
I1U51C4	0.1337	1.00	354.0	356.9	11.615	11.659	2287	188.5	0.972	0.010
I1U21B1	0.1302	1.00	221.0	218.8	9.184	9.135	1922	121.2	0.600	0.002
I1U21B2	0.1302	1.00	221.0	220.3	9.184	9.167	1923	128.5	0.753	0.008
I1U21B3	0.1350	1.00	221.0	217.5	9.184	9.107	2060	124.0	1.000	0.011
I1U61A1	0.1350	1.00	88.5	90.7	5.812	5.880	1260	36.9	0.120	
I1U21A2	0.1291	1.00	88.5	88.4	5.812	5.806	1276	34.0	0.098	
I1U72C1	0.1317	0.75	354.0	350.9	11.694	11.640	1899	252.0	1.028	0.015
I1U42C2	0.1328	0.75	354.0	354.1	11.694	11.692	1967	235.4	1.355	0.016
I1U42C3	0.1328	0.75	354.0	353.8	11.694	11.688	1952	272.6	1.224	0.021
I1U12B1	0.1326	0.75	221.0	220.7	9.240	9.230	1804	123.2	0.637	0.004
I1U12B2	0.1326	0.75	221.0	220.0	9.240	9.216	1856	126.2	0.601	0.010
I1U12B3	0.1326	0.75	221.0	219.6	9.240	9.208	1775	121.0	0.623	0.007
I1U12A1	0.1292	0.75	88.5	89.3	5.847	5.873	1255	38.0	0.256	
I1U52A2	0.1337	0.75	88.5	89.4	5.847	5.876	1236	34.8	0.319	
I1U53C1	0.1339	0.50	354.0	355.9	11.715	11.742	1591	314.7	0.753	0.064
I1U73C2	0.1324	0.50	354.0	353.6	11.724	11.714	1593	295.0	0.864	0.067
I1U53C3	0.1339	0.50	354.0	352.7	11.724	11.699	1662	324.1	0.994	0.132
I1U43B1	0.1325	0.50	221.0	222.1	9.263	9.283	1530	122.0	0.806	0.007
I1U73B2	0.1317	0.50	221.0	222.4	9.263	9.290	1592	142.0	0.678	0.014
I1U33B3	0.1335	0.50	221.0	222.3	9.257	9.281	1542	132.9	0.582	0.013
I1U63A1	0.1351	0.50	88.5	89.3	5.862	5.888	1153	35.1	0.357	
I1U63A2	0.1351	0.50	88.5	89.5	5.862	5.893	1217	35.3	0.261	

*Unimpacted baseline specimens

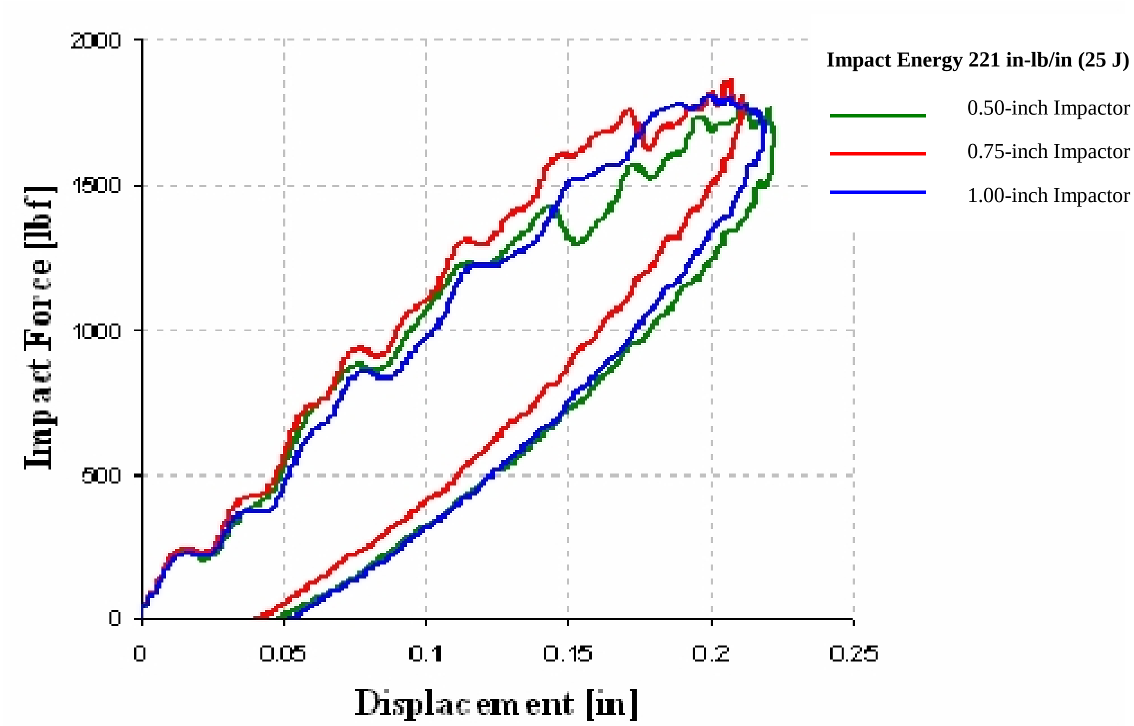

Figure B-2. Typical Force vs Displacement Plot for FGSW

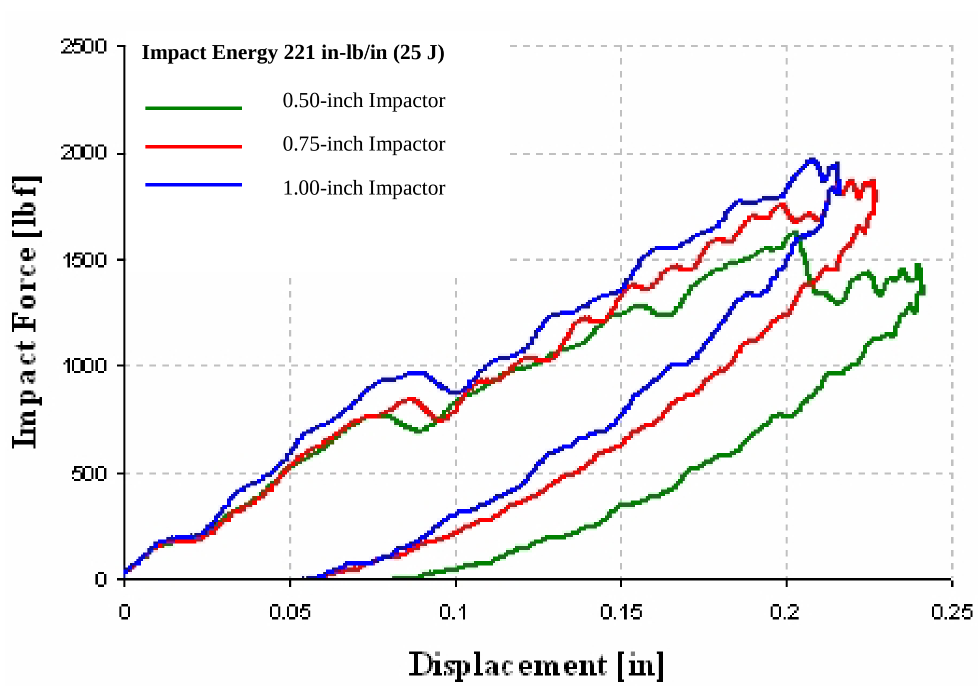

Figure B-3. Typical Force vs Displacement Plot for CFPW

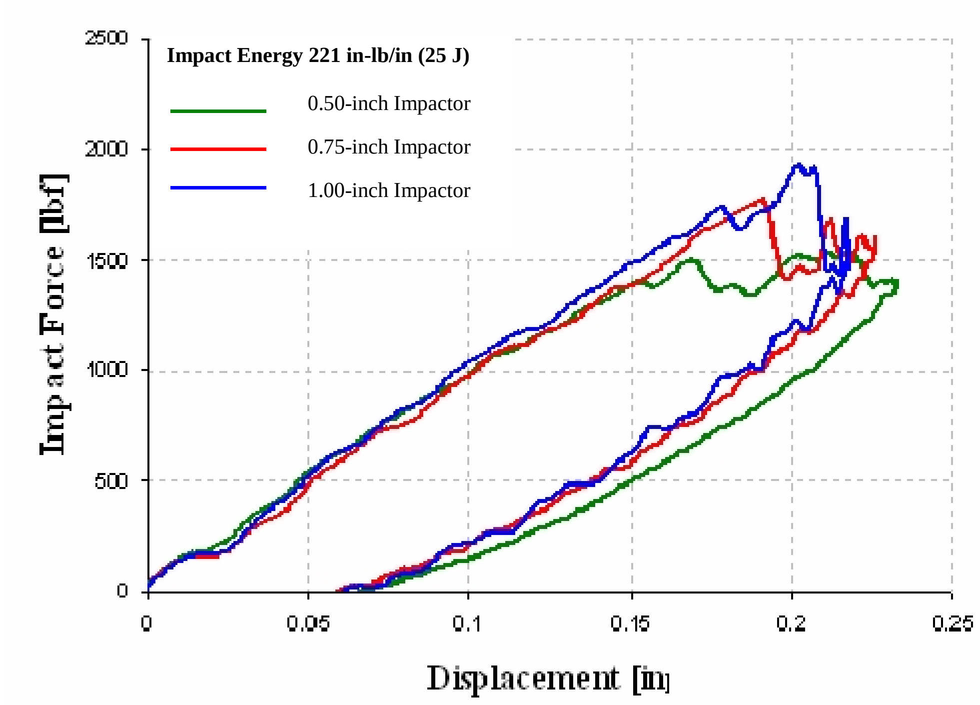

Figure B-4. Typical Force vs Displacement Plot for CFUT

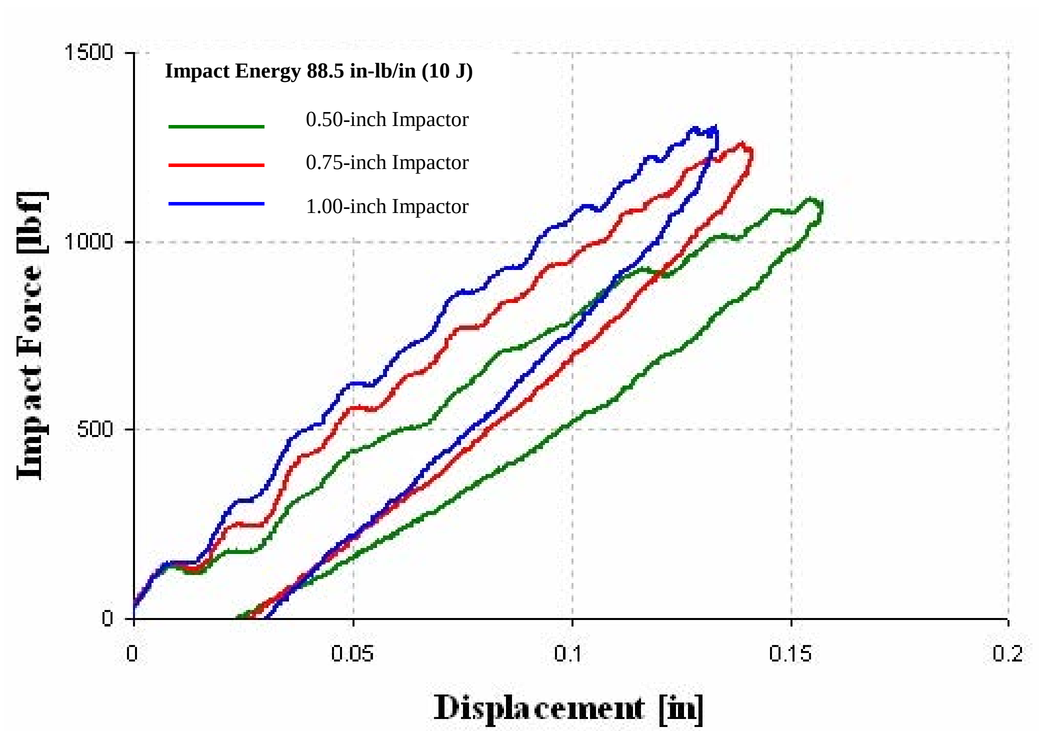

Figure B-5. Typical Force vs Displacement Plot for FGSW

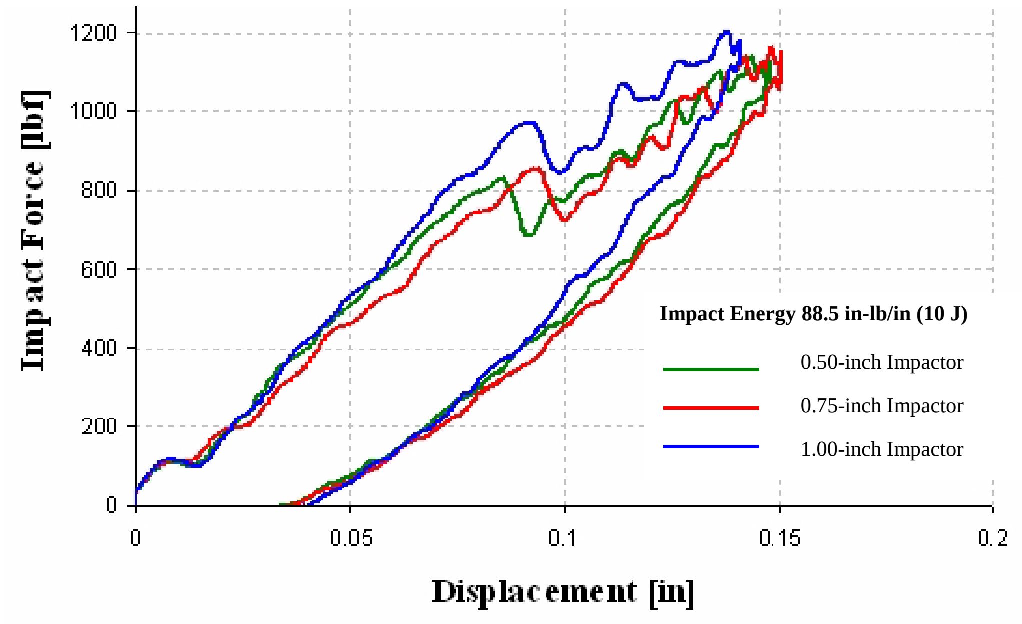

Figure B-6. Typical Force vs Displacement Plot for CFPW

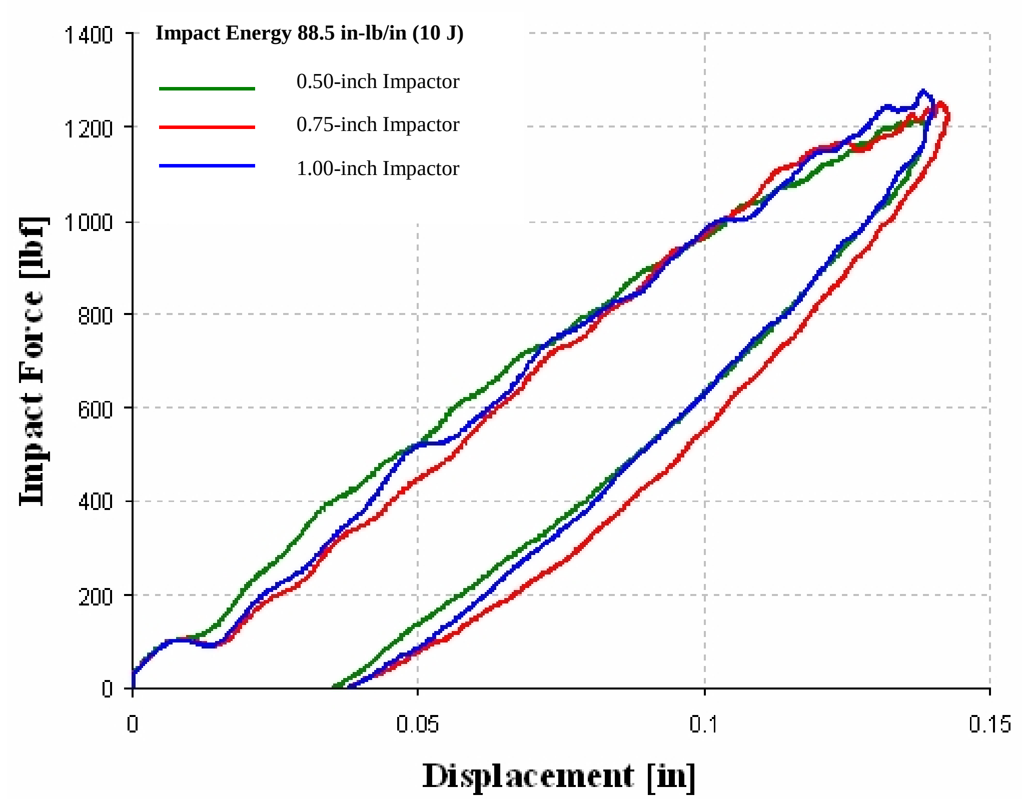

Figure B-7. Typical Force vs Displacement Plot for CFUT

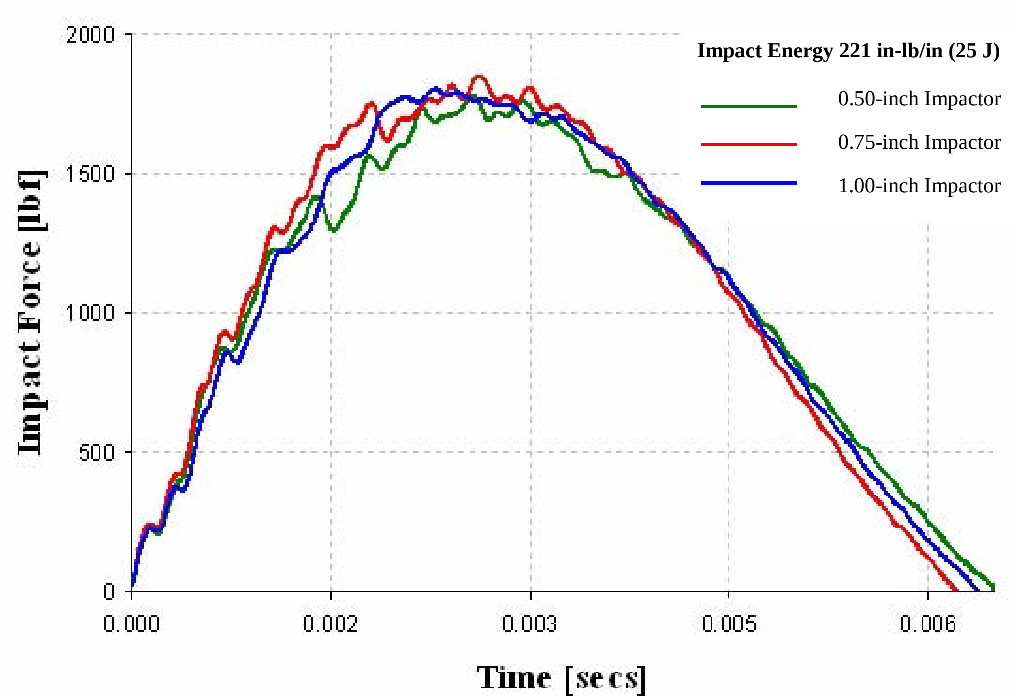

Figure B-8. Typical Force vs Time Plot for FGSW

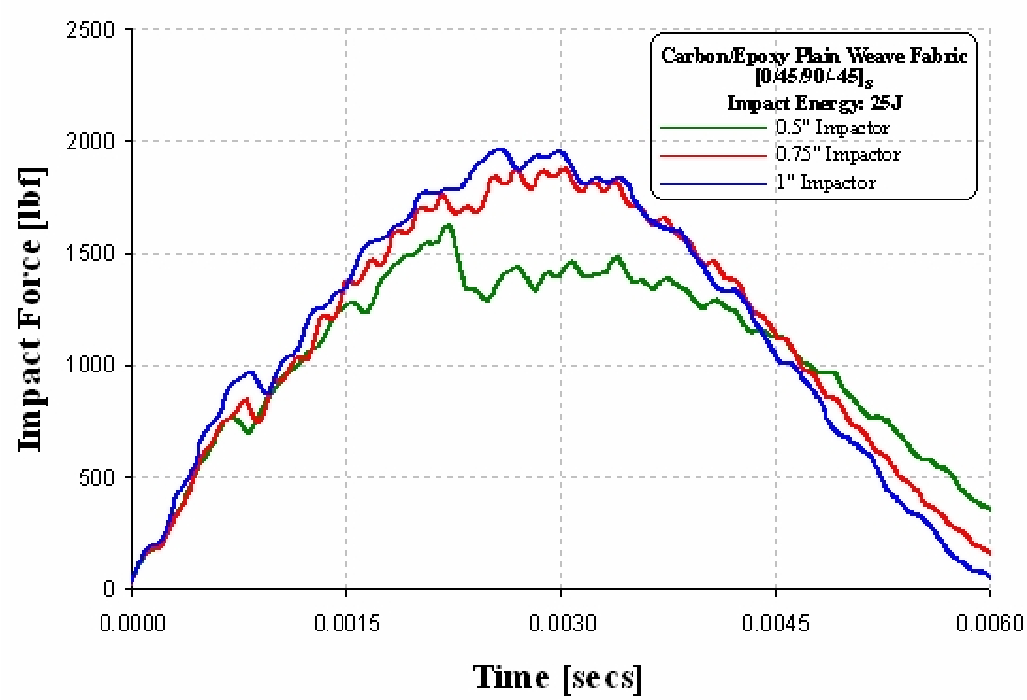

Figure B-9. Typical Force vs Time Plot for CFPW

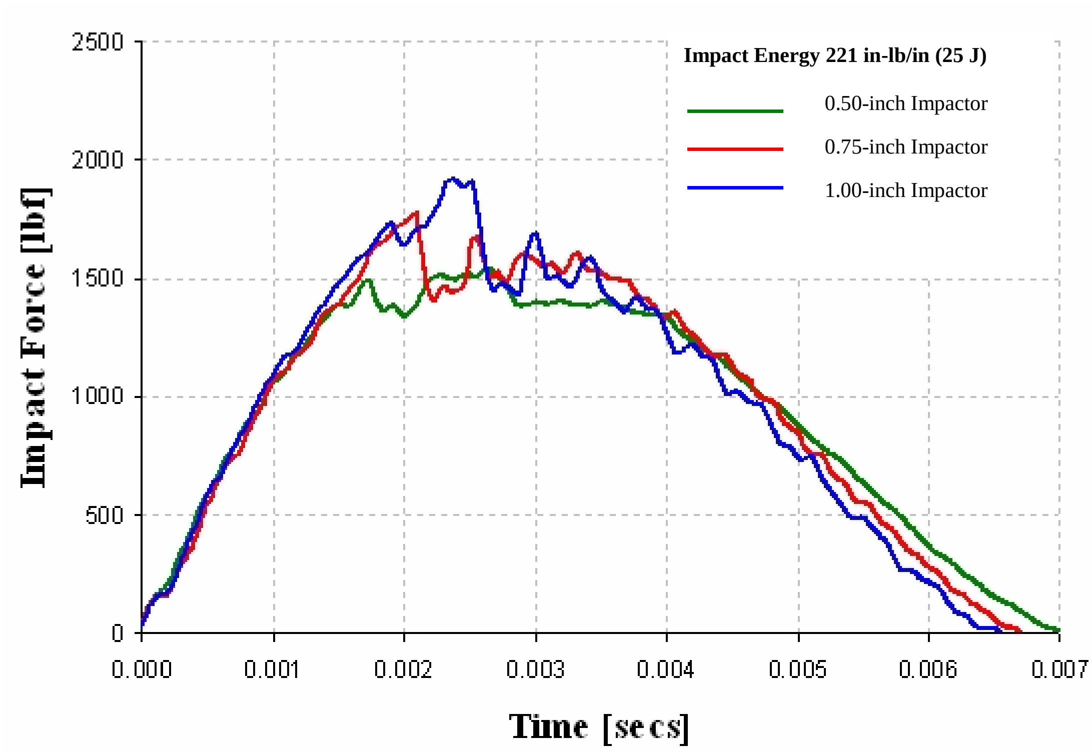

Figure B-10. Typical Force vs Time Plot for CFUT

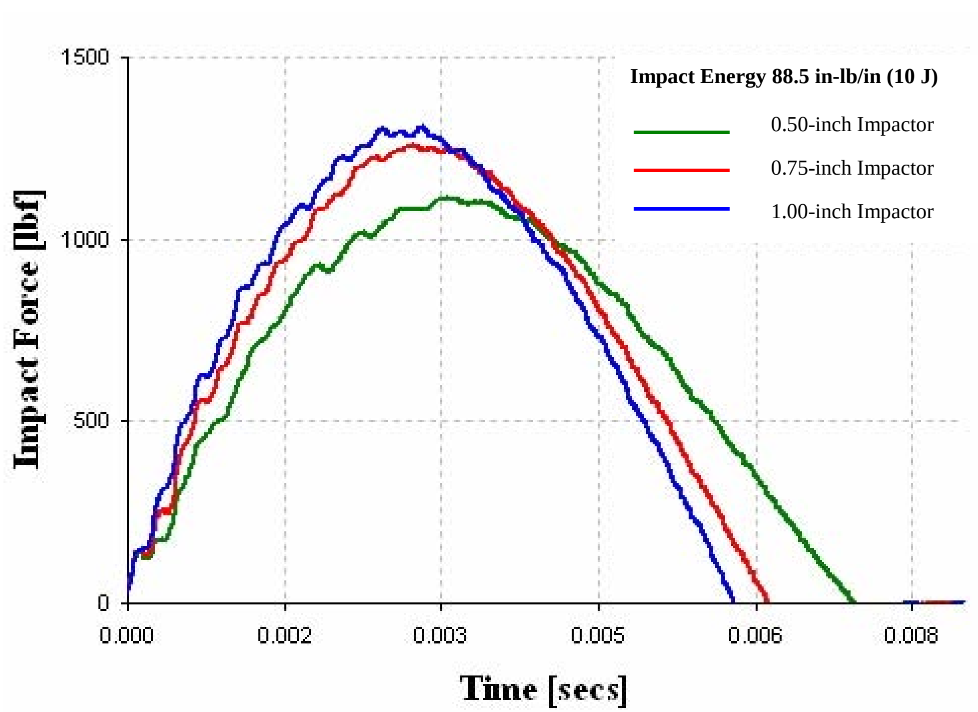

Figure B-11. Typical Force vs Time Plot for FGSW

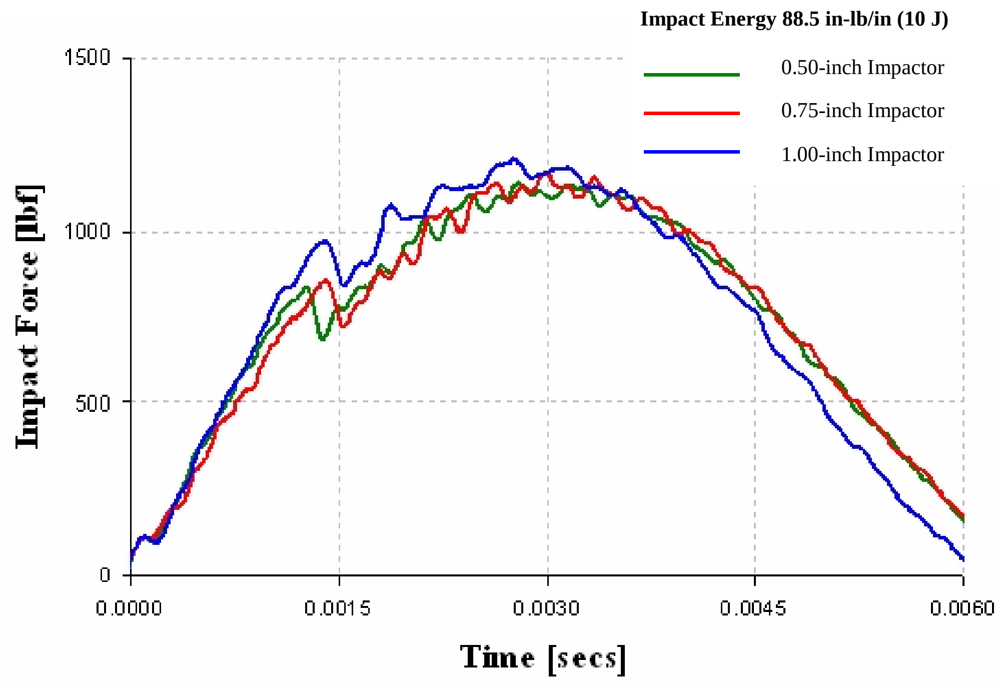

Figure B-12. Typical Force vs Time Plot for CFPW

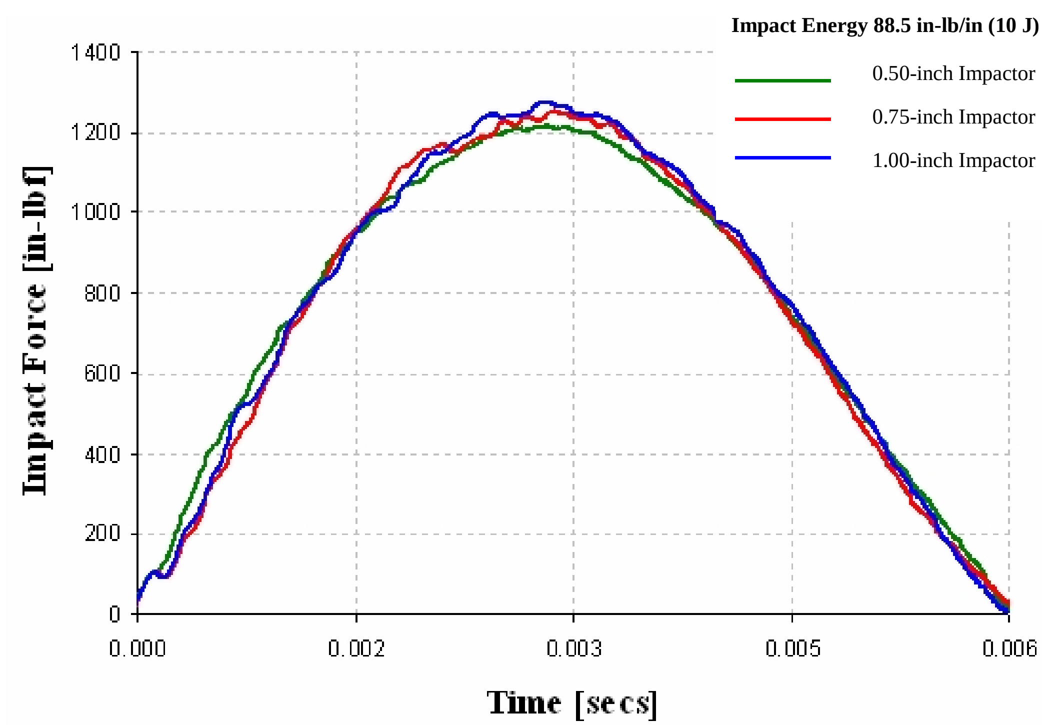

Figure B-13. Typical Force vs Time Plot for CFUT

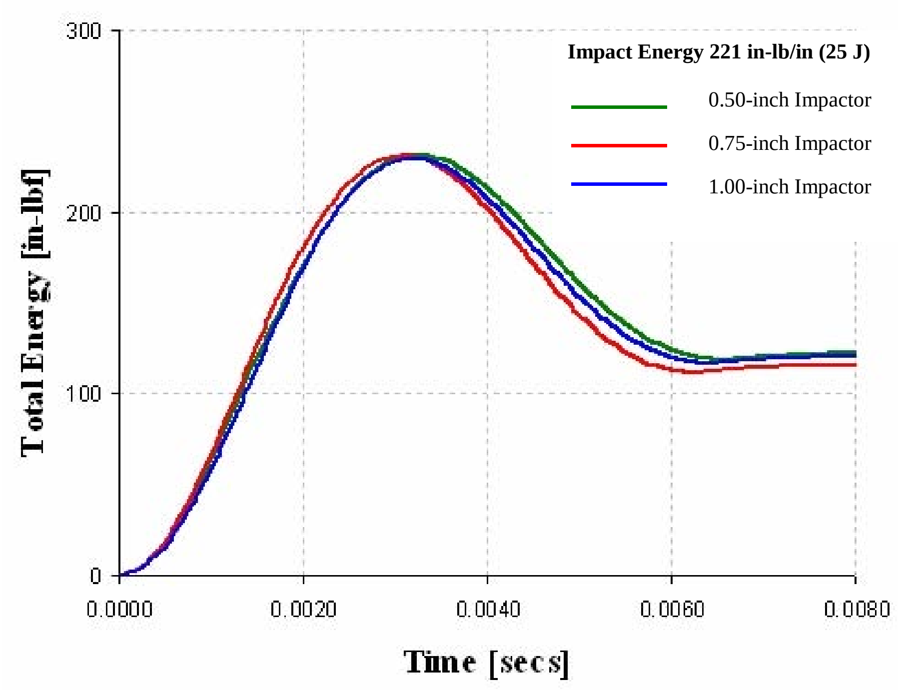

Figure B-14. Typical Energy vs Time Plot for FGSW

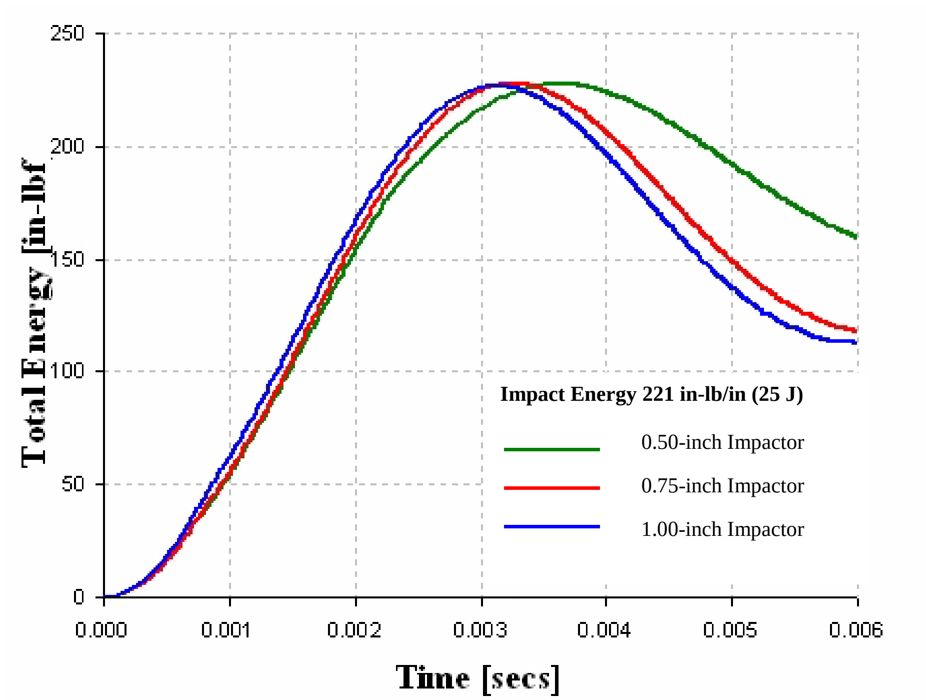

Figure B-15. Typical Energy vs Time Plot for CFPW

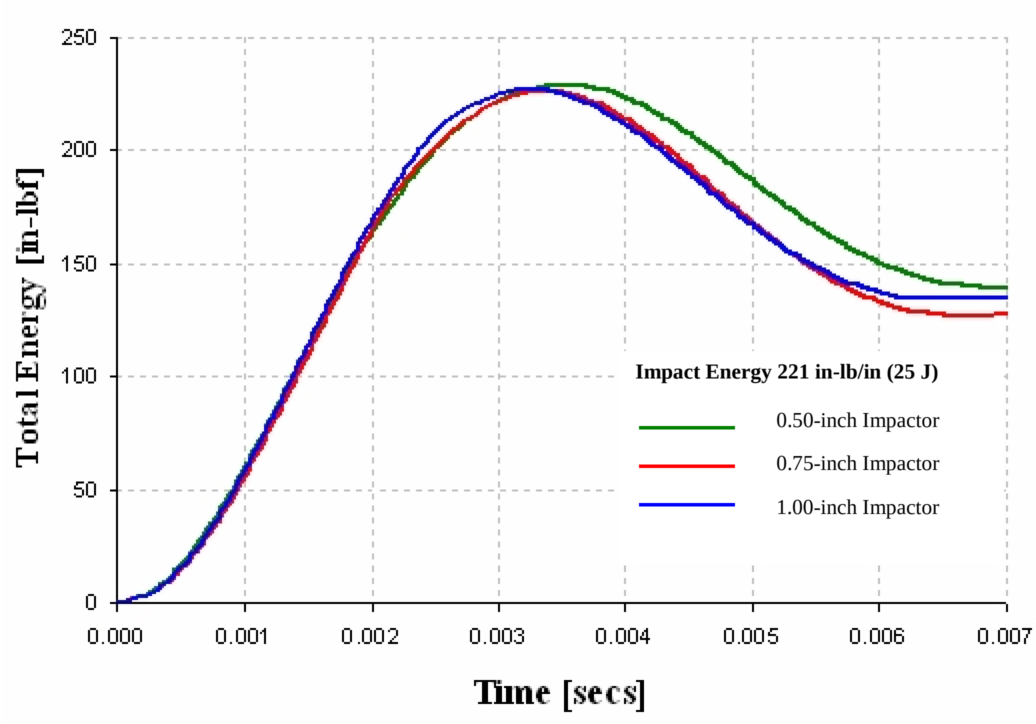

Figure B-16. Typical Energy vs Time Plot for CFUT

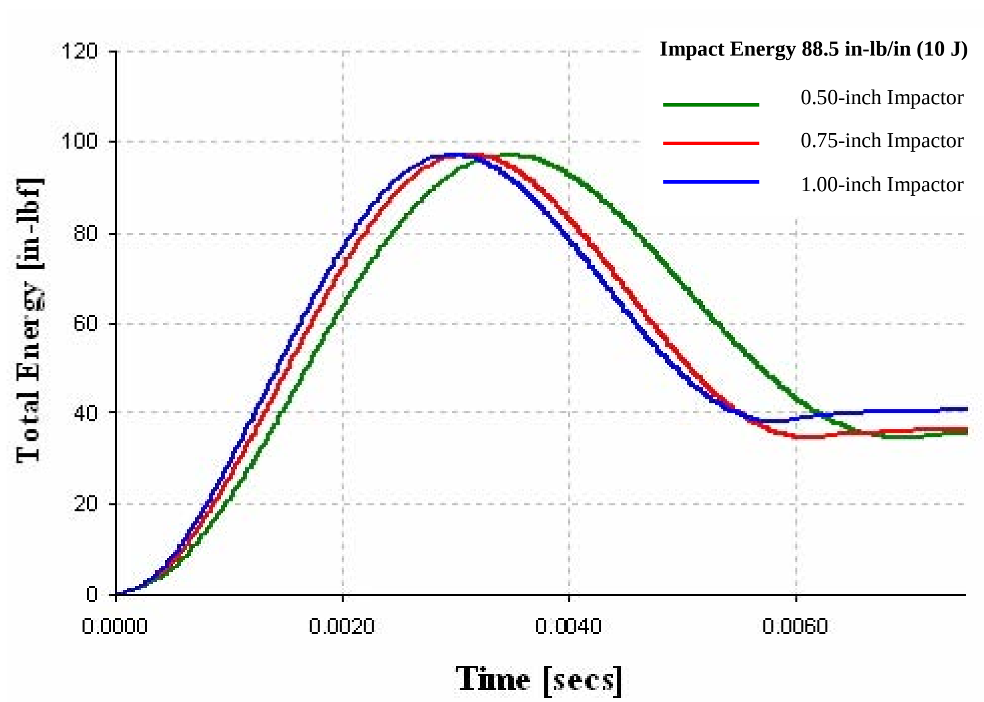

Figure B-17. Typical Energy vs Time Plot for FGSW

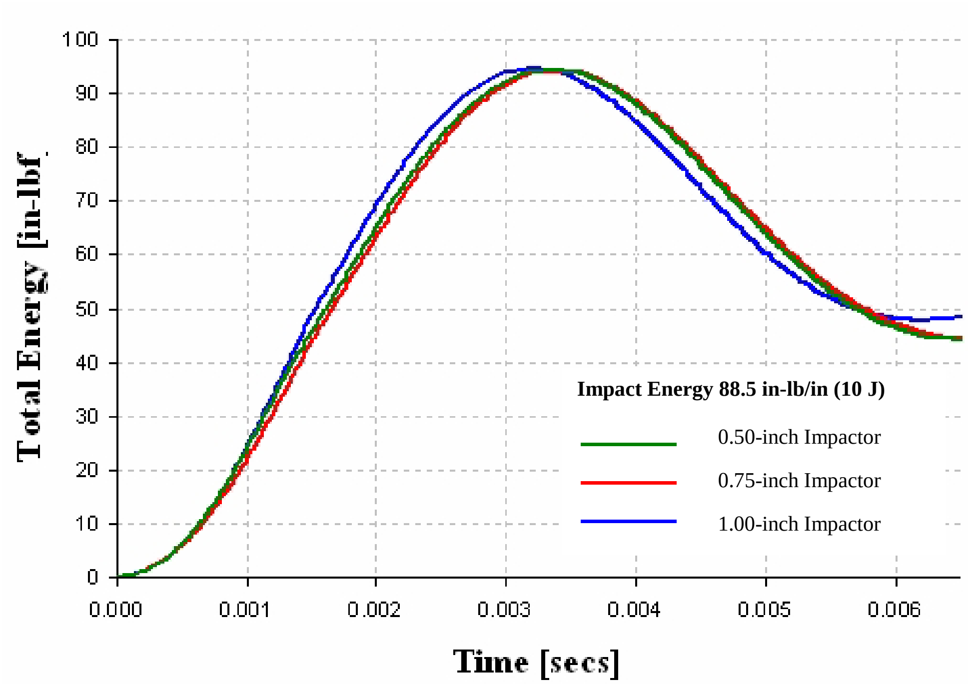

Figure B-18. Typical Energy vs Time Plot for CFPW

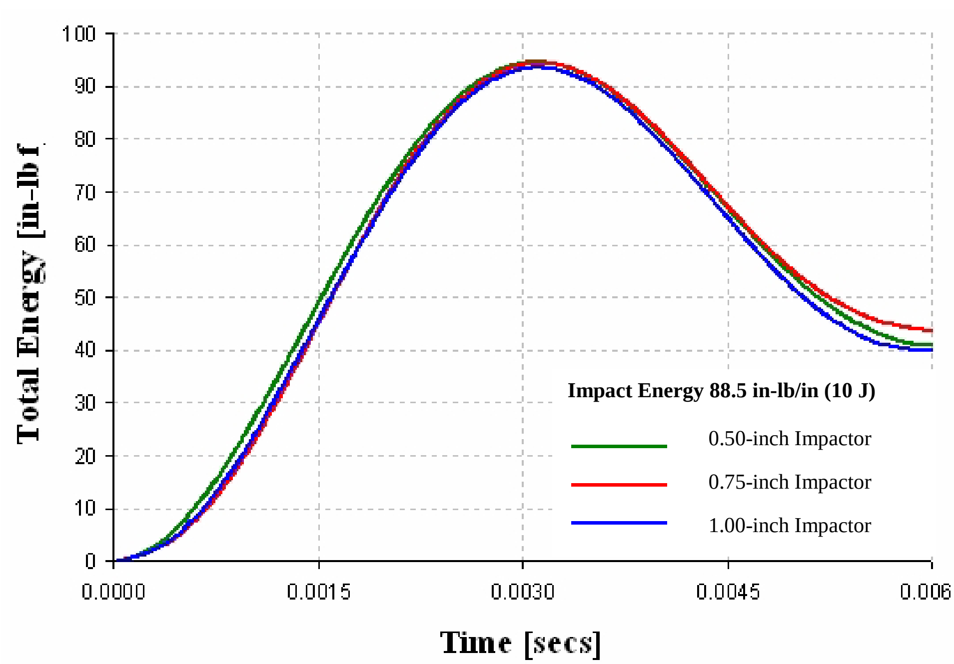

Figure B-19. Typical Energy vs Time Plot for CFUT